Università degli Studi di Padova
Dipartimento di Fisica e Astronomia “G. Galilei”

Corso di Dottorato di Ricerca in Astronomia
Ciclo XXXII
Anno Accademico 2018/2019

DEMOGRAPHY OF COMPACT-OBJECT BINARIES IN THE ERA OF MULTI-MESSENGER ASTRONOMY

Coordinatore: Prof. Giampaolo Piotto
Supervisore: Prof.ssa Michela Mapelli
Co-Supervisore: Dr. Mario Spera

Dottorando: Nicola Giacobbo

Valutatori:
Prof.ssa Rosalba Perna
Prof. Thomas Tauris

Dedication

I dedicate this work to my parents, who taught me how to walk and to Michela Rubino that decided to share the road with me.

ABSTRACT

The first direct detection of gravitational waves (GWs), GW150914, opened the era of GW astronomy. Besides GW150914, other ten GW detections were reported during the first two observing runs (O1 and O2). Nine of them are interpreted as the merger of two black holes (BHs), while the remaining one, GW170817, is associated to the merger between two neutron stars (NSs). In addition, GW170817 was accompanied by the emission of electromagnetic radiation observed over a large range of wavelengths. Now that both double BH binaries (BHBs) and double neutron stars (DNSs) have been detected by the LIGO-Virgo Collaboration (LVC), the coalescence of a NS with a BH is the only missing merger event that we expect to observe in the frequency range of ground-based GW detectors. However, preliminary analysis in the current observing run (O3) seems to suggest that a signal might be originated from merging BHNS systems.

Hence, GW detection confirmed that BHBs can merge within a Hubble time. Moreover, GW observations have proven the existence of heavy stellar-mass BHs, with mass larger than $\gtrsim 30$ $M_\odot$, and the relation between the merger of two NSs and short gamma-ray-bursts (sGRBs).

Despite the importance of stellar-born compact objects for a plethora of astrophysical processes (i.e. X-ray binary, GW emission, GRB, etc), their mass spectrum is still matter of debate. The two most important processes affecting the formation of compact stellar remnants are stellar winds and supernova (SN) explosions. Massive stars where stellar winds are effective can lose most of their mass during their life and the SN explosion at the end of their life can remove most of the remaining mass. This is expected to produce light BHs ($\lesssim 20$ $M_\odot$). On the other hand, stellar winds depend on stellar metallicity. We expect that stellar winds are more efficient in metal-rich stars than in metal-poor ones. In particular, stellar winds in metal-poor stars ($\lesssim 0.5$ $Z_\odot$) can be so ineffective that stars retain enough material to directly collapse into BHs avoiding SN explosion. In this scenario, the resulting BHs are substantially heavier. According to these predictions, massive BHs ($\gtrsim 30$ $M_\odot$) might be explained as remnants of metal-poor progenitors ($\lesssim 0.5$ $Z_\odot$).

The formation of compact-object binaries (COBs) is also matter of intense debate. A COB can merge within a Hubble time only if its initial orbital separation is of the order of tens of solar radii. What are the evolutionary channels that can lead to the formation of such extremely tight COBs?

Several pathways have been proposed for the formation of COBs and the most important one is represented by the evolution of massive isolated binaries. In fact,

the vast majority of stars, and especially massive stars, are born in binary systems. Close binary stars undergo several complex processes, that may strongly affect the mass of the final compact objects and their orbital separation (e.g. mass transfer and common envelope). Some of these processes are only barely understood.

The goal of my Thesis is to study the formation of COBs through the evolution of isolated massive binaries. My aim is to help constraining the origin of GW events observed by the LVC and to make predictions for future detections. In oder to study COBs, I used population-synthesis simulations. When I started this project, most of the available population-synthesis codes did not include the most recent stellar wind models and SN prescriptions. During my PhD, I developed MOBSE (which stands for 'Massive Objects in Binary Stellar Evolution'), a customized and upgraded version of the popular binary population-synthesis code BSE (Hurley et al., 2002). With respect to the public version of BSE, MOBSE contains up-to-date equations for metallicity-dependent stellar winds, including the dependence of stellar winds on the electron-scattering Eddington factor. Furthermore, I have implemented in MOBSE several recent prescriptions for core-collapse and electron-capture SNe, a treatment for the (pulsational) pair instability SNe and new recipes to calculate natal kicks. These ingredients are essential to capture the evolution of massive stars. In particular, with MOBSE it is possible to form BHs with mass up to $\sim 65\,M_\odot$ depending on metallicity, while with the old prescriptions we were not able to produce the most massive BHs observed by the LVC.

I used MOBSE to simulate the evolution of large grids of massive binary stars ($\gtrsim 10^8$ systems per grid). Then, I analyzed such simulations to investigate how the progenitor's metallicity (Z), common envelope (CE) and natal kicks impact the properties of the populations of (merging) COBs. I found that the most massive BHBs ($\gtrsim 100\,M_\odot$) can form only at low metallicity ($Z \lesssim 0.1 Z_\odot$). Such systems with total mass $\gtrsim 100\,M_\odot$ do not merge within a Hubble because of their large semi-major axes. Since the merger timescale by GW emission strongly depends on compact-object mass, metallicity also affects the merger rate of both BHBs and BHNSs. I defined the merger efficiency (η) as the total number of mergers integrated over a Hubble time in a coeval population divided by the total mass of that population ($\eta \propto \frac{N_{\rm mergers}}{M_{\rm tot}}$). I found that the merger efficiency is about four orders of magnitude higher at low metallicity ($\eta \sim 10^{-4}\,M_\odot^{-1}$ at $Z \simeq 0.01 Z_\odot$) than at high metallicity (η is $\sim 10^{-8}\,M_\odot^{-1}$ at $Z \simeq Z_\odot$).

From my simulations, it is also apparent that CE efficiency (measured by the parameter α) plays an important role in the formation of merging COBs. For DNSs, I found that the easier the envelope is ejected (high α), the higher η. In particular, η is

boosted by about an order of magnitude if I assume $\alpha = 5$ instead of $\alpha \leq 1$. For both BHBs and BHNSs the dependence on α is more complicated. This arises from the fact that the evolution of the radii of BH progenitors is more sensitive to metallicity and stellar radii are crucial to determine the outcome of the CE phase.

One of the important quantities that the LVC can infer from GW detections is the local merger rate density ($R_{\rm loc}$). I adopted a data-driven approach to estimate $R_{\rm loc}$ starting form my simulations. In practice, I combined η (from my simulations) with some prescriptions for the cosmological metallicity evolution and the star formation rate (SFR) density evolution. With this formalism, I have estimated a BHNS local merger rate density of up to few tens of mergers Gpc^{-3} yr^{-1} for all the different combinations of α, natal kicks, cosmological metallicity evolution and SFR I have considered, consistent with the upper limit inferred by the LVC ($R_{\rm loc,BHNS} \lesssim 610$ Gpc^{-}3yr^{-1}).

On the other hand, my prediction for the BHB merger rate density ($R_{\rm loc,BHB}$) matches that inferred by the LVC ($R_{\rm loc,BHB} \simeq 24-112$ Gpc^{-3}yr^{-1}) only for specific combinations of SFR, cosmological metallicity evolution and α. In particular, the merger rate density of BHBs is very sensitive to the cosmological metallicity evolution. Finally, I was able to match the LVC merger rate density for DNSs ($R_{\rm loc,DNS} \simeq 110-3840$ Gpc^{-3}yr^{-1}) only if I considered high α and relatively low natal kicks.

In particular, I proposed a new prescription for the treatment of natal kicks. The basic idea is that the strength of the natal kick is proportional to the mass ejected during the SN explosion as suggested by recent hydrodynamical studies. With respect to the other prescriptions currently adopted by population-synthesis codes, this new approach allows to match both the natal kick distribution of young Galactic pulsars and the local merger rate inferred by the LVC. Still, to match the LVC merger rate I needed to adopt an high CE efficiency ($\alpha \gtrsim 2$).

PAPERS

Here below you find a complete list of the papers I published during my PhD Thesis. This Thesis work is based on them (especially but not only on those papers I wrote as first author).

Published papers

M. C. Artale, M. Mapelli, Y. Bouffanais, **N. Giacobbo**, M. Pasquato, and M. Spera, *Mass and star formation rate of the host galaxies of compact binary mergers across cosmic time*, MNRAS, p. 2787, Nov 2019.

M. Toffano, M. Mapelli, **N. Giacobbo**, M. C. Artale, and G. Ghirlanda, *The host galaxies of double compact objects across cosmic time*, MNRAS, vol. 489, pp. 4622-4631, Nov 2019.

V. Baibhav, E. Berti, D. Gerosa, M. Mapelli, **N. Giacobbo**, Y. Bouffanais, and U. N. Di Carlo, *Gravitational-wave detection rates for compact binaries formed in isolation: LIGO/Virgo O3 and beyond*, Phys. Rev. D, vol. 100, p. 064060, Sep 2019.

G. Gnocchi, A. Maselli, T. Abdelsalhin, **N. Giacobbo**, and M. Mapelli, *Bounding alternative theories of gravity with multiband GW observations*, Phys. Rev. D, vol. 100, p. 064024, Sep 2019.

U. N. Di Carlo, **N. Giacobbo**, M. Mapelli, M. Pasquato, M. Spera, L. Wang, and F. Haardt, *Merging black holes in young star clusters*, MNRAS, vol. 487, pp. 2947-2960, Aug 2019.

M. C. Artale, M. Mapelli, **N. Giacobbo**, N. B. Sabha, M. Spera, F. Santoliquido, and A. Bressan, *Host galaxies of merging compact objects: mass, star formation rate, metallicity, and colours*, MNRAS, vol. 487, pp. 1675-1688, Aug 2019.

F. Zappa, S. Bernuzzi, F. Pannarale, M. Mapelli, and **N. Giacobbo**, *Black-Hole Remnants from Black-Hole-Neutron-Star Mergers*, Phys. Rev. Lett., vol. 123, p. 041102, Jul 2019.

M. Mapelli, **N. Giacobbo**, F. Santoliquido, and M. C. Artale, *The properties of merging black holes and neutron stars across cosmic time*, MNRAS, vol. 487, pp. 2-13, July 2019.

M. Spera, M. Mapelli, **N. Giacobbo**, A. A. Trani, A. Bressan, and G. Costa, *Merging black hole binaries with the SEVN code*, MNRAS, vol. 485, pp. 889-907, May 2019.

N. Giacobbo and M. Mapelli, *The impact of electron-capture supernovae on merging double neutron stars*, MNRAS, vol. 482, pp. 2234-2243, Jan. 2019.

M. Mapelli, **N. Giacobbo**, M. Toffano, E. Ripamonti, A. Bressan, M. Spera, and M. Branchesi, *The host galaxies of double compact objects merging in the local Universe*, MNRAS, vol. 481, pp. 5324-5330, Dec. 2018.

N. Giacobbo and M. Mapelli, *The progenitors of compact-object binaries: impact of metallicity, common envelope and natal kicks*, MNRAS, vol. 480, pp. 2011-2030, Oct. 2018.

M. Mapelli and **N. Giacobbo**, *The cosmic merger rate of neutron stars and black holes*, MNRAS, vol. 479, pp. 4391-4398, Oct. 2018.

N. Giacobbo, M. Mapelli, and M. Spera, *Merging black hole binaries: the effects of progenitor's metallicity, mass-loss rate and Eddington factor*, MNRAS, vol. 474, pp. 2959-2974, Mar. 2018.

M. Mapelli, **N. Giacobbo**, E. Ripamonti, and M. Spera, *The cosmic merger rate of stellar black hole binaries from the Illustris simulation*, MNRAS, vol. 472, pp. 2422-2435, Dec. 2017.

Papers under review

U. N. Di Carlo, M. Mapelli, Y. Bouffanais, **N. Giacobbo**, S. Bressan, M. Spera, and F. Haardt, *Binary black holes in the pair-instability mass gap*, arXiv e-prints, p. arXiv:1911.01434, Nov 2019.

N. Giacobbo and M. Mapelli, *Revising natal kick prescriptions in population synthesis simulations*, arXiv e-prints, p. arXiv:1909.06385, Sep 2019.

M. Mapelli, M. Spera, E. Montanari, M. Limongi, A. Chieffi, **N. Giacobbo**, and A. Bressan, *Impact of progenitor's rotation and compactness on the mass of black holes*, arXiv e-prints, p. arXiv:1909.01371, Sep 2019.

Y. Bouffanais, M. Mapelli, D. Gerosa, U. N. Di Carlo, **N. Giacobbo**, E. Berti, and V. Baibhav, *Constraining the fraction of binary black holes formed in isolation and young star clusters with gravitational-wave data*, arXiv e-prints, May 2019.

Table of Contents

CHAPTER 1

INTRODUCTION

On 2015 September 14, about a hundred years after the formulation of *General Relativity* (GR) by Albert Einstein (Einstein, 1915; Einstein, 1916a), one of the most exotic and wanted predictions (Einstein, 1916b; Einstein, 1918) was confirmed. Einstein himself was skeptical about the possibility of detecting gravitational radiation. Despite this, on that day the two ground-based LIGO interferometers (Aasi et al. et al. 2015) detected the very first gravitational wave (GW) signal, GW150914, which was interpreted as the merger between two black holes (BHs) at redshift $z \sim 0.1$ (Abbott et al., 2016d). GW150914 marks the beginning of a new era for astronomy and fundamental physics.
After GW150914, the LIGO-Virgo collaboration (LVC) has observed other ten binary BHs and one binary neutron star (NS; Abbott et al., 2016a; Abbott et al., 2016b; Abbott et al., 2016c; Abbott et al., 2017b; Abbott et al., 2017e; Abbott et al., 2017a). In 2017, the Virgo interferometer in Italy joined the two LIGO detectors, leading to a dramatic improvement in sky localization and polarization measurements. The third observing run (O3) of the LIGO interferometers has started in April 2019 and is currently ongoing. Several new triggers were already announced: we expect to know several tens of binary BHs, several binary NSs and possibly even some BHNS binaries by the end of O3.

GW detections have revolutionized our knowledge about the Universe teaching us several crucial concepts (Abbott et al., 2016a). First, GW150914 and the other binary BH mergers Abbott et al., 2018 have confirmed the existence of double black hole binaries (BHBs), as it has been predicted long time ago (Tutukov et al., 1973; Thorne, 1987; Kulkarni et al., 1993; Sigurdsson and Phinney, 1993; Bethe, 1990; Portegies Zwart and McMillan, 2000; Colpi et al., 2003; Belczynski et al., 2004), and have also proven that BHBs can merge within a Hubble time. Moreover, some of

the merging BHBs host surprisingly massive BHs ($\gtrsim 30\,M_\odot$ see Table 3 in Abbott et al., 2018), whose existence was predicted only by few models (Mapelli et al., 2009; Mapelli et al., 2010; Belczynski et al., 2010; Fryer et al., 2012; Mapelli et al., 2013; Ziosi et al., 2014; Spera et al., 2015). Before GW detections, an accurate dynamical mass estimation was available only for a dozen of BHs, all of them in the very nearby Universe (the Milky Way and other galaxies in the Local Group). The mass of these BHs is always $\lesssim 20\ M_\odot$ (Özel et al., 2010) with the possible exception of a $\approx 30\ M_\odot$ BH candidate[1] in IC 10 (Prestwich et al., 2007; Silverman and Filippenko, 2008).

Before GW150914 the existence of GWs was supported only by the observation of indirect effects. In 1974, Hulse and Taylor discovered that the decay of the orbital period of the binary pulsar PSR 1913+16 is consistent with the energy loss by gravitational radiation, according to GR (Nobel Prize 1993; Hulse and Taylor 1974; Hulse and Taylor 1975; Taylor et al. 1979). Since the discovery of PSR 1913+16, the number of similar systems observed has increased to 19 (Tauris et al., 2017; Farrow et al., 2019; Zhang et al., 2019 and references therein) and one of them is a double pulsar (Burgay et al., 2003; Lyne et al., 2004). These systems are excellent astrophysical laboratories to investigate the behaviour of matter under extreme conditions and highly relativistic processes. On 2017 August 17, the interferometers LIGO and Virgo captured the signal produced by the merger of two NSs (Abbott et al., 2017e). An electromagnetic counterpart to this signal has been observed over a wide range of wavelengths (Abbott et al., 2017f; Alexander et al., 2017; Chornock et al., 2017; Coulter et al., 2017; Cowperthwaite et al., 2017; Goldstein et al., 2017; Margutti et al., 2017; Nicholl et al., 2017; Pian et al., 2017; Soares-Santos et al., 2017; Savchenko et al., 2017), marking a new era in *multi-messenger astronomy*. In particular, the observation of a short gamma-ray burst (SGRB) GRB 170817A (Abbott et al., 2017f; Goldstein et al., 2017; Savchenko et al., 2017) in conjunction with the event GW170817 provides a strong evidence for the hypothesis that SGRBs are associated with the merger of two NSs. These are exciting times for the study of compact objects: theoretical models must meet the challenge posed by this new wealth of GW data.

In my Thesis, I have investigated the formation channels of COBs, by means of astrophysical modelling and population-synthesis simulations. This introductory chapter is organized as follows. First, I briefly discuss GWs and GW emission from

[1] The dynamical mass measurement of IC 10 X-1 is controversial, because the features interpreted as orbital velocity in the spectrum of the companion, a Wolf-Rayet star, might be the signature of stellar outflows (see Laycock et al. 2015).

compact object binaries (Section 1.1). In Section 1.2, I shortly describe the formation of compact remnants and in Section 1.3 the evolution of binary systems, as well as the main tools I have used to study them, namely population-synthesis simulations. Finally, I briefly describe the content of each Chapters in Section 1.4.

1.1 Gravitational waves

According to GR, mass distorts the geometry of space and the flow of time. It is also possible to demonstrate that such perturbations propagate at the speed of light in the form of waves. As shown by Einstein (1916b), the wave-like solution can be obtained by 'simply' solving the vacuum field equation of general relativity. The fundamental result (Einstein, 1918) is that gravitational radiation is of quadrupolar or higher nature, and is directly linked to the change of the quadrupole moment of mass distribution Q (or moment of inertia or second moment of mass). Indeed, monopole radiation is forbidden by mass conservation (in analogy with charge conservation in electromagnetic theory). The dipole moment of mass is proportional to the linear momentum, which also is a conserved quantity. It possible to obtain an estimate of the strength of a GW h, commonly called $strain$, as

$$h \simeq \frac{2G}{c^4}\frac{\ddot{Q}}{r}, \tag{1.1}$$

where r is the source distance, G is the universal gravitational constant and c is the speed of light. Let us now define the characteristic time T, as the time scale needed for a test mass to move from one side to another of the system:

$$T = \sqrt{R^3/GM}, \tag{1.2}$$

and let us remember that the moment of inertia of a system is approximately $Q \simeq MR^2$, where M is the fraction of mass that moves and R is the size of the system. Hence, if R varies over T, equation 1.1 becomes:

$$h \simeq \frac{GM}{c^4}\frac{(R/T)^2}{r} = \frac{GM}{c^2}\frac{1}{r}\frac{v^2}{c^2} = \frac{2G}{r}\frac{\epsilon E_{\rm kin}}{c^4}, \tag{1.3}$$

where v is the velocity of the moving parts of the system and ϵ (with $\epsilon \in [0-1]$) is a measure of the grade of asymmetry of the system. As a consequence, $\epsilon E_{\rm kin}$ represents the fraction of kinetic energy of the system available to produce GWs. From equation 1.3 it also emerges that only systems with a quadrupolar moment variable in time are able to produce gravitational radiation. Therefore, in analogy with the electromagnetic field, GWs are produced by an accelerated mass whose motion is

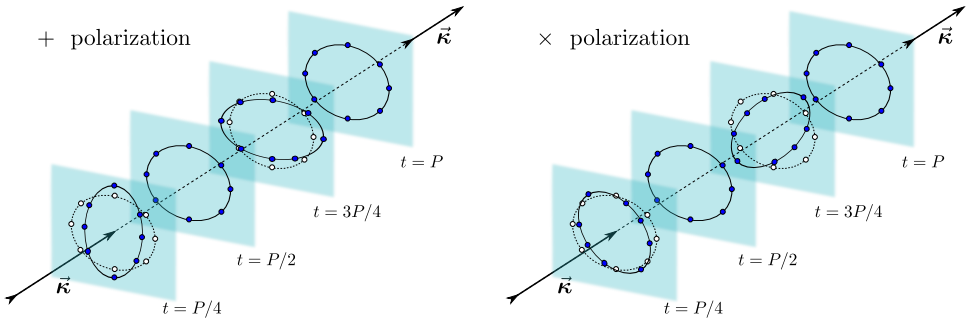

Figure 1.1: Original illustrations from Bishop and Rezzolla (2016) showing the deformations produced by the two polarized modes of GWs passing through a ring of freely-falling particles. The solid lines with blue filled dots show the positions of the particles at different times, while the dashed lines with open white dots represent the unperturbed positions.

not perfectly spherically symmetric (e.g. contraction or expansion of a sphere) or rotationally symmetric (e.g. a spinning disk or sphere). Moreover, equation 1.2 provides a rough estimate of the characteristic frequency, as $f = 1/T$, of GWs emitted from the system.
Since GWs are perturbations of the space-time, their passage has the important effect of stretching and compressing space perpendicular to the direction of propagation. In particular, GWs have two different polarization modes called plus (+) and cross (×) modes. Figure 1.1 is a cartoon of the effect of the two modes passing through a ring of test masses.

Due to the nature of the gravitational interaction, detectable levels of gravitational radiation can be produced only if very massive and compact objects at relativistic speeds are involved. In equation 1.3 the first factor is approximately the Schwarzschild radius ($R_S = 2GM/c^2$) of a black hole of mass M, while v^2/c^2 is a measurement of the absolute strength of the gravity. Thus, h approaches the unity only in the proximity of a black hole that is moving at about the speed of light. In contrast, the strain in the vicinity of Earth is very small, of the order of 10^{-21} or smaller, even for extremely violent astrophysical sources. It appears obvious that such weak signals are extremely difficult to detect.

1.1.1 Gravitational waves from binaries

Among all the possible sources of GWs, COBs composed of two BHs, two NSs or a NS and a BH are the most relevant for this thesis. Our way to model GW emission

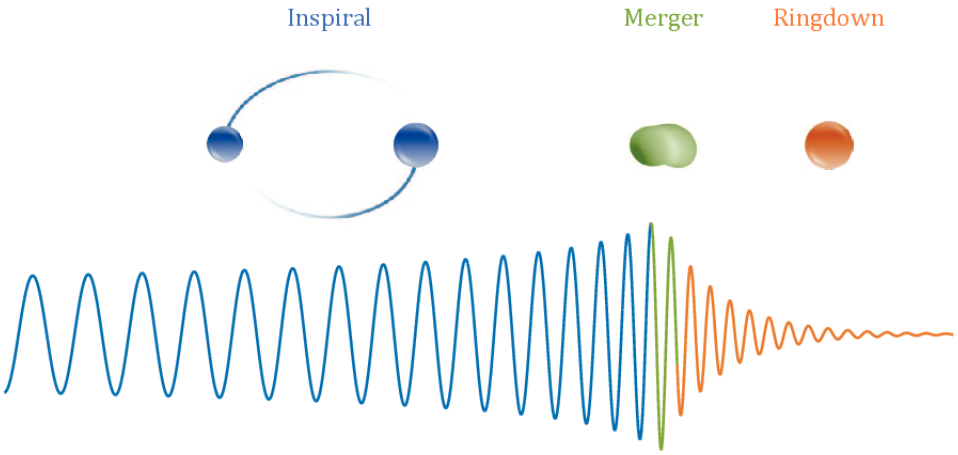

Figure 1.2: The three phases in the temporal evolution of a binary system. In the inspiral phase the two object are orbiting and approaching each other. In the merger phase the two objects fuse into one. In the ring-down phase the resulting object relaxes to a stationary state. Source: adapted from Figure 2 in Antelis and Moreno (2017).

by COBs depends on whether these are in the inspiral, merger or ring-down phases (see Figure 1.2). In the inspiral phase, the members of the binary are still orbiting around each other and spiral in because of GW emission, while the merger phase occurs when the two objects coalesce becoming a single object. Finally, during the ring-down phase the new object settles down.

During the inspiral phase, the motion of the binary creates a time-varying mass quadrupole moment, causing the emission of GWs, which carry away energy from the system; consequently, the binary orbit decays. If $P_{\rm GW}$ is the power emitted in GWs (from GR), then the variation of the orbital energy of a COB during the inspiral can be written as

$$P_{\rm GW} = -\frac{dE}{dt} = -\frac{G m_1 m_2}{2a}\frac{da}{dt}. \tag{1.4}$$

From Peters (1964), we can write the evolution of the semi-major axis of the COB as

$$\frac{da}{dt} = -\frac{64}{5}\frac{G^3 m_1\, m_2 (m_1+m_2)}{c^5\, a^3 (1-e)^{\frac{7}{2}}}, \tag{1.5}$$

which is a first-order approximation valid for small eccentricity e. Integrating equation 1.5 from the initial separation to zero, we can obtain an estimate of the merger timescale

$$t_{\rm gw} = \frac{5}{264}\frac{c^5 (1-e)^{\frac{7}{2}}}{G^3 m_1 m_2 (m_1+m_2)} a^4 \,. \tag{1.6}$$

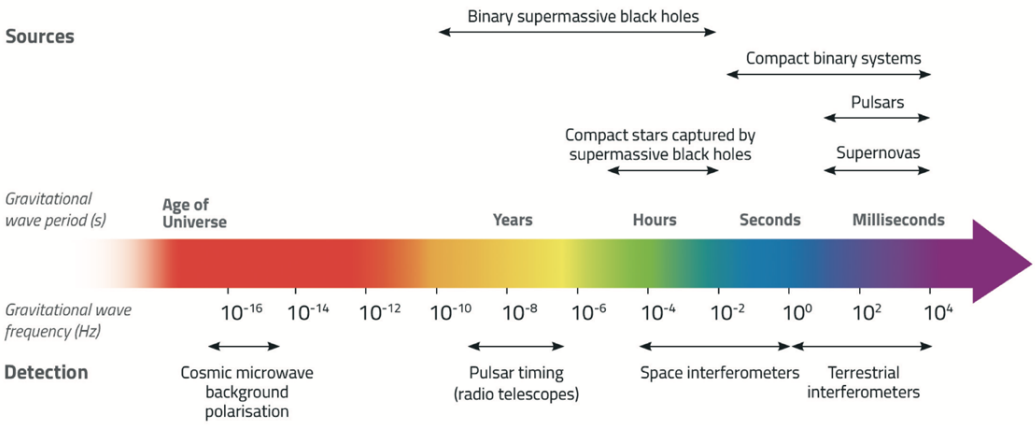

Figure 1.3: Gravitational radiation spectrum as a function of GW frequency in Hz. Top part: astrophysical sources within the frequency range they are expected to emit; bottom part: operating frequency range of different types of detectors. Source: adapted from https://lisa.nasa.gov.

Equation 1.5 shows that the time for a COB to reach coalescence strongly depends on the semi-major axis, on the orbital eccentricity and on the masses of the two compact objects.

Moreover, if the Keplerian approximation is valid during the inspiral phase, it can be shown that $\omega_{\rm gw} = 2\,\omega_{\rm orb}$, where $\omega_{\rm gw}$ is the frequency of GWs, while $\omega_{\rm orb} = \sqrt{\frac{GM}{a^3}}$ is the orbital frequency of the binary. Then, after some math, the strain produced by the passage of GWs can be written as

$$h = \frac{4\,G}{c^4}\frac{\mu\omega_{\rm orb}^2 a^2}{r}, \tag{1.7}$$

where $\mu \equiv \frac{m_1\,m_2}{m_1+m_2}$ is the reduced mass. From equation 1.7 we can estimate the minimum orbital separation needed to produce an observable perturbation ($h \sim 10^{-21}$). For example, let us consider a binary with members of 10 $M_\odot$ placed at 1 Mpc from Earth. The minimum orbital separation needed to emit a strain of the order of $h \sim 10^{-21}$ is $\sim 5\times10^{-2}$ $R_\odot$ and becomes $\sim 5\times10^{-4}$ $R_\odot$ if $m_1 = m_2 = 1$ $M_\odot$. The component of such close binaries can only be compact objects like BHs and NSs. In the next sections, we will discuss how it is possible to form such extreme COBs.

1.1.2 Gravitational wave spectrum

Gravitational radiation is expected to be produced over a wide range of frequencies and by a large variety of astrophysical sources. Figure 1.3 shows the frequency

spectrum of GWs together with the possible astrophysical sources expected to emit at each frequency, plus the frequency range in which different types of detectors operate. At very low frequencies, down to about 10^{-16} Hz, gravitational radiation is produced only by quantum fluctuations in the early Universe. At these frequencies, experiments like BICEP2 (Background Imaging of Cosmic Extragalactic Polarization) and Keck Array[2] look for the imprints left by GWs on the polarization of the cosmic microwave background (CMB) radiation.

Moving towards higher frequencies, binary compact objects become the principal source of GWs. In particular, binary super-massive black holes (SMBHs), which are located in galactic nuclei, emit in the frequency range between $\sim 10^{-10} - 10^{-2}$ Hz. At those frequencies, gravitational radiation can be investigated with the Pulsar Timing Array (PTA) or with space-borne laser interferometers. In practice, PTA observatories like NANOGrav[3] (North American Nanohertz Observatory for Gravitational Waves) or the European Pulsar Timing Array (EPTA) monitor a set of near pulsars looking for variations in their periods due to the effect of passing-by GWs. As shown in Figure 1.4, the future SKA[4] (Square Kilometer Array) observatory might be able to detect mergers of SMBHs of about 10^9 $M_\odot$.

Mergers of 'lighter' SMBHs ($10^4 - 10^6$ $M_\odot$) will be observable with space interferometers, like the LISA observatory (ESA L3 mission). LISA, whose launch is planned for the early 2030s, will operate in the frequency range $\sim 10^{-4} - 10^{-1}$ Hz (Amaro-Seoane et al. 2017). In addition, LISA might be able to observe GWs from stellar-mass compact object binaries from a few Myr to days before their merger (Sesana, 2016; Wong et al., 2018) and extreme mass ratio inspirals of stellar-mass compact objects around SMBHs (Bortolas and Mapelli, 2019).

From few Hz up to $\sim 10^3$ Hz we enter in the domain of ground-based interferometers, like LIGO[5] and Virgo[6].Figure 1.4 shows that LIGO and Virgo are sensitive to GWs produced during the merger between stellar compact objects like BHs and NSs (Abbott et al., 2018), which are the only sources of GWs observed so far. Moreover, at these frequencies ($\sim 10 - 10^5$ Hz) also rotating NSs and supernovae explosions emit GWs but their typical strain is fainter. See Ciufolini and Fidecaro (1996) and Sathyaprakash and Schutz (2009) and references therein for a more complete discussion about the possible sources.

[2] Their results are available at http://bicepkeck.org
[3] http://nanograv.org
[4] https://www.skatelescope.org/challenging-einstein/
[5] https://www.ligo.caltech.edu
[6] http://www.virgo-gw.eu

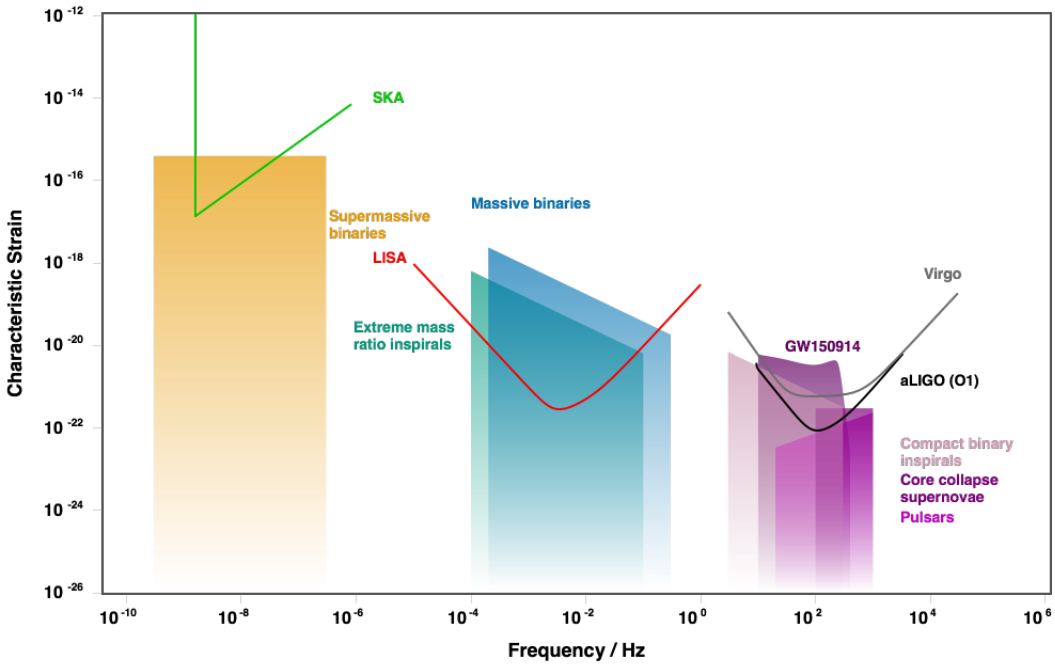

Figure 1.4: Schematic representation of the characteristic strain of gravitational radiation emitted by different GW sources as a function of frequency, together with the sensitivity curves of some GW observatories: green for SKA, red for LISA, while gray and black grey are the design sensitivity of Virgo and LIGO, respectively. Source: produced via `http://gwplotter.com`.

1.2 Compact remnants as the death of massive stars

Compact objects play a crucial role in a plethora of astrophysical processes, such as GWs, radio jets and X-ray emission. Despite their importance, NSs and especially BHs are still elusive objects: their formation and evolution are affected by a number of barely understood physical processes.

It is believed that NSs and BHs are the remnants of massive stars ($\gtrsim 8$ $M_\odot$). The link between compact-object formation and the evolution of their progenitor stars is still matter of debate. Two processes are expected to crucially affect the formation and the final mass of a compact object evolved from an isolated star: mass loss through *stellar winds* and *supernova* (SN) *explosion* mechanisms.

In the last few years, both the theory of massive star evolution (e.g. Chen et al., 2014; Tang et al., 2014) and the models for SN explosions (see Heger et al., 2003; Smartt, 2009; Limongi, 2017 for some reviews) have been revised. In the following, I shortly present the state-of-the-art knowledge about stellar winds and SN explosions.

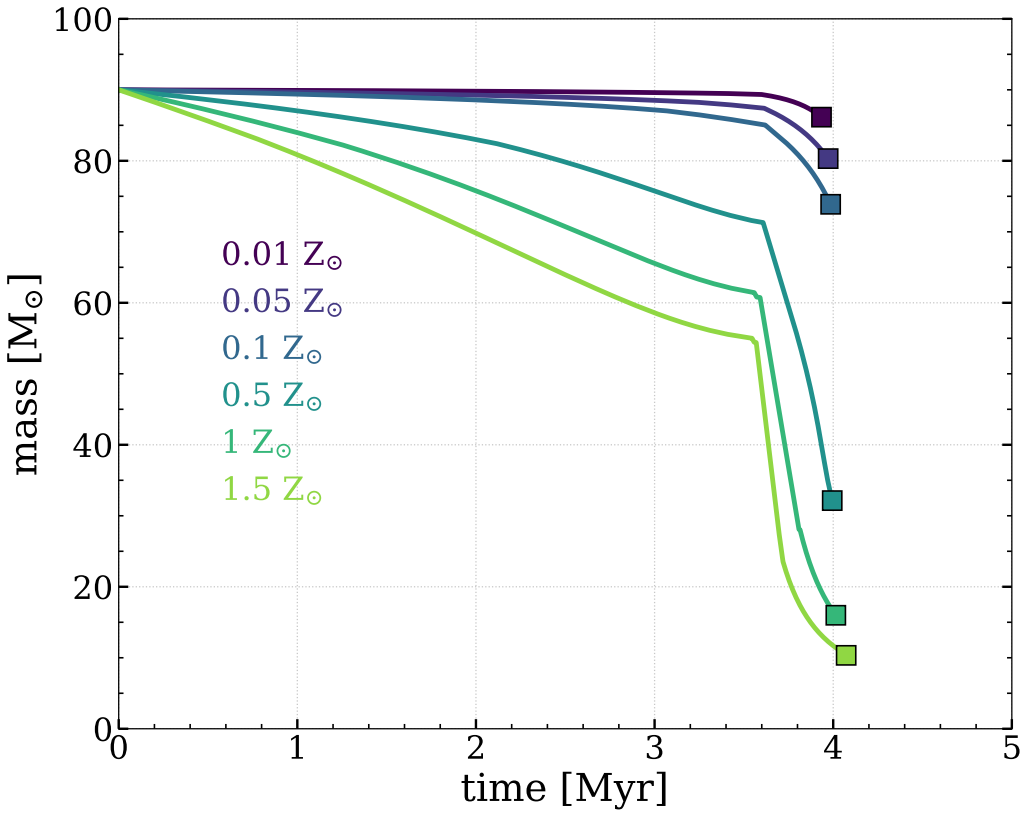

Figure 1.5: Mass evolution of a star with $M_{\rm ZAMS}$ = 90 $M_\odot$ at metallicity of Z = 1.5, 1, 0.5, 0.1, 0.05, 0.01 $Z_\odot$ computed with MOBSE. The markers identify the mass of the star at the end of Carbon burning.

1.2.1 Stellar winds

Stellar winds are outflows of gas that escape from the upper atmosphere of a star. The mechanisms that power these ejections are different according to the stellar type. In cold stars (e.g. red giant and asymptotic giant branch stars) the main engine that produces stellar winds is represented by radiation pressure on dust (see, for example, van Loon et al., 2005). In contrast, stellar winds of hot massive stars, like O- and B- main sequence (MS) stars, Wolf-Rayet (WR) and luminous blue variable (LBV) stars, are caused by the coupling between the linear momentum of photons and that of metal ions in the stellar photosphere (see Bresolin and Kudritzki, 2004 for a review).

The chemical composition of a star plays an important role in the mechanism of stellar winds. For O- and B- stars, metallicity Z is expected to modulate the mass-loss rate $\dot{M}$ according the following relationship $\dot{M} \propto Z^{\beta}$, where β is assumed to

take a value between 0.5 – 0.9 according to the considered physical models (e.g. Abbott and Lucy, 1985; Kudritzki et al., 1987; Nieuwenhuijzen and de Jager, 1990; Leitherer et al., 1992; Vink et al., 2001 and Kudritzki and Puls, 2000; Vink, 2011 for reviews). Vink et al. (2001) predict that the mass-loss rate of O- and B- stars is not only a function of Z, but depends also on the temperature. They found that around 25000 Kelvin the mass-loss rate drastically increases because of the *bi-stability jump* (see Vink et al., 2010 for details). Vink (2018) suggest that the bi-stability jump might be important even for the mass-loss of LBVs (see also Petrov et al., 2016), but for evolved stars (beyond the MS) the uncertainties are larger (Vink and de Koter, 2005b; Meynet and Maeder, 2005). For example, Gräfener and Hamann (2008) find that for WR stars stellar winds do not depend solely on Z but also on the electron-scattering Eddington factor $\Gamma_e = \chi_e L/(4\pi c G M)$, where χ_e is the electron scattering opacity, L the luminosity and M the mass of the star. Despite the importance of Γ_e has been supported by further works (e.g Gräfener et al., 2011; Vink et al., 2011; Gräfener et al., 2012; Vink, 2017b), only few stellar evolution models account for its effects. Among them, it is worth mentioning PARSEC (Bressan et al., 2012), which adopts $\dot{M} \propto Z^{\beta}$ with $\beta = 0.85$ if $\Gamma_e < 2/3$ and $\beta = 2.45 - 2.4\Gamma_e$ if $2/3 \leq \Gamma_e \leq 1$ (Tang et al., 2014; Chen et al., 2015). This prescription accounts for the fact that when a star approaches the Eddington Limit, turning into a radiation dominated star, stellar winds become almost insensitive to metallicity.
Figure 1.5 shows the mass evolution of a massive star with zero-age main sequence (ZAMS) mass of 90 $M_\odot$ at 6 different metallicities (Z = 1.5, 1, 0.5, 0.1, 0.05, 0.01 $Z_\odot$) as obtained with MOBSE (see Giacobbo et al., 2018 and the next chapters of this Thesis for details). At high metallicity, the star loses most of its mass by the end of its life, while at low Z the star retains almost all of its mass.
Stellar winds are the primary cause of mass loss during the life of single stars and strongly impact the pre-SN mass of a star. Understanding the behavior of stellar winds is crucial for the study of compact objects, because the pre-SN mass (both total mass and core mass) of a star is expected to highly affect the result of the SN explosion (e.g. Fryer, 1999; Fryer et al., 2001; Mapelli et al., 2009; Yoon et al., 2010; Fryer et al., 2012; Langer, 2012).

1.2.2 Supernova explosions

SN explosions are extremely energetic events (the binding energy of the Fe core of a star can reach 10^{53} erg) ,which involve very complex physical processes (see e.g. Fryer 1999; Heger and Woosley 2002; Heger et al. 2003; Fryer 2006; O'Connor and

Ott 2011; Fryer et al. 2012; Janka 2012; Ugliano et al. 2012; Burrows 2013; Ertl et al. 2016). The final outcomes of SN explosions are still highly uncertain.

There are several different flavours of SNe and one of them are the *iron-core-collapse* SNe. An iron-core-collapse SN occurs when a sufficiently massive star (with ZAMS mass $\gtrsim 10$ $M_\odot$) is able to ignite oxygen burning. Subsequent nuclear reactions proceed quickly until an inner core of iron is formed. Approaching the Chandrasekhar limit (1.4 $M_\odot$), electron pressure becomes insufficient to counteract the gravitational force. In addition, protons in nuclei capture electrons producing neutrons and neutrinos. At this point, the core collapses uncontrollably. Protons and neutrons end up into a proto-NS (supported by neutron-degeneracy pressure), that halts the collapse of the core abruptly, producing a bounce shock. The shock moves outward, until the neutrinos lose their energy causing the stalling of the shock. Hence, the SN explosion occurs only if there is a mechanism able to revive the shock. For example, the *convective engine* scenario (Herant et al., 1994; Burrows et al., 2006; Fryer, 2006; Scheck et al., 2008; Bruenn et al., 2009; Janka, 2012; Fryer et al., 2012; Janka, 2017) predicts that instabilities develop in the region between the proto-NS surface and the position of the stalling shock. These instabilities convert the energy leaking out from the NS (in form of neutrinos) into kinetic energy pushing outwards the convective region. Thus, if the convective energy is enough to overcome the ram pressure of the infalling outer layers of the star the explosion takes place, otherwise the SN fails (*failed SN*; Bethe 1990; Janka et al. 2007; Burrows 2013; Janka 2012). It is worth mentioning that, even if the most commonly studied mechanism is the neutrino-driven convective engine I have just described, other mechanisms have been proposed, like rotationally-driven SNe and/or magnetically-driven SNe (e.g. Janka 2012; Fryer 2014; Foglizzo et al. 2015b and references therein).

Fryer et al., 2012 propose a simple approach to estimate the mass of compact objects. They suggest that the mass of the compact remnant essentially depends on two quantities: the mass of the carbon-oxygen core $M_{\rm CO}$ and the total final mass $M_{\rm fin}$ of the star (see also Fryer, 1999; Fryer et al., 2001; Fryer, 2006 and Appendix A). On the other hand, other studies O'Connor and Ott, 2011; Ugliano et al., 2012; Sukhbold and Woosley, 2014; Sukhbold et al., 2016; Ertl et al., 2016) claim that the relationship between the mass of the compact remnant and the properties of the progenitor star might be more complex and suggest that the critical parameter to distinguish between a successful and a failed SN might be the *compactness* of the stellar core at the onset of the SN. The compactness for a mass m is defined as $\xi_{\rm m} = \frac{m/{\rm M}_\odot}{R/1000{\rm km}}$, where R is the radius that encloses the mass m (usually $m = 2.5$

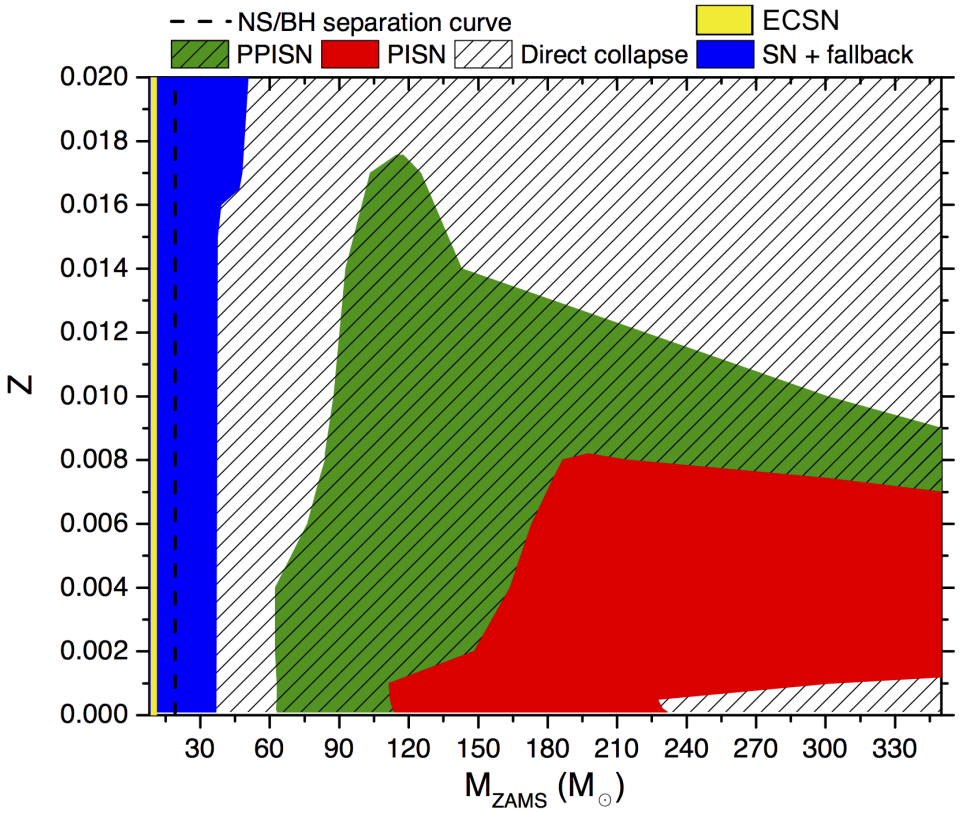

Figure 1.6: Representation in the $Z - M_{\mathrm{ZAMS}}$ space of different SN mechanisms. Stars that end their life through a core-collapse SN with fallback lie in the blue area. NSs formed via electron-capture SN (ECSN) are in the yellow region (to the very left). PPISNe and PISNe occur in the green and red region, respectively. The hatched area indicates the direct collapse (failed SN). The vertical line is a simplified division between stars that form NSs from those collapsing into BHs. Source: adapted from Figure 3 in Spera and Mapelli (2017).

$M_\odot$ is chosen). Limongi (2017) and Limongi and Chieffi (2018) show that there is a strong correlation between the final carbon-oxygen mass and the compactness at the onset of collapse (see Figure 21 in Limongi, 2017).

For massive stars ($\gtrsim 60$ $M_\odot$), pair-instability and pulsational pair-instability are an important possible engine for SN explosions Barkat et al., 1967; Woosley et al., 2007; Woosley, 2017. When the Helium core grows above ~ 30 $M_\odot$, the core temperature becomes $\gtrsim 7 \times 10^8$ K and collisions between atomic nuclei and gamma rays (which produce electron-positron pairs) are so efficient that they reduce the photon pressure and cause a sudden collapse, even before the formation of a iron core. The outcome of such collapse strongly depends on the Helium mass. In particular, if the Helium mass is > 135 $M_\odot$ the collapse cannot be stopped and the result is the direct formation of a BH Woosley, 2017. For an Helium mass in the range $64-135$ $M_\odot$, the explosive burning of heavy elements, ignited by the collapse, completely disrupts

the star leaving no remnant. In less massive Helium cores ($32-64$ $M_\odot$), the process of pair production is less effective and generates a series of pulsations of the core (pulsational pair-instability), enhancing mass loss. As a consequence of that, the final BH will be significantly lighter than in the case of direct collapse.
Finally, another important explosion mechanism is represented by *electron-capture* SNe (ECSNe, Miyaji et al., 1980; Nomoto, 1984; Nomoto, 1987; Nomoto and Kondo, 1991; Kitaura et al., 2006; Fisher et al., 2010; Jones et al., 2013; Takahashi et al., 2013; Schwab et al., 2015a; Jones et al., 2016; Jones et al., 2019, see also Chapter 3). They are similar to iron-core-collapse SNe, but less energetic and faster. ECSNe occur in less massive stars, that produce a degenerate core made of oxygen, neon and magnesium (ONeMg). When this core reaches the critical mass of about 1.37 $M_\odot$, it collapses due to electron capture on ^{24}Mg and/or ^{20}Ne (Miyaji et al., 1980; Nomoto, 1984; Nomoto, 1987); otherwise it forms an ONe white dwarf. The outcome of the electron-capture collapse is an NS of about 1.26 $M_\odot$.
Figure 1.6 shows the occurrence of different SN types in the $Z - M_{\rm ZAMS}$ plane (Spera and Mapelli, 2017). The yellow region indicates where the ECSNe occur. Stars that form compact remnants through core-collapse with fallback are in the blue area. The green and red area indicate the region where pulsation pair-instability SNe (PPISNe) and pair-instability SNe (PISNe) occur, respectively. Finally, the hatched area represents the region where BHs are expected to form via direct collapse. It is worth noticing that the lower limit for direct collapse (in term of $Z - M_{\rm ZAMS}$) depends on metallicity.

1.2.3 Mass spectrum of compact objects

In the previous sections, we discussed the possible dependence of compact-object mass on both stellar winds and SN explosion mechanisms. Figure 1.7 shows the mass of the compact remnant as a function of the ZAMS mass of the progenitor star for different metallicities, according to the model by Spera and Mapelli, 2017. There is an evident dependence on the metallicity for massive stars ($M_{\rm ZAMS} \gtrsim 30$ $M_\odot$), which indicates the importance of stellar winds. In most cases, the lower the metallicity is, the higher the maximum mass of the BH (Mapelli et al., 2009; Mapelli et al., 2010; Belczynski et al., 2010; Spera et al., 2015; Spera and Mapelli, 2017, see also Chapter 2). Moreover, as shown in Figure 1.6, PPISNe and PISNe do not affect metal-rich stars ($Z \geq 10^{-2}$), while they have a strong impact on metal-poor stars ($Z \leq 10^{-3}$). For intermediate-mass stars ($8 \lesssim M_{\rm ZAMS}/M_\odot < 30$), the dependence

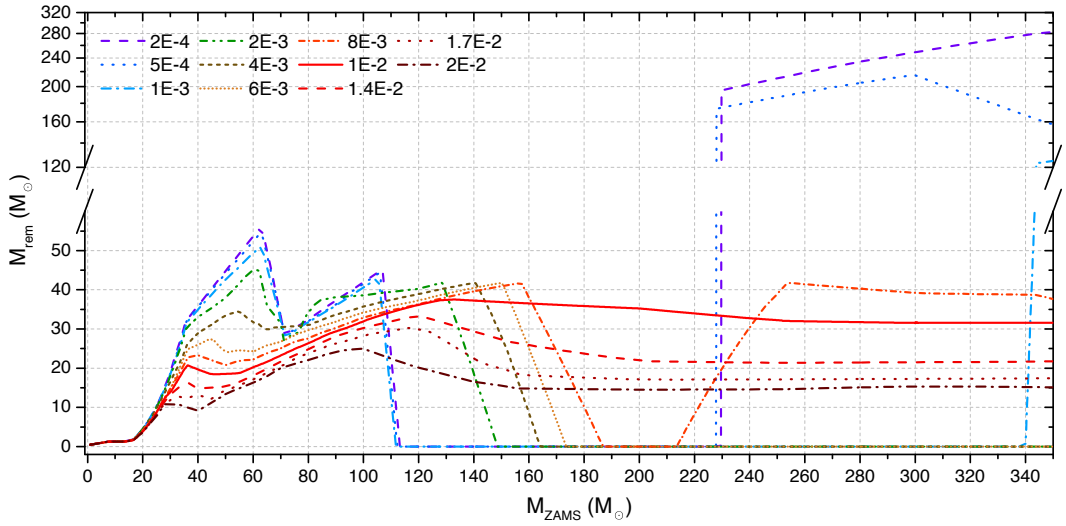

Figure 1.7: Mass of the compact remnant as function of the ZAMS mass of the progenitor for different metallicities. Source: Figure 2 of Spera and Mapelli (2017).

on progenitor's metallicity tends to vanish and the decisive factor becomes the SN engine model (Fryer et al., 2012).

1.3 Stellar evolution in binaries

The formation of COBs can follow different paths. One of the most studied channels is represented by the evolution of *isolated binaries*, i.e. binary systems composed of two stars that are gravitationally bound since their birth (Tutukov et al., 1973; Portegies Zwart and McMillan, 2000; Belczynski et al., 2002; Voss and Tauris, 2003; Bogomazov et al., 2007; Dominik et al., 2012; Tauris et al., 2015; de Mink and Belczynski, 2015; Belczynski et al., 2016b; Giacobbo and Mapelli, 2018; Tauris et al., 2017; Kruckow et al., 2018). If we consider that the vast majority of massive stars are thought to be born in binaries (see e.g. Sana et al., 2013), it easy to understand the importance of this formation channel.
We have seen in Section 1.2 that single stellar evolution is far to be understood and things become even more uncertain if we consider the evolution of stellar binaries. Indeed, stars in binaries might undergo physical processes that strongly affect their evolution (e.g. tides, mass transfer and mass accretion). Among them, *common envelope* (CE) and *natal kicks* from SNe are two of the most important processes for COB formation, and are two of the most uncertain as well. They are essential to explain the formation of a wide variety of binary systems including: progenitors of SNe Ia, X-ray binaries and even GW sources.

Before describing CE and natal kicks in detail, it is worth saying that there are several alternative evolutionary channels for COBs. In dense environments (e.g. young star clusters, open clusters, globular clusters and nuclear star clusters), COBs might form through dynamical processes involving single objects and/or binary systems (e.g. Sigurdsson and Phinney, 1993; Portegies Zwart and McMillan, 2000; Colpi et al., 2003; Mapelli et al., 2013; Ziosi et al., 2014; Rodriguez et al., 2015; Mapelli, 2016; Askar et al., 2017; Rastello et al., 2019; Di Carlo et al., 2019). Alternatively, primordial BHs (born from gravitational collapses in the early Universe) might pair forming BHBs (e.g. Carr and Hawking, 1974; Carr et al., 2016; Inomata et al., 2017).

1.3.1 Common envelope

When a binary is sufficiently tight, a stellar component might overfill its *Roche lobe*[7] starting to transfer mass through the Lagrangian point L_1 to its companion. This mechanism is called Roche lobe overflow. To understand the fate of the system it is crucial whether this process takes place in a stable or unstable way and on which timescale. In particular, if mass transfer is dynamically unstable, namely the star expands (due to mass loss) faster than its Roche lobe, we expect the binary begins a CE phase. This phase it is characterized by the fact that both the donor and its companion are surrounded by a shared envelope (Paczynski, 1976). It is worth to notice that a binary enters a CE phase only if the donor has a well-developed core distinguishable from the envelope (see Ivanova and Taam, 2004). If not, the result is the direct merger of the binary (e.g Taam and Sandquist, 2000). Also, the CE phase can be the consequence of the simultaneous overfilling of the Roche lobes of both stars.

At the beginning of the CE phase, the stellar cores (or in the case of a single degenerate binary the core and the compact object) start to spiral in because of the gas drag generated by the envelope. Indeed, when a system enters CE, the envelope stops co-rotating with the cores. During the spiral-in phase, the two cores lose orbital energy in favour of the envelope and this energy is converted into kinetic energy that tends to unbound the envelope. If the energy released during this process is enough to completely eject the envelope the system survives and the outcome is a binary composed of two naked stellar cores (or a compact object and a naked core). Additionally, the new system will be characterized by a much smaller orbital

[7] The innermost equipotential surface which encloses both stars defines the critical Roche lobe of each star and this equipotential surface passes through the Lagrangian point L_1. Thus, the Roche lobe represents the region around an object in a binary system where the orbiting material is gravitational bound to that object.

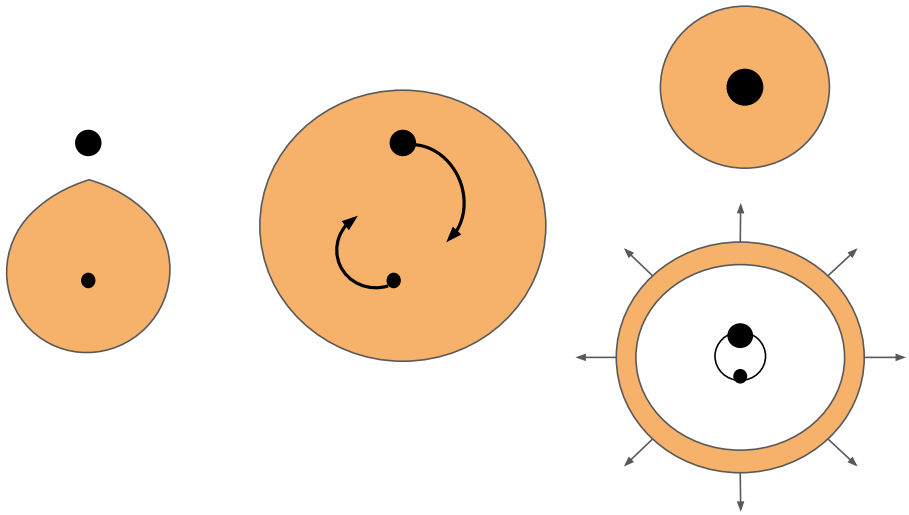

Figure 1.8: The key stages of the CE evolution of a system composed of an evolved star and a compact object. Left: the evolved star fills its Roche lobe. Middle: the companion is engulfed. the core and the compact object spiral in inside a common envelope. Right: the envelope is ejected (bottom) or the stellar core merge with the compact object (top).

separation with respect to the orbital separation at the onset of CE phase. If the survived system forms a BHB, the orbital shrinkage will be crucial to enable the system to merge by GW emission within a Hubble time (see Chapter 2). On the contrary, if the transferred energy is not sufficient, the two components keep spiralling in until they merge. Figure 1.8 shows a cartoon of the evolution of a binary system passing through the CE phase and the possible outcomes (e.g. see Iben and Livio, 1993; Taam and Sandquist, 2000; Podsiadlowski, 2001; Ivanova et al., 2013 for a general review).

One of the main uncertainties in modelling the evolution of CE concerns the conditions leading to the removal of the envelope. The most used formalism to predict the outcome of the CE phase is the so-called $\alpha\lambda$*-energy formalism* (van den Heuvel, 1976; Webbink, 1984; Livio and Soker, 1988; Iben and Livio, 1993). The basic idea is that the energy required to remove the envelope comes entirely from the dissipation of the orbital energy of the binary. The fraction of the orbital energy of the two cores which goes into unbinding the envelope can be expressed as

$$\alpha \Delta E_{\rm orb} = \alpha \left(\frac{-G m_1 m_2}{2 a_{\rm i}} + \frac{G m_{1,{\rm c}} m_2}{2 a_{\rm f}} \right), \tag{1.8}$$

where $a_{\rm i}$ and $a_{\rm f}$ are the initial and final orbital separation, respectively, m_1 and m_2 are the masses at the onset and $m_{1,{\rm c}}$ is the core mass of the donor star that has lost

its envelope. The parameter α represents the *common-envelope efficiency* and indicates the available fraction of orbital energy that can be used to eject the envelope. A second free parameter λ is introduced to account for different stellar structures in the calculation of the binding energy of the envelope $E_{\rm bind} = \frac{m_1 m_{1,\rm env}}{\lambda R_1}$ (de Kool, 1990a; Dewi and Tauris, 2000). By imposing $E_{\rm bind} = \alpha \Delta E_{\rm orb}$, we can derive what is the value of the final semi-major axis a_f for which the envelope is ejected. If $a_{\rm f}$ is larger than the sum of the core radii (or than the sum of the Roche lobe radii), then the system will survive and it will exit the CE with the new orbital separation $a_{\rm f}$, otherwise, the cores will merge during the CE phase.

It is well known that this simple formalism is not able to capture all the physics of CE. It is expected that λ is not the same for all stars. Indeed, it should change a lot from star to star and even during the evolution of CE phase (Dewi and Tauris, 2000; Tauris and Dewi, 2001; Loveridge et al., 2011; Wang et al., 2016). In literature there are many different definitions for λ that depend on which contribution, apart of the gravitational energy, the different authors include in their calculation of the binding energy (e.i thermal energy, enthalpy, recombination energy). In addition, λ is also extremely sensitive to the location of the bifurcation point that define the boundary between the core and the envelope (Tauris and Dewi, 2001; Ivanova et al., 2013).

Moreover, there is a number of observed systems that require $\alpha \geq 1$, but it is evident, from equation 1.8, that an α that exceeds the unit is un-physical, unless we do consider to have other source of energy. In particular, this might mean that we are neglecting (or underestimating) some potentially important energy sources i) that contribute to the total internal energy (e.g. recombination energy, enthalpy Ivanova and Chaichenets, 2011; Ivanova et al., 2015) or ii) external energy sources (e.g. nuclear burning from accreted material during in-spiral, see Ivanova et al., 2013 for good review).

In particular, we should expect that the value of α changes according to the different classes of post-CE binaries, since time-scales, energy sources and sinks should vary. For example, recent works seem to suggest a very high CE efficiency α for the formation of merging double NSs (e.g. $\alpha \simeq 5$ Fragos et al., 2019; $2 \lesssim \alpha$ Giacobbo and Mapelli, 2018; Giacobbo and Mapelli, 2019a).

Even if in the last years a lot of effort has been put on studying the CE, there are still many open questions. For example, since the CE event consists in a number of sub-phases that are guided by different physical processes on different time-scales, none of the available numerical methods is able to grasp all the physics involved (Ivanova et al., 2013). Finally, from both theoretical and observational perspective,

the CE phase involving massive stars is less clear and much more difficult to study. Thus, CE phase remains one of the most critical aspects to describe the evolution of massive stars in binaries.

1.3.2 Natal kicks

Compact objects are thought to receive a kick at birth (natal kick), because of asymmetric supernova (SN) explosions (e.g Janka and Mueller, 1994; Burrows and Hayes, 1996) or anisotropic emission of neutrinos (e.g. Woosley, 1987; Bisnovatyi-Kogan, 1993; Fryer and Kusenko, 2006; Kusenko et al., 2008; Sagert and Schaffner-Bielich, 2008; Nagakura et al., 2019). In addition, if the SN occurs in a binary star, we expect the so-called Blaauw kick to affect the orbital properties of the binary system, even if mass loss is completely symmetric (Blaauw, 1961).
Most observational estimates of natal kicks come from pulsar proper motions (Lyne and Lorimer, 1994; Hansen and Phinney, 1997; Arzoumanian et al., 2002; Hobbs et al., 2005; Faucher-Giguère and Kaspi, 2006). The kick distribution we can infer from these data is still matter of debate. Hobbs et al. (2005) study proper motions of 233 Galactic pulsars. Restricting their analysis to the 73 pulsars younger than $\sim$ 3 Myr (whose proper motions were less affected by the environment), they fit a Maxwellian distribution to the natal kick velocity, with one dimensional root-mean square (rms) velocity $\sigma = 265$ km s^{-1}.
Other works suggest a bimodal velocity distribution of pulsars, with a first peak at low velocities (e.g. ~ 0 km s^{-1} according to Fryer et al., 1998 or ~ 90 km s^{-1} according to Arzoumanian et al., 2002) and a second peak at high velocities (~ 500 km s^{-1} according to Arzoumanian et al., 2002, or even > 600 km s^{-1}, Fryer et al., 1998). Similarly, the recent work of Verbunt et al. (2017) indicates that a double Maxwellian distribution provides a significantly better fit to the observed velocity distribution than a single Maxwellian distribution.
Beniamini and Piran (2016) follow a different approach: they focus on double neutron stars (DNSs) only and find a strong preference for small mass ejection (≤ 0.5 M$_\odot$) and small natal kicks ($v_{\rm kick} \leq 30$ km s^{-1}) in DNSs. Similarly, from the analysis of $r-$process material in ultra-faint dwarf galaxies Beniamini and Piran (2016) find further support for a prevalence of small natal kicks in dNSs.
A possible explanation for those results is that natal kicks strongly depends on the NS type and on the binarity of the NS's progenitor. Indeed, evolved stars in close binary with a compact object might undergo an *ultra-stripped* SN explosion (Tauris et al., 2013; Tauris et al., 2015; Tauris et al., 2017). An ultra-stripped SN occurs when

an evolved star has been considerably stripped by the companion (due to mass transfer). It is expected that ultra-stripped SNe produce slow NSs because of the small mass ejected ($\lesssim 0.2\,M_\odot$) during the explosion (Suwa et al., 2015; Janka, 2017). The situation for black hole (BH) natal kicks is even more uncertain, because data are scanty and difficult to interpret (Brandt et al., 1995; Nelemans et al., 1999; Mirabel et al., 2001; Mirabel et al., 2002; Mirabel and Rodrigues, 2003; Gualandris et al., 2005; Fragos et al., 2009; Repetto et al., 2012; Repetto et al., 2017; Wong et al., 2014). While recent studies (e.g. Repetto et al., 2017; Atri et al., 2019) suggest that several Galactic BHs received a relatively high natal kick (~ 100 km s^{-1}), we are still far from inferring a distribution of BH kicks from observations.
From a theoretical perspective, hydrodynamical simulations of SN explosion have successfully shown that explosion asymmetries may arise from non-radial hydrodynamic instabilities in the collapsing core (Blondin and Mezzacappa, 2006; Scheck et al., 2006; Foglizzo et al., 2007; Foglizzo et al., 2015a; Janka, 2012; Janka, 2013). Hydrodynamical simulations show that large kick magnitudes can be achieved (Wongwathanarat et al., 2013), similar to the ones reported by Hobbs et al. (2005). However, recently, Janka (2017), using the gravitational tug-boat mechanism in asymmetric neutrino-driven core-collapse SNe, derived a simple scaling between the natal kick, the energy of the explosion and the amount of asymmetries. Even if recent works (Bray and Eldridge, 2016; Bray and Eldridge, 2018; Giacobbo and Mapelli, 2019a see also Chapter 5) seem to indicate that we are on the right track, natal kicks are far from being fully understood, as well as their implications in the formation of COBs.

1.3.3 Binary population synthesis simulations

One of the most powerful tools available for studying the formation and evolution of isolated binaries are the so-called *binary population-synthesis codes*. A binary population-synthesis code is a Monte-Carlo based code coupling single stellar evolution (including the prescription for the outcomes of SN explosions) with a treatment of binary-evolution processes. In principle, to study a population of binaries we should carefully follow the evolution of each system, from the ZAMS to the stellar death and the possible formation of a remnant. However, this approach is not feasible. In fact, the physical processes that must be taken into account (tides, mass transfer, nuclear reactions, etc) cover a large range of time-scales, making this task too computationally expensive. On top of that, some binary evolution processes are very difficult to model in detail, one for all the CE (see Ivanova et al., 2013 and

also Section 1.3.1). Therefore, the implementation of binary evolution processes is usually based on simplifying assumptions and it is not rare that such processes are modelled by using some parameters (that encapsulate our lack of knowledge of the phenomenon).
In general, there are essentially three different approaches to implement stellar evolution in binary population-synthesis codes:

- the most common approach consists in adopting *polynomial fitting formulas* to describe the evolution of the fundamental stellar parameters (luminosity, radius, mass, temperature and chemical composition) as a function of time. The big advantage is that population-synthesis codes based on fitting formulas are computationally very fast, while the main drawback is that fitting formulas are difficult to update. Some examples of BPSs based on fitting formulas are SeBa (Portegies Zwart and Verbunt, 1996a), BSE (Hurley et al., 2002), Brussels code(De Donder and Vanbeveren, 2004), Binary_c (Izzard et al., 2004), StarTrack (Belczynski et al., 2008), COMPAS (Barrett et al., 2017; Stevenson et al., 2017) and MOBSE (Mapelli et al., 2017; Giacobbo et al., 2018).

- As an alternative to the fitting formulas, it is possible to perform the *integration of stellar evolution on the fly*, as done in BPASS (Eldridge and Stanway, 2016) and MESA (Paxton et al., 2011). This approach is far more computationally expensive than the fitting formulas, but provides a more detailed stellar evolution impossible to achieve with the fitting formulas.

- The third possibility is to use *look-up tables* (Voss and Tauris, 2003). These tables contain grids of stellar evolution models that are read and interpolated by BPS codes on the fly (see SEVN Spera et al., 2019 and ComBine Kruckow et al., 2018). This approach is both computationally convenient and versatile. Indeed, stellar models can be easily updated by simply changing the tables.

1.4 Thesis summary

The next four chapters of this Thesis contain original research works, that aim to improve our understanding of COB formation, by means of numerical and analytical tools. The last chapter is a summary of the conclusions of this work.

In **Chapter 2**, we study the demography of BHBs through population-synthesis simulations. In particular, we investigate the formation channels of BHBs and how

different prescriptions for stellar winds might impact the properties of BHB populations. We find that accounting for the dependence of stellar winds on the Eddington factor has a strong impact on the mass spectrum of BHs. We also confirm the importance of progenitor's metallicity to determine the mass of the BH. In addition, we show that even the number of mergers is affected by metallicity. Finally, we find that our most massive BHBs (with total mass > 100 $M_{\odot}$) do not merge within a Hubble time, because their typical orbital separations are too large.

In **Chapter 3**, we focus our attention on the evolutionary pathways that lead to the formation of merging DNSs. In particular, we analyze the impact of the electron-capture SN mechanism. It is expected that electron-capture SNe generate slower NSs than core-collapse SNe. We show that slow (but not zero) natal kicks velocities increase the probability that a binary system is not disrupted and favour the formation of merging DNSs. Our simulations indicate that the first SN explosion is the most critical one for the survival of the system. We also confirm that in binary systems the incidence of electro-capture SNe is higher than in a population of single stars.

Chapter 4 is a detailed study on the populations of BHBs, BHNSs and DNSs. In particular, we investigate how CE and natal kicks affect the formation of COBs. We confirm that CE is crucial to tighten binaries, facilitating the merger via GW emission. We show that also eccentricity is important to drive mergers of COBs in less than a Hubble time and natal kicks may help producing highly eccentric systems. We also develop a data-driven method to estimate the local merger rate starting from our population-synthesis simulations, combined with the cosmic star formation rate density and with a simple description of metallicity evolution. With our data-driven method, we can match the merger rate density inferred by the LVC for several combinations of metallicity evolution, CE efficiency and natal kick prescriptions. Intriguingly we can match the inferred local merger rate of DNSs only if we assume small natal kicks.

Chapter 5 describes a new prescription for the treatment of natal kicks in population-synthesis codes. It is based on the idea (supported by hydrodynamical studies) that the strength of the kicks depends on the mass of the ejecta. With respect to previous prescriptions, this new approach allows us to match the LVC local merger rate density and, at the same time, to reproduce the natal kicks of the observed young Galactic pulsars.

CHAPTER 2

MERGING BLACK HOLE BINARIES: THE EFFECTS OF PROGENITOR'S METALLICITY, MASS-LOSS RATE AND EDDINGTON FACTOR

The first four gravitational wave events detected by LIGO were all interpreted as merging black hole binaries (BHBs), opening a new perspective on the study of such systems. Here we use our new population-synthesis code MOBSE*, an upgraded version of* BSE *(Hurley et al., 2002), to investigate the demography of merging BHBs.* MOBSE *includes metallicity-dependent prescriptions for mass loss of massive hot stars. It also accounts for the impact of the electron-scattering Eddington factor on mass loss. We perform* $> 10^8$ *simulations of isolated massive binaries, with 12 different metallicities, to study the impact of mass loss, core-collapse supernovae and common envelope on merging BHBs. Accounting for the dependence of stellar winds on the Eddington factor leads to the formation of black holes (BHs) with mass up to* 65 $M_\odot$ *at metallicity* $Z \sim 0.0002$*. However, most BHs in merging BHBs have masses* $\lesssim 40\ M_\odot$*. We find merging BHBs with mass ratios in the* $0.1-1.0$ *range, even if mass ratios* > 0.6 *are more likely. We predict that systems like GW150914, GW170814 and GW170104 can form only from progenitors with metallicity* $Z \leq 0.006$*,* $Z \leq 0.008$ *and* $Z \leq 0.012$*, respectively. Most merging BHBs have gone through a common envelope phase, but up to* ~ 17 *per cent merging BHBs at low metallicity did not undergo any common envelope phase. We find a much higher number of mergers from metal-poor progenitors than from metal-rich ones: the number of BHB mergers per unit mass is* $\sim 10^{-4}\ M_\odot^{-1}$ *at low metallicity (*$Z = 0.0002-0.002$*) and drops to* $\sim 10^{-7}\ M_\odot^{-1}$ *at high metallicity (*$Z \sim 0.02$*).*

Based on:
Giacobbo N., Mapelli M., Spera M., MNRAS, 2018, 474, p.2959-2974

2.1 Introduction

The first four direct detections of gravitational waves (GWs, Abbott et al., 2016b; Abbott et al., 2016d; Abbott et al., 2016a; Abbott et al., 2017b; Abbott et al., 2017d) revolutionised our knowledge of black hole binaries (BHBs). Thanks to them, we now know that coalescing BHBs exist and can host massive black holes (BHs), with mass $\gtrsim 30$ M$_\odot$ (as in the case of GW150914, GW170104 and GW170814).

The formation and evolution of BHBs have been investigated for a long time (e.g. Tutukov et al., 1973; Thorne, 1987; Schutz, 1989; Kulkarni et al., 1993; Sigurdsson and Phinney, 1993; Portegies Zwart and McMillan, 2000; Colpi et al., 2003; Belczynski et al., 2004). Already before the first LIGO detection, several theoretical studies predicted the existence of stellar BHs with mass $\gtrsim 30$ M$_\odot$ (e.g. Heger et al., 2003; Mapelli et al., 2009; Mapelli et al., 2010; Belczynski et al., 2010; Fryer et al., 2012; Mapelli et al., 2013; Spera et al., 2015). The basic idea is that if the pre-supernova mass of a star is sufficiently large (Fryer, 1999; Fryer et al., 2001) and/or its pre-supernova compactness sufficiently high (O'Connor and Ott, 2011), the star can collapse to a BH directly, producing a more massive remnant than in case of a supernova (SN) explosion.

Unfortunately, state-of-the-art theoretical models of BHBs still suffer from major uncertainties. The main issues are the treatment of core-collapse supernovae, stellar winds, and common envelope (CE, e.g. Dominik et al., 2012). The impact of stellar dynamics on the formation of BHBs is also matter of debate (e.g. Ziosi et al., 2014; Rodriguez et al., 2015; Rodriguez et al., 2016; Mapelli, 2016; Askar et al., 2016; Antonini et al., 2017; Banerjee, 2018).

The physics of core-collapse SNe is remarkably complex and barely understood (e.g. Fryer, 1999; Heger and Woosley, 2002; Heger et al., 2003; Fryer, 2006; O'Connor and Ott, 2011; Fryer et al., 2012; Janka, 2012; Burrows, 2013; Pejcha and Prieto, 2015; Woosley, 2017). The key point is to understand the connection between the final stages of a massive star's life and the outcome of a SN (for a review, see Limongi, 2017). In particular, it is crucial to assess what are the conditions for a star to directly collapse into a BH, without an explosion (e.g. Bethe, 1990; Fryer, 1999; Fryer et al., 2001; Janka et al., 2007; O'Connor and Ott, 2011; Janka, 2012; Burrows, 2013; Ertl et al., 2016).

Mass loss by stellar winds is also crucial, because it governs the final mass $M_{\rm fin}$ of a star, i.e. the mass of a star just before the SN (see e.g. Mapelli et al., 2009; Belczynski et al., 2010; Fryer et al., 2012; Mapelli et al., 2013). In the last decade, models of line-driven stellar winds were profoundly revised. Current models suggest a strong

dependence of mass loss on metallicity ($\dot{M} \propto Z^{\alpha}$, with $\alpha \sim 0.85$, Vink et al., 2001; Vink et al., 2011; Muijres et al., 2012) not only during the main sequence (MS) but also after, including the Wolf-Rayet (WR) stage (see e.g. Vink and de Koter, 2005a; Meynet and Maeder, 2005; Gräfener and Hamann, 2008; Vink et al., 2011; Tang et al., 2014; Chen et al., 2015).

In addition, there has been a debate regarding the importance of stationary versus eruptive mass loss for massive star evolution (Vink and Gräfener, 2012). Clumping of stellar winds results in a reduction of the mass-loss rate. Recent theoretical models (e.g. Vink et al., 2001) predict lower mass-loss rates by a factor of 2 – 3 with respect to unclumped empirical mass-loss rates, consistent with a moderate wind clumping.

Finally, some of the most recent wind models (e.g. Gräfener and Hamann, 2008; Gräfener et al., 2011; Vink et al., 2011; Vink, 2017a) and observations (e.g. Bestenlehner et al., 2014) suggest that mass loss also depends on the electron-scattering Eddington factor Γ_e of the star. In particular, if a star approaches the Eddington limit (i.e. $\Gamma_e \lesssim 1$), stellar winds become almost insensitive to metallicity. Most stellar evolution models do not include this dependence, with very few exceptions (e.g. PARSEC, Chen et al., 2015). Population-synthesis codes, which are used to study the demography of BHs and BHBs, should also account for these updated models of stellar winds and massive star evolution.

Currently, only few population-synthesis codes adopt up-to-date metallicity-dependent prescriptions for stellar winds (e.g. Belczynski et al., 2010; Toonen et al., 2012; Mapelli et al., 2013; Spera et al., 2015; Spera and Mapelli, 2017; Banerjee, 2018). The dependence of stellar winds on the Eddington factor is implemented only in the SEVN code (where SEVN is the acronym for 'Stellar EVolution for N-body' Spera et al., 2015; Spera and Mapelli, 2017). In its published version, SEVN only evolves single stars and is currently undergoing a major upgrade to include the main binary evolution processes (Spera et al., 2019).

Here we present our upgraded version of BSE (acronym for 'Binary Stellar Evolution'), one of the most popular population-synthesis codes (Hurley et al., 2000; Hurley et al., 2002). In the following, we refer to our new version of BSE as MOBSE (which stands for 'Massive Objects in Binary Stellar Evolution'). With respect to BSE, MOBSE includes up-to-date equations for metal-dependent stellar winds (based on Belczynski et al., 2010 and on Chen et al., 2015) and new prescriptions for core-collapse SNe (based on Fryer et al., 2012). Moreover, MOBSE includes the dependence of stellar winds on the Eddington factor, adopting the prescriptions by Chen et al. (2015).

We use MOBSE to investigate the formation of BHBs from isolated binaries, comparing different models of stellar winds and SNe. We also examine the role played by the CE phase in the formation of BHBs.

2.2 Methods

In this Section, we describe the main features of MOBSE with respect to BSE.
MOBSE adopts the following prescriptions for stellar winds. For O and B stars with effective temperature $12500\,\mathrm{K} \leq T \leq 25000\,\mathrm{K}$ we adopt equation 25 of Vink et al. (2001):

$$\begin{aligned}\log \dot{M} = \quad & -6.688 + 2.210 \log\left(\frac{L}{10^5\ \mathrm{L}_\odot}\right) \\ & -1.339 \log\left(\frac{M}{30\ \mathrm{M}_\odot}\right) - 1.601 \log\left(\frac{V}{2.0}\right) \\ & +\alpha \log\left(\frac{Z}{\mathrm{Z}_\odot}\right) + 1.07 \log\left(\frac{T}{20000\ \mathrm{K}}\right),\end{aligned} \tag{2.1}$$

where L is the stellar luminosity, M is the stellar mass, α expresses the dependence of mass loss on metallicity and $V = v_{inf}/v_{esc} = 1.3$ is the ratio of the wind velocity at infinity (v_{inf}) to escape velocity (v_{esc}).
For O and B stars stars with $25000\ \mathrm{K} < T \leq 50000\ \mathrm{K}$ we use equation 24 of Vink et al. (2001):

$$\begin{aligned}\log \dot{M} = \quad & -6.697 + 2.194 \log\left(\frac{L}{10^5 L_\odot}\right) \\ & -1.313 \log\left(\frac{M}{30\ \mathrm{M}_\odot}\right) - 1.226 \log\left(\frac{V}{2.0}\right) \\ & +\alpha \log\left(\frac{Z}{\mathrm{Z}_\odot}\right) + 0.933 \log\left(\frac{T}{40000\ \mathrm{K}}\right) \\ & 10.92 \left[\log\left(\frac{T}{40000\ \mathrm{K}}\right)\right]^2,\end{aligned} \tag{2.2}$$

where $V = v_{inf}/v_{esc} = 2.6$. The above dichotomy is due to the bi-stability jump, i.e. a sudden jump in the mass-loss rate related to the fact that the iron ions driving the wind recombine at $T \sim 25000$ K, and again below 12500 K (for more details see Vink et al., 1999; Petrov et al., 2016).
We express the mass loss of luminous blue variable (LBV) stars as

$$\dot{M} = 10^{-4} f_{\mathrm{LBV}} \left(\frac{Z}{\mathrm{Z}_\odot}\right)^{\alpha} \mathrm{M}_\odot\,\mathrm{yr}^{-1}, \tag{2.3}$$

where f_{LBV} is a parameter (we choose $f_{\mathrm{LBV}} = 1.5$, in agreement with Belczynski et al., 2010).

Finally, for Wolf-Rayet (WR) stars we use equation 9 of Belczynski et al. (2010):

$$\dot{M}_{\rm WR} = 10^{-13} L^{1.5} \left(\frac{Z}{Z_\odot}\right)^{\alpha} \ {\rm M}_\odot \ {\rm yr}^{-1} \ . \tag{2.4}$$

For the other stars, MOBSE adopts the same mass loss formalism as the original version of BSE.

MOBSE1

Equations 2.1, 2.2, 2.3 and 2.4, contain the parameter α which expresses the dependence of mass loss on metallicity. In our fiducial version of MOBSE (hereafter, MOBSE1), we define α in the following way:

$$\alpha = \begin{cases} 0.85 & \text{if} \ \ \Gamma_{\rm e} < 2/3 \\ 2.45 - 2.4\,\Gamma_{\rm e} & \text{if} \ \ 2/3 \leq \Gamma_{\rm e} \leq 1 \ , \end{cases} \tag{2.5}$$

where Γ_e is expressed as (see equation 8 of Gräfener et al., 2011):

$$\log\Gamma_e = -4.813 + \log(1 + X_{\rm H}) + \log(L/L_\odot) - \log(M/M_\odot), \tag{2.6}$$

where $X_{\rm H}$ is the Hydrogen fraction.
According to this definition, the dependence of mass loss on metallicity almost vanishes when the star is radiation pressure dominated ($\Gamma_e \sim 1$). This expression for α was derived by Tang et al. (2014) and Chen et al. (2015), based on the results of Gräfener and Hamann, 2008. In fact, Gräfener and Hamann (2008) and Vink et al. (2011) show that the mass-loss rate is strongly enhanced when the star approaches the electron-scattering Eddington limit Γ_e. This means that increasing Γ_e the metallicity dependence becomes weaker.

MOBSE2

Other population-synthesis codes (e.g. STARTRACK, Belczynski et al., 2010) do not take into account the effect of Γ_e on mass loss. To quantify the importance of Γ_e and to compare our results with previous work, we also introduce a second version of our MOBSE code (which we will refer to as MOBSE2), where we do not include the effect of Γ_e.
In MOBSE2, the parameter α is defined as

$$\alpha = \begin{cases} 0.85 & \text{in equations 2.1 and 2.2} \\ 0 & \text{in equation 2.3} \\ 0.86 & \text{in equation 2.4.} \end{cases} \tag{2.7}$$

The values of α defined in equation 2.7 are the same as adopted by Belczynski et al. (2010). This implies that in MOBSE2 mass loss of O and B-type stars scales as $\dot{M} \propto Z^{0.85}$ (Vink et al., 2001). WR stars also show a similar dependence ($\alpha \sim 0.86$, Vink and de Koter, 2005a). Finally, the mass loss of LBVs does not depend on metallicity, as in equation 8 of Belczynski et al. (2010). This means that mass loss of LBVs is constant, while mass loss of MS and WR stars does not depend on Γ_e.

2.2.1 Supernovae

The physics of core-collapse SNe is uncertain and several different models exist (see Smartt, 2009 for a review). For this reason, we have implemented two different prescriptions for core-collapse SNe (described in details by Fryer et al., 2012): i) the *rapid* SN model and ii) the *delayed* SN model.
The main difference between them is that they assume a different time-scale at which the explosion occurs: in the rapid (delayed) model the explosion takes place $t < 250$ ms ($t \gtrsim 0.5$ s) after core bounce.
Both the prescriptions depend only on the final mass of the Carbon-Oxygen (CO) core ($M_{\rm CO}$) and on the final mass of the star ($M_{\rm fin}$), which determines the amount of fallback.
Other studies suggest a more complex relation between the properties of the star at the onset of collapse and the compact remnant mass (e.g. O'Connor and Ott, 2011; Janka, 2012; Ugliano et al., 2012; Pejcha and Prieto, 2015; Ertl et al., 2016) and provide alternative formalisms to predict the remnant mass (e.g. the compactness criterion by O'Connor and Ott, 2011 or the two-parameter criterion by Ertl et al., 2016). However, we cannot adopt these alternative formalisms in BSE, because

they rely on the inner structure of the star at the onset of collapse, which is not calculated in BSE. Figure 21 of the recent review by Limongi (2017) shows that there is a strong correlation between the compactness parameter and the CO mass of the progenitor star, suggesting that our formalism based on the CO mass should give results similar to the formalism based on the compactness parameter in most cases (see also Figures 21 and 22 of Spera et al., 2015).

Furthermore, the rapid and delayed SN models do not distinguish between neutron stars (NSs) and BHs, because they are general prescriptions for the formation of compact remnants. According to the Tolman-Oppenheimer-Volkoff limit (Oppenheimer and Volkoff, 1939), we assume that the minimum mass for a BH is $3.0\,M_\odot$ and all compact SN remnants with mass $< 3.0\,M_\odot$ are NSs.

The details of the implementation of core-collapse SNe in MOBSE can be found in Appendix A.

In MOBSE, we also added a formalism for pair-instability SNe (PISNe, Ober et al., 1983; Bond et al., 1984; Heger et al., 2003; Woosley et al., 2007) and pulsational pair-instability SNe (PPISNe, Barkat et al., 1967; Woosley et al., 2007; Chen et al., 2014; Yoshida et al., 2016), which are not included in BSE and in most population-synthesis codes. Our description of PISNe is based on the results by Heger et al. (2003): if the final Helium core mass ($M_{\rm He,f}$) of a star is $64\,M_\odot \lesssim M_{\rm He,f} \lesssim 135\,M_\odot$, we assume that the star leaves no remnant, because the ignition of Oxygen and Silicon releases enough energy to disrupt the entire star. If $M_{\rm He,f} > 135\ M_\odot$, the star is expected to avoid the PISN and to directly collapse into a BH.

Our description of PPISNe is based on the formalism presented in Spera et al. (2016) and Spera and Mapelli (2017) (see also Belczynski et al., 2016a; Woosley, 2017). If the final mass of the Helium core is $32\,M_\odot \lesssim M_{\rm He,f} \lesssim 64\,M_\odot$, the star undergoes a PPISN and leaves a compact remnant whose mass is described by the fitting formulas in Appendix B.

We also updated the natal kick for BHs ($V_{\rm kick}$) as follows (Fryer et al., 2012):

$$V_{\rm kick} = (1 - f_{\rm fb})\, W_{\rm kick}, \tag{2.8}$$

where $f_{\rm fb}$ is the fallback factor (the explicit expression can be found in Appendix A). $W_{\rm kick}$ is randomly drawn from a Maxwellian distribution with a one dimensional root-mean square $\sigma = 265$ km s^{-1}. This distribution was derived by Hobbs et al. (2005), based on the proper motions of 233 isolated Galactic pulsars.

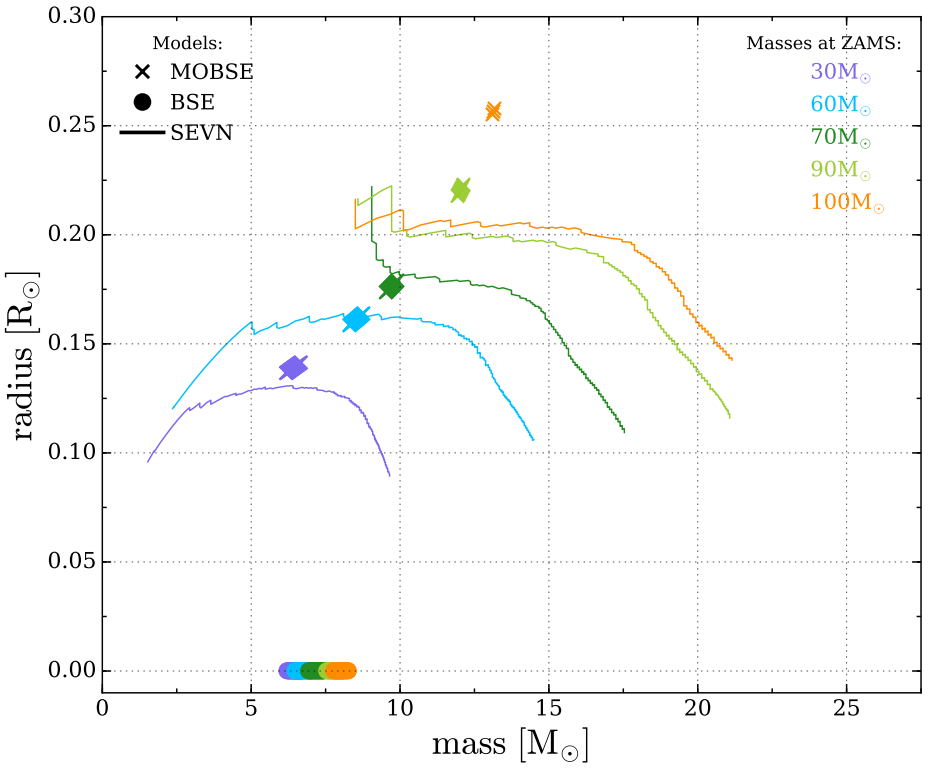

Figure 2.1: Radius versus mass of the CO core for five stars with zero-age main sequence (ZAMS) mass $M_{\rm ZAMS} = 30, 60, 70, 90, 100\,{\rm M}_{\odot}$, at solar metallicity ($Z = 0.02$). Solid line: SEVN; crosses: MOBSE ; circles: BSE.

2.2.2 Additional changes in MOBSE

We also added to MOBSE the fitting formulas described in Hall and Tout (2014), to compute the core radius of evolved stars. The core radius is crucial to determine the final fate of a CE system. Figure 2.1 shows the differences between the CO core radii computed with BSE (triangles), MOBSE (circles) and SEVN (lines) as a function of the core mass. The CO core radii derived with MOBSE are of the same order of magnitude as those obtained with SEVN, while BSE predicts unphysically small CO core radii. Our treatment of WR and LBV stars does not account for envelope inflation, which might increase the effective photospheric radii by a factor of ~ 10 (Gräfener et al., 2012). We will include this effect in forthcoming studies.

Another critical issue of CE is the treatment of Hertzsprung Gap (HG) donors (e.g. de Mink and Belczynski, 2015). During the HG phase, stars do not present a steep density gradient between the core and the envelope and for this reason their response to the CE phase should be similar to that of MS stars (see Ivanova and Taam,

2004). In BSE, when a MS star enters a CE phase as donor it merges with the accretor, while HG donors are allowed to survive the CE phase. On the contrary, in MOBSE we imposed that even HG donors merge with their companions if they enter a CE phase (Dominik et al., 2012).
Finally, we also extended the mass range of BSE to include stars up to 150 $M_\odot$. Because of the fitting formulas by Hurley et al. (2000) might be inaccurate for very massive stars (> 100 $M_\odot$) we imposed that the values of the stellar radii of single star are consistent with PARSEC stellar evolution tracks (Chen et al., 2015), as discussed in Mapelli (2016). We do not consider stars with zero-age main sequence (ZAMS) mass $M_{\rm ZAMS} > 150\ M_\odot$, because the mismatch between BSE fitting formulas and PARSEC tracks increases significantly above this mass (see e.g. Fig. 2.2).

2.2.3 Simulations and initial distributions

In this section we detail the initial conditions of our population synthesis simulations. The mass of the primary star (m_1) is randomly extracted from a Kroupa initial mass function (Kroupa, 2001),

$$\mathfrak{F}(m_1) \propto m_1^{-2.3} \qquad \text{with } m_1 \in [5-150]\,M_\odot\,. \tag{2.9}$$

We sampled the mass of the secondary m_2 according to the distribution proposed by Sana et al. (2012)

$$\mathfrak{F}(q) \propto q^{-0.1} \qquad \text{with } q = \frac{m_2}{m_1} \in [0.1-1]\ m_1\,, \tag{2.10}$$

We adopt the distributions proposed by Sana et al. (2012) also for the orbital period P and the eccentricity e:

$$\mathfrak{F}(P) \propto (P)^{-0.55} \qquad \text{with } P = \log_{10}(P/\text{day}) \in [0.15-5.5] \tag{2.11}$$

and

$$\mathfrak{F}(e) \propto e^{-0.42} \qquad \text{with } 0 \le e < 1\,. \tag{2.12}$$

For the CE phase we adopted the same formalism used by Hurley et al. (2002) and described in detail in Ivanova et al. (2013). This formalism depends on two free parameters, α and λ, where, α is the fraction of orbital energy which can be used to unbind the envelope and λ describes the geometry of the envelope. In this work, we consider three different combinations of these parameters: $\alpha = 1.0$, $\lambda = 0.1$ (which is well motivated for massive stars, see e.g. Xu and Li, 2010; Loveridge et al., 2011), $\alpha = 3.0$, $\lambda = 0.5$ and $\alpha = 0.2$, $\lambda = 0.1$.

Table 2.1: Initial conditions.

ID	Winds	SN	α	λ
MOBSE1_D	MOBSE 1	delayed	1.0	0.1
MOBSE1_R	MOBSE 1	rapid	1.0	0.1
MOBSE2_D	MOBSE 2	delayed	1.0	0.1
MOBSE2_R	MOBSE 2	rapid	1.0	0.1
MOBSE1_D1.5	MOBSE 1	delayed	3.0	0.5
MOBSE1_D0.02	MOBSE 1	delayed	0.2	0.1
MOBSE2_D1.5	MOBSE 2	delayed	3.0	0.5
MOBSE2_D0.02	MOBSE 2	delayed	0.2	0.1

Column 1: simulation name; column 2: stellar wind model (MOBSE1 and MOBSE2); column 3: SN model (delayed and rapid from Fryer et al., 2012); column 4 and 5: values of α and λ in the CE formalism.

We ran eight sets of simulations (see Table 2.1) in order to test different combinations of stellar wind models, SN explosion mechanisms and values of α and λ.
For each set of simulations we performed 12 sub-sets with different metallicities $Z = 0.0002$, 0.0004, 0.0008, 0.0012, 0.0016, 0.002, 0.004, 0.006, 0.008, 0.012, 0.016 and 0.02. The polynomial fitting formulas implemented in BSE (Hurley et al., 2000) and the prescriptions for mass loss adopted in MOBSE have been shown to hold in this metallicity range (e.g. Kudritzki, 2002; Bresolin and Kudritzki, 2004). In each sub-set, we simulate 10^7 binary systems. Thus, each of the eight sets of simulations is composed of 1.2×10^8 massive binaries.

2.3 Results

2.3.1 Mass loss by stellar winds

In this Section, we discuss the evolution of single massive stars obtained with MOBSE1 and MOBSE2, in comparison to other open-source population synthesis codes, namely BSE (Hurley et al., 2000; Hurley et al., 2002) and SEVN (Spera et al., 2015; Spera et al., 2016; Spera and Mapelli, 2017). BSE is the original code from which MOBSE derives, while SEVN is a more recent code. In BSE single stellar evolution is implemented using polynomial fitting formulas (Hurley et al., 2000), while in SEVN stellar evolution is calculated from look-up tables (the current default tables are based on the recent PARSEC stellar evolution code, Bressan et al., 2012; Tang et al., 2014; Chen et al., 2015).

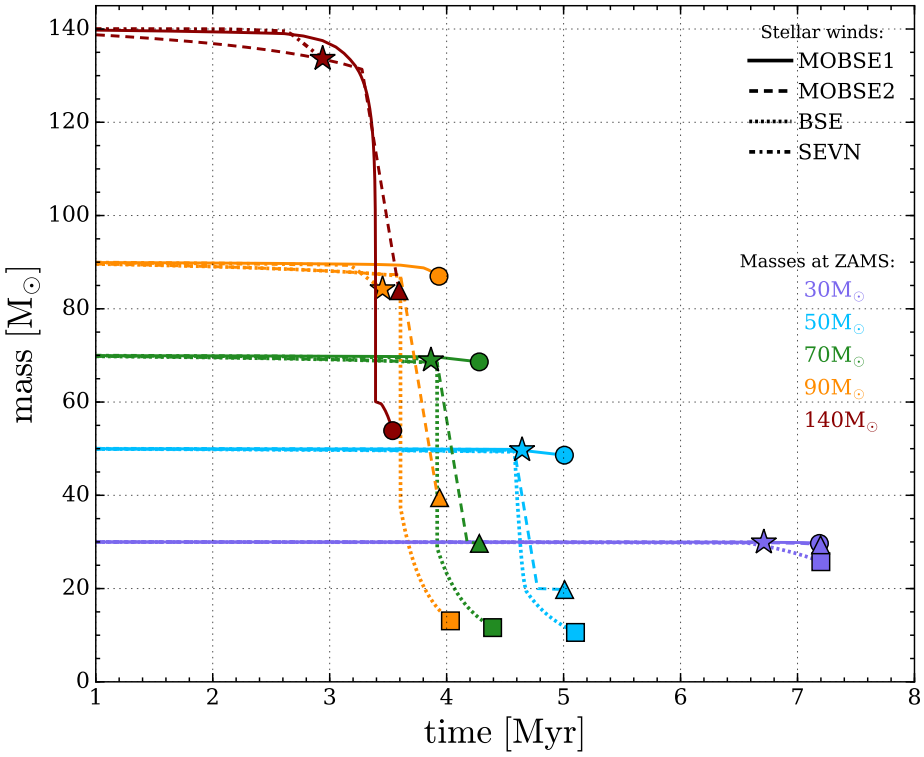

Figure 2.2: Stellar mass evolution with time for five different $M_{\rm ZAMS}$ at $Z = 0.0002$ computed with MOBSE, BSE and SEVN. Solid lines: MOBSE1; dashed lines: MOBSE2; dotted lines: BSE; dash-dot lines: SEVN. The markers identify the final mass of the stars: circles for MOBSE1, triangles for MOBSE2, squares for BSE and stars for SEVN.

Figure 2.2 shows the evolution of stellar mass at $Z = 0.0002$ for various ZAMS masses. At low ZAMS masses ($\lesssim 30$ M$_\odot$) the behavior of the considered codes is quite indistinguishable. The main difference is the duration of stellar life in BSE and MOBSE with respect to the more updated SEVN code (see Fig. 2.2).

For larger ZAMS masses, there is a pronounced difference in the late evolutionary stages, due to the different stellar wind models. These differences are highlighted in Figure 2.3, which shows the final stellar mass ($M_{\rm fin}$), as a function of the ZAMS mass ($M_{\rm ZAMS}$) at $Z = 0.0002$. MOBSE1 is in remarkable agreement with SEVN for stars lighter than $M_{\rm ZAMS} \simeq 100\,{\rm M}_\odot$, predicting a low mass loss during the entire star's life. For more massive stars ($M_{\rm ZAMS} > 100\,{\rm M}_\odot$), SEVN follows the same trend as for lighter stars, i.e. mass loss is extremely quenched, while the value of $M_{\rm fin}$ in model MOBSE1 drops to $\sim 50\,{\rm M}_\odot$.

The evolution of the stellar mass in MOBSE2 is generally intermediate between that of BSE and that of both SEVN and MOBSE1. This difference arises mainly

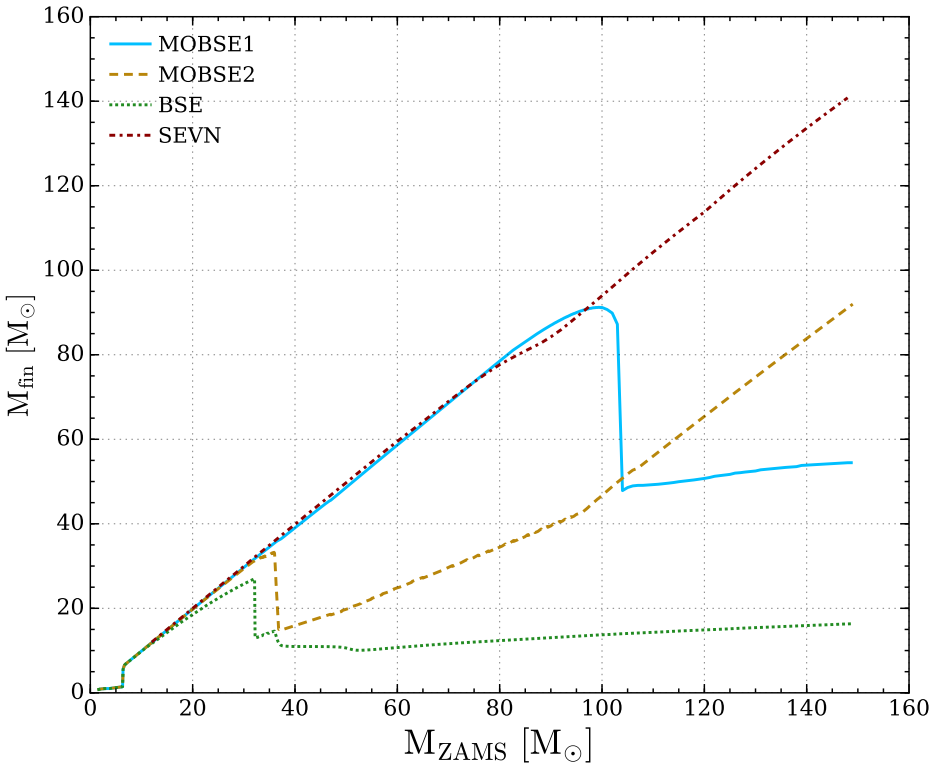

Figure 2.3: Final mass of a star ($M_{\rm fin}$) as a function of its ZAMS mass at $Z = 0.0002$. Solid line: MOBSE1; dashed line: MOBSE2; dotted line: BSE; dash-dot line: SEVN. In all cases we considered the delayed SN model.

from the treatment of LBV stars. In both MOBSE1 and SEVN the mass loss scales as $\dot{M} \propto Z^{0.85}$, unless a star is radiation-pressure dominated ($\Gamma_e > 2/3$, see equations 2.5). In contrast, MOBSE2 assumes a strong mass loss rate for LBVs, independent of metallicity even if $\Gamma_e < 2/3$ (see equation 2.7).

2.3.2 Mass spectrum of compact remnants

Figure 2.4 shows the trend of the remnant mass ($M_{\rm rem}$) as a function of $M_{\rm ZAMS}$, for different values of the metallicity ($0.0002 \leq Z \leq 0.02$). In this Figure, we adopt the delayed mechanism for SN explosions. The upper and the lower panel show the results of MOBSE1 and MOBSE2, respectively. As expected, there is a relation between the maximum mass of the compact remnants and the metallicity: the lower the metallicity is, the higher the mass of the heaviest remnant.
At high metallicity ($Z = 0.02$) MOBSE1 and MOBSE2 are almost indistinguishable. In both models, the remnant mass increases monotonically with the ZAMS mass,

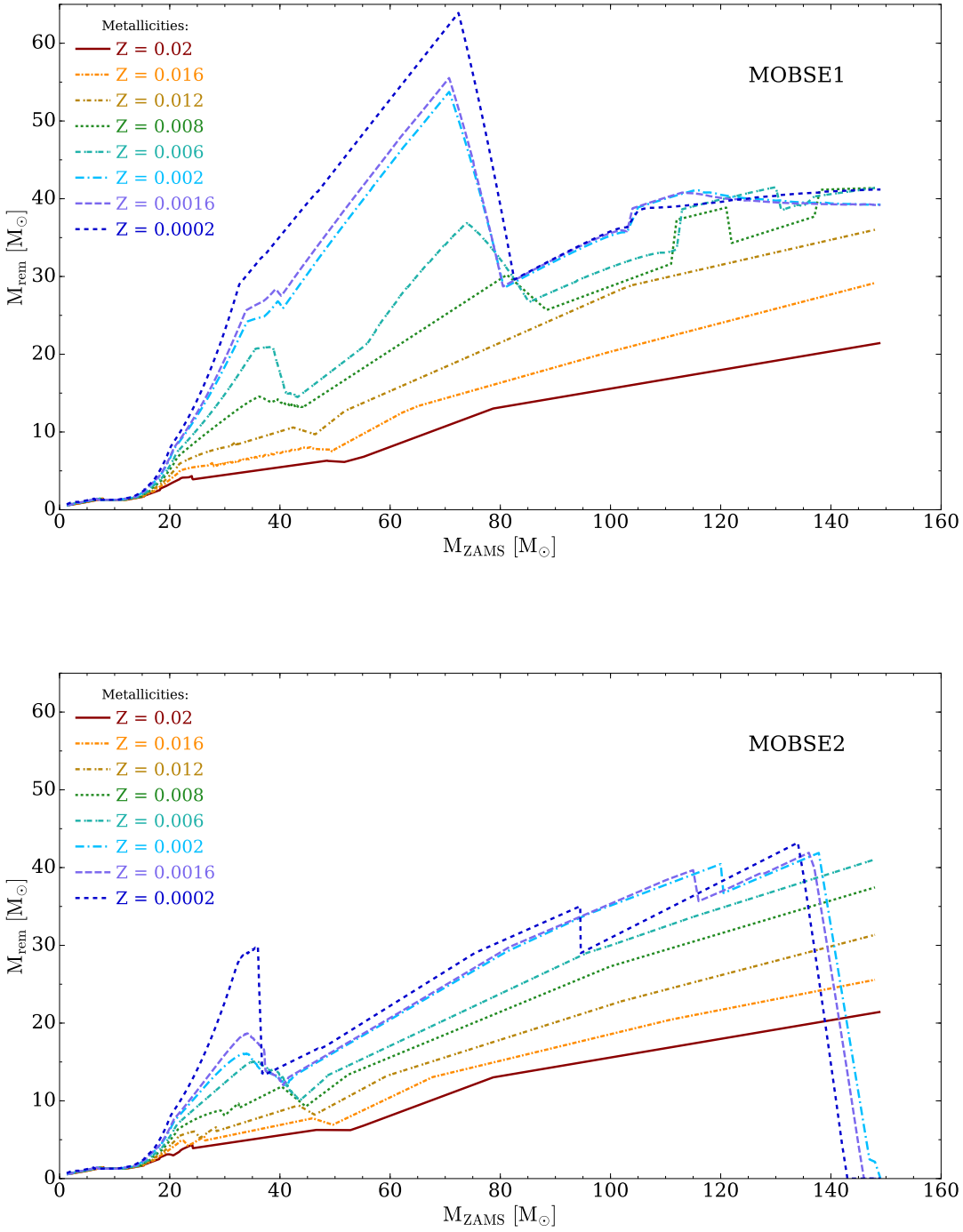

Figure 2.4: Mass of the compact remnant ($M_{\rm rem}$) as a function of the ZAMS mass of the progenitor star, for different metallicities between $Z = 0.0002$ and 0.02. Top: MOBSE1. Bottom: MOBSE2. In both cases we assume the delayed SN model.

until it reaches $M_{\rm rem} \sim 20\,{\rm M}_{\odot}$.
At lower metallicities ($Z = 0.002$ and $Z = 0.0002$), MOBSE1 and MOBSE2 differ significantly, especially for $M_{\rm ZAMS} > 30\,{\rm M}_{\odot}$. In MOBSE1 the remnant mass rapidly increases with $M_{\rm ZAMS}$ untill it reaches its maximum ($M_{\rm rem} \sim 50-65$ M$_{\odot}$) at $M_{\rm ZAMS} \sim 70\,{\rm M}_{\odot}$. For larger ZAMS masses, the remnant mass drops to ~ 40 M$_{\odot}$. In MOBSE2 the remnant mass has a local maximum for $M_{\rm ZAMS} \sim 30\,{\rm M}_{\odot}$. For larger ZAMS masses, it drops and then rises steadily to a global maximum of $M_{\rm rem} \sim 40\,{\rm M}_{\odot}$ at $M_{\rm ZAMS} > 120$ M$_{\odot}$.
Thus, the maximum BH mass predicted by MOBSE1 is $50-65$ M$_{\odot}$, significantly higher than the maximum BH mass predicted by MOBSE2 (~ 40 M$_{\odot}$). The main reason for this difference is, again, the dependence of mass loss on the Eddington factor implemented in MOBSE1 but not in MOBSE2.
Figure 2.5 compares the mass spectrum of compact remnants obtained with MOBSE, SEVN and BSE at three different metallicities. The dependence on metallicity is weaker for BSE, and stronger for both MOBSE and SEVN. At solar metallicity, all codes predict remnant masses < 30 M$_{\odot}$. At metallicity $Z = 0.002$ and $Z = 0.0002$, BSE is the only code predicting $M_{\rm rem} < 30$ M$_{\odot}$, because of the stellar wind prescriptions. Both MOBSE and SEVN predict larger masses. We note that the BH mass spectrum obtained with MOBSE2 is in agreement with Belczynski et al. (2016b), who adopt similar prescriptions for the stellar winds (Belczynski et al., 2010).
At low metallicity ($Z < 0.002$) SEVN and MOBSE1 are in good agreement, while the remnant masses obtained with MOBSE2 are significantly different from both SEVN and MOBSE1. The key ingredient is again the fact that the stellar wind prescriptions implemented in SEVN and MOBSE1 depend on both the metallicity and the Eddington factor.
The good agreement between SEVN and MOBSE1 is particularly remarkable, because SEVN (Spera and Mapelli, 2017) adopts very recent stellar evolution models (from PARSEC, Bressan et al., 2012; Chen et al., 2015), while MOBSE1 is still based on the polynomial fitting formulas described by Hurley et al. (2000). This result confirms the importance of accounting for the Eddington factor in mass loss models.
In Figure 2.5 we can also note the effect of PISNe and PPISNe on the most massive metal-poor stars (see also Figure B1 in Appendix B). At metallicity $Z \leq 0.002$, very massive stars leave no remnant as an effect of PISNe in both MOBSE2 and SEVN. PISNe do not occur in MOBSE1 and BSE, because the final Helium core mass is always below the threshold for PISNe (~ 64 M$_{\odot}$). PPISNe occur in MOBSE1, MOBSE2

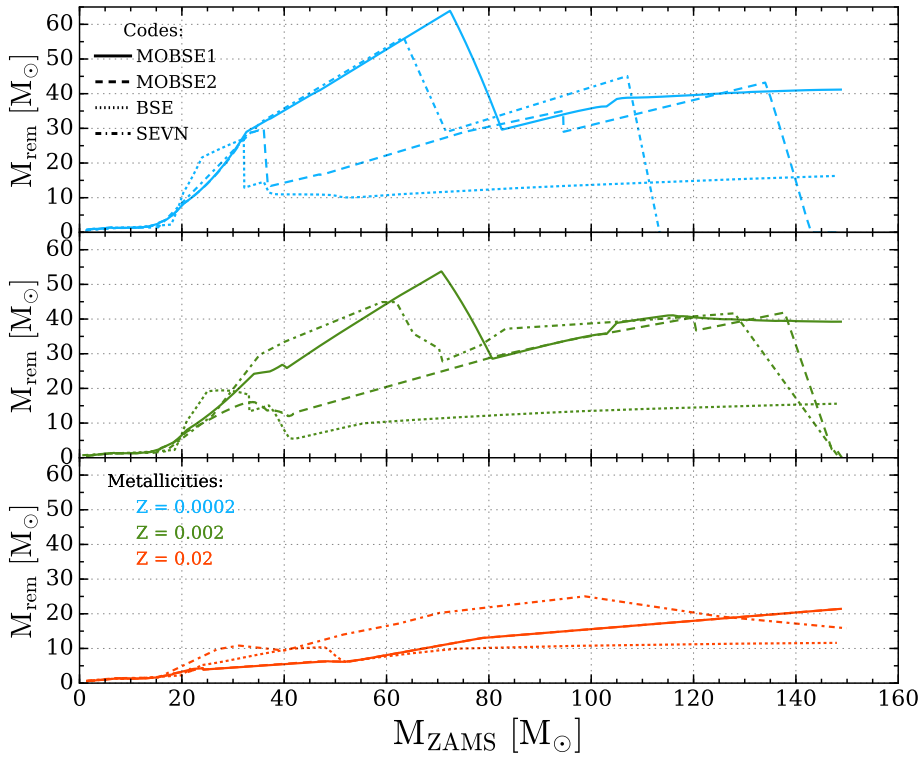

Figure 2.5: Mass of the compact remnant ($M_{\rm rem}$) as a function of the ZAMS mass of the progenitor stars, for $Z = 0.02$ (bottom panel), $Z = 0.002$ (central panel) and $Z = 0.0002$ (top panel). Solid lines: MOBSE1; dashed lines: MOBSE2; dash-dot lines: SEVN; dotted lines: BSE. In all cases the delayed SN model is assumed.

and SEVN at low metallicity ($Z \leq 0.008$ for MOBSE1 and SEVN and $Z \leq 0.002$ for MOBSE2) for stars with $32\,{\rm M}_\odot \lesssim M_{\rm He,f} \lesssim 64\,{\rm M}_\odot$. Their effect is a substantial decrease of the remnant mass with respect to the final mass of the star ($M_{\rm fin}$, Figure 2.3). PPISNe do not occur in BSE, because the final Helium core mass does not reach the threshold for PPISNe in BSE.

Figure 2.6 compares the rapid and the delayed core-collapse SN models. ZAMS masses larger than 50 $\rm M_\odot$ are not shown, because the rapid and the delayed SN models produce exactly the same remnant mass for $M_{\rm ZAMS} > 50\ {\rm M}_\odot$, in agreement with Fryer et al. (2012) and Spera et al. (2015).

The main difference between rapid and delayed SN model is the number of remnants with mass $2 < M_{\rm rem} < 5\,{\rm M}_\odot$. The rapid SN model predicts a mass gap between the lightest BHs ($\sim 5\,{\rm M}_\odot$) and the heaviest NSs ($\sim 2\,{\rm M}_\odot$), while the delayed model predicts no gap. This result is consistent with previous studies (Fryer et al., 2012; Spera et al., 2015). Dynamical mass measurements of compact objects in X-ray binaries show marginal indications for the existence of a mass gap (e.g. Özel et al., 2010; Farr et al., 2011), possibly suggesting a preference for a rapid SN explosion.

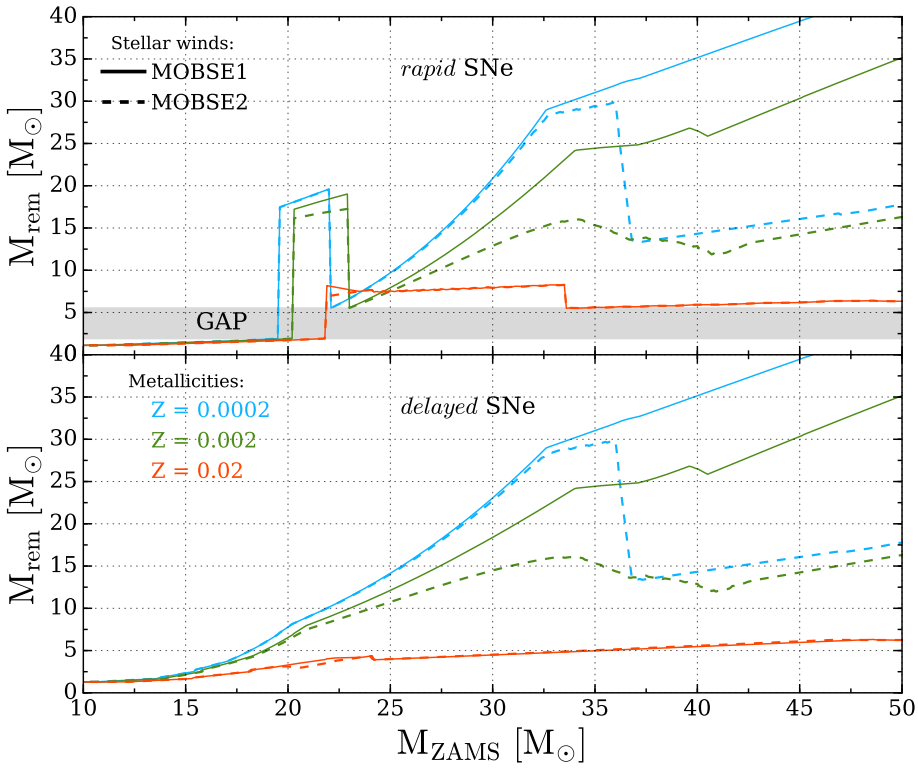

Figure 2.6: Mass of the compact remnant ($M_{\rm rem}$) as a function of the ZAMS mass of the progenitor star ($M_{\rm ZAMS}$) for two different core-collapse SN models: rapid SN model (upper panel) and delayed SN model (bottom panel). Red lines: metallicity $Z = 0.02$; green lines: $Z = 0.002$; blue lines: $Z = 0.0002$. Solid lines: MOBSE1, dashed lines: MOBSE2. In the top panel the mass gap between the heaviest NSs and the lightest BHs ($\sim 2\,M_\odot$ to $\sim 5\,M_\odot$) is highlighted by a shaded area.

2.3.3 Black hole binaries

In this section, we focus on the properties of BHBs derived from our binary population-synthesis simulations with MOBSE. The left-hand panels of Figures 2.7 and 2.8 show the chirp mass[1] ($m_{\rm chirp} = (m_{\rm p}\, m_{\rm s})^{3/5}/(m_{\rm p} + m_{\rm s})^{1/5}$, where $m_{\rm p}$ and $m_{\rm s}$ are the masses of the primary and secondary BH, respectively) and the total mass distributions of all BHBs which formed in our simulations MOBSE1_D and MOBSE2_D, including both BHBs which merge and BHBs which do not merge in a Hubble time. Simulations labelled as MOBSE1_D (MOBSE2_D) were run with MOBSE1 (MOBSE2), adopting the delayed SN model and assuming $\alpha = 1$, $\lambda = 0.1$ for the CE (see Table 2.1 for details on the simulations).

[1]The chirp mass is named that because it is this combination of $m_{\rm p}$ and $m_{\rm s}$ that determines how fast the binary sweeps, or chirps, through a frequency band. In fact, it can be shown that the amplitude and the frequency of GWs scale as $m_{\rm chirp}^{5/3}$ and $m_{\rm chirp}^{-5/8}$, respectively (Maggiore, 2008).

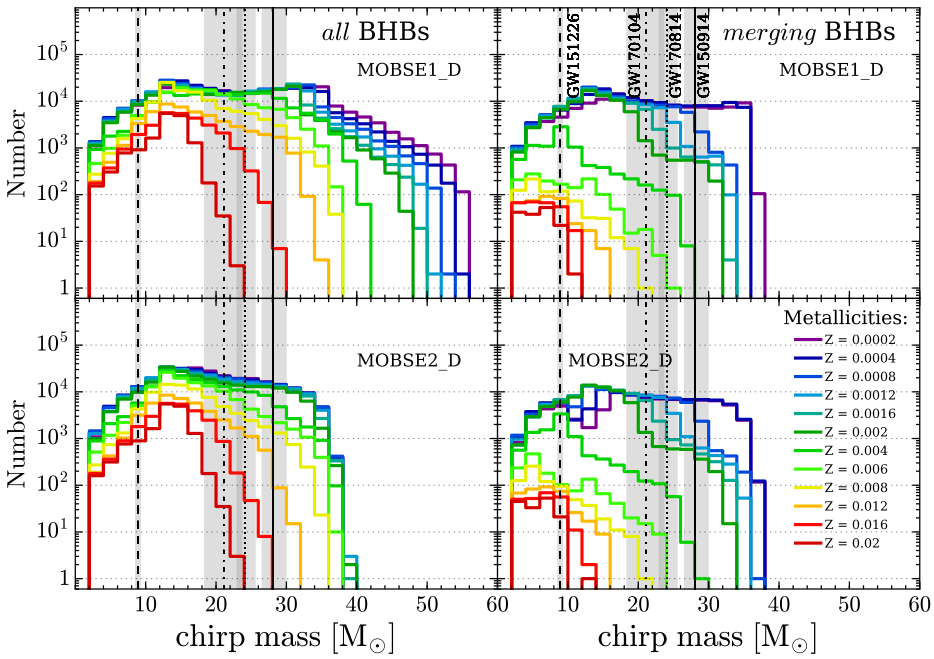

Figure 2.7: Chirp mass distribution of BHBs for MOBSE1_D (upper panels) and MOBSE2_D (lower panels). Left-hand column: chirp mass distribution for all BHBs. Right-hand column: chirp mass distribution for the merging BHBs only. Solid lines represent the chirp mass distributions at different metallicity, ranging from 0.0002 to 0.02. The vertical lines in all panels are the chirp masses of GW151226, GW150914 (Abbott et al., 2016b), GW170104 (Abbott et al., 2017b) and GW170814 (Abbott et al., 2017d) with the corresponding uncertainties (at the 90 per cent credible level, shadowed regions).

At low metallicity ($Z \lesssim 0.0004$), MOBSE1 produces very massive BHBs, with total mass up to $M_{\rm tot} \simeq 150\,{\rm M}_\odot$ and chirp mass up to $M_{\rm chirp} \simeq 55\,{\rm M}_\odot$, while the heaviest BHBs obtained with MOBSE2 have $M_{\rm tot} \simeq 90\,{\rm M}_\odot$ and $M_{\rm chirp} \simeq 40\,{\rm M}_\odot$. At solar metallicity ($Z = 0.02$), the maximum chirp mass (total mass) is $M_{\rm chirp} \simeq 20\,{\rm M}_\odot$ ($M_{\rm tot} \simeq 50\,{\rm M}_\odot$) for both MOBSE1 and MOBSE2.

We now restrict our attention to merging BHBs. The right-hand panels of Figures 2.7 and 2.8 show the chirp mass and the total mass distributions for the sub-sample of merging BHBs (defined as BHBs which merge within a Hubble time). It is apparent that the maximum mass of merging BHBs is significantly smaller than the maximum mass of non-merging BHBs. This difference persists at all metallicities, and is more pronounced in MOBSE1 than in MOBSE2.

The heaviest merging BHs have $M_{\rm BH,max} \simeq 45\,{\rm M}_\odot$ (only few systems have a primary BH $\gtrsim 55$ M$_\odot$, in model MOBSE1) at $Z \leq 0.0002$ and $M_{\rm BH,max} \simeq 20\,{\rm M}_\odot$ at $Z = 0.02$. The maximum values of the chirp masses are $M_{\rm chirp} \simeq 40\,{\rm M}_\odot$ and $M_{\rm chirp} \simeq 10\,{\rm M}_\odot$ at $Z = 0.0002$ and $Z = 0.02$, respectively. The masses of merging BHBs predicted

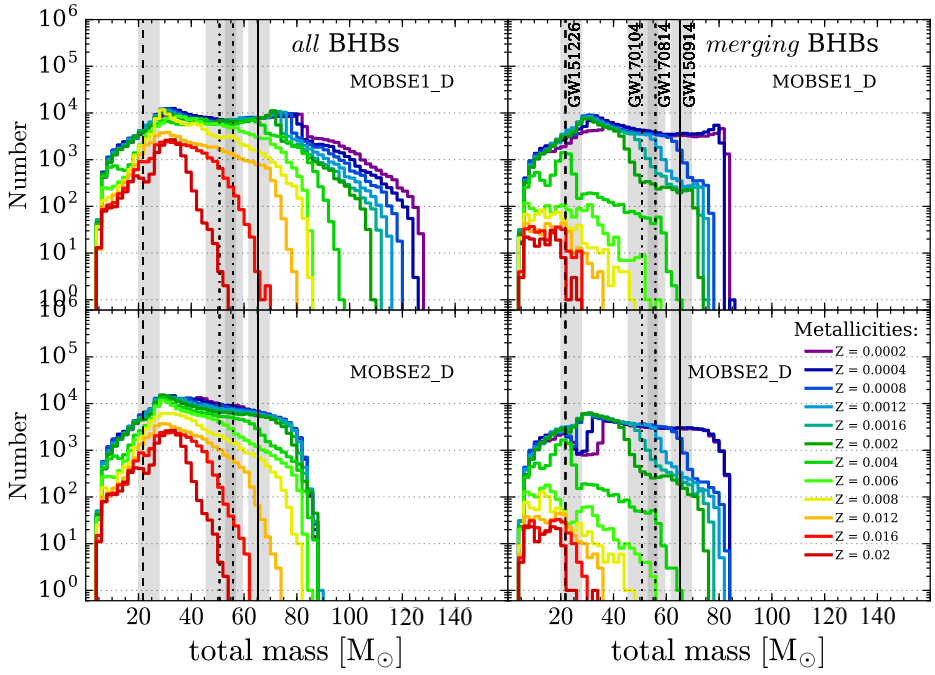

Figure 2.8: Same as Figure 2.7, but for the distribution of total masses.

by MOBSE1 are remarkably similar to those predicted by MOBSE2. This fundamental difference between merging BHBs and other BHBs holds for all eight sets of simulations performed in this paper, included those which are not shown in Figures 2.7 and 2.8. This happens because the most massive BHBs in MOBSE1 come from massive ($\sim 60-80\,M_\odot$) progenitors which die as red super-giant stars. Thus, all such BHBs form with very large semi-major axis (otherwise their progenitors merge prematurely, due to their large radii) and cannot merge within a Hubble time.

Figures 2.7 to 2.8 also show that the number of BHBs scales inversely with the metallicity of the progenitors. This trend is particularly strong if we consider only merging BHBs. This result originates from several factors. At higher metallicity, stars radii are larger, and thus a larger fraction of binaries merge before becoming a BHB. Moreover, we assume stronger SN kicks for lower BH masses. Thus, SN kicks are more efficient in unbinding light binaries, which are more common at high metallicity.

Figure 2.9 shows the distribution of masses of the primary BH (i.e. the most massive one) and of the secondary BH (i.e. the least massive one) for all merging BHBs in the four runs with MOBSE1. Figure 2.10 is the same for the four runs with MOBSE2. There are no significant differences between merging BHB masses in MOBSE1 and

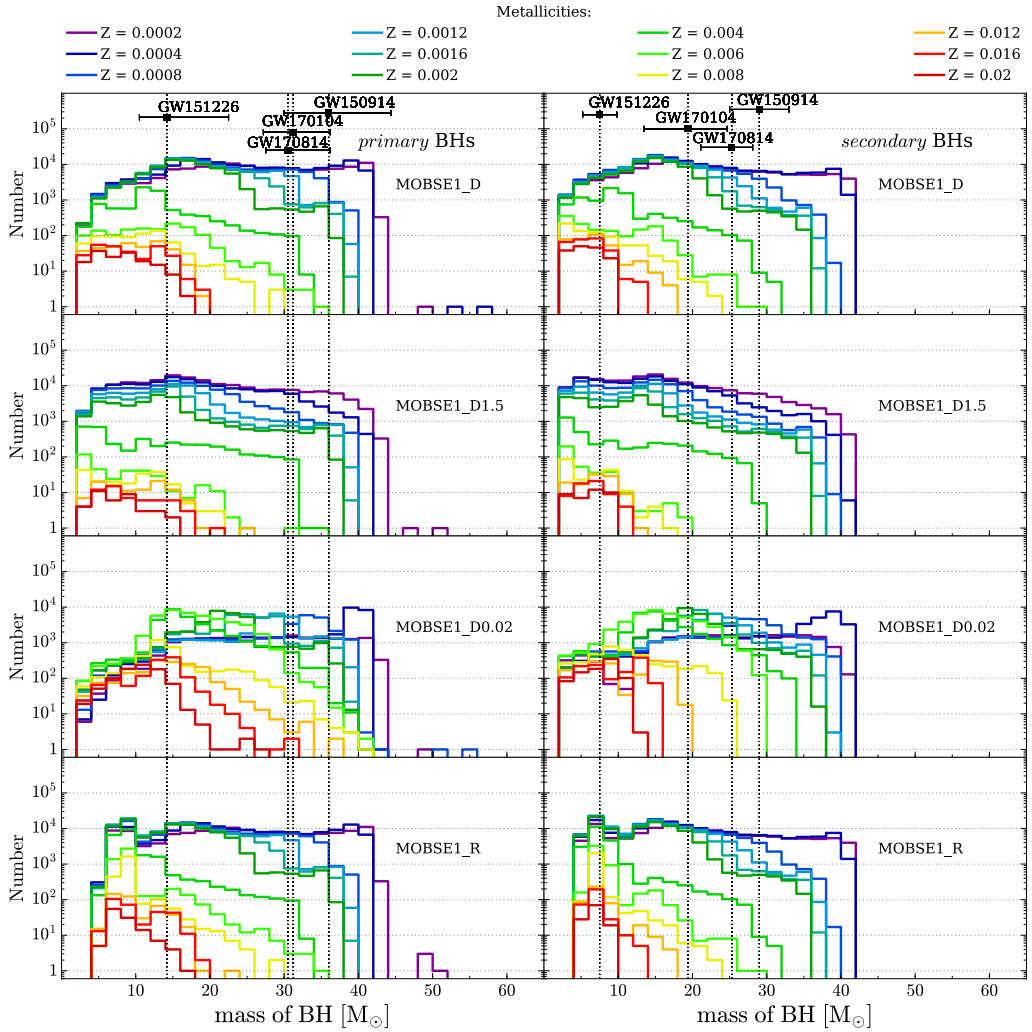

Figure 2.9: Mass distribution of primary (left-hand column) and secondary members (right-hand column) of merging BHBs in the eight simulation sets. Line colours (from red to violet) correspond to decreasing metallicity (from $Z = 0.02$ to $Z = 0.0002$). From top to bottom: MOBSE1_D, MOBSE1_D1.5, MOBSE1_D0.02, and MOBSE1_R. See Table 2.1 for details on each simulation. The vertical lines on the left-hand (right-hand) column are the mass of the primary (secondary) BH in GW151226, GW150914 (Abbott et al., 2016b), GW170104 (Abbott et al., 2017b) and GW170814 (Abbott et al., 2017d). The error bars show the uncertainties on each mass (at the 90 per cent credible level).

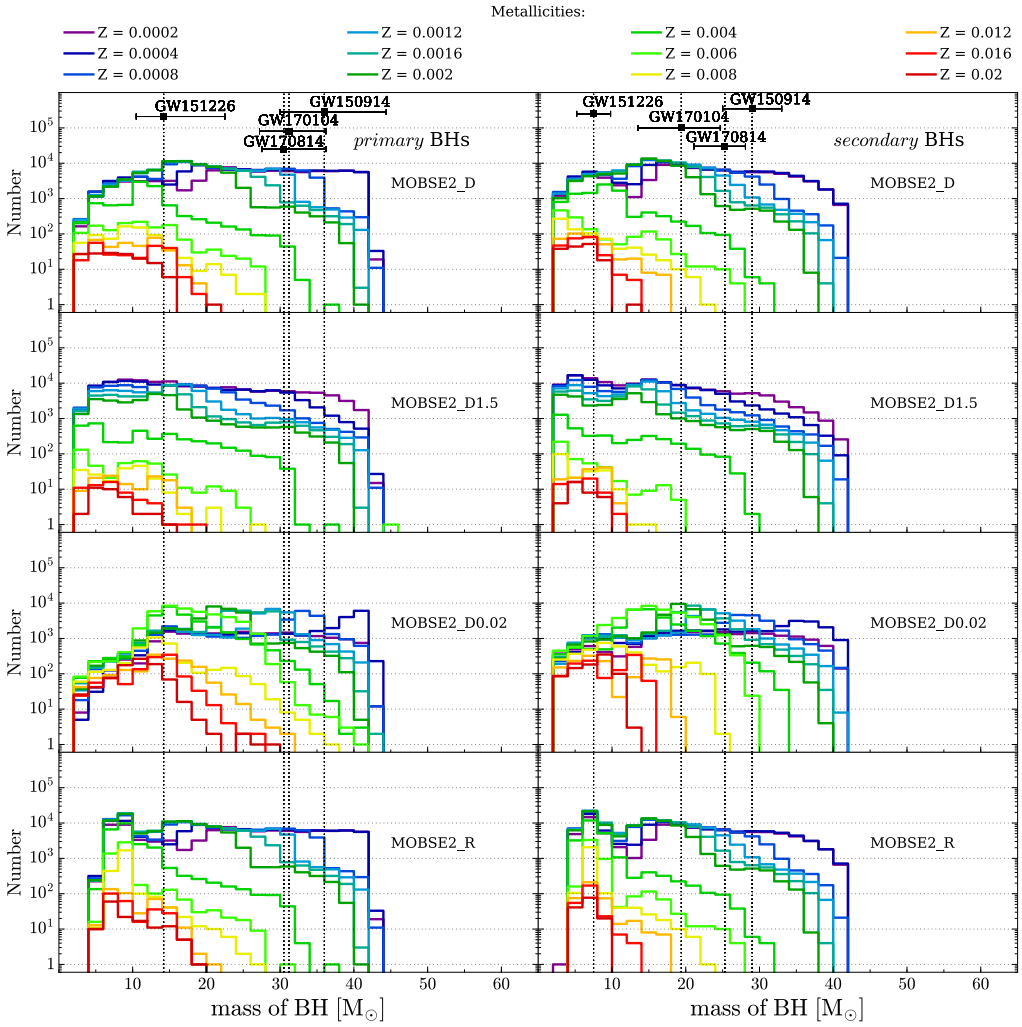

Figure 2.10: Same as Fig. 2.9 but for simulation with MOBSE2. From top to bottom: MOBSE2_D, MOBSE2_D1.5, MOBSE2_D0.02, and MOBSE2_R.

Table 2.2: Minimum metallicity of progenitors of GW events.

	MOBSE1				MOBSE2			
GW event	D1.5	D	D0.02	R	D1.5	D	D0.02	R
GW150914	$Z \leq 0.002$	$Z \leq 0.004$	$Z \leq 0.006$	$Z \leq 0.004$	$Z \leq 0.002$	$Z \leq 0.004$	$Z \leq 0.006$	$Z \leq 0.004$
LVT151012	$Z \leq 0.008$	$Z \leq 0.012$	$Z \leq 0.016$	$Z \leq 0.012$	$Z \leq 0.006$	$Z \leq 0.012$	$Z \leq 0.016$	$Z \leq 0.012$
GW151226	$Z \leq 0.02$	$Z \leq 0.02$	$Z \leq 0.02$	$Z \leq 0.02$	$Z \leq 0.02$	$Z \leq 0.02$	$Z \leq 0.02$	$Z \leq 0.02$
GW170104	$Z \leq 0.006$	$Z \leq 0.006$	$Z \leq 0.012$	$Z \leq 0.006$	$Z \leq 0.004$	$Z \leq 0.006$	$Z \leq 0.008$	$Z \leq 0.006$
GW170814	$Z \leq 0.004$	$Z \leq 0.006$	$Z \leq 0.008$	$Z \leq 0.006$	$Z \leq 0.004$	$Z \leq 0.004$	$Z \leq 0.008$	$Z \leq 0.004$

Column 1: GW detection; column 2-9: maximum star metallicity at which we can obtain merging BHBs with the same mass as the detected ones in runs MOBSE1_D1.5, MOBSE1_D, MOBSE1_D0.02, MOBSE1_R, MOBSE2_D1.5, MOBSE2_D, MOBSE2_D0.02, and MOBSE2_R (see Table 2.1).

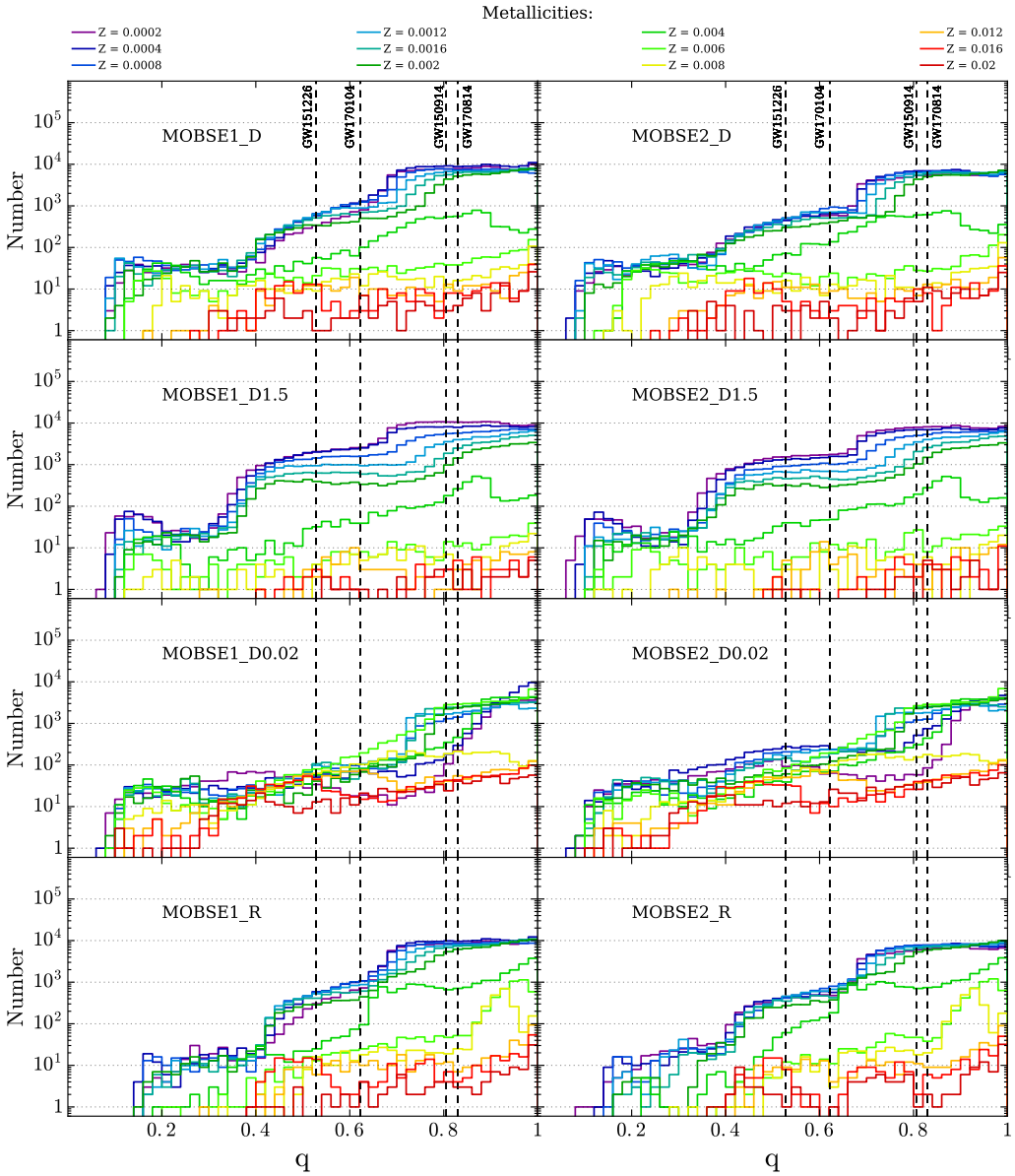

Figure 2.11: Distribution of the mass ratio $q = m_s/m_p$ (where m_p and m_s are the mass of the primary and of the secondary, respectively) of merging BHBs. Left-hand panel, from top to bottom: MOBSE1_D, MOBSE1_D1.5, MOBSE1_D0.02, MOBSE1_R. Right-hand panel, from top to bottom: MOBSE2_D, MOBSE2_D1.5, MOBSE2_D0.02, MOBSE2_R. The vertical lines are the mass ratio of GW151226, GW150914 (Abbott et al., 2016b), GW170104 (Abbott et al., 2017b) and GW170814 (Abbott et al., 2017d).

MOBSE2, regardless of the SN model or CE prescription. The maximum mass of merging BHBs does not seem to depend significantly on the assumed SN model or on the assumed CE parameters. The minimum mass of merging BHBs does depend on the assumed SN model, because the rapid SN model (MOBSE1_R and MOBSE2_R) does not allow to form compact remnants with mass in the range of $2-5\,M_\odot$.

The main difference between different values of the CE parameters is the number of merging BHBs with relatively high metallicity ($0.006 \leq Z \leq 0.02$). The two models MOBSE1_D0.02 and MOBSE2_D0.02, which adopt $\alpha\,\lambda = 0.02$, form a significantly larger number of merging BHBs with relatively high metallicity ($0.006 \leq Z \leq 0.02$) than models with a larger value of $\alpha\,\lambda$. As already discussed in Mapelli et al. (2017), this is likely due to the fact that a lower value of $\alpha\,\lambda$ makes the spiral in of the cores much more efficient, bringing the two cores on a much smaller final orbital separation. Thus, even binaries with a very large initial orbital separation might give birth to a merging BHB system, provided that they can enter a CE phase. Entering a CE phase is much easier for metal-rich stars, because their radii are larger than those of their metal-poor analogues.

On the other hand, MOBSE1_D0.02 and MOBSE2_D0.02 also form a significantly smaller number of *light* merging BHBs ($< 12\,M_\odot$) with relatively low metallicity ($Z < 0.006$) than models with a larger value of $\alpha\,\lambda$. This can be explained as follows. Assuming a lower value of $\alpha\lambda$ means that it is harder to eject the CE during the CE phase. This implies that the minimum semi-major axis ($a_{\rm min}$) above which a binary system survives the CE without merging is larger for a lower value of $\alpha\lambda$.

In the case of (both metal-rich and metal-poor) massive stars, the maximum stellar radii are always $\geq a_{\rm min}$ for the considered range of $\alpha\lambda$. This means that changes of $\alpha\lambda$ (and consequently of $a_{\rm min}$) do not affect the number of massive binary systems which merge prematurely (before becoming BHBs). In contrast, for light ($\lesssim 30\,M_\odot$) meta-poor stars ($Z \leq 0.006$) this difference in $a_{\rm min}$ is crucial, because the maximum stellar radii are $< a_{\rm min}$ for $\alpha\lambda = 0.02$ but $> a_{\rm min}$ for $\alpha\lambda \geq 0.1$. Therefore, the same binary will not survive the CE phase in the case with $\alpha\lambda = 0.02$, while it will survive without merging prematurely in the case with $\alpha\lambda \geq 0.1$. This effect explains the dearth of merging BHBs with $M < 12\,M_\odot$ in MOBSE1_D0.02 and MOBSE2_D0.02 simulations respect to MOBSE1_D, MOBSE2_D, MOBSE1_D1.5 and MOBSE2_D1.5 simulations.

In addition, for metal-rich stars there is another effect that plays a role. Indeed, the spiral-in during CE is more efficient for small values of $\alpha\lambda$, so even initial larger binaries can become close binaries and eventually evolve into merging BHBs.

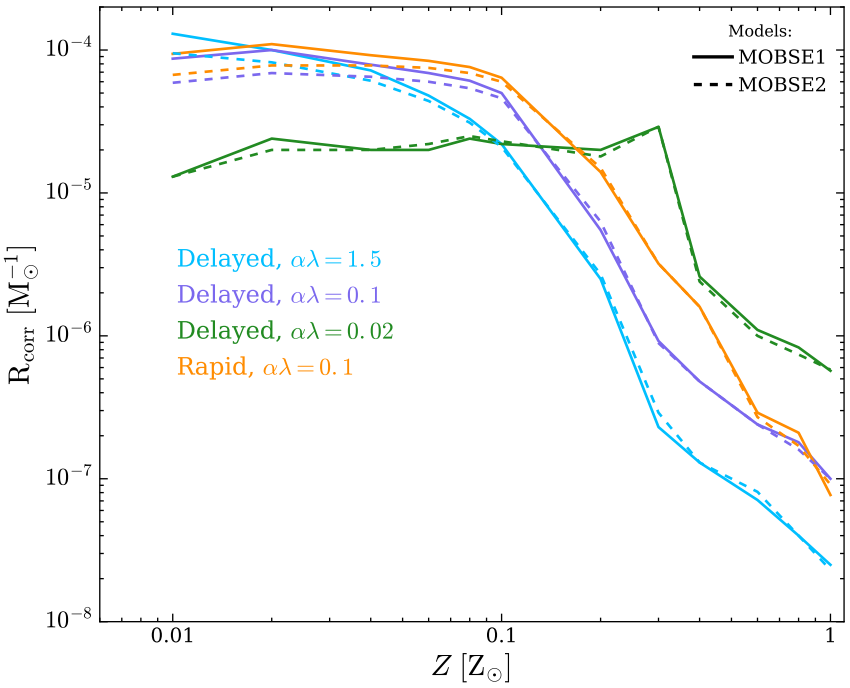

Figure 2.12: Corrected number of mergers per unit mass as a function of the metallicity for all sets of simulations ($Z_\odot = 0.02$). The colors identify different assumptions for the SN mechanism and for the values of CE parameters α and λ. Solid (dashed) lines: MOBSE1 (MOBSE2).

From Figures 2.9 and 2.10 and from Table 2.2 it is apparent that our models can account for all four GW events reported so far. The most massive systems (GW150914, GW170104 and GW170814) can be generated only by metal-poor progenitors. In particular, GW150914-like systems are produced only for $Z \leq 0.006$, GW170814-like systems for $Z \leq 0.008$, GW170104-like systems for $Z \leq 0.012$, and LVT151012-like systems for $Z \leq 0.016$, while GW151226-like systems exist at all metallicities ($Z \leq 0.02$, see Table 2.2 for details). From Tabbe 2.2 it is also interesting to note that the higher $\alpha\lambda$ is, the lower the maximum metallicity to produce the observed GW events.

Finally, Figure 2.11 shows the mass ratio between the secondary BH and the primary BH in the merging BHBs. While nearly equal-mass systems are more common in our models, we find merging BHBs with nearly all possible mass ratios, down to $q \sim 0.1$. This is at odds with models of BHB formation through chemically homogeneous evolution (Marchant et al., 2016; de Mink and Mandel, 2016; Mandel and de Mink, 2016), which predict the formation of nearly equal mass merging BHBs, but is consistent with the mass ratio of the four GW detections.

2.3.4 Mergers per unit mass

For each simulation, we calculate the number of merging BHBs per unit mass as

$$\mathcal{R} = \frac{N_{\rm merger}}{M_{\rm tot,sim}}\,, \tag{2.13}$$

where $N_{\rm merger}$ is the number of merging BHBs in each sub-sample and $M_{\rm tot,sim}$ is the total mass of the corresponding sub-sample.
This number must be corrected to account for the fact that we simulate only massive ($m_1 > 5$ M$_\odot$) binary systems (no single stars). We thus introduce the corrected number of merging BHBs per unit mass as

$$\mathcal{R}_{\rm cor} = f_{\rm bin}\, f_{\rm IMF}\, \mathcal{R}, \tag{2.14}$$

where $f_{\rm bin}$ is the correction factor used to take into account that we only simulate binary systems. We put $f_{\rm bin} = 0.5$, assuming that 50 per cent of stars are in binaries (see e.g. Sana et al., 2013). The correction factor $f_{\rm IMF} = 0.285$ accounts for the fact that we actually simulate only systems with primary mass $m_1 \geq 5\,$M$_\odot$. The values of $\mathcal{R}_{\rm cor}$ are shown in Tables 2.3 and 2.4, respectively.
Figure 2.12 shows $\mathcal{R}_{\rm cor}$ as a function of the metallicity Z for all simulations. $\mathcal{R}_{\rm cor}$ strongly depends on the metallicity. In particular, $\mathcal{R}_{\rm cor}$ is $\gtrsim 2$ orders of magnitude higher at low metallicity ($Z \lesssim 0.002$) than at high metallicity ($Z \sim 0.02$). This means that we form much more merging BHBs if the progenitors are metal-poor stars (see Tables 2.3 and 2.4).

2.3.5 Formation channels of merging BHBs

In Tables 2.5 and 2.6 we report the most common evolutionary pathways followed by merging BHBs in simulations MOBSE1 and MOBSE2, respectively. We distinguish three different formation channels: systems that pass through a single CE phase (SCE); systems which experience multi-CE phases (MCE); and systems that merge without CE phase (ZCE).
The vast majority of progenitors of merging BHBs undergo one CE phase (> 80%), even if, especially at low metallicity ($Z < 0.004$), about $10-20$% of progenitors of merging BHBs do not experience any CE. Merging BHBs that went through multiple CE phases are a negligible fraction.
The percentage of ZCE systems increases with decreasing metallicity in both MOBSE1 and MOBSE2. The same trend was also noted by Dominik et al. (2012), but our results show a stronger dependence on the metallicity than Dominik et al. (2012).

Table 2.3: Merging BHBs in MOBSE1.

	MOBSE1_D1.5		MOBSE1_D		MOBSE1_D0.02		MOBSE1_R	
Z	N_{merger}	R_{cor} [$M_{\odot}{}^{-1}$]	N_{merger}	R_{cor} [$M_{\odot}{}^{-1}$]	N_{merger}	R_{cor} [$M_{\odot}{}^{-1}$]	N_{merger}	R_{cor} [$M_{\odot}{}^{-1}$]
0.0002	189837	1.3E-04	131819	8.7E-05	20259	1.3E-05	142137	9.4E-05
0.0004	157034	1.0E-04	152054	1.0E-04	35744	2.4E-05	164478	1.1E-04
0.0008	108094	7.2E-05	119200	7.9E-05	29503	2.0E-05	139294	9.2E-05
0.0012	73138	4.8E-05	104021	6.9E-05	30550	2.0E-05	126791	8.4E-05
0.0016	49989	3.3E-05	91747	6.1E-05	36228	2.4E-05	115196	7.6E-05
0.002	32747	2.2E-05	74888	5.0E-05	33812	2.2E-05	97099	6.4E-05
0.004	3766	2.5E-06	8356	5.5E-06	30511	2.0E-05	21602	1.4E-05
0.006	347	2.3E-07	1397	9.2E-07	43555	2.9E-05	4867	3.2E-06
0.008	203	1.3E-07	730	4.8E-07	3901	2.6E-06	2379	1.6E-06
0.012	107	7.1E-08	365	2.4E-07	1729	1.1E-06	438	2.9E-07
0.016	60	4.0E-08	276	1.8E-07	1260	8.3E-07	311	2.1E-07
0.02	38	2.5E-08	157	1.0E-07	867	5.7E-07	117	7.7E-08

Table 2.3. Column 1: metallicity; column 2-3: total number of merging BHBs and number of merging BHBs per unit mass at each metallicity for simulations MOBSE1_D1.5; column 4-5: same for MOBSE1_D; column 6-7: same for MOBSE1_D0.02;column 8-9: same for MOBSE1_R. **Turn the tables**

Table 2.4: Merging systems in MOBSE2.

Z	MOBSE2_D1.5		MOBSE2_D		MOBSE2_D0.02		MOBSE2_R	
	N_{merger}	R_{cor} [$M_{\odot}^{-1}$]	N_{merger}	R_{cor} [$M_{\odot}^{-1}$]	N_{merger}	R_{cor} [$M_{\odot}^{-1}$]	N_{merger}	R_{cor} [$M_{\odot}^{-1}$]
0.0002	142912	9.5E-05	89309	5.9E-05	19491	1.3E-05	100555	6.7E-05
0.0004	124392	8.2E-05	103508	6.9E-05	29680	2.0E-05	117595	7.8E-05
0.0008	92003	6.1E-05	97539	6.5E-05	30338	2.0E-05	118335	7.8E-05
0.0012	66391	4.4E-05	91225	6.0E-05	32842	2.2E-05	113580	7.5E-05
0.0016	46703	3.1E-05	81349	5.4E-05	37037	2.5E-05	104239	6.9E-05
0.002	31499	2.1E-05	68936	4.6E-05	34330	2.3E-05	90655	6.0E-05
0.004	4030	2.7E-06	9472	6.3E-06	27772	1.8E-05	22906	1.5E-05
0.006	438	2.9E-07	1351	8.9E-07	43231	2.9E-05	4821	3.2E-06
0.008	197	1.3E-07	722	4.8E-07	3598	2.4E-06	2414	1.6E-06
0.012	122	8.1E-08	369	2.4E-07	1567	1.0E-06	406	2.7E-07
0.016	60	4.0E-08	240	1.6E-07	1121	7.4E-07	259	1.7E-07
0.02	34	2.3E-08	153	1.0E-07	869	5.8E-07	138	9.1E-08

Same as Table 2.3 but for simulations MOBSE2_D1.5, MOBSE2_D, MOBSE2_D0.02 and MOBSE2_R.

2.4 Conclusions

We present the MOBSE code, our upgraded version of BSE. MOBSE includes up-to-date prescriptions for core-collapse SNe and for stellar winds. We account not only for the metallicity dependence of mass loss, but also for the effect of the Eddington factor (Vink et al., 2011; Chen et al., 2015; Vink, 2017a). We discuss two versions of MOBSE, MOBSE1 and MOBSE2. MOBSE2 implements the metallicity-dependent prescriptions described in Belczynski et al. (2010) and does not account for the effect of the Eddington factor, while MOBSE1 updates these prescriptions by accounting also for the Eddington factor (following Chen et al., 2015). Both versions of MOBSEalso include recipes for PISNe and PPISNe, following Spera and Mapelli (2017).

The most massive BHs in MOBSE1 form at low metallicity ($Z \sim 0.0002 - 0.002$), reach a mass of $\sim 50 - 65$ M$_\odot$ and come from progenitor stars with ZAMS mass $M_{\rm ZAMS} \sim 60 - 80$ M$_\odot$. In contrast, the most massive BHs in MOBSE2 form at low metallicity ($Z \sim 0.0002 - 0.002$), but reach a lower mass of ~ 45 M$_\odot$ and come from progenitor stars with ZAMS mass $M_{\rm ZAMS} \gtrsim 120$ M$_\odot$ (Figure 2.4).

The distribution of BH masses derived with MOBSE2 is in good agreement with the one discussed by Belczynski et al. (2010) and Belczynski et al. (2016b), who adopt similar prescriptions for stellar winds and SNe. The distribution of BH masses obtained with MOBSE1 is significantly different from that produced by MOBSE2 and is remarkably similar to the one derived with the SEVN code (Spera and Mapelli, 2017). This is not surprising, because both MOBSE1 and SEVN account for the impact of the Eddington factor on mass loss, but is quite remarkable, because stellar evolution in MOBSE is still based on the polynomial fitting formulas described in Hurley et al. (2000), while SEVN adopts the recent PARSEC stellar evolution models (Bressan et al., 2012; Chen et al., 2015). This result also indicates that the Eddington factor has a large impact on the distribution of BH masses.

We have studied the demography of BHBs, performing a large set of population-synthesis simulations with both MOBSE1 and MOBSE2. We perform simulations with different models of core-collapse SN (delayed versus rapid models, Fryer et al., 2012) and changing the efficiency of CE.

The distribution of simulated BHB masses covers the entire mass spectrum of BHs predicted by MOBSE1 and MOBSE2 from single stellar evolution (Fig. 2.4). However, if we consider only merging BHBs (defined as BHBs which are expected to merge in a Hubble time), their maximum mass is significantly lower. Even at the lowest metallicity, the maximum mass of merging BHBs is ~ 55 M$_\odot$ and ~ 45 M$_\odot$

in MOBSE1 and in MOBSE2, respectively. This indicates that the most massive BHBs in MOBSE1 do not merge. The most likely explanation is that these BHBs come from massive ($\sim 60-80$ $M_\odot$) progenitors which die as red super-giant stars. Thus, all such BHBs form with very large semi-major axis (otherwise their progenitors merge prematurely, due to their large radii) and do not merge in a Hubble time. This feature is nearly independent of the CE parameters and of the SN model.

The maximum mass of merging BHs formed in our simulations (≈ 45 $M_\odot$) is consistent with the possible upper mass gap suggested by LIGO-Virgo detections (i.e. the dearth of merging BHs with mass in the $\sim 50-135$ $M_\odot$ range, Fishbach and Holz, 2017).

We find merging BHBs with mass ratios in the $0.1-1.0$ range, even if mass ratios > 0.6 are more likely. The masses of our merging BHBs match those of the four observed GW events. In our MOBSE1 and MOBSE2 simulations, systems like GW150914, LVT151012, GW151226, GW170104 and GW170814 could have formed only from binaries with metallicity $Z \leq 0.006$, ≤ 0.016, ≤ 0.02, ≤ 0.012 and ≤ 0.008, respectively.

The vast majority of progenitors of merging BHBs undergo one CE phase ($> 80\%$), even if, especially at low metallicity ($Z < 0.004$), about $10-20\%$ of progenitors of merging BHBs do not experience any CE. Merging BHBs that went through multiple CE phases are a negligible fraction.

Merging BHBs form much more efficiently from metal-poor than from metal-rich binaries, both in MOBSE1 and in MOBSE2. The number of BHB mergers per unit mass is $\sim 10^{-4}$ $M_\odot^{-1}$ at low metallicity ($Z = 0.0002-0.002$) and drops to $\sim 10^{-7}$ $M_\odot^{-1}$ at high metallicity ($Z \sim 0.02$, Fig. 4.15). This trend of the number of BHB mergers per unit mass with the progenitor's metallicity potentially has a crucial impact on GW observations across cosmic time.

Table 2.5: Formation channels of BHBs in MOBSE1_D.

Z	N° of mergers	Channels	Fraction
0.02	157	ZCE	0%
		SCE	100%
		MCE	0%
0.016	276	ZCE	0.36%
		SCE	98.19%
		MCE	1.45%
0.012	365	ZCE	0.27%
		SCE	95.89%
		MCE	3.84%
0.008	730	ZCE	0.41%
		SCE	95.21%
		MCE	4.38%
0.006	1397	ZCE	1.00%
		SCE	95.71%
		MCE	3.29%
0.004	8356	ZCE	17.52%
		SCE	81.08%
		MCE	1.40%
0.002	74888	ZCE	8.42%
		SCE	91.01%
		MCE	0.57%
0.0016	91747	ZCE	7.94%
		SCE	91.34%
		MCE	0.72%
0.0012	104021	ZCE	8.13%
		SCE	90.73%
		MCE	1.14%
0.0008	119200	ZCE	8.97%
		SCE	89.43%
		MCE	1.60%
0.0004	152054	ZCE	9.16%
		SCE	89.99%
		MCE	0.86%
0.0002	131819	ZCE	12.68%
		SCE	86.35%
		MCE	0.97%

Column 1: metallicity; column 2: total number of BHBs that merge within an Hubble time; column 3: formation channels, considering systems that evolve with zero CE phase (ZCE), with single CE phase (SCE) and with multiple CE phases (MCE); column 4: percentage of the merging BHBs which evolve through a given channel.

Table 2.6: Formation channels of BHBs in MOBSE2_D.

Z	N° of mergers	Channels	Fraction
0.02	153	ZCE	0.65%
		SCE	96.73%
		MCE	2.61%
0.016	240	ZCE	0.00%
		SCE	96.67%
		MCE	3.33%
0.012	369	ZCE	0.27%
		SCE	96.75%
		MCE	2.98%
0.008	722	ZCE	0.83%
		SCE	94.32%
		MCE	4.85%
0.006	1351	ZCE	2.74%
		SCE	92.23%
		MCE	5.03%
0.004	9472	ZCE	16.69%
		SCE	82.19%
		MCE	1.12%
0.002	68936	ZCE	9.66%
		SCE	89.91%
		MCE	0.43%
0.0016	81349	ZCE	9.62%
		SCE	89.90%
		MCE	0.48%
0.0012	91225	ZCE	10.14%
		SCE	88.61%
		MCE	1.25%
0.0008	9705	ZCE	11.71%
		SCE	86.37%
		MCE	1.93%
0.0004	103508	ZCE	13.71%
		SCE	85.07%
		MCE	1.22%
0.0002	89309	ZCE	17.46%
		SCE	81.13%
		MCE	1.41%

Same as Table 2.5 but for MOBSE2.

CHAPTER 3

THE IMPACT OF ELECTRON-CAPTURE SUPERNOVAE ON MERGING DOUBLE NEUTRON STARS

Natal kicks are one of the most debated issues about double neutron star (DNS) formation. Several observational and theoretical results suggest that some DNSs have formed with low natal kicks ($\lesssim 50$ km s^{-1}), which might be attributed to electron-capture supernovae (ECSNe). We investigate the impact of ECSNe on the formation of DNSs by means of population synthesis simulations. In particular, we assume a Maxwellian velocity distribution for the natal kick induced by ECSNe with one dimensional root-mean-square $\sigma_{\rm ECSN} = 0, 7, 15, 26, 265$ km s^{-1}. The total number of DNSs scales inversely with $\sigma_{\rm ECSN}$ and the number of DNS mergers is higher for relatively low kicks. This effect is particularly strong if we assume low efficiency of common-envelope ejection (described by the parameter $\alpha = 1$), while it is only mild for high efficiency of common-envelope ejection ($\alpha = 5$). In most simulations, more than 50 per cent of the progenitors of merging DNSs undergo at least one ECSN and the ECSN is almost always the first SN occurring in the binary system. Finally, we have considered the extreme case in which all neutron stars receive a low natal kick ($\lesssim 50$ km s^{-1}). In this case, the number of DNSs increases by a factor of ten and the percentage of merging DNSs which went through an ECSN is significantly suppressed (< 40 per cent).

Based on:
Giacobbo N., Mapelli M., MNRAS, 2018, 482, p.2234-2243

3.1 Introduction

GW170817, the first detection of a merger between two neutron stars (NS; Abbott et al., 2017e), marked the beginning of multi-messenger astronomy. For the first time, electromagnetic emission accompanying the gravitational wave (GW) event was observed (Abbott et al., 2017a), ranging from gamma rays (e.g. Abbott et al., 2017a; Goldstein et al., 2017; Savchenko et al., 2017) to X-rays (e.g. Margutti et al., 2017), to optical, near-infrared (e.g. Coulter et al., 2017; Soares-Santos et al., 2017; Chornock et al., 2017; Cowperthwaite et al., 2017; Nicholl et al., 2017; Pian et al., 2017) and radio wavelengths (e.g. Alexander et al., 2017).

The formation of merging double NSs (DNSs) like GW170817 is still matter of debate: understanding this process would provide crucial insights for both stellar evolution and GW astrophysics. Merging DNSs are expected to form either from the evolution of isolated close binaries (e.g. Flannery and van den Heuvel, 1975; Bethe and Brown, 1998; Belczynski et al., 2002; Voss and Tauris, 2003; Dewi and Pols, 2003; Podsiadlowski et al., 2004; Dewi et al., 2005; Andrews et al., 2015; Tauris et al., 2017; Chruslinska et al., 2017; Kruckow et al., 2018; Vigna-Gómez et al., 2018; Giacobbo and Mapelli, 2018; Mapelli and Giacobbo, 2018; Mapelli et al., 2018) or through dynamical interactions in star clusters (e.g. Grindlay et al., 2006; East and Pretorius, 2012; Lee et al., 2010; Ziosi et al., 2014).

Many uncertainties still affect both formation channels. In particular, one of the most debated and also one of the most important physical ingredients for the formation of DNSs is the magnitude of the natal kick imparted by the supernova (SN) explosion to the newborn NS (Janka, 2012).

From a study on the proper motion of 233 young isolated pulsars, Hobbs et al. (2005) estimated that their velocity distribution follows a Maxwellian curve with a one dimensional root-mean-square (1D rms) velocity $\sigma = 265$ km s^{-1} and an average natal kick speed of ~ 420 km s^{-1}. On the other hand, there is increasing evidence that some NSs form with a significantly smaller natal kick.

Several studies (Cordes and Chernoff, 1998; Arzoumanian et al., 2002; Brisken et al., 2003; Schwab et al., 2010; Verbunt et al., 2017) claim that the velocity distribution proposed by Hobbs et al. (2005) underestimates the number of pulsars with a low velocity and suggest that the natal kick distribution of NSs is better represented by a bimodal velocity distribution. This bimodal distribution might result from two different mechanisms of NS formation. For instance, two out of nine accurate pulsar velocities computed by Brisken et al. (2002) are smaller than 40 km s^{-1}. Moreover, Pfahl et al. (2002) study a new class of high-mass X-ray binaries with small eccen-

tricities and long orbital periods, which imply a low natal kick velocity ($\lesssim 50$ km s^{-1}) for the newborn NSs. Similarly, Knigge et al. (2011) show that Be X-ray binaries could be divided in two sub-populations: one with short (~ 10 s) and one with long (~ 200 s) spin period. The two populations are characterized also by different orbital period and eccentricity distributions, indicative of two natal kick distributions. Even considerations about the orbital elements of some Galactic DNSs suggest that a low natal kick is required (van den Heuvel, 2007; Beniamini and Piran, 2016).

It has been proposed that NSs with a low natal kick come from electron-capture SNe (ECSNe, Miyaji et al., 1980; Nomoto, 1984; Nomoto, 1987; van den Heuvel, 2007), a more rapid and less energetic process with respect to iron core-collapse SNe (CCSNe, Dessart et al., 2006; Kitaura et al., 2006). In ECSN explosions, the asymmetries are more difficult to develop and the newborn NS receives a lower kick (Dessart et al., 2006; Jones et al., 2013; Schwab et al., 2015a; Gessner and Janka, 2018).

Low natal kicks might occur not only in ECSNe, but in all low-mass progenitors ($\lesssim 10$ M$_\odot$), because of their steep density profile at the edge of the core, which allows for rapid acceleration of the SN shock wave. The shock is revived on a shorter time scale than in more massive progenitors, and therefore there is less time for large-scale asymmetries (which would result in a larger kick) to develop (see e.g. Müller, 2016).

Alternatively, the low kick of some DNSs could be explained also by the fact that they come from ultra-stripped SNe, i.e. from the SN explosion of a naked Helium star that was stripped by its compact companion (Tauris et al., 2013; Tauris et al., 2015; Tauris et al., 2017). In this case, the natal kick is thought to be lower because of the low mass of the ejecta.

In this paper, we use our new population-synthesis code MOBSE (Giacobbo et al., 2018), to investigate the impact of ECSNe and low natal kicks on the formation of merging DNSs. We show that ECSNe are an important channel for the formation of DNSs, if they are associated to low natal kicks. Moreover, we discuss the extreme case in which all NSs receive a small kick, regardless of the SN process.

3.2 Methods

MOBSEis an updated version of the BSE code (Hurley et al., 2000; Hurley et al., 2002). Here we summarize the main characteristics of MOBSE and we describe the new features we have added to it for this work. A more detailed discussion of MOBSE can be found in Giacobbo et al. (2018) and in Mapelli et al., 2017. In this

Table 3.1: Definition of the simulation sets.

ID	$\sigma_{\rm ECSN}$ [km s^{-1}]	$\sigma_{\rm CCSN}$ [km s^{-1}]	α
EC0α1	0.0	265.0	1
EC7α1	7.0	265.0	1
EC15α1	15.0	265.0	1
EC26α1	26.0	265.0	1
EC265α1	265.0	265.0	1
EC0α5	0.0	265.0	5
EC7α5	7.0	265.0	5
EC15α5	15.0	265.0	5
EC26α5	26.0	265.0	5
EC265α5	265.0	265.0	5
CC15α1	15.0	15.0	1
CC15α5	15.0	15.0	5

Column 1: simulation name; column 2-3: 1D rms of the Maxwellian natal kick distribution for ECSNe and CCSNe, respectively; column 4: values of α in the CE formalism. Simulations CC15α1 and CC15α5 are the same as we already presented in Giacobbo and Mapelli, 2018.

paper, we adopt the version of MOBSE described as MOBSE1 in Giacobbo et al. (2018).

The main differences between MOBSE and BSE are the treatment of stellar winds of massive stars and the prescriptions for SN explosions. Stellar winds of O and B-type stars are implemented in MOBSE as described by Vink et al. (2001), while the mass loss of Wolf-Rayet (WR) stars is implemented following Belczynski et al. (2010). Finally, the mass loss of luminous blue variable (LBV) stars is described as

$$\dot{M} = 10^{-4} f_{\rm LBV} \left(\frac{Z}{Z_\odot}\right)^{\beta} {\rm M_\odot\,yr^{-1}}, \tag{3.1}$$

where $f_{\rm LBV} = 1.5$ (Belczynski et al., 2010) and Z is the metallicity.

In MOBSE, all massive hot massive stars (O, B, WR and LBV stars) lose mass according to $\dot{M} \propto Z^{\beta}$, where β is defined as (Chen et al., 2015)

$$\beta = \begin{cases} 0.85 & \text{if } \Gamma_{\rm e} < 2/3 \\ 2.45 - 2.40\,\Gamma_{\rm e} & \text{if } 2/3 \leq \Gamma_{\rm e} \leq 1 \\ 0.05 & \text{if } \Gamma_{\rm e} > 1, \end{cases} \tag{3.2}$$

where Γ_e is the electron-scattering Eddington ratio, expressed as (see eq. 8 of Gräfener et al., 2011):

$$\log\Gamma_e = -4.813 + \log(1 + X_H) + \log(L/L_\odot) - \log(M/M_\odot). \tag{3.3}$$

In equation 3.3, X_H is the Hydrogen fraction, L is the star luminosity and M is the star mass.

The new prescriptions for core-collapse SNe (CCSNe) in MOBSE include the rapid and the delayed SN model described by Fryer et al. (2012) (see also Spera et al., 2015). The rapid SN model is adopted for the simulations presented in this paper, because it allows us to reproduce the remnant mass gap between ~ 2 $M_\odot$ and ~ 5 $M_\odot$ (Özel et al., 2010; Farr et al., 2011). Pair-instability and pulsational pair-instability SNe are also implemented in MOBSE using the fitting formulas by Spera and Mapelli (2017).

Finally, we have also updated the prescriptions for core radii following Hall and Tout (2014), we have extended the mass range up to 150 $M_\odot$ (Mapelli, 2016), and we have revised the treatment of Hertzsprung-gap (HG) donors in common envelope (CE): HG donors are assumed to always merge with their companions if they enter a CE phase.

For this work, we have added several updates to the description of ECSNe and natal kicks in MOBSE, as we describe in the following sections.

3.2.1 Electron-capture SNe

NSs can form via CCSN, via ECSN or through the accretion-induced collapse of a white dwarf (WD). In MOBSE, the outcome of a CCSN is considered a NS if its mass is less than 3.0 $M_\odot$ and a black hole (BH) otherwise. This approach is overly simplified, but more constraints on the equation of state of a NS are required for a better choice of the transition between NS and BH.

In the case of both an ECSN and an accretion-induced WD collapse, the NS forms when the degenerate Oxygen-Neon (ONe) core collapses as a consequence of electron-capture reactions, inducing a thermonuclear runaway (Miyaji et al., 1980; Nomoto, 1984; Nomoto, 1987; Nomoto and Kondo, 1991; Kitaura et al., 2006; Fisher et al., 2010; Jones et al., 2013; Takahashi et al., 2013; Schwab et al., 2015a; Jones et al., 2016).

In MOBSE, we decide whether a star will undergo an ECSN by following the procedure described by Hurley et al., 2000 and Fryer et al., 2012. First, we look at

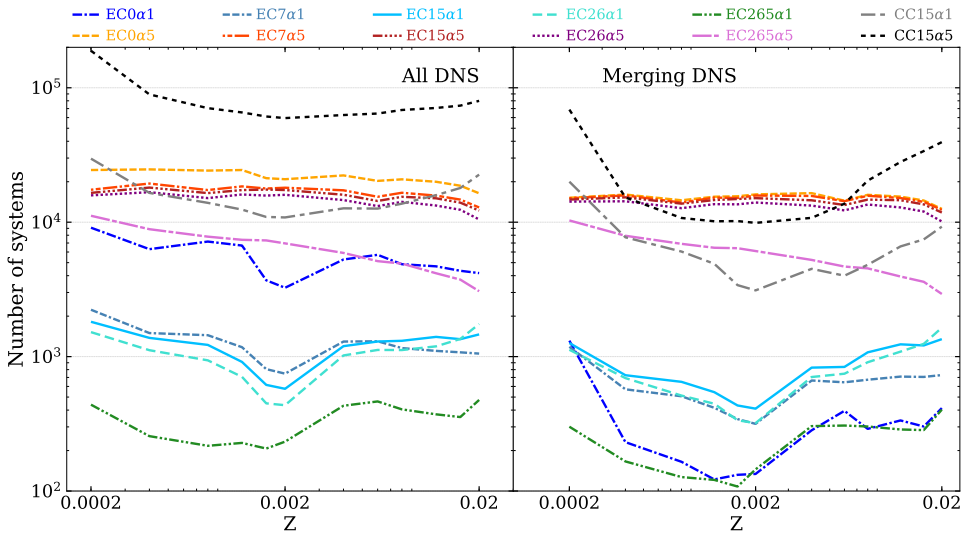

Figure 3.1: Impact of different kick velocities for ECSNe on the number of DNSs. Left: number of DNSs in each set of simulations (see Table 3.1) as a function of progenitor's metallicity. Right: number of DNSs merging in less than a Hubble time (hereafter: merging DNSs) as a function of progenitor's metallicity. Different runs are indicated by different lines, as explained in the legend and in Table 3.1.

the Helium core mass at the base of the asymptotic giant branch[1] ($M_{\rm BABG}$). If 1.6 $M_\odot \leq M_{\rm BABG} < 2.25$ $M_\odot$, the star forms a partially degenerate Carbon-Oxygen (CO) core. If the CO core grows larger than ~ 1.08 $M_\odot$, it can form a degenerate ONe core. If this degenerate ONe core reaches the mass $M_{\rm ECSN} = 1.38$ $M_\odot$, it collapses due to the electron-capture on ^{24}Mg and on ^{20}Ne (Miyaji et al., 1980; Nomoto, 1984; Nomoto, 1987), otherwise it forms an ONe WD, which can still collapse to a NS if it will accrete sufficient mass.

The outcome of the electron-capture collapse is a NS with baryonic mass $M_{\rm rem,bar} = M_{\rm ECSN}$, which becomes

$$M_{\rm rem,grav} = \frac{\sqrt{1+0.3M_{\rm rem,bar}}-1}{0.15} = 1.26\,{\rm M}_\odot\,, \tag{3.4}$$

considering the mass loss due to neutrinos and by using the formula suggested by Timmes et al. (1996).

Even if only a few per cent of all SN events should be produced by electron-capture reactions in single stars (Poelarends, 2007; Doherty et al., 2015), this fraction could drastically raise if we consider binary systems (Podsiadlowski et al., 2004). In binary systems the possibility of accreting material by a companion broadens the mass range of progenitor stars in which the electron-capture collapse may occur, because

[1] Mass loss during the asymptotic giant branch and dredge-up efficiency are assumed to be the same as in Hurley et al., 2000.

mass transfer can significantly change the evolution of the core (Sana et al., 2012; Dunstall et al., 2015; Poelarends et al., 2017). In appendix C, we show that the mass range of ECSNe is crucially affected by binary evolution. In particular, we find that mass transfer tends to widen the mass range of ECSNe.
Recently, Jones et al. (2016) have shown that an ECSN might lead to the ejection of a portion of the degenerate core, rather than to the collapse into a NS. The collapse and the formation of a NS takes place only if the ignition density is $\gtrsim 2 \times 10^{10}$ g cm^{-3}. This finding must be taken into account when interpreting the outcomes of our simulations: our results should be regarded as upper limits to the impact of ECSNe on the statistics of DNSs.

3.2.2 Natal kicks

The natal kick of a NS is drawn from a Maxwellian velocity distribution

$$f(v,\sigma) = \sqrt{\frac{2}{\pi}} \frac{v^2}{\sigma^3} \exp\left[-\frac{v^2}{2\sigma^2}\right] \qquad v \in [0,\infty) \tag{3.5}$$

where σ is the one dimensional root-mean-square (1D rms) velocity and v is the modulus of the velocity.
Given the uncertainties on the natal kick distribution, we have implemented in MOBSE the possibility to draw the natal kick from two Maxwellian curves with a different value of the 1D rms: $\sigma_{\rm CCSN}$ and $\sigma_{\rm ECSN}$, for iron CCSNe and ECSNe, respectively.
$\sigma = 265$ km s^{-1} is adopted as a default value for CCSNe in MOBSE. This value was derived by Hobbs et al. (2005), studying the proper motion of 233 young isolated Galactic pulsars and corresponds to an average natal kick speed of ~ 420 km s^{-1}.
In this paper, we consider different values of $\sigma_{\rm ECSN}$, ranging from 0 to 265 km s^{-1}, to investigate the impact of ECSNe on the statistics of DNSs.
Because low natal kicks might originate not only from ECSNe, but also from iron CCSNe involving low-mass progenitors and from ultra-stripped SNe, we have run also an extreme case ($\sigma_{\rm CCSN} = \sigma_{\rm ECSN} = 15$ km s^{-1}), in which all NSs receive a low natal kick independently on the SN type (see Table 3.1). We will discuss this extreme case in Section 3.3.4.

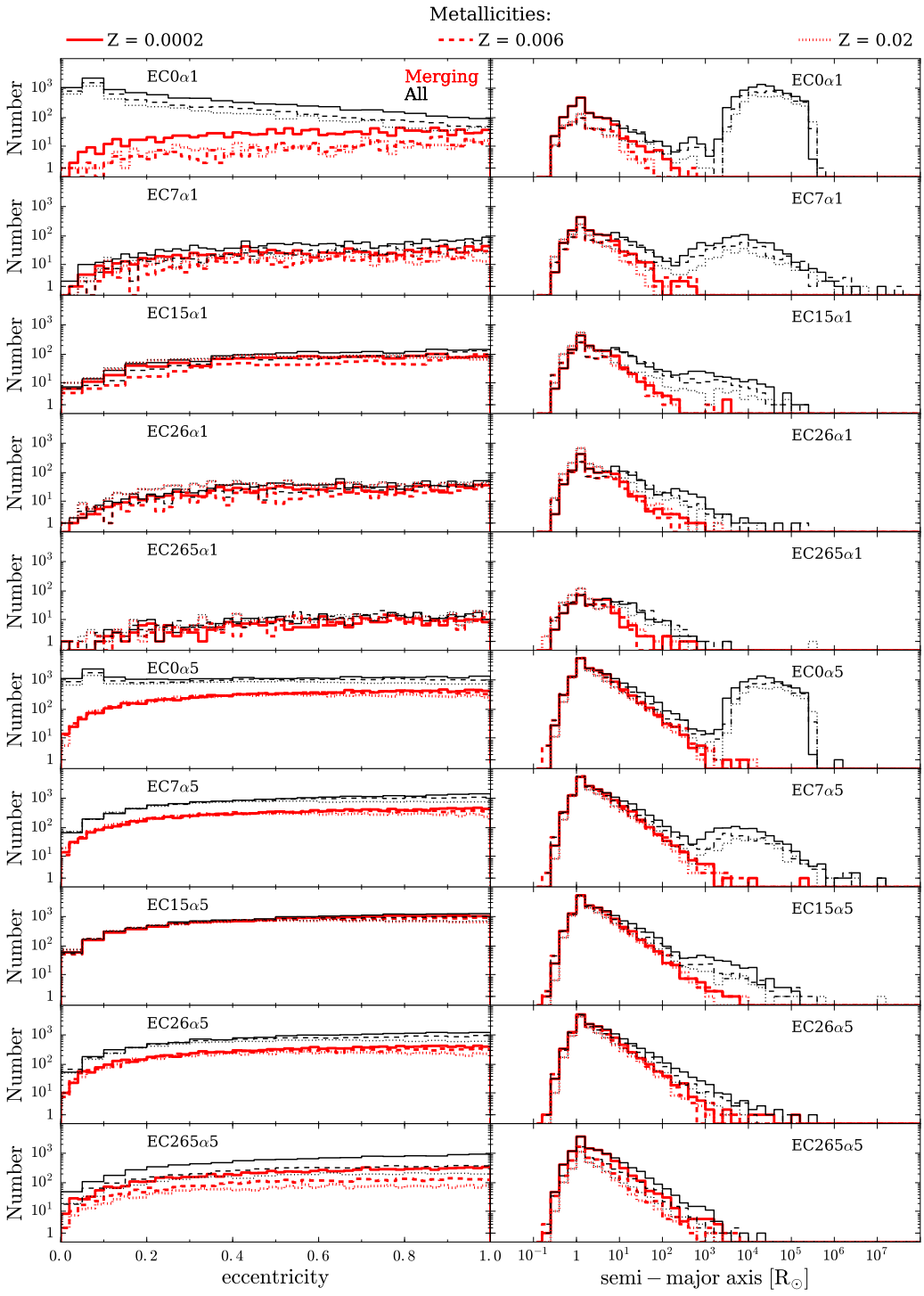

Figure 3.2: Distribution of eccentricity (left-hand column) and semi-major axis (right-hand column) for all DNSs (black thin lines) and only for merging DNSs (red thick lines). For each simulation we show the distributions obtained at three different metallicities: $Z = 0.02$ (dotted lines), 0.006 (dashed lines), and 0.0002 (solid lines). Simulations CC15α1 and CC15α5 are not shown in this Figure, because they have already been discussed in Giacobbo and Mapelli (2018).

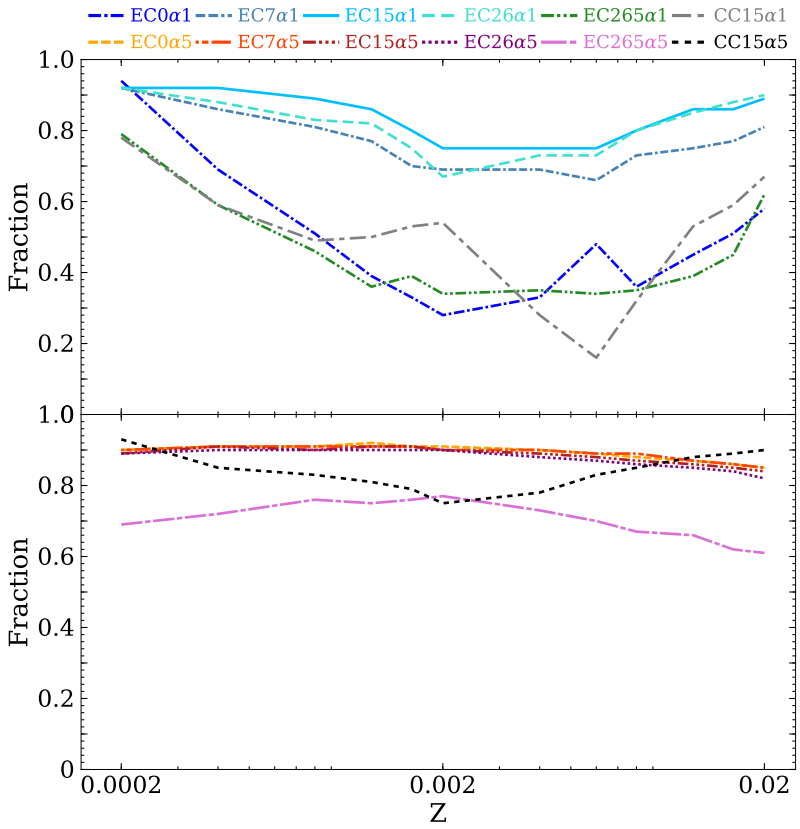

Figure 3.3: The percentage of merging DNSs which follow the standard scenario (see Sec. 3.2) as a function of progenitor's metallicity. Top: simulations with $\alpha = 1$. Bottom: simulations with $\alpha = 5$.

3.2.3 Simulations and initial distributions

Here we describe the initial conditions used to perform our population-synthesis simulations. We randomly draw the mass of the primary star (m_1) from a Kroupa initial mass function (IMF; Kroupa, 2001

$$\mathfrak{F}(m_1) \propto m_1^{-2.3} \qquad \text{with} \quad m_1 \in [5-150]\,\mathrm{M}_\odot\,. \tag{3.6}$$

The other parameters (mass of the secondary, period and eccentricity), are sampled according to the distributions proposed by Sana et al. (2012). In particular, we obtain the mass of the secondary m_2 as follows

$$\mathfrak{F}(q) \propto q^{-0.1} \qquad \text{with} \quad q = \frac{m_2}{m_1} \in [0.1-1]\,, \tag{3.7}$$

the orbital period P and the eccentricity e from

$$\mathfrak{F}(P) \propto (P)^{-0.55} \text{ with } P = \log_{10}(P/\mathrm{day}) \in [0.15-5.5] \tag{3.8}$$

and

$$\mathfrak{F}(e) \propto e^{-0.42} \qquad \text{with} \quad 0 \leq e < 1 \tag{3.9}$$

respectively.

For the CE phase we have adopted the $\alpha\lambda$ formalism (see Webbink, 1984; Ivanova et al., 2013). This formalism relies on two parameters, λ (which measures the concentration of the envelope) and α (which quantifies the energy available to unbind the envelope). To compute λ we used the prescriptions derived by Claeys et al. (2014) (see their Appendix A for more details) which are based on Dewi and Tauris (2000).

We have run 12 sets of simulations, by changing the value of α and that of both $\sigma_{\rm ECSN}$ and $\sigma_{\rm CCSN}$ (see Table 3.1).

In the first 10 simulations reported in Table 3.1, we have fixed $\sigma_{\rm CCSN} = 265$ km s^{-1} and we have varied $\alpha = 1, 5$ and $\sigma_{\rm ECSN} = 0, 7, 15, 26, 265$ km s^{-1} (corresponding to an average natal kick of about $0, 11, 23, 41, 420$ km s^{-1}, respectively).

In the last two simulations reported in Table 3.1 (CC15α1 and CC15α5), we have set $\sigma_{\rm CCSN} = \sigma_{\rm ECSN} = 15$ km s^{-1} for both $\alpha = 1, 5$. We will discuss simulations CC15α1 and CC15α5 in Section 3.3.4, while in the following sections we will focus on the other 10 simulations (i.e. on the effect of $\sigma_{\rm ECSN}$ on the statistics of DNSs).

Finally, for each set of simulations we considered 12 sub-sets with different metallicities $Z = 0.0002$, 0.0004, 0.0008, 0.0012, 0.0016, 0.002, 0.004, 0.006, 0.008, 0.012, 0.016 and 0.02. In each sub-set, we simulated 10^7 binary systems. Thus, each of sets of simulations is composed of 1.2×10^8 massive binaries.

3.3 Results

3.3.1 Impact of $\sigma_{\rm ECSN}$ on DNSs

The left-hand panel of Figure 3.1 shows all DNSs formed in our simulations as a function of metallicity. It is apparent that the lower $\sigma_{\rm ECSN}$ is, the higher the total number of DNSs. This is not surprising, because a lower $\sigma_{\rm ECSN}$ implies a lower probability to unbind the system.

This effect is particularly strong for the simulations with $\alpha = 1$, in which the number of DNSs is $\sim 10-25$ times higher if $\sigma_{\rm ECSN} = 0$ than if $\sigma_{\rm ECSN} = 265$ km s^{-1}. In the simulations with $\alpha = 5$, the number of DNSs is $3-6$ times higher if $\sigma_{\rm ECSN} = 0$ than if $\sigma_{\rm ECSN} = 265$ km s^{-1}. We also note that DNSs form more efficiently if $\alpha = 5$ than if $\alpha = 1$.

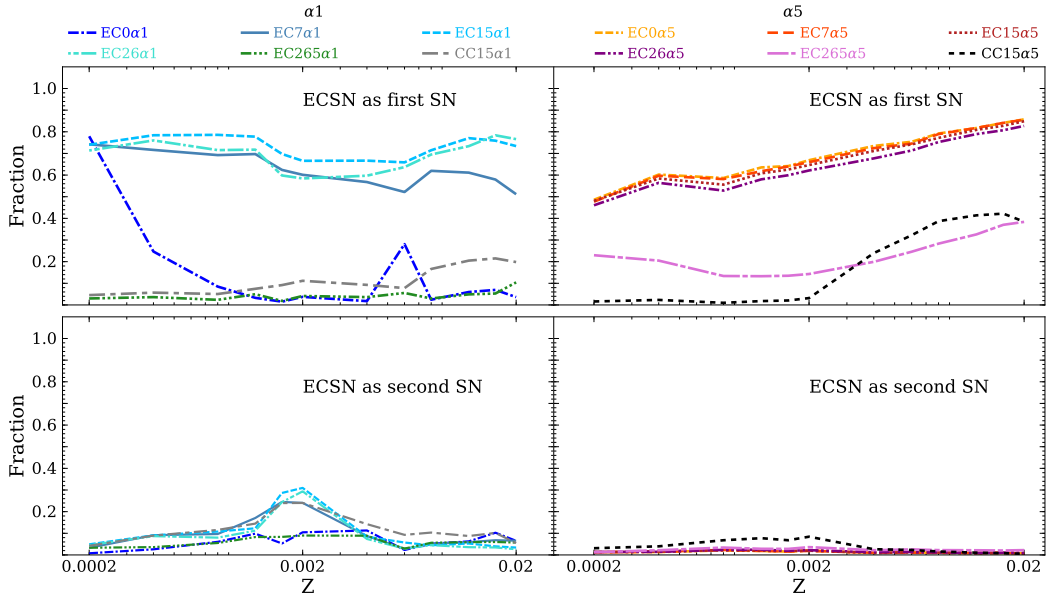

Figure 3.4: Top (bottom) panels: fraction of merging DNSs in which the first (second) SN is an ECSN as a function of progenitor's metallicity. Left-hand (right-hand) panels: simulations with $\alpha = 1$ ($\alpha = 5$).

In our simulations, the number of DNSs depends on metallicity, especially if $\alpha = 1$. In particular, the number of DNSs is minimum for $Z \sim 0.002$. This trend originates from the evolution of stellar radii of $\sim 8-20$ $M_\odot$ stellar progenitors, which are significantly larger for $Z \sim 0.002$, than for the other metallicities (especially in the terminal main sequence and in the HG phases). The trend is stronger for $\alpha = 1$ than for $\alpha = 5$, because a low value of α corresponds to a more efficient shrinkage of the orbit during CE: two main sequence or HG stars are more likely to merge during CE if α is low.

The right-hand panel of Figure 3.1 shows only the DNSs which merge in less than a Hubble time (hereafter: merging DNSs). In the simulations with $\alpha = 5$, we find again a monotonic trend with $\sigma_{\rm ECSN}$, but the differences are much less significant. In the simulations with $\alpha = 1$ the number of merging DNSs does not show a monotonic trend with $\sigma_{\rm ECSN}$: runs with $\sigma_{\rm ECSN} = 7-26$ km s^{-1} produce a factor of ~ 5 more merging DNSs than simulations with $\sigma_{\rm ECSN} = 0$ and 265 km s^{-1}. The only exception is represented by very metal-poor stars ($Z = 0.0002$), for which the number of merging DNSs with $\sigma_{\rm ECSN} = 0$ is similar to the one of systems with $\sigma_{\rm ECSN} = 7-26$ km s^{-1}. This behavior can be easily explained by considering that the merging time ($t_{\rm gw}$) due to GW emission depends on both the eccentricity (e) and the semi-major axis

(a) as (Peters, 1964)

$$t_{\rm gw} = \frac{5}{256}\frac{c^5}{G^3}\frac{a^4(1-e^2)^{7/2}}{m_1 m_2(m_1+m_2)}\,, \tag{3.10}$$

where c is the speed of light, G is the gravitational constant, and m_1 (m_2) is the mass of the primary (secondary) member of the binary.

Equation 3.10 implies that more eccentric binaries have a shorter merging time. Moderate natal kicks do not unbind a binary, but increase its eccentricity, shortening its merging time. Since most binaries evolve through processes which tend to circularize their orbits (e.g. tidal torques, mass transfer and CE phase), the natal kicks are a fundamental ingredient to obtain highly eccentric orbits.

This behavior is shown in the left-hand column of Figure 3.2, where the initial eccentricity distribution of all DNSs is compared with that of the merging DNSs (here "initial" refers to the time when the second NS is formed). A large number of DNSs have initial eccentricity close to zero in run EC0α1 (corresponding to $\sigma_{\rm ECSN} = 0$ and $\alpha = 1$), but only very few of them merge within a Hubble time.

Many DNSs have initial eccentricity close to zero and most of them do not merge within a Hubble time also in run EC0α5 (corresponding to $\sigma_{\rm ECSN} = 0$ and $\alpha = 5$). However, run EC0α5 is also efficient in producing DNSs with non-zero eccentricity, which are able to merge within a Hubble time. In contrast, only few DNSs with eccentricity close to zero form in the other runs, because of the SN kicks. We note that the second NS originates from an ECSN in the vast majority of DNSs with eccentricity $e \sim 0$.

The right-hand column of Figure 3.2 compares the distribution of the initial semi-major axis of all DNSs with that of the merging systems. We see that increasing $\sigma_{\rm ECSN}$ the widest systems tend to disappear, because they can be disrupted more easily by the natal kicks.

3.3.2 DNS formation channels

From our simulations we find that the most likely formation channel for merging DNSs is consistent with the standard scenario described in Tauris et al. (2017) (see their Figure 1): first the primary star expands and fills its Roche lobe, transferring mass to the companion; then the primary explodes leaving a NS; when the secondary expands, the system enters CE; after CE ejection, the system is composed of a NS and a naked Helium star and the NS starts stripping its companion; the stripped Helium star undergoes a SN explosion, which is most likely an ultra-stripped SN (Tauris et al., 2013; Tauris et al., 2015; Tauris et al., 2017); the final system is a close DNS which will merge within a Hubble time.

Figure 3.3 shows the fraction of merging DNSs which follow the standard scenario we have just described ($f_{\rm std}$). For $\alpha = 5$, $f_{\rm std}$ is nearly independent of the metallicity of the progenitor, while it depends on the natal kicks. At low kicks ($\sigma_{\rm ECSN} \leq 26$ km s^{-1}) >> 80 per cent of merging DNSs form via the standard scenario, while if $\sigma_{\rm ECSN} = 265$ km s^{-1} the percentage lowers to $\sim 60-70$ per cent.
For $\alpha = 1$, $f_{\rm std}$ depends on both the metallicity and the natal kicks. For a given kick distribution, $f_{\rm std}$ is minimum at metallicity $Z \sim 0.0016-0.006$ (especially in run EC0α1 and EC265α1), while for a fixed metallicity $f_{\rm std}$ is maximum ($\sim 80-90$ per cent) for $\sigma_{\rm ECSN} = 7-26$ km s^{-1}.
This behavior confirms that ECSNe are a fundamental process for the formation of DNSs, but what is the fraction of systems undergoing an ECSN? Is ECSN more frequently the first or the second SN of a merging system?
Figure 3.4 shows the fraction of merging DNSs in which at least one of the two SN explosions is an ECSN. Most merging DNSs ($\sim 50-90$ per cent) undergo at least one ECSN in the vast majority of simulations (EC7α1, EC15α1, EC26α1, EC0α5, EC7α5, EC15α5 and EC26α5). In the simulation EC0α1 ($\sigma_{\rm ECSN} = 0$ and $\alpha = 1$), ECSNe are important at low metallicity ($Z = 0.0002$) and negligible for intermediate and high metallicity. Only in the simulations with large ECSN kicks (runs EC265α1 and EC265α5), the fraction of DNSs undergoing at least one ECSN is always less than 50 per cent.
Moreover, in simulations with $\alpha = 5$ the percentage of DNSs which undergo at least one ECSN increases with the progenitor's metallicity.
Overall, we find that the ECSN is the first SN in the vast majority of merging DNSs. Less than ~ 10 per cent of merging DNSs go through an ECSN as second SN, independently of the assumptions about natal kicks and CE efficiency. This result is in agreement with Chruslinska et al. (2017) and Kruckow et al. (2018) (but see Tauris et al., 2017 for a different argument).
This is likely due to the fact that the first SN explosion occurs before that other processes (e.g. a CE phase) are able to shrink the binary; therefore the system is less bound and it can be more easily disrupted if the natal kick of the newborn NS is too strong. In contrast, the second SN explosion tends to occur after a CE, when the system is usually on a very close and less eccentric orbit, hence it can survive even stronger kicks. Moreover, the fact that the second SN explosion induces a high kick velocity facilitates the formation of highly eccentric orbits, which are more likely to merge via GW emission.
The fact that the ECSN is often the first SN occurring in a merging DNS might seem awkward, because ECSN progenitors are usually less massive than iron CCSN pro-

genitors. Indeed, this happens because most merging DNSs originate from very close binary systems, in which the primary has lost a significant fraction of its mass by mass transfer during Roche lobe overflow. Because of mass loss, the primary enters the regime of ECSNe. In contrast, the secondary accretes part of the mass lost by the primary and enters the regime of iron CCSNe. This explains why the first SN is more often an ECSN in the progenitors of merging DNSs.

3.3.3 GW170817-like systems

Figure 3.5 shows the number of GW170817-like systems that form in our simulations. We define as GW170817-like systems those merging DNSs with $M_{\rm rem,1} \in [1.36, 1.60]\,{\rm M}_\odot$ and $M_{\rm rem,2} \in [1.17, 1.36]\,{\rm M}_\odot$ ($M_{\rm rem,1}$ and $M_{\rm rem,2}$ being the mass of the primary and of the secondary NS, assuming effective spin ≤ 0.05, Abbott et al., 2017e). Because of its large mass ($1.36 - 1.60\,{\rm M}_\odot$), the most massive component of GW170817-like systems cannot have formed via ECSN. In other words, at least one of the two SNe must be a CCSN, in order to form a GW170817-like system.
Figure 3.5 shows that at high metallicity ($Z \gtrsim 0.002$ for $\alpha = 1$ and $Z \gtrsim 0.012$ for $\alpha = 5$) all simulations follow a similar trend independently of the value of $\sigma_{\rm ECSN}$, while for lower metallicities the number of GW170817-like systems becomes sensitive to the value of $\sigma_{\rm ECSN}$. In particular, the higher $\sigma_{\rm ECSN}$ is, the lower the number of GW170817-like systems. Furthermore, in the simulations with $\alpha = 5$ the number of GW170817-like systems increases with decreasing metallicity.
The reason is that at high metallicity the majority of GW170817-like systems form from binaries which undergo two iron CCSNe (see Figure 3.6), while at low metallicity most of the progenitors pass through at least one ECSN. Figure 3.6 shows that the effect of increasing the value of α is to increase the maximum metallicity at which the majority of GW170817-like systems form through at least one ECSN from $Z \sim 0.002$ ($\alpha = 1$) to $Z \sim 0.012$ ($\alpha = 5$).

3.3.4 Low kicks in iron core-collapse SNe

Low natal kicks might occur not only in ECSNe but also in iron CCSNe, especially in the case of low-mass progenitors (Müller, 2016) and ultra-stripped SNe (Tauris et al., 2017). Moreover, Giacobbo and Mapelli (2018) and Mapelli and Giacobbo

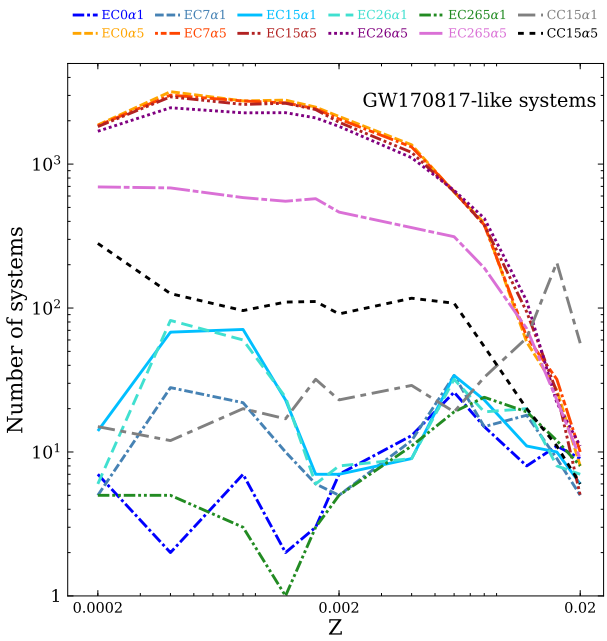

Figure 3.5: Number of GW170817-like simulated merging DNSs as a function of progenitor's metallicity.

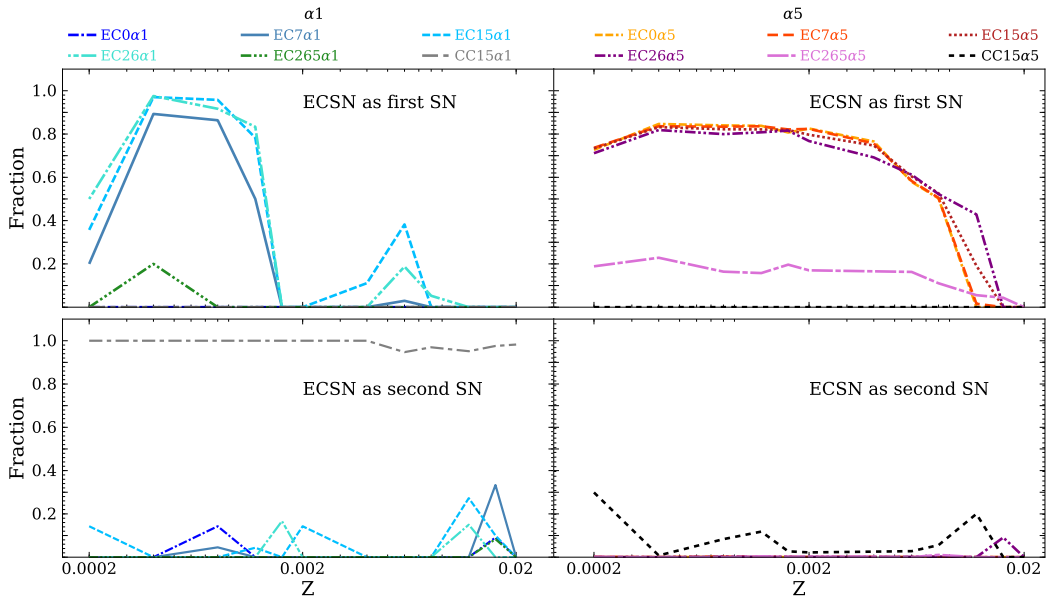

Figure 3.6: Top (Bottom) panels: fraction of GW170817-like systems in which the first (second) SN is an ECSN as a function of progenitor's metallicity. The left-hand (right-hand) panels are for the simulation with $\alpha = 1$ ($\alpha = 5$).

(2018) have shown that population-synthesis simulations can reproduce the local merger rate of DNSs inferred from GW170817 (Abbott et al., 2017e) only if low natal kicks ($\lesssim 50$ km s^{-1}) are assumed for all DNSs.
Thus, in this Section we discuss how much the main results of this paper change if we make the extreme assumption that all NSs receive a low natal kick, i.e. $\sigma_{\rm ECSN} = \sigma_{\rm CCSN} = 15$ km s^{-1}. To this purpose, we have considered two additional runs: CC15α1 and CC15α5, which have been already presented in Giacobbo and Mapelli (2018) and Mapelli and Giacobbo (2018). Simulation CC15α1 (CC15α5) differs from simulation EC15α1 (EC15α5) only for the choice of $\sigma_{\rm CCSN}$ (see Table 3.1).
From Figure 3.1 it is apparent that the number of DNSs is about one order of magnitude larger in simulation CC15α1 (CC15α5) than in simulation EC15α1 (EC15α5). This is not surprising, because a lower CCSN kick implies a lower probability to unbind the system.
On the other hand, if we consider only the DNSs merging within a Hubble time, we find an interesting difference. The number of merging DNSs is a factor of ten larger in simulation CC15α1 than in simulation EC15α1, whereas the number of merging DNSs in simulations CC15α5 and EC15α5 are comparable. Moreover, simulations CC15α5 and EC15α5 show a significantly different trend with metallicity. As already discussed in Giacobbo and Mapelli (2018), there is a strong interplay between the effects of natal kicks and those of CE efficiency.
Figure 3.4 shows that the percentage of merging DNSs which underwent at least one ECSN is dramatically affected by the choice of $\sigma_{\rm CCSN}$: less than ~ 40 per cent of all merging DNSs underwent at least one ECSN if $\sigma_{\rm CCSN} = 15$ km s^{-1}. This difference is particularly strong for the first SN. In fact, the binary system is still quite large at the time of the first SN explosion and can be easily broken by the SN kick.
This result has relevant implications for the GW170817-like systems. As shown in Fig. 3.6, no GW170817-like systems underwent an ECSN as first SN in simulations CC15α1 and CC15α5. This comes from the trend we described above, plus the fact that the first SN usually produces the most massive NS of the system in runs CC15α1 and CC15α5. In our models, the mass of a NS born from ECSN is assumed to be 1.26 M$_\odot$, insufficient to match the mass of the primary member of GW170817 (under the assumption of low spins). In contrast, the second SN is always an ECSN in the GW170817-like systems formed in simulation CC15α1. We stress, however, that this result critically depends on the assumption about the mass of a NS formed via ECSN Hurley et al., 2000; Fryer et al., 2012.

3.4 Summary

We have investigated the importance of ECSNe on the formation of DNSs. ECSNe are thought to occur frequently in interacting binaries (Podsiadlowski et al., 2004; Tauris et al., 2017) and to produce relatively small natal kicks (Dessart et al., 2006; Jones et al., 2013; Schwab et al., 2015a). We assumed that natal kicks generated by ECSNe (iron CCSNe) are distributed according to a Maxwellian function with 1D rms $\sigma_{\rm ECSN}$ ($\sigma_{\rm CCSN}$).

First, we have assumed $\sigma_{\rm CCSN} = 265$ km s^{-1} (according to Hobbs et al., 2005) and we have explored five different values of $\sigma_{\rm ECSN} = 0$, 7, 15, 26 and 265 km s^{-1}. Moreover, we have also investigated the impact of CE, by considering $\alpha = 1$ and $\alpha = 5$.

We find that the number of simulated DNSs scales inversely with $\sigma_{\rm ECSN}$. In particular, the largest (smallest) number of DNSs form if $\sigma_{\rm ECSN} = 0$ ($\sigma_{\rm ECSN} = 265$ km s^{-1}). This effect is maximum for $\alpha = 1$, while it is only mild for $\alpha = 5$.

The number of DNSs merging within a Hubble time also depends on $\sigma_{\rm ECSN}$, but with a rather different trend depending on the assumed value for α. For $\alpha = 5$, the number of merging systems follows the same trend as the total number of DNSs. For $\alpha = 1$ the number of DNS mergers is maximum for $\sigma_{\rm ECSN} = 7 - 26$ km s^{-1}, while it drops by a factor of $\sim 3 - 10$ if $\sigma_{\rm ECSN} = 0$ and if $\sigma_{\rm ECSN} = 265$ km s^{-1}.

The reason is that very large kicks ($\sigma_{\rm ECSN} = 265$ km s^{-1}) completely break the binary, while moderate kicks ($\sigma_{\rm ECSN} = 7 - 26$ km s^{-1}) leave the binary bound but increase its eccentricity. A larger eccentricity implies a shorter timescale for merger by GW emission, as shown by Peters (1964). In contrast, null natal kicks produce a large number of systems with zero initial eccentricity, which have longer merger times.

A large percentage ($\sim 50 - 90$ per cent) of merging DNSs undergo at least one ECSN explosion in most of our simulations. This percentage drops below 40 per cent only if $\sigma_{\rm ECSN} = 265$ km s^{-1}, or if $\sigma_{\rm CCSN} = 15$ km s^{-1}, or if $\sigma_{\rm ECSN} = 0$ km s^{-1}, $\alpha = 1$ and $Z > 0.0002$.

In the majority of merging DNSs, the ECSN is the first SN occurring in the binary. This happens because, in most cases, the first SN occurs before the binary has shrunk significantly (e.g. by CE) and is easily broken if the kick is too strong.

Moreover, we have selected the simulated DNSs whose mass matches that of GW170817. We call these systems GW170817-like systems. At high metallicity ($Z \gtrsim 0.002$ for $\alpha = 1$ and $Z \gtrsim 0.012$ for $\alpha = 5$) the formation of GW170817-like systems is independent of $\sigma_{\rm ECSN}$, because most GW170817-like systems form through iron CCSNe, while for lower metallicity most GW170817-like systems undergo at least one ECSN and their statistics depends on $\sigma_{\rm ECSN}$.

Finally, we have considered an extreme case in which not only ECSNe but also CC-SNe are associated to low kicks, by imposing $\sigma_{\rm CCSN} = \sigma_{\rm ECSN} = 15$ km s^{-1}. Mapelli and Giacobbo (2018) and Giacobbo and Mapelli (2018) suggest that this extreme assumption is necessary to match the local DNS merger rate density inferred from GW170817 (Abbott et al., 2017e).
The number of simulated DNSs increases by a factor of ten if we assume $\sigma_{\rm CCSN} =$ 15 km s^{-1}, because less binary systems are disrupted by the first SN explosion. Moreover, this assumption strongly suppresses the percentage of merging DNSs (especially GW170817-like systems) which evolved through an ECSN as first SN. These results confirm the importance of natal kicks to understand the properties of merging DNSs.

CHAPTER 4

THE PROGENITORS OF COMPACT-OBJECT BINARIES: IMPACT OF METALLICITY, COMMON ENVELOPE AND NATAL KICKS

Six gravitational wave events have been reported by the LIGO-Virgo collaboration (LVC), five of them associated with black hole binary (BHB) mergers and one with a double neutron star (DNS) merger, while the coalescence of a black hole-neutron star (BHNS) binary is still missing. We investigate the progenitors of double compact object binaries with our population-synthesis code MOBSE. MOBSE *includes advanced prescriptions for mass loss by stellar winds (depending on metallicity and on the Eddington ratio) and a formalism for core-collapse, electron-capture and (pulsational) pair instability supernovae. We investigate the impact of progenitor's metallicity, of the common-envelope parameter α and of the natal kicks on the properties of DNSs, BHNSs and BHBs. We find that neutron-star (NS) masses in DNSs span from 1.1 to 2.0 $M_\odot$, with a preference for light NSs, while NSs in merging BHNSs have mostly large masses (*$1.3-2.0\ M_\odot$*). BHs in merging BHNSs are preferentially low mass (*$5-15\ M_\odot$*). BH masses in merging BHBs strongly depend on the progenitor's metallicity and span from* ~ 5 *to* $\sim 45\ M_\odot$. *The local merger rate density of both BHNSs and BHBs derived from our simulations is consistent with the values reported by the LVC in all our simulations. In contrast, the local merger rate density of DNSs matches the value inferred from the LVC only if low natal kicks are assumed. This result adds another piece to the intricate puzzle of natal kicks and DNS formation.*

Based on:
Giacobbo N., Mapelli M., MNRAS, 2018, 480, p.2011-2030

4.1 Introduction

On August 17 2017, the LIGO-Virgo collaboration (LVC, Aasi et al. et al., 2015; Acernese et al., 2015) captured the first gravitational wave (GW) signal from a double neutron star (DNS) merger (Abbott et al., 2016a; Abbott et al., 2017f). GW170817 was accompanied by electromagnetic radiation over a large range of wavelengths, from radio to gamma-rays (Abbott et al., 2017c; Goldstein et al., 2017; Savchenko et al., 2017; Margutti et al., 2017; Coulter et al., 2017; Soares-Santos et al., 2017; Chornock et al., 2017; Cowperthwaite et al., 2017; Nicholl et al., 2017; Pian et al., 2017; Alexander et al., 2017), marking the beginning of multi-messenger astronomy. Besides GW170817, five other GW detections were reported so far (GW150914, GW151226, GW170104, GW170608, GW170814), all of them interpreted as the merger of two black holes (BHs, Abbott et al., 2016d; Abbott et al., 2016c; Abbott et al., 2016b; Abbott et al., 2016d; Abbott et al., 2017b; Abbott et al., 2017d; Abbott et al., 2017e).

Unlike BH binaries (BHBs), whose very existence was revealed by direct detections of GWs (Abbott et al., 2016d), DNSs were observed well before GW170817: PSR $B1913+16$ was discovered already in 1974 (Hulse and Taylor, 1975), followed by about a dozen similar binaries Tauris et al., 2017, including a double pulsar (Burgay et al., 2003; Lyne et al., 2004). Together with GW170817, these highly relativistic systems give us a unique grasp on the behaviour of matter under extreme conditions.

Now that both BHBs and DNSs have been detected by the LVC, the coalescence of a neutron star (NS) with a BH is the only missing merger event that we expect to observe in the frequency range of ground-based GW detectors. No BH-NS binaries (BHNSs) have been discovered so far by radio surveys.

Previous work investigates the formation of DNSs, BHNSs and BHBs both from isolated binaries (e.g. Tutukov et al., 1973; Flannery and van den Heuvel, 1975; Bethe and Brown, 1998; Belczynski et al., 2002; Voss and Tauris, 2003; Dewi and Pols, 2003; Podsiadlowski et al., 2004; Podsiadlowski et al., 2005; Dewi et al., 2005; Tauris and van den Heuvel, 2006; Portegies Zwart and Yungelson, 1998; Portegies Zwart and McMillan, 2000; Belczynski et al., 2007; Bogomazov et al., 2007; Dominik et al., 2012; Dominik et al., 2013a; Dominik et al., 2015; Mennekens and Vanbeveren, 2014; Tauris et al., 2015; Tauris et al., 2017; de Mink and Belczynski, 2015; de Mink and Mandel, 2016; Marchant et al., 2016; Chruslinska et al., 2018; Mapelli et al., 2017; Giacobbo et al., 2018; Kruckow et al., 2018; Shao and Li, 2018) and from dynamics (e.g. Kulkarni et al., 1993; Sigurdsson and Phinney, 1993; Sigurdsson and

Hernquist, 1993; Sigurdsson and Phinney, 1995; Phinney, 1996; Colpi et al., 2003; Mapelli et al., 2005; Grindlay et al., 2006; Ivanova et al., 2008; Clausen et al., 2013; Mapelli and Zampieri, 2014; Ziosi et al., 2014; Rodriguez et al., 2015; Rodriguez et al., 2016; Mapelli, 2016; Askar et al., 2016; Antonini et al., 2017; Petrovich and Antonini, 2017; Banerjee, 2018; Belczynski et al., 2018).

Despite this effort, the evolution of compact-object binaries is still highly uncertain. The merger rate density of DNSs inferred from GW170817 is $R_{\rm DNS} = 1540^{+3200}_{-1220}$ Gpc^{-3} yr^{-1}, consistent with recent estimates from short gamma-ray bursts ($\sim 8-1800$ Gpc^{-3} yr^{-1} according to Coward et al., 2012; $\sim 500-1500$ Gpc^{-3} yr^{-1} based on the analysis of Petrillo et al., 2013; $\sim 92-1154$ Gpc^{-3} yr^{-1} as estimated by Siellez et al., 2014, and 270^{+1580}_{-180} Gpc^{-3} yr^{-1} according to Fong et al., 2015), but quite large with respect to the rate predicted from kilonovae ($\sim 63^{+63}_{-31}$ Gpc^{-3} yr^{-1}, Jin et al., 2015). Simulations of isolated and dynamically formed DNSs show that it is very difficult to match such a high rate, unless rather extreme assumptions about common envelope (e.g. Chruslinska et al., 2018) or natal kicks (e.g. Giacobbo and Mapelli, 2018; Mapelli and Giacobbo, 2018) are made.

In this paper, we use our population-synthesis code MOBSE Giacobbo et al., 2018 to investigate the formation of DNSs, BHNSs and BHBs from isolated binaries and to analyze the effect of natal kicks and common-envelope efficiency on the merger rate of DNSs, BHBs and BHNSs. In its current version, MOBSE includes up-to-date prescriptions for stellar winds (accounting for the metallicity and for the Eddington ratio of the progenitor star), for core-collapse supernovae (SNe), electron-capture SNe, pulsational pair-instability SNe and pair-instability SNe.

4.2 Methods

MOBSE, which stands for "massive objects in binary stellar evolution", is an updated version of the populations synthesis code BSE Hurley et al., 2000; Hurley et al., 2002. MOBSE is meant to improve the treatment of massive stars and stellar remnants. We refer to Giacobbo et al., 2018 and Mapelli et al., 2017 for a detailed description of MOBSE. Here, we just summarize the main features of MOBSE with respect to BSE.

4.2.1 Single star evolution and SNe

MOBSEincludes a new treatment of stellar winds for hot massive stars, based on Vink et al. (2001) for O-type and B-type stars, on Vink and de Koter (2005a) for Wolf-

Rayet stars, and on Belczynski et al. (2010) for luminous blue variable stars. For all types of hot massive stars, we adopt a description of the mass loss as $\dot{M} \propto Z^{\beta}$, where Z is the metallicity and $\beta = 0.85$ if the Eddington ratio $\Gamma < 2/3$, $\beta = 2.45 - 2.4\,\Gamma$ if $2/3 \leq \Gamma < 1$, and $\beta = 0.05$ if $\Gamma \geq 1$ (Chen et al., 2015).

We have also updated the prescriptions for core radii following Hall and Tout, 2014 and we have extended the mass range up to 150 $M_{\odot}$ (Mapelli, 2016).

The treatment of SNe was also deeply revised: we have included pulsational pair instability and pair instability SNe as described in Spera and Mapelli (2017), and we have added two new prescriptions for iron core-collapse SNe: the delayed and the rapid models presented in Fryer et al. (2012) (see also Spera et al., 2015). In this paper, we always adopt the rapid core-collapse SN mechanism, because it allows us to reproduce the mass gap of compact objects between ~ 2 and ~ 5 $M_{\odot}$ (Özel et al., 2010; Farr et al., 2011), as it can be seen from Figure 4.1.

We have also updated the treatment for electron-capture SNe. In the case of both an electron-capture SN and an accretion-induced white dwarf (WD) collapse, the NS forms when the degenerate Oxygen-Neon (ONe) core collapses as a consequence of electron-capture reactions, inducing a thermonuclear runaway. In MOBSE, we assume that if a growing degenerate ONe core reaches the mass $M_{\rm ECSN} = 1.38$ $M_{\odot}$ it collapses due to the electron-capture on ^{24}Mg and on ^{20}Ne (Miyaji et al., 1980; Nomoto, 1984; Nomoto, 1987; Nomoto and Kondo, 1991; Kitaura et al., 2006; Fisher et al., 2010; Jones et al., 2013; Takahashi et al., 2013; Schwab et al., 2015a; Jones et al., 2016), otherwise it forms a ONe WD, which can still collapse to a NS if it will accrete sufficient mass.

The outcome of the electron-capture collapse is a NS. We compute the final mass of the newly-born NS by using the formula suggested by Timmes et al. (1996)

$$M_{\rm rem,grav} = \frac{\sqrt{1 + 0.3 M_{\rm rem,bar}} - 1}{0.15} = 1.26\,{\rm M}_{\odot}\,, \tag{4.1}$$

where $M_{\rm rem,bar} = M_{\rm ECSN}$ is the baryonic mass of the NS including neutrinos, and $M_{\rm rem,grav}$ is the final mass of the NS considering the mass loss due to neutrinos emission.

The current version of MOBSE does not include any specific treatment for the initial spin of BHs and NSs. What drives the initial spin magnitude and direction of a compact object is still poorly understood and constrained. We refer to Postnov and Kuranov (2019), Wysocki et al. (2018), Belczynski et al. (2017) and Arca Sedda and Benacquista (2019) for a more detailed discussion of BH spins.

4.2.2 SN kicks

In MOBSE, the natal kick of a NS is drawn from a Maxwellian velocity distribution,

$$f(v,\sigma) = \sqrt{\frac{2}{\pi}}\frac{v^2}{\sigma^3}\exp\left[-\frac{v^2}{2\sigma^2}\right] \qquad v \in [0,\infty) \tag{4.2}$$

where σ is the one dimensional root-mean-square.

Here, we have implemented in MOBSE the possibility to draw the natal kick from two Maxwellian curves with a different root-mean-square: $\sigma_{\rm CCSN}$ and $\sigma_{\rm ECSN}$, for core-collapse and electron-capture SNe, respectively.

For electron-capture SNe, we draw the kicks from a Maxwellian with one-dimensional root-mean square (1D rms) $\sigma_{\rm ECSN}$ = 15 km s^{-1}, corresponding to an average velocity of $\sim$ 23 km s^{-1} (Giacobbo and Mapelli, 2018). This approach is justified by the fact that an electron-capture collapse is a more rapid process with respect to the iron core-collapse explosion and for that reason the asymmetries are more difficult to develop (Kitaura et al., 2006; Dessart et al., 2006; Janka, 2012). The consequence is that the newborn NS has a low natal kick (Dessart et al., 2006; Jones et al., 2013; Schwab et al., 2015a).

For iron core-collapse SNe the situation is more puzzling. Hobbs et al. (2005) report the proper motion of 233 Galactic single pulsars and describe the kick velocities using a Maxwellian with 1D rms $\sigma_{\rm CCSN}$ = 265 km s^{-1}, corresponding to an average velocity of $\sim$ 420 km s^{-1}. Several studies (Cordes and Chernoff, 1998; Arzoumanian et al., 2002; Brisken et al., 2003; Schwab et al., 2010; Verbunt et al., 2017) claim that the velocity distribution proposed by Hobbs et al. (2005) underestimates the number of pulsars with a low velocity and suggest that the natal kick distribution of NSs is better represented by a bimodal velocity distribution. For instance, two out of nine accurate pulsar velocities computed by Brisken et al. (2002) are smaller than 40 km s^{-1}. Moreover, Pfahl et al. (2002) study a new class of high-mass X-ray binaries with small eccentricities and long orbital periods, which imply a low natal kick velocity ($\lesssim$ 50 km s^{-1}) for the newborn NSs. This bimodal distribution might result from two different mechanisms of NS formation (van den Heuvel, 2007; Beniamini and Piran, 2016).

Finally Tauris et al. (2017) suggest that not only electron-capture SNe, but even iron core-collapse SNe could be associated with low kicks $\lesssim$ 50 km s^{-1}, when the SN is *ultra-stripped* (Tauris et al., 2013; Tauris et al., 2015; Bray and Eldridge, 2016). A SN is ultra-stripped if the exploding star is member of a binary system and was heavily stripped by its companion. In this case, the mass ejected during the SN is small ($\lesssim$ 0.1 M$_\odot$) and thus the kick is also small (< 50 km s^{-1}, e.g. Suwa et al., 2015). This

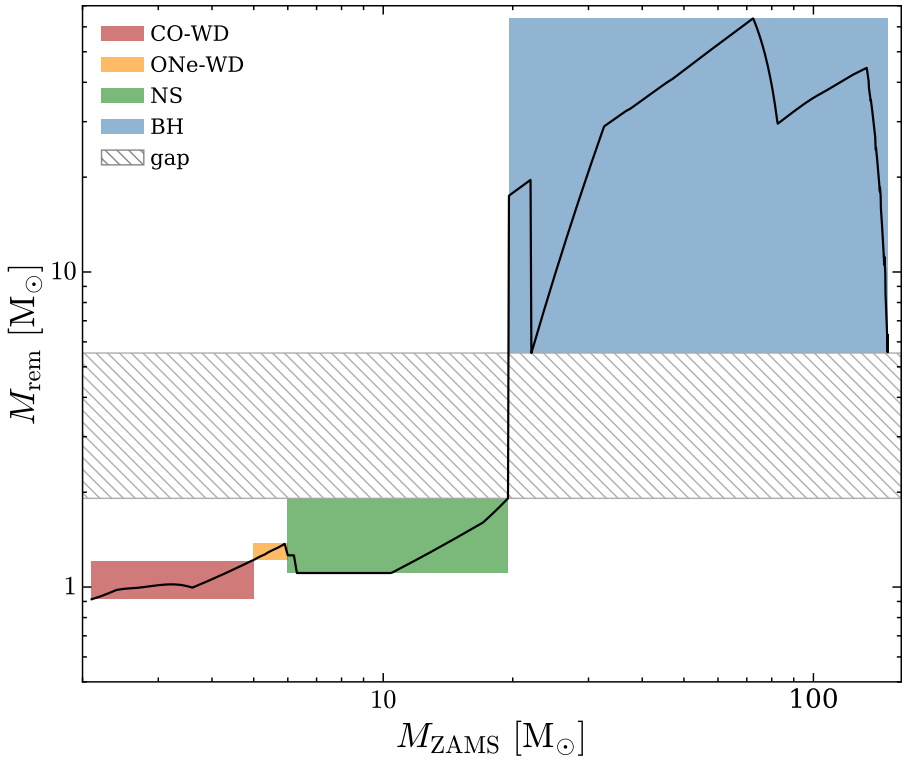

Figure 4.1: Mass spectrum of compact remnants as a function of the zero-age main sequence (ZAMS) mass of the progenitor stars. The coloured regions (red, orange, green and blue) identify the mass ranges of different compact objects (Carbon-Oxygen WDs, Oxygen-Neon WDs, NSs and BHs, respectively). The hashed region shows the mass gap between NSs and BHs predicted by the rapid core-collapse SN model Fryer et al., 2012. The metallicity is $Z = 0.0002$.

suggests that the natal kicks of single NSs could be significantly different from the kicks of NSs born in close binary systems (see also Tauris and Bailes, 1996).
Given this uncertainty, we decided to simulate two extreme cases for the kick of iron core-collapse SNe. In the first case (hereafter: high-velocity kicks), we draw core-collapse SN kicks from a Maxwellian distribution with 1D rms $\sigma_{\rm CCSN} = 265$ km s^{-1}, as derived by Hobbs et al. (2005). In the second case (hereafter: low-velocity kicks), we draw core-collapse SN kicks from a Maxwellian distribution with 1D rms $\sigma_{\rm CCSN} = 15$ km s^{-1}, i.e. the same as for electron-capture SNe (see Table 4.1).
Finally, while NSs receive the full kick drawn from the Maxwellian distribution, BHs receive a natal kick that is reduced by the amount of fallback as $v_{\rm BH} = (1 - f_{\rm fb})\, v$, where $f_{\rm fb}$ is the fallback parameter and v is the velocity randomly sampled from the Maxwellian curve (Fryer et al., 2012).

Table 4.1: Initial conditions of the MOBSEsimulations.

ID	$\sigma_{\rm ECSN}$	$\sigma_{\rm CCSN}$	SN	α
$\alpha1$	15.0 km/s	265.0 km/s	rapid	1.0
$\alpha3$	15.0 km/s	265.0 km/s	rapid	3.0
$\alpha5$	15.0 km/s	265.0 km/s	rapid	5.0
CC15$\alpha1$	15.0 km/s	15.0 km/s	rapid	1.0
CC15$\alpha3$	15.0 km/s	15.0 km/s	rapid	3.0
CC15$\alpha5$	15.0 km/s	15.0 km/s	rapid	5.0

Column 1: simulation name; columns 2 and 3: 1D rms of the Maxwellian distribution for electron-capture SN kicks and for iron core-collapse SN kicks (see sec. 4.2.2); column 4: SN model (Fryer et al., 2012; Giacobbo et al., 2018); column 5: values of α adopted in the CE formalism.

4.2.3 Binary evolution

The description of binary evolution is the same as in Hurley et al. (2002), apart from several features of the common envelope (CE) phase.

To describe the CE phase, we adopt the $\alpha\lambda$ formalism (see Webbink, 1984; Ivanova et al., 2013), where α quantifies the energy available to unbind the envelope, and λ measures the concentration of the envelope. In our simulations, λ depends on the stellar type (i.e. mass and luminosity) to account for the contribution of recombinations. To compute λ we used the prescriptions derived by Claeys et al. (2014) (see their Appendix A for more details) which are based on Dewi and Tauris (2000).

In contrast, α is a free parameter. In this paper, we assume $\alpha = 1, 3$ and 5 (see Table 4.1).

With respect to Hurley et al. (2002), we have revised the treatment of Hertzsprung-gap (HG) donors in CE: HG donors are assumed to always merge with their companions if they enter a CE phase. This is justified by the fact that HG stars have not yet developed a steep density gradient between core and envelope, and allows us to match the merger rate of BHBs (Mapelli et al., 2017) inferred from LIGO-Virgo observations (Abbott et al., 2016d).

4.2.4 Simulations and initial distributions

Here we describe the initial conditions used to perform our population-synthesis simulations. We randomly draw the mass of the primary star (m_1) from a Kroupa initial mass function (IMF; Kroupa, 2001)

$$\mathfrak{F}(m_1) \propto m_1^{-2.3} \qquad \text{with } m_1 \in [5-150]\,{\rm M}_\odot\,. \tag{4.3}$$

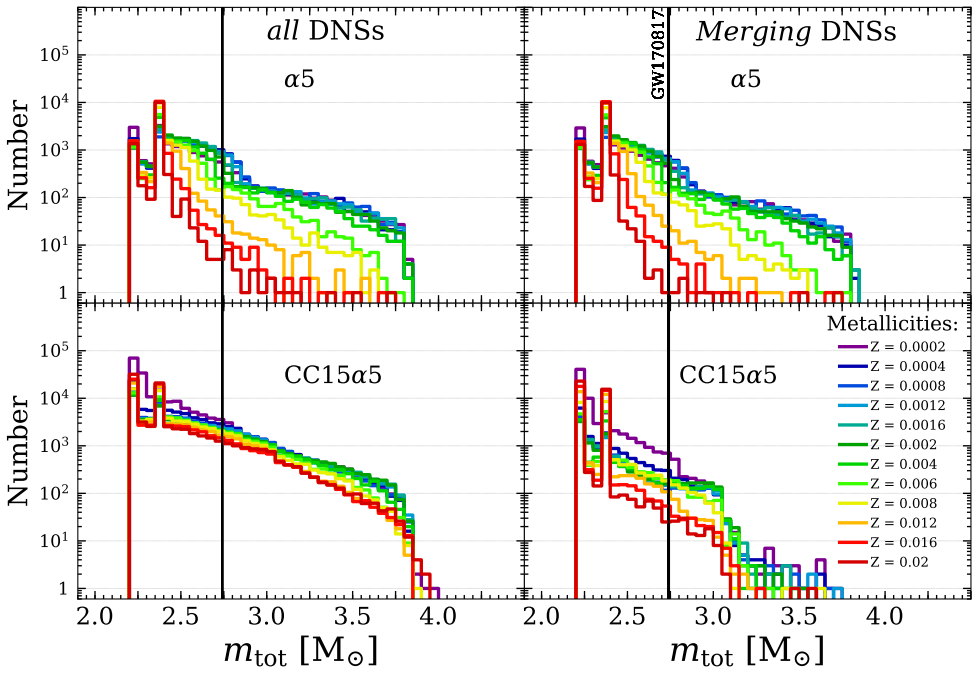

Figure 4.2: Distribution of total masses of DNSs in simulations $\alpha5$ (top panels) and CC15$\alpha5$ (bottom panels). Left-hand panels: all DNSs that formed in our simulations are shown. Right-hand panels: only DNSs merging in less than a Hubble time are shown. The vertical lines are the total mass of the GW event GW170817 (Abbott et al., 2016a). The bin width is 0.05 $M_\odot$.

The mass ratio between the secondary and the primary member of the binary $q = m_2/m_1$ is derived as Sana et al. (2012)

$$\mathfrak{F}(q) \propto q^{-0.1} \qquad \text{with} \quad q = \frac{m_2}{m_1} \in [0.1-1]\,. \tag{4.4}$$

The orbital period P and the eccentricity e are also extracted according to Sana et al., 2012:

$$\mathfrak{F}(P) \propto (P)^{-0.55} \text{ with } P = \log_{10}(P/\text{day}) \in [0.15-5.5] \tag{4.5}$$

and

$$\mathfrak{F}(e) \propto e^{-0.42} \qquad \text{with} \quad 0 \le e < 1. \tag{4.6}$$

We ran six sets of simulations (see Tab. 4.1), in order to test the effect of natal kicks and CE efficiency on the formation of double compact-object binaries (DNSs, BHNSs and BHBs). In particular, we assume three different values of the parameter of CE efficiency $\alpha = 1, 3$ and 5, and we draw iron core-collapse SN kicks from a Maxwellian distribution with 1D rms $\sigma_{\rm CCSN} = 15$ and 265 km s^{-1}.
For each set of simulations we considered 12 sub-sets with different metallicities $Z = 0.0002,\ 0.0004,\ 0.0008,\ 0.0012,\ 0.0016,\ 0.002,\ 0.004,\ 0.006,\ 0.008,\ 0.012,\ 0.016$

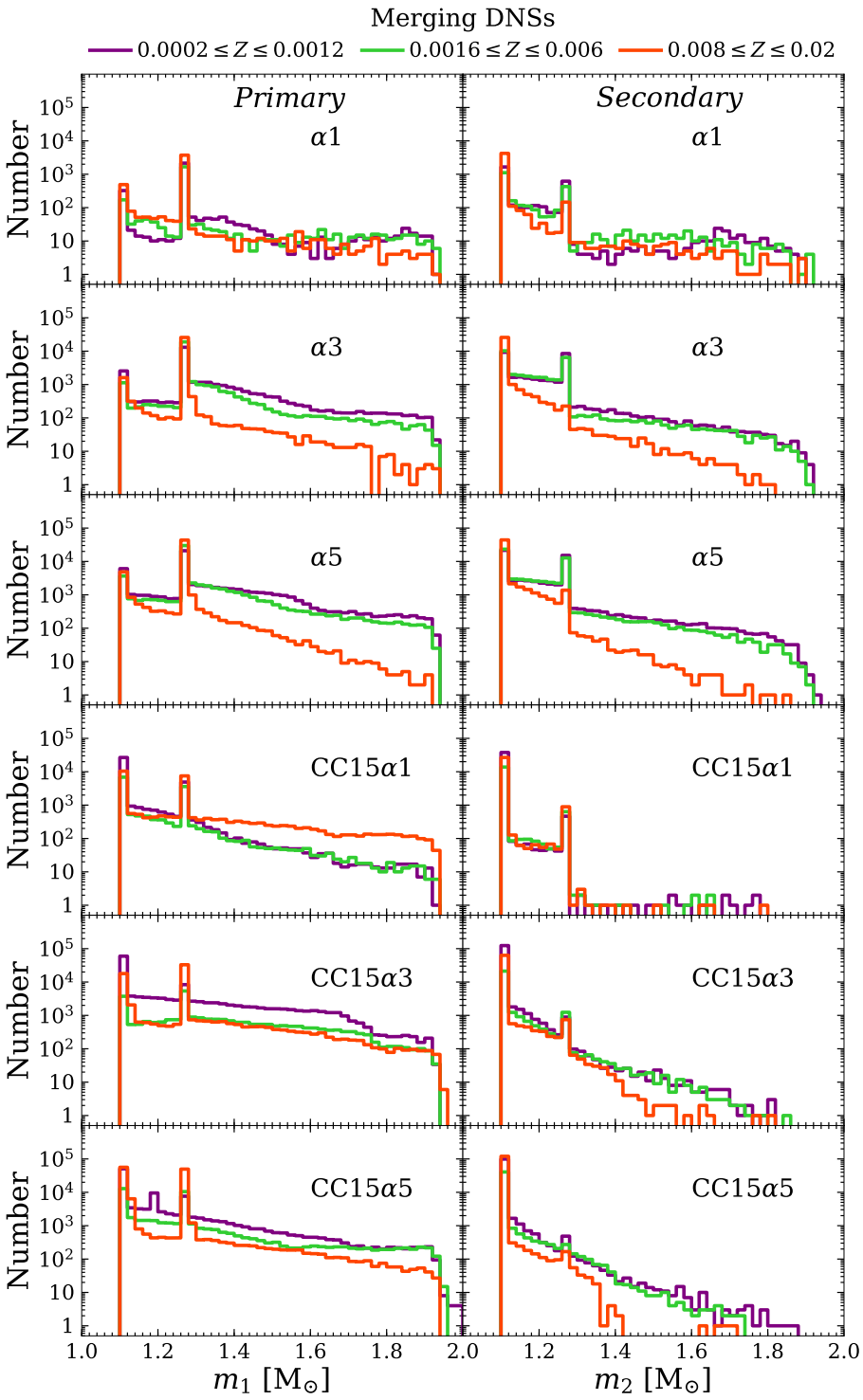

Figure 4.3: Primary masses (m_1, left-hand panels) and secondary masses (m_2, right-hand panels) of DNSs merging within a Hubble time in all simulations presented in this paper. Violet histogram: merging DNSs with metallicity $0.0002 \leq Z \leq 0.0012$; green histogram: merging DNSs with metallicity $0.0016 \leq Z \leq 0.006$; red histogram: merging DNSs with metallicity $0.008 \leq Z \leq 0.02$. The bin width for both m_1 and m_2 is 0.02 $M_\odot$.

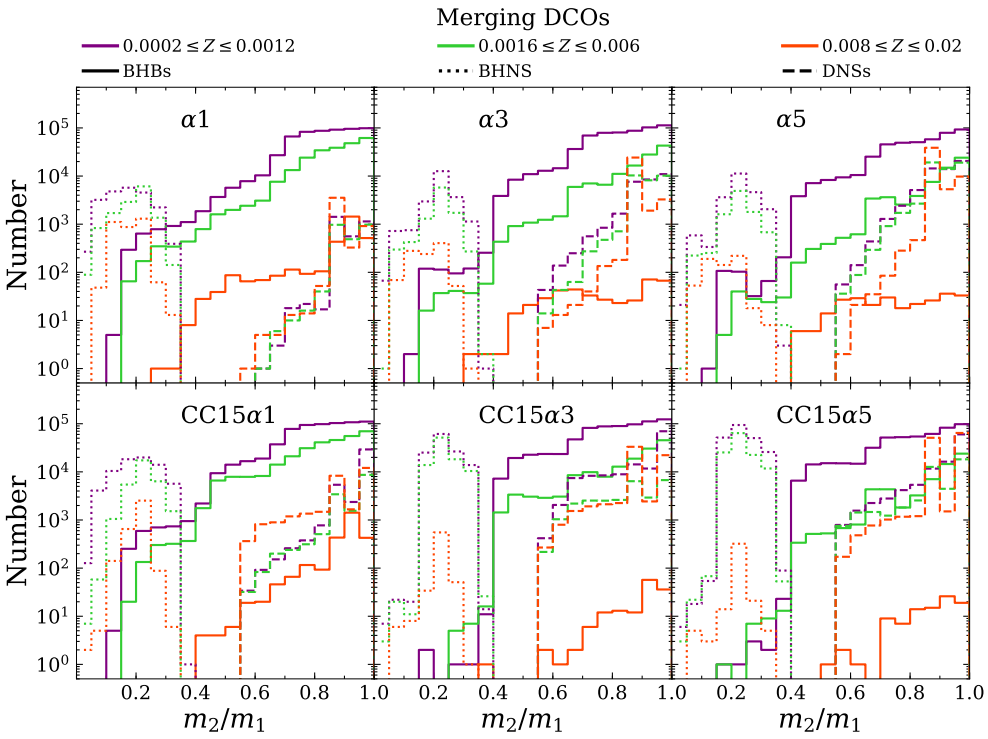

Figure 4.4: Mass ratio of the secondary to the primary member of merging double compact objects (DCOs) in all our simulations. Dashed lines: DNSs; dotted lines: BHNSs; solid lines: BHBs. Violet histogram: merging DCOs with metallicity $0.0002 \leq Z \leq 0.0012$; green histogram: merging DCOs with metallicity $0.0016 \leq Z \leq 0.006$; red histogram: merging DCOs with metallicity $0.008 \leq Z \leq 0.02$. The bin width is 0.05.

and 0.02. In each sub-set, we simulated 10^7 binary systems. Thus, each set of simulations is composed of 1.2×10^8 massive binaries.

4.3 Results

4.3.1 Masses and orbital properties of double neutron stars

Figure 4.2 shows the total mass of DNSs ($m_{\rm tot} = m_1 + m_2$, where m_1 and m_2 are the masses of the primary and of the secondary NS, respectively) in simulations $\alpha 5$ (with large core-collapse SN kicks) and CC15$\alpha 5$ (with low SN kicks). In particular, the left-hand panels show the mass distribution of all DNSs formed in our simulations $\alpha 5$ (top) and CC15$\alpha 5$ (bottom), while the right-hand panels show the mass distribution of DNSs merging within a Hubble time.

In simulation $\alpha 5$, most ($\sim 83-96$ per cent) DNSs merge within a Hubble time. The mass distribution of merging DNSs is not significantly different from the mass distribution of all DNSs. DNSs have a total mass ranging from 2.2 to ~ 4 $M_\odot$, but lower

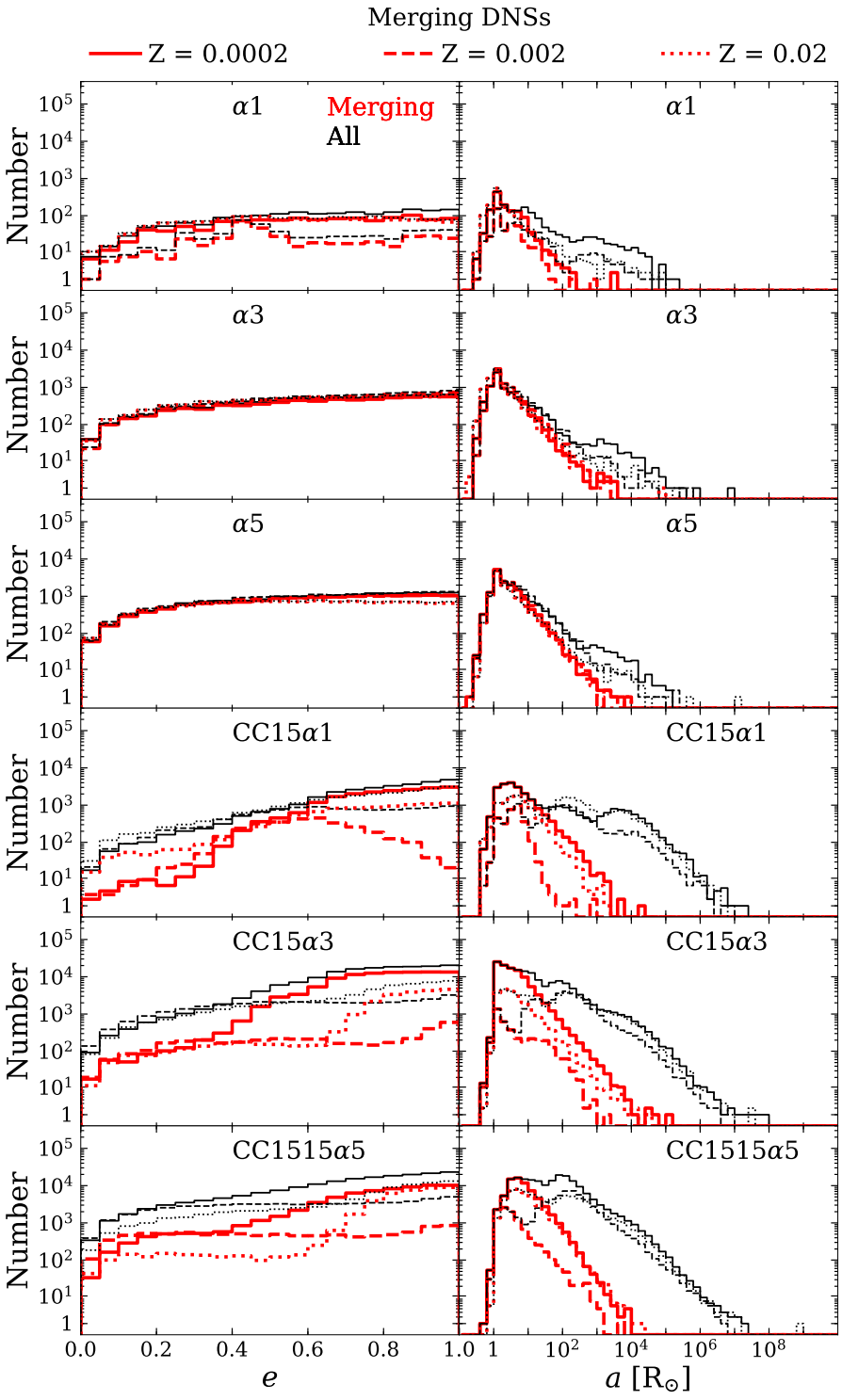

Figure 4.5: Eccentricity (left-hand panels) and semi-major axis (right-hand panels) of DNSs after the second SN explosion has led to the formation of the second NS (hereafter: initial eccentricity and initial semi-major axis). The bin width is 0.05 for the eccentricity and $\log(a/\mathrm{R}_\odot) = 0.2$ for the semi-major axis. All simulations are shown. Black thin lines: all simulated DNSs. Red thick lines: DNSs merging within a Hubble time. Solid lines: $Z = 0.0002$; dashed lines: $Z = 0.002$; dotted lines $Z = 0.02$.

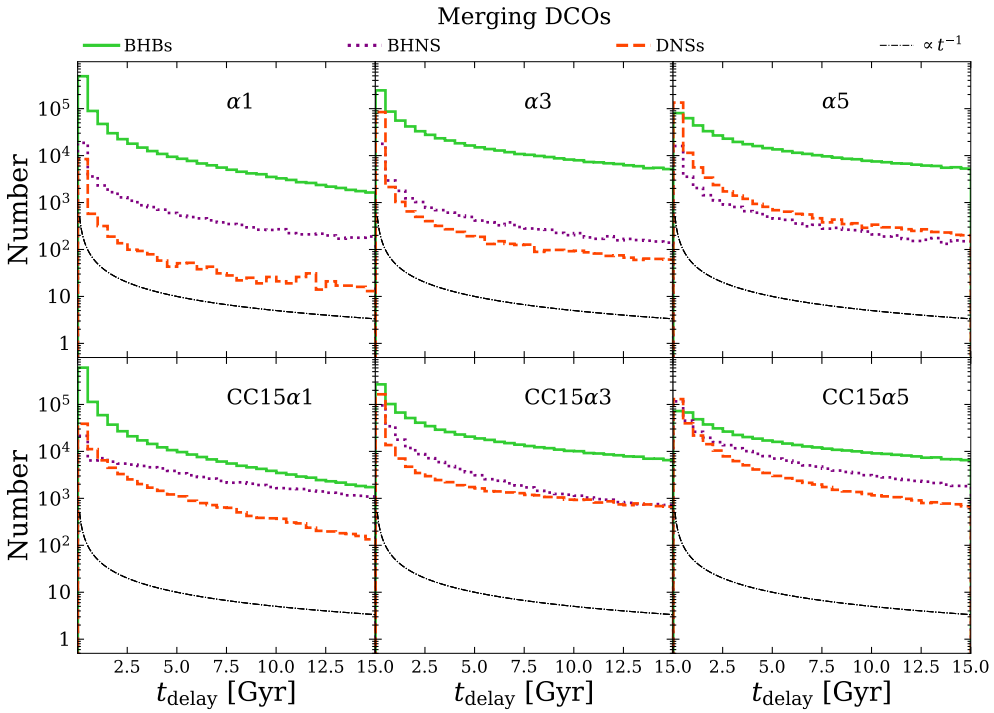

Figure 4.6: Delay time $t_{\rm delay}$ distribution for DNSs (dashed red line), BHNSs (dotted violet line) and BHBs (green solid line) for all simulation sets. We sum over different metallicities. Thin dot-dashed black line: $dN/dt \propto t^{-1}$. The bin width is 0.5 Gyr.

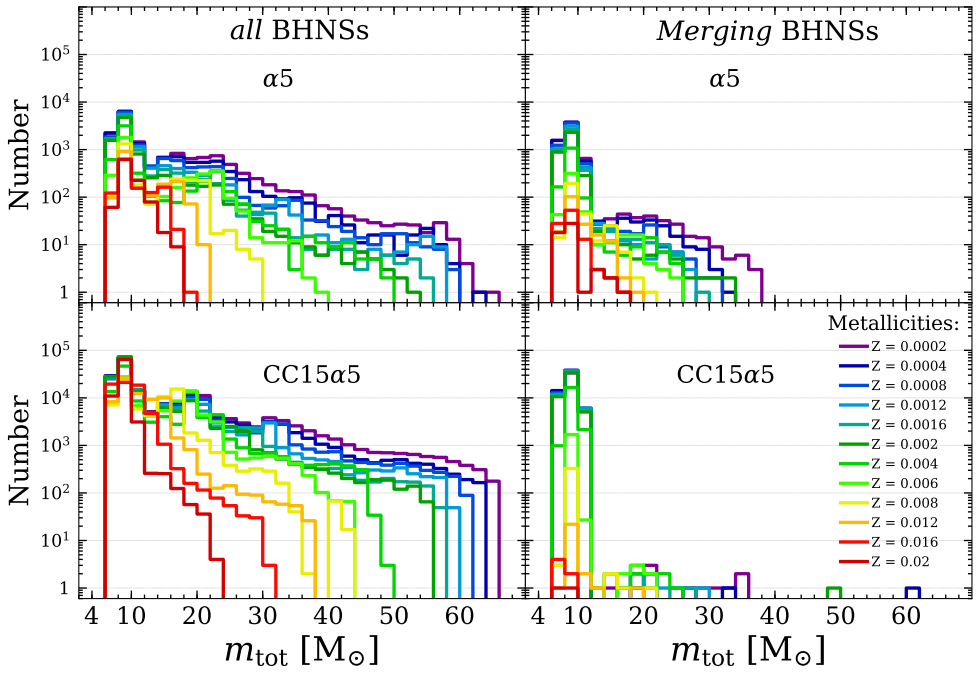

Figure 4.7: Same as Figure 4.2 but for BHNS systems. The bin width is 2 M$_\odot$.

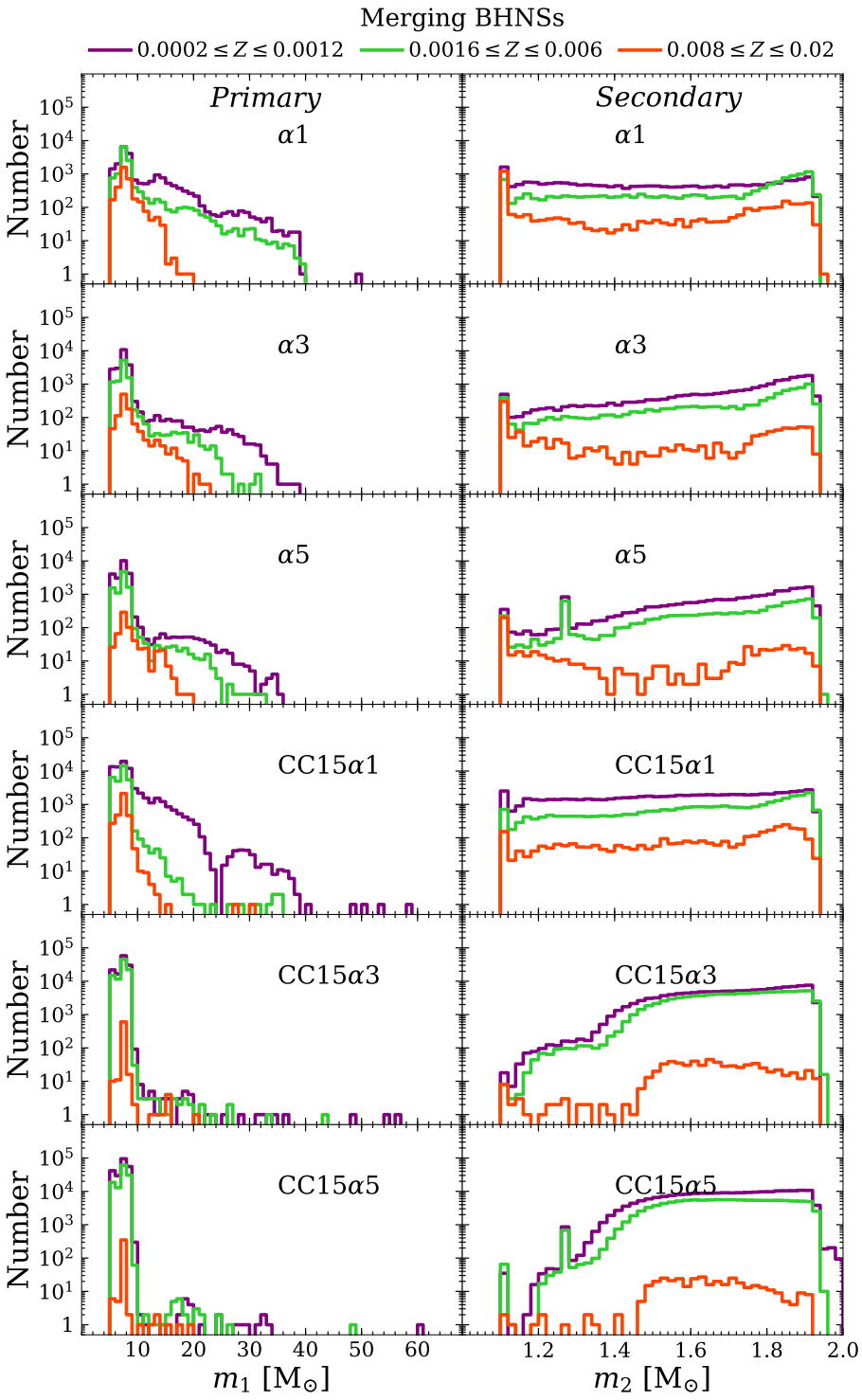

Figure 4.8: Same as Figure 4.3 but for BHNS systems. The bin width is 1 $M_\odot$ and 0.02 $M_\odot$ for m_1 and m_2, respectively.

masses ($m_{\rm tot} \lesssim 2.75$ M$_\odot$) are more common than large masses. The distributions have two peaks at $m_{\rm tot} \sim 2.2$ and 2.4 M$_\odot$, corresponding to the mergers of two NSs with mass $m_1 \sim m_2 \sim 1.1$ M$_\odot$ and $m_1 \sim 1.3$, $m_2 \sim 1.1$ M$_\odot$, respectively. These two favoured masses come from the adopted SN model. In particular, 1.1 M$_\odot$ is the minimum mass of a NS formed from a core-collapse SN according to the rapid SN model of Fryer et al. (2012), while ~ 1.26 M$_\odot$ is the minimum mass of a NS formed from an electron-capture SN according to Fryer et al. (2012). Larger masses are indicative of some amount of fallback, while mass accretion from a companion is mostly negligible (in agreement with e.g. Tauris et al., 2017). In simulation $\alpha5$, the mass distribution of both merging and all DNSs slightly depends on the metallicity of the progenitor star: lower metallicities tend to produce more massive NSs, because fallback is slightly more efficient.

In simulation CC15$\alpha5$ (representative of the simulations assuming a low natal kick for core-collapse SNe), the number of merging DNSs is significantly lower than the number of all DNSs: only 15−50 per cent of DNSs merge within a Hubble time. This happens because most systems survive the explosion of a core-collapse SN with such a low kick, including DNSs with large orbital separations, while in simulation $\alpha5$ only the closest systems (which are more likely to merge within a Hubble time) remain bound after the core-collapse SN explosion.

In simulation CC15$\alpha5$ there is also a clear difference between the mass range of all DNSs and the mass range of DNSs merging within a Hubble time: the former span from 2.2 to 4 M$_\odot$, while the latter range from 2.2 to 3.75 M$_\odot$ and very few merging DNSs have $m_{\rm tot} > 3.2$ M$_\odot$. Similar to $\alpha5$, low mass systems ($m_{\rm tot} \lesssim 2.75$ M$_\odot$) are more common and there are two peaks corresponding to $m_{\rm tot} \sim 2.2$ and 2.4 M$_\odot$. There is only a slight trend with the metallicity of the progenitor stars.

The total mass of GW170817 is also shown in Figure 4.2 (Abbott et al., 2016a). In our simulations we form a large number of systems with mass consistent with GW170817. The number of systems in the mass bin consistent with the total mass of GW170817 is ($\sim 2-10$) $\sim 5-20$ per cent the number of (merging) systems in the peak of the distribution.

Figure 4.3 shows the mass of the primary and the mass of the secondary member of DNSs which merge within a Hubble time, for all simulations considered in this paper. For primary (secondary) we mean the most (least) massive member of the binary. This is independent of which NS forms first.

For each simulation, we gather different metallicities into three groups: $0.0002 \leq Z \leq 0.0012$, $0.0016 \leq Z \leq 0.006$, $0.008 \leq Z \leq 0.02$. In all cases we clearly see the two peaks at ~ 1.1 M$_\odot$ (minimum mass of NSs formed from iron core-collapse SNe

in the rapid model) and ~ 1.26 $M_\odot$ (minimum mass of NSs formed from electron-capture SNe) for both the primary and the secondary NS. There is a weak trend with metallicity in simulations with large α ($\alpha3$, $\alpha5$, CC15$\alpha3$ and CC15$\alpha5$), while simulations with $\alpha = 1$ ($\alpha1$ and CC15$\alpha1$) show a more uncertain behavior.
Primary masses span from ~ 1.1 to ~ 2.0 $M_\odot$ in all simulations. As for the secondary masses, there is a clear difference between simulations with large core-collapse SN kicks ($\alpha1$, $\alpha3$ and $\alpha5$) and simulations with low core-collapse SN kicks (CC15$\alpha1$, CC15$\alpha3$ and CC15$\alpha5$). In the latter simulations, the secondary NSs have generally lower mass than in the former ones. The main reason is that lower mass NSs in our simulations form mostly from iron core-collapse SNe, while high mass NSs form mainly from electron-capture SNe. If the core-collapse SN kicks are lower, the majority of merging secondary NSs forms through core-collapse SNe.
Figure 4.4 shows the ratio of the secondary to the primary NS mass (dashed lines) for merging DNSs in our simulations. The mass ratio of merging DNSs is always > 0.5.
Figure 4.5 shows the eccentricity (e) and the semi-major axis (a) of DNSs after the second SN has taken place, i.e. as soon as the simulated system has become a DNS. While these quantities are hardly comparable to any observations, they are useful, on a theoretical ground, to understand the formation pathways of double compact objects. From Figure 4.5 we see that DNSs form with relatively large initial eccentricities (with respect to BHNSs and BHBs), as an effect of the natal kick. As we could expect, most merging DNSs have small ($< 10^3$ $R_\odot$) semi-major axis after the second SN explosion. There is a clear difference between the runs with low SN kicks and those with high SN kicks: in the former a high number of NSs have very large semi-major axes ($10^2 - 10^8$ $R_\odot$) and do not merge unless they have extreme eccentricity. This explains why much less than 50 per cent of all DNSs merge in the simulations with low core-collapse SN kicks.
Finally, Figure 4.6 shows the distribution of the delay time $t_{\rm delay}$ (i.e. the time elapsed from the formation of the progenitor binary to the merger of the two compact objects). Previous studies (Belczynski et al., 2016b; Lamberts et al., 2016; Mapelli et al., 2017) indicate that the distribution of delay times should approximately scale as t^{-1}. Overall, this trend $dN/dt \propto t^{-1}$ is confirmed in our simulations, but we notice also a slight dependence of $t_{\rm delay}$ distribution on α and on the natal kicks.

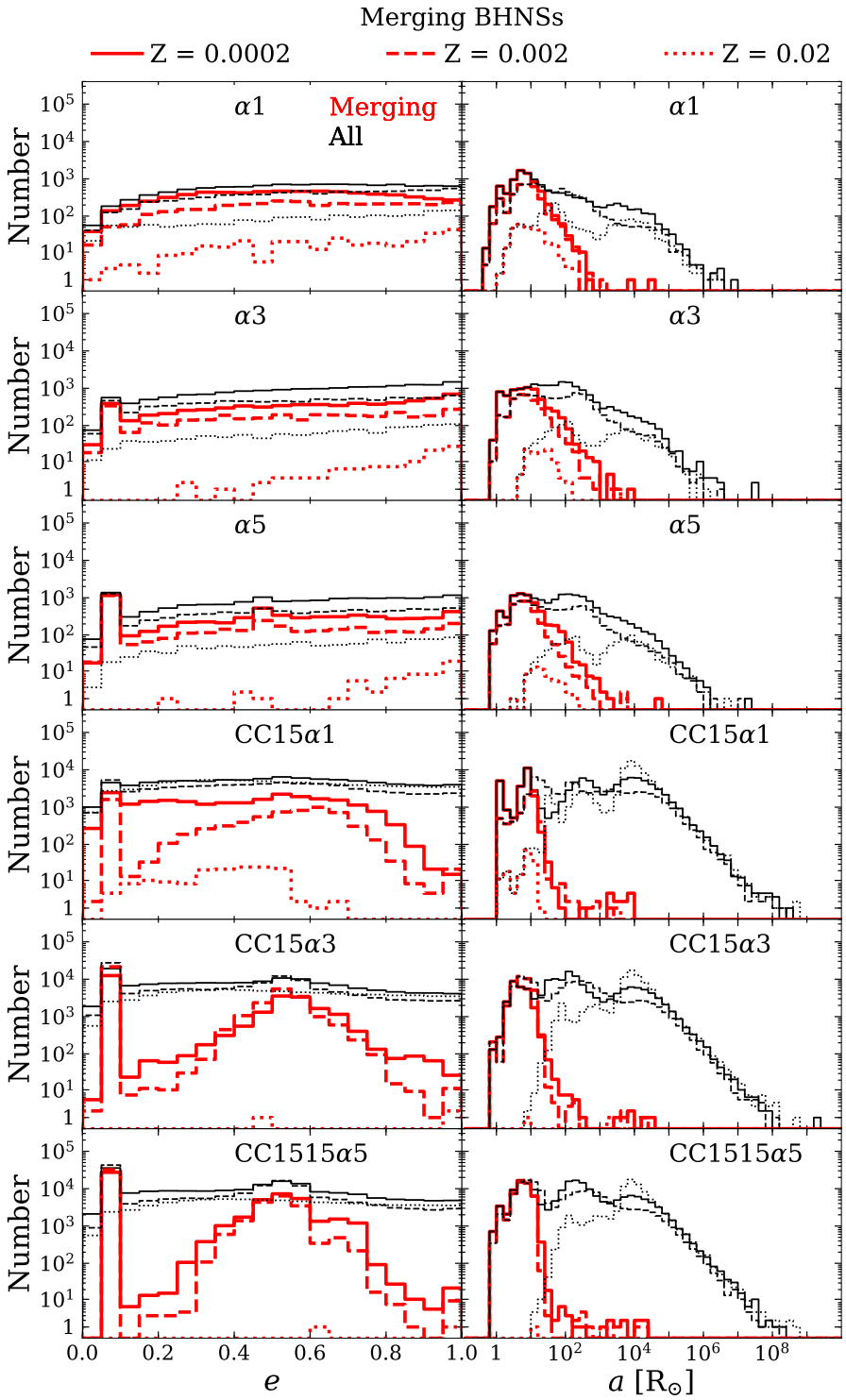

Figure 4.9: Same as Figure 4.5 but for BHNS systems.

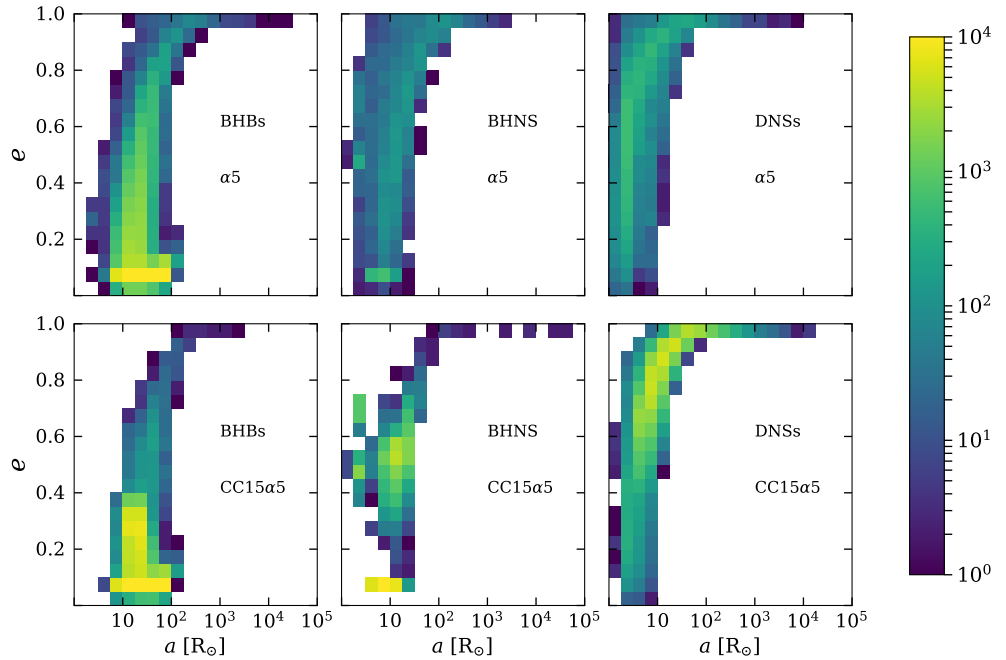

Figure 4.10: Initial semi-major axis versus initial eccentricity of merging DCOs (BHBs, BHNSs and DNSs). The logarithmic colour-coded map indicates the number of merging systems. Top (bottom) panels show simulations with $\alpha = 5$ and high-velocity (low-velocity) core-collapse SN kicks. From left to right: BHBs, BHNSs and DNSs. The bin width is 0.05 for the eccentricity and $\log(a/R_\odot) = 0.5$ for the semi-major axis.

4.3.2 Masses and orbital properties of BHNSs

Figure 4.7 shows the total mass distribution of BHNSs in simulations $\alpha5$ and CC15$\alpha5$. If we consider all BHNSs formed in our simulations (left-hand panels), the total masses of BHNSs span from ~ 6 to ~ 66 $M_\odot$ in both $\alpha5$ and CC15$\alpha5$, although the distributions peak at relatively low masses ($\sim 6-14$ $M_\odot$). There is a clear trend with metallicity for both $\alpha5$ and CC15$\alpha5$, which is essentially due to the dependence of BH masses on stellar winds (see e.g. Giacobbo et al., 2018).

If we consider only those BHNSs which merge within a Hubble time (right-hand panels), we find that low-mass BHNSs are more likely to merge than high-mass BHNSs. In the case $\alpha5$, the maximum total mass of merging BHNSs is $\lesssim 40$ $M_\odot$ and the most common systems have mass $\sim 6-12$ $M_\odot$. In the case CC15$\alpha5$ the situation is even more extreme: almost all merging BHNSs have mass $\sim 6-12$ $M_\odot$ and only few systems have larger mass (up to ~ 60 $M_\odot$). The behaviour of BHNS total mass distributions in the other simulations is intermediate between that of $\alpha5$ and that of CC15$\alpha5$.

Figure 4.8 shows the mass distribution of the BH (left-hand panels) and of the NS (right-hand panels) for BHNSs merging within a Hubble time. From this Figure, we

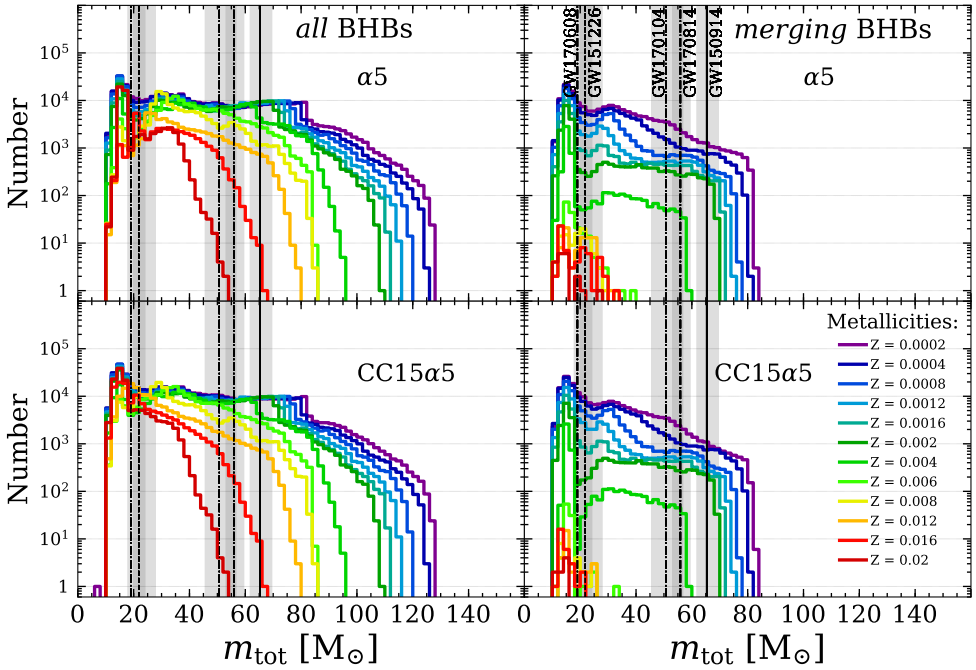

Figure 4.11: Same as Figure 4.2 but for BHBs. The vertical lines are the median values of the total masses of the GW events and their 90 per cent credible intervals: GW150914, GW151226 (Abbott et al., 2016d), GW170104 (Abbott et al., 2017b), GW170608 (Abbott et al., 2017e) and GW170814 (Abbott et al., 2017d). The bin width is 2 M$_\odot$. Note that the distribution of the observed masses will favor higher value of the mass because of observation selection effects.

see that the simulations CC15α3 and CC15α5 are the most extreme cases: most of the BHs in merging BHNSs have mass < 15 M$_\odot$ and most of the NSs have mass $\gtrsim$ 1.3 M$_\odot$.

Even in the other simulations (α1, α3, α5 and CC15α1), the NS mass distribution in the case of BHNSs is skewed toward significantly higher values than in the case of merging DNSs. In all simulations we see a trend with metallicity: more merging BHNSs form from metal-poor progenitors than from metal-rich ones.

Figure 4.4 shows that the ratio between the NS mass and the BH mass in merging BHNSs is always $q \lesssim 0.4$ ($q = 0.4$ is the maximum possible value by construction, because the maximum possible mass of a NS is ~ 2 M$_\odot$ and the minimum possible mass of a BH is ~ 5 M$_\odot$, according to the rapid core-collapse SN model by Fryer et al. (2012)), while the most likely value is ≈ 0.2.

Finally, Figure 4.9 shows the eccentricity and the semi-major axis of the simulated BHNSs just after both compact objects have formed (hereafter: initial eccentricity and initial semi-major axis). The initial semi-major axes of merging BHNSs are $\lesssim 10^3$ R$_\odot$, as in the case of DNSs. We also note that in the three simulations with low core-collapse SN kicks (CC15α1, CC15α3 and CC15α5) merging BHNSs have

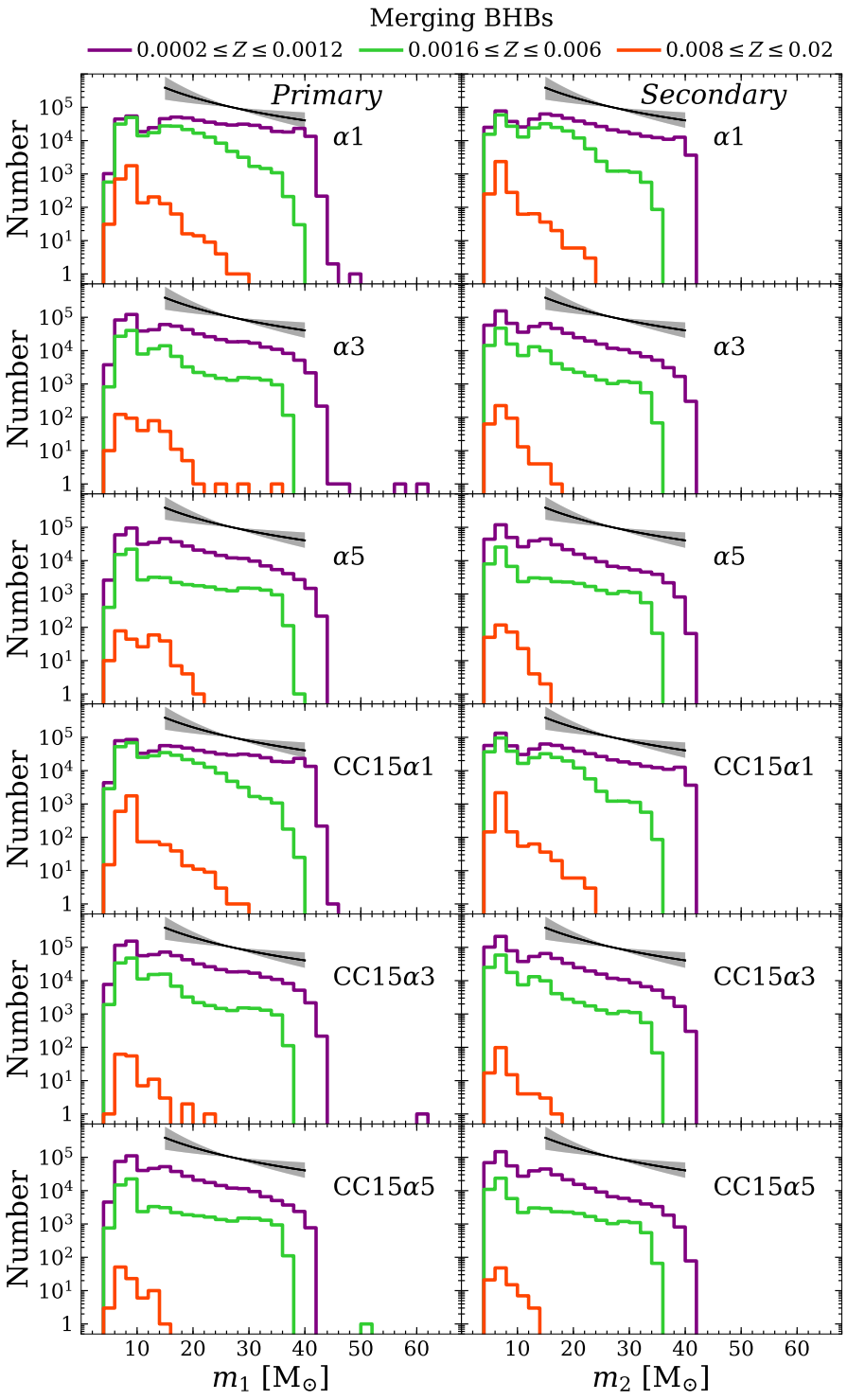

Figure 4.12: Same as Figure 4.3 but for BHBs. The black line in each panel represents the power-law index inferred from the mass distribution of GW events observed in O1 plus GW170104 ($2.3^{+1.3}_{-1.4}$, Abbott et al., 2017b) and the shadowed region is the corresponding 90 per cent credible interval. The bin width is 2 $M_\odot$ for both m_1 and m_2.

significantly smaller initial semi-major axes ($\lesssim 10^2$ R$_\odot$) than in the other runs. This can be explained if we look also at the distribution of initial eccentricities.

The initial eccentricities of merging BHNSs in the simulations with low core-collapse SN kicks have two main peaks: a sharp peak at $e \sim 0$ and a broad peak at $e \sim 0.5$.

The sharp peak with $e = 0$ is produced by BHNSs in which the BH forms after the NS and is born by direct collapse. In this case the BH is assigned low or no natal kick (Fryer et al., 2012) and the binary, which has circularized during previous evolution, remains circular.

In contrast, the broad peak at $e \sim 0.5$ is populated mostly by BHNSs in which the BH forms before the NS. This peak originates from the combination of two effects. First, there are very few BHNSs with semi-major axis $\lesssim 10^3$ R$_\odot$ and eccentricity $e \gg 0.5$ (as we can see from Figure 4.10), because the SN kick is not strong enough to produce large eccentricities in close BHNSs. If we had a number of such highly eccentric systems with small semi-major axis, they would merge within a Hubble time, but we do not have them because of the low kicks.

Second, we have several systems with semi-major axis $\lesssim 10^3$ R$_\odot$ and eccentricity $e \ll 0.5$, but they are expected to merge in a timescale longer than the Hubble time. In fact, we can estimate the merger timescale by GW decay as (Peters, 1964)

$$t_{\rm GW} = \frac{5}{256}\frac{c^5}{G^3}\frac{a^4\,(1-e^2)^{7/2}}{m_1\,m_2\,(m_1+m_2)}, \tag{4.7}$$

where c is the light speed, G the gravity constant, a the binary semi-major axis, e the orbital eccentricity, m_1 the mass of the primary and m_2 the mass of the secondary. If we substitute $m_1 = 7$ M$_\odot$, $m_2 = 1.5$ M$_\odot$ (which are typical values for our BHNSs, see e.g. Fig. 4.8) and $a = 10$ R$_\odot$ (which is a very close semi-major axis) into equation 4.7, we obtain $t_{\rm GW} \sim 6.2$, 17 Gyr for $e = 0.5$ and 0.0, respectively.

The combination of these two effects produces the broad peak centred at $e \sim 0.5$.

In simulations $\alpha1$, $\alpha3$ and $\alpha5$ we see no peak at $e \sim 0.5$, but rather the eccentricities are skewed toward higher values, because the second compact object forms with a higher natal kick, which can unbind the binary or make it very eccentric.

4.3.3 Masses and orbital properties of BHBs

Figure 4.11 shows the total mass distribution of BHBs in simulations $\alpha5$ (top) and CC15$\alpha5$ (bottom) for all simulated BHBs (left) and only for BHBs merging within a Hubble time (right). This is analogous to Figure 8 of Giacobbo et al. (2018) but here we consider a significantly different model of core-collapse SN, different kick

distributions, and a different value of α. The main results of Giacobbo et al. (2018) still hold also for this model: if we consider all BHBs formed in our simulations (left-hand panels of Figure 4.11), the maximum total mass[1] is ~ 130 M$_\odot$.
In contrast, if we look at the total mass of BHBs merging within a Hubble time (right-hand panels of Figure 4.11), we find that the most massive merging BHBs have $m_{\rm tot} \sim 80-90$ M$_\odot$. The reason why our most massive BHB systems do not merge in a Hubble time is that they come from the evolution of stars which develop large radii during their super-giant phase: if the initial orbital separation of these massive progenitors is large ($\gtrsim 10^3$ R$_\odot$), they evolve into very massive BHBs which do not merge in a Hubble time. In contrast, if their initial orbital separation is relatively small, the massive progenitors either merge before becoming BHs, or undergo non-conservative mass transfer episodes leading to strong mass loss and to the formation of two smaller BHs. On the other hand, dynamical evolution in star clusters might accelerate the merger of the most massive BHBs which form in our simulations, by means of three-body encounters and exchanges Mapelli, 2016.
As in Giacobbo et al. (2018), we confirm that there is a strong dependence on metallicity. Not only does the maximum mass of BHBs strongly depend on the progenitor's metallicity, but also the number of BHBs, especially if we look at systems merging in less than a Hubble time. This strong dependence is an effect of stellar evolution: (i) metal-poor stars tend to produce more massive BHs because they lose less mass by stellar winds (Mapelli et al., 2009; Mapelli et al., 2010; Belczynski et al., 2010; Mapelli et al., 2013; Spera et al., 2015), while (ii) metal-rich stars tend to develop larger radii than metal-poor ones and thus are more likely to merge before becoming BHBs; hence, the number of BHBs formed from metal-poor progenitors is larger than that of BHBs formed from metal-rich ones.
We find no significant differences between the simulation $\alpha5$ and CC15$\alpha5$, because most BHBs get a low natal kick in all our models, given our assumption that the kick is modulated by the amount of fallback (see e.g. Giacobbo et al., 2018).
Figure 4.12 shows the mass of the primary (i.e. the more massive) and the secondary (i.e. the less massive) BH in BHBs merging within a Hubble time for all simulations discussed in this paper. In all cases, we see a clear trend with metallicity, in terms of both maximum BH mass and number of merging BHBs. Especially at low metallicity ($0.0002 \leq Z \leq 0.0012$), the mass distribution is broadly consistent

[1] There is a typo in the $x-$axis label of Figure 8 of Giacobbo et al. (2018). The most massive BHBs in this figure have $m_{\rm tot} \sim 130$ M$_\odot$, although from the labels of this Figure it may seem that they have $m_{\rm tot} \sim 150$ M$_\odot$.

with a power law with slope ≈ 2.3, in good agreement with the one inferred from GW events (Abbott et al., 2016d).
Figure 4.4 confirms that merging BHBs in our simulations have preferentially a large mass ratio, but systems with any possible mass ratio down to $m_2/m_1 \sim 0.1$ can form, consistent with Giacobbo et al. (2018).
Finally, Figure 4.13 shows the initial eccentricity distribution of BHBs. Most BHBs have relatively low eccentricity, because SN kicks are assumed to be low, depending on the fallback. The initial semi-major axis of merging BHs is generally $\lesssim 10^2$ $R_\odot$, with a tail of eccentric systems merging with initial semi-major axis up to $\sim 10^4$ $R_\odot$. Another interesting feature of merging BHBs is the dependence of $t_{\rm delay}$ on the value of α (Figure 4.6): the number of systems with short delay time increases significantly for a smaller value of α. Small values of α correspond to a more efficient shrinking of the binary system during CE, resulting in a faster merger. This effect appears to be particularly important for BHBs.

4.3.4 Mergers per unit stellar mass

For each set of simulations, we compute the number of merging double compact objects (DCOs) per unit mass $\mathcal{N}_{\rm cor}$ in the same way as described in our previous work (see Mapelli et al., 2017; Giacobbo et al., 2018):

$$\mathcal{N}_{\rm cor,i} = {\rm f_{bin}}\,{\rm f_{IMF}}\,\frac{N_{\rm merger,i}}{M_{\rm tot,sim}} \qquad i \in [{\rm DNS, BHNS, BHB}], \tag{4.8}$$

where $N_{\rm merger,i}$ is the number of merging DCOs (DNS, BHNS or BHBs); $M_{\rm tot,sim}$ is the total initial mass of the simulated stellar population; $\rm f_{bin}$ is the correction factor used to take into account the fact that we only simulate binary systems (we assume that 50 per cent of the stars are in binaries $f_{\rm bin} = 0.5$ Sana et al., 2013); $\rm f_{IMF} = 0.285$ corrects for the fact that we have simulated only systems which have the primary component more massive than $5\,M_\odot$.
Figure 4.14 shows $\mathcal{N}_{\rm cor}$ as a function of the metallicity Z for all the simulations and separately for each type of DCO: DNSs, BHNSs and BHBs. In Giacobbo et al. (2018) we have already shown a similar figure for BHBs, but here we consider different SN prescriptions, CE parameters and SN kicks.
The number of mergers per unit mass spans a large range of values for both DNSs, BHNSs and BHBs, depending on natal kicks, on CE efficiency and on progenitor's metallicity.

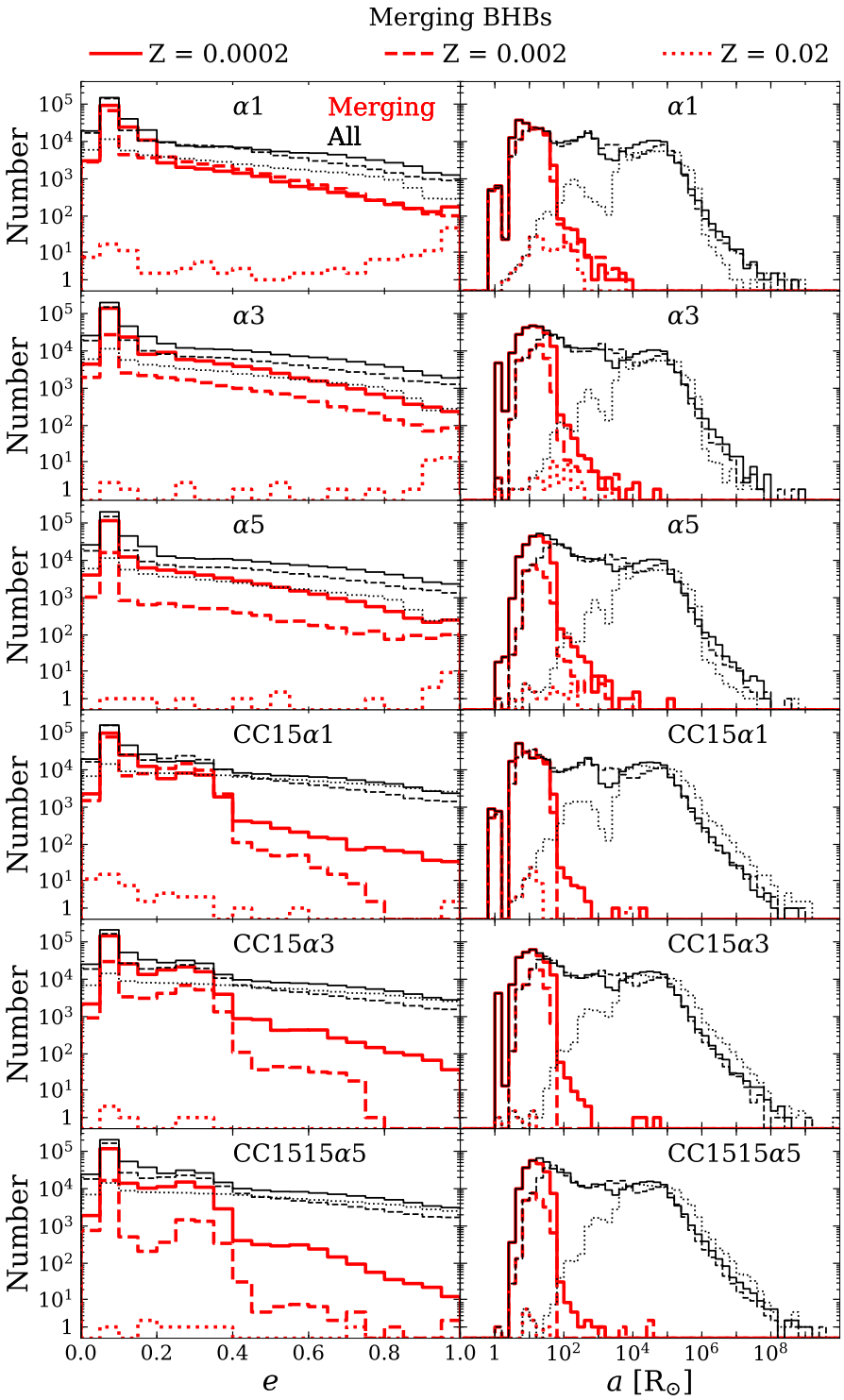

Figure 4.13: Same as Figure 4.5 but for BHBs.

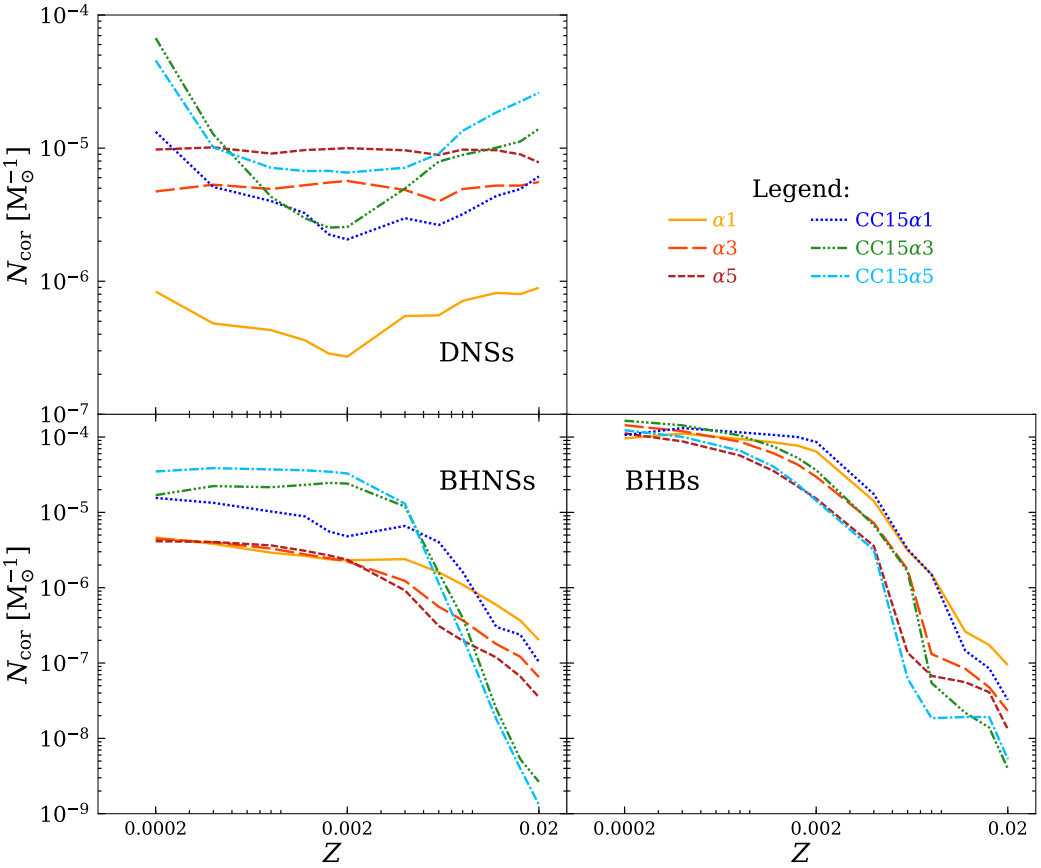

Figure 4.14: Number of merging DCOs per unit mass (N_{cor}) as a function of progenitor's metallicity for all our simulations (see Table 4.1). Top-left panel: merging DNSs; bottom-left panel: BHNS; bottom-right panel: BHBs.

N_{cor} strongly depends on progenitor's metallicity for both BHBs and BHNSs. In particular, $N_{cor,BHB}$ ($N_{cor,BHNS}$) is $\gtrsim 3$ ($\gtrsim 2$) orders of magnitude higher at low metallicity than at high metallicity.

In contrast, the number of DNS mergers per unit mass $N_{cor,DNS}$ is almost insensitive to progenitor's metallicity in runs $\alpha 3$ and $\alpha 5$. In the other simulations ($\alpha 1$, CC15$\alpha 1$, CC15$\alpha 3$ and CC15$\alpha 5$) $N_{cor,DNS}$ is significantly lower for progenitor metallicity $Z \sim 0.002$ than for progenitors with higher or lower metallicity. This happens because stellar radii in the HG and giant phase tend to reach larger values at $Z \sim 0.002$ than at other metallicities in MOBSE. When SN kicks are low or inspiral by CE is particularly efficient (i.e. $\alpha \leq 1$), a larger number of binaries merge before forming a DNS if the stellar radii are larger. For the same reason, $N_{cor,DNS}$ is larger if α is larger (i.e. if CE is less efficient in merging binaries prematurely).

Table 4.2: Local merger rate density.

ID	Method	$R_{\rm loc,DNS}$ ($\rm Gpc^{-3}\ yr^{-1}$)	$R_{\rm loc,BHNS}$ ($\rm Gpc^{-3}\ yr^{-1}$)	$R_{\rm loc,BHB}$ ($\rm Gpc^{-3}\ yr^{-1}$)
	$Z = 0.02$	1.3×10^{1}	5.7×10^{0}	3.6×10^{0}
	$Z = 0.002$	6.0×10^{0}	5.5×10^{1}	1.8×10^{3}
$\alpha1$	$Z = 0.0002$	1.5×10^{1}	9.5×10^{1}	1.4×10^{3}
	$Model\ 1$	1.0×10^{1}	5.3×10^{1}	1.0×10^{3}
	$Model\ 2$	1.4×10^{1}	1.3×10^{1}	4.3×10^{1}
	$Z = 0.02$	8.6×10^{1}	2.5×10^{0}	9.4×10^{-1}
	$Z = 0.002$	9.1×10^{1}	5.5×10^{1}	1.2×10^{3}
$\alpha3$	$Z = 0.0002$	7.7×10^{1}	9.1×10^{1}	3.7×10^{3}
	$Model\ 1$	8.1×10^{1}	4.3×10^{1}	1.1×10^{3}
	$Model\ 2$	8.7×10^{1}	7.0×10^{0}	7.4×10^{1}
	$Z = 0.02$	1.3×10^{2}	9.9×10^{-1}	2.6×10^{-1}
	$Z = 0.002$	1.9×10^{2}	5.7×10^{1}	6.1×10^{2}
$\alpha5$	$Z = 0.0002$	1.8×10^{2}	9.5×10^{1}	3.6×10^{3}
	$Model\ 1$	1.8×10^{2}	4.2×10^{1}	6.4×10^{2}
	$Model\ 2$	1.3×10^{2}	5.0×10^{0}	5.0×10^{1}
	$Z = 0.02$	1.4×10^{2}	4.2×10^{0}	1.5×10^{0}
	$Z = 0.002$	7.8×10^{1}	2.0×10^{2}	2.3×10^{3}
CC15$\alpha1$	$Z = 0.0002$	2.2×10^{2}	3.7×10^{2}	1.5×10^{3}
	$Model\ 1$	9.1×10^{1}	2.5×10^{2}	1.2×10^{3}
	$Model\ 2$	1.1×10^{2}	4.7×10^{1}	4.5×10^{1}
	$Z = 0.02$	2.4×10^{2}	3.3×10^{-2}	1.3×10^{-1}
	$Z = 0.002$	5.9×10^{1}	6.7×10^{2}	1.7×10^{3}
CC15$\alpha3$	$Z = 0.0002$	1.3×10^{3}	3.3×10^{2}	4.3×10^{3}
	$Model\ 1$	9.4×10^{1}	4.5×10^{2}	1.5×10^{3}
	$Model\ 2$	2.7×10^{2}	1.6×10^{1}	8.6×10^{1}
	$Z = 0.02$	5.5×10^{2}	3.9×10^{-3}	1.8×10^{-1}
	$Z = 0.002$	1.4×10^{2}	1.0×10^{3}	6.0×10^{2}
CC15$\alpha5$	$Z = 0.0002$	1.2×10^{3}	8.6×10^{2}	4.1×10^{3}
	$Model\ 1$	1.5×10^{2}	7.8×10^{2}	7.2×10^{2}
	$Model\ 2$	5.1×10^{2}	3.5×10^{1}	5.6×10^{1}

Column 1: simulation's name; column 2: method (single metallicity, Z, or evolution of metallicity: $model\ 1$ and $model\ 2$); columns 3, 4 and 5: local merger rate density of DNSs, BHNSs and BHBs.

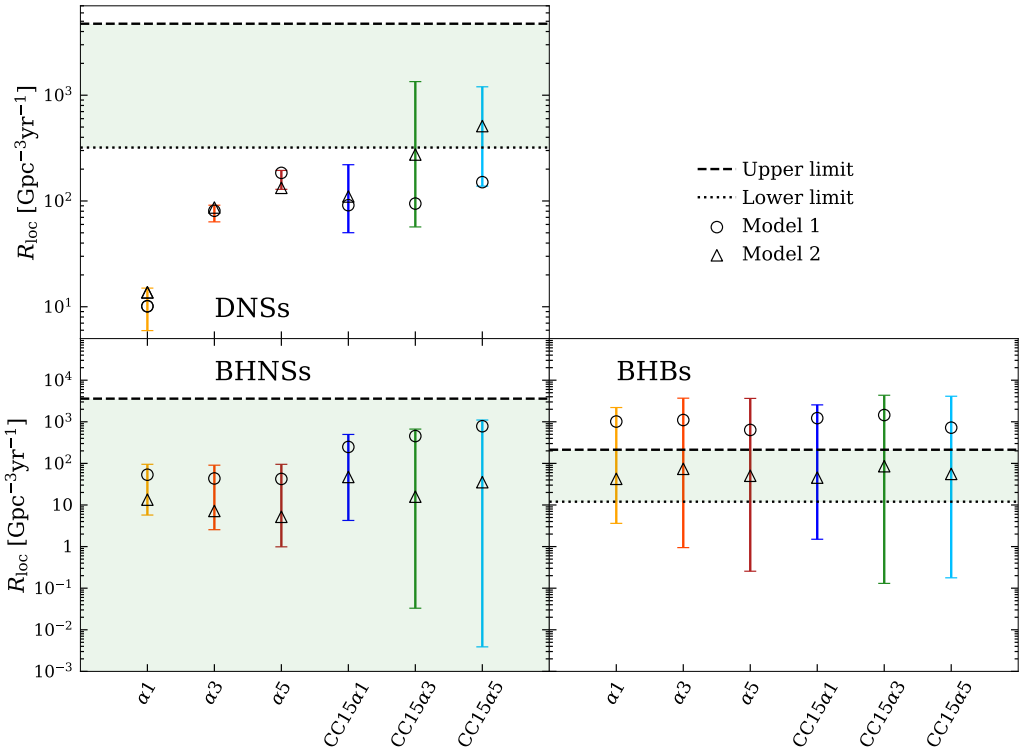

Figure 4.15: Local merger rate density $R_{\rm loc}$ calculated from equation 4.10 for each simulation. Top-left: local merger rate density for DNSs. Bottom-left: local merger rate density for BHNSs. Bottom-right: local merger rate density for BHBs. The error bars show the maximum difference between estimates of $R_{\rm loc}$ for different metallicities. Open circles (open triangles) are $R_{\rm loc}$ obtained assuming *model* 1 (*model* 2) for the cosmic evolution of metallicity. Green shaded areas: local merger rate density inferred from LIGO-Virgo observations (from Abbott et al., 2016a, Abbott et al., 2016e and Abbott et al., 2017b for DNSs, BHNSs and BHBs, respectively).

4.3.5 Merger rate density

We developed a simple procedure to estimate the merger rate per unit volume and unit time in the local Universe, based on the number of mergers per unit mass.
First, we consider the cosmic star formation rate (SFR) density adopting the fit by Madau and Dickinson (2014),

$$\mathrm{SFR}(z) = 0.015\frac{(1+z)^{2.7}}{1+[(1+z)/2.9]^{5.6}}\ \ \mathrm{M_{\odot}Mpc^{-3}yr^{-1}}. \tag{4.9}$$

We use equation 4.9 to compute the SFR at different redshifts, from $z = 15$ to $z = 0.0$ with a step $\Delta z = 0.1$.
Then, we calculate the total mass of stars formed within a specific redshift bin, assuming that the SFR is constant in each bin of redshift. The total mass of stars formed in the bin is multiplied by $N_{\rm cor,BHB}$, $N_{\rm cor,BHNS}$ and $N_{\rm cor,DNS}$ in order to obtain the total number of merging BHBs, BHNSs and DNSs formed in each redshift bin

per unit volume. We repeat these operations for all bins of redshift and for each bin we take only the fraction of merging systems which have a delay time (Figure 4.6) such that they merge in the local Universe (namely, $z \in [0, 0.1]$). By summing them up, we obtain the total number of mergers occurring at $z \leq 0.1$ per unit volume[2]. Finally, we divide the result by the look-back time corresponding to $z = 0.1$. The following formula summarizes the aforementioned procedure:

$$\mathcal{R}_{\rm loc,i} = \frac{1}{t_{\rm lb}(z=0.1)} \sum_{z=15}^{0.1} f_{\rm loc}(z)\ {\rm SFR}(z)\ [t_{\rm lb}(z+\Delta z) - t_{\rm lb}(z)]\ , \tag{4.10}$$

where $\mathcal{R}_{\rm loc,i}$ is the local merger rate per unit volume and unit time, i can be either BHB, BHNS or DNS, $t_{\rm lb}(z)$ is the look-back time and $f_{\rm loc}(z)$ is the fraction of merging systems formed at a given redshift z which merge in the local Universe ($z \leq 0.1$) per unit mass. We calculate $f_{\rm loc}(z) = \mathcal{N}_{\rm cor,i}(z_{\rm form} = z, z_{\rm merg} \leq 0.1)$, where $\mathcal{N}_{\rm cor,i}(z_{\rm form} = z, z_{\rm merg} \leq 0.1)$ is the number of compact objects per unit mass which form at redshift $z_{\rm form} = z$ and merge at redshift $z_{\rm merg} \leq 0.1$. For our calculations we assume the cosmological parameters from *Planck* 2015 (Planck Collaboration et al., 2016).

In equation 4.10, the dependence of the merger rate on metallicity is contained in the term $f_{\rm loc}(z)$. Our knowledge of the stellar metallicity evolution in the Universe is quite more uncertain than our knowledge of the SFR density evolution (see e.g. ; Mannucci et al., 2009; Madau and Dickinson, 2014 and references therein). Thus, we decided to make minimal assumptions on the metallicity evolution.

In the simplest case, we assume that all stars in the Universe form with the same metallicity Z and we calculate equation 4.10 for each of the 12 metallicities considered in our simulations. Hence, we estimate that the uncertainty of the local merger rate density is the maximum difference between values of $\mathcal{R}_{\rm loc,i}$ calculated with all considered metallicities (error bars in Figure 4.15). This procedure results in relatively small error bars for the DNSs, which do not depend much on progenitor's metallicity (see Figure 4.14), while the uncertainty on the merger rate density of both BHBs and BHNSs spans several orders of magnitude.

Then, we adopt two different models for the evolution of metallicity. In *model 1*, we assume that all stars formed in a given redshift bin Δz have the same metal-

[2] In this work, we estimate the local merger rate within $z \leq 0.1$. This redshift interval is actually smaller than the current instrumental horizon of LIGO and Virgo for BHBs, which depends on BHB mass. On the other hand, the merger rate density in the comoving frame is expected to grow mildly with redshift, as shown by Mapelli et al. (2017). We decided not to account for this effect in the current paper, because the uncertainty is dominated by other approximations in the calculation described here (e.g. the assumption about the metallicity). A more accurate study of the merger rate as a function of redshift is provided in the companion paper Mapelli and Giacobbo (2018).

licity and we calculate this metallicity as $\log Z(z)/Z_\odot = -0.19\,z - 0.74$ if $z \leq 1.5$ and $\log Z(z)/Z_\odot = -0.22\,z - 0.66$ if $z > 1.5$. This relation between metallicity and redshift was derived by Rafelski et al. (2012) based on the chemical abundance of a sample of damped Lyα systems up to redshift ~ 5.

In *model 2* we assume that all stars formed in a given redshift bin Δz have the same metallicity, but we calculate this metallicity as $\log Z(z)/Z_\odot = -0.19\,z$ if $z \leq 1.5$ and $\log Z(z)/Z_\odot = -0.22\,z$ if $z > 1.5$, which corresponds to rescaling the formula by Rafelski et al. (2012), to obtain $Z(z=0) = Z_\odot$. In fact, the absolute metallicity calibration of the damped Lyα sample is quite uncertain, while the average metallicity of galaxies in the nearby Universe obtained from the Sloan Digital Sky Survey is consistent with the solar value (Gallazzi et al., 2008; Madau and Dickinson, 2014).

In Table 4.2, we report our estimate of $\mathcal{R}_{\rm loc,i}$ for all simulations and for these two models.

Figure 4.15 shows the local merger rate density of DNSs, BHNSs and BHBs for all simulations. The error bars account for the maximum difference between $\mathcal{N}_{\rm cor,i}$ calculated for all metallicities. The uncertainty is relatively small (up to one order of magnitude) for DNSs, while it is very large (up to five orders of magnitude) for both BHNSs and BHBs, because the number of BHNS and BHB mergers strongly depends on the progenitor's metallicity, while the number of DNS mergers is only mildly sensitive to progenitor's metallicity (Figure 4.14).

Our estimate of $\mathcal{R}_{\rm loc,DNS}$ spans from ~ 5 Gpc^{-3} yr^{-1} (for $\alpha 1$) to $\sim 10^3$ Gpc^{-3} yr^{-1} (for CC15α3 and CC15α5). The local merger rate density of BHNSs $\mathcal{R}_{\rm loc,BHNS}$ spans from $\sim 10^{-2}$ to $\sim 10^3$ Gpc^{-3} yr^{-1}, while the local merger rate density of BHBs $\mathcal{R}_{\rm loc,BHB}$ spans from $\sim 10^{-1}$ to $\sim 4 \times 10^3$ Gpc^{-3} yr^{-1}.

The simulations with high core-collapse SN kicks ($\alpha 1$, $\alpha 3$ and $\alpha 5$) are not consistent with the local merger rate density of DNSs inferred from GW170817 (Abbott et al., 2016a). In contrast, the simulations with low core-collapse SN kicks and $\alpha \geq 3$ (CC15α3 and CC15α3) are fairly consistent with the local merger rate of DNSs inferred from GW170817. *Model 2* applied to CC15α5 gives an estimate of the local merger rate density of DNSs which is in good agreement with the value inferred from GW170817.

All simulations are consistent with the upper limit to the local merger rate density of BHNSs inferred from O1 data (Abbott et al., 2016e). *Model 1* produces systematically larger rates than *model 2*, because it includes more metal-poor stars by construction.

Finally, the uncertainty on the simulated BHB merger rate density is very large, much larger than the 90 per cent credible levels inferred from O1 data plus

GW170104 (Abbott et al., 2017b). *Model 1* predicts $\mathcal{R}_{\rm loc,BHB} \gtrsim 1000$ Gpc^{-3} yr^{-1}, which is substantially larger than the 90 per cent credible levels inferred from current LIGO-Virgo results, whereas *model 2* predicts $\mathcal{R}_{\rm loc,BHB} \sim 40-90$ Gpc^{-3} yr^{-1}, which is perfectly within the LIGO-Virgo 90 per cent credible interval.
In a companion paper (Mapelli and Giacobbo, 2018) we model the metallicity evolution of the Universe by taking this information from a cosmological simulation. The local merger rate densities estimated by Mapelli and Giacobbo (2018) are consistent with the ones derived in this paper, within the uncertainties.
Overall, we confirm the results of previous papers (e.g. Chruslinska et al., 2018; Kruckow et al., 2018; Belczynski et al., 2018): it is quite hard to match the local merger rate density of DNSs inferred from GW170817. Unlike Chruslinska et al. (2018), who need to assume a different physics for CE evolution of DNS and BHB progenitors[3], we are able to match both the DNS and the BHB merger rates with the same physics, provided that low natal kicks are assumed for iron core-collapse SNe in binary systems. Natal kicks of core-collapse SNe are still matter of debate and addressing this open question is beyond the aims of this paper. Here, we simply show that assuming low kicks for iron core-collapse SNe in binary systems allows us to match the local merger rate of DNSs, BHNSs and BHBs all together.

4.4 Conclusions

We have investigated the formation of DNSs, BHNSs, BHBs from isolated binaries by means of our population-synthesis code MOBSE. MOBSEincludes an updated formalism for mass loss by stellar winds, which depends on metallicity and Eddington ratio (Giacobbo et al., 2018), and incorporates several prescriptions for core-collapse SNe, electron-capture SNe, pulsational pair instability SNe and pair instability SNe. Here, we investigate the importance of CE ejection efficiency (assuming $\alpha = 1$, 3 and 5) and the impact of natal kicks of iron core-collapse SNe. In fact, the distribution of natal kicks is still matter of debate, and it might be that kicks in close binaries are lower than kicks in single stars (e.g. Beniamini and Piran, 2016; Bray and Eldridge, 2016; Tauris et al., 2017). Overall, we consider six sets of simulations: three with high core-collapse SN kicks (modeled through a Maxwellian curve with 1D rms 265 km s^{-1}, Hobbs et al., 2005) and with CE parameter $\alpha = 1$, 3 and 5 (simulations $\alpha1$, $\alpha3$ and $\alpha5$, see Table 4.1) and three with low core-collapse SN

[3] Chruslinska et al., 2018 show that they can reproduce the merger rate of DNSs only if they allow some HG donors to survive a CE phase, but this assumption leads to a significant overestimate of the local BHB merger rate.

kicks (modeled through a Maxwellian curve with 1D rms 15 km s^{-1}) and with CE parameter $\alpha = 1$, 3 and 5 (simulations CC15α1, CC15α3 and CC15α5).

We first look at the masses of DNSs, BHNSs and BHBs. The masses of NSs in DNSs span from ~ 1.1 to ~ 2 $M_\odot$, although low masses are more common than high masses, especially in merging DNSs formed with low natal kicks (simulations CC15α1, CC15α3 and CC15α5, Figs 4.2 and 4.3). In contrast, the masses of NSs in merging BHNSs tend to be preferentially high ($1.3-2.0$ $M_\odot$), while the masses of BHs in merging BHNSs tend to be preferentially low ($\sim 5-15$ $M_\odot$), especially in simulations with low natal kicks (simulations CC15α1, CC15α3 and CC15α5, Figs 4.7 and 4.8).

The masses of BHs in BHBs strongly depend on the progenitor's metallicity, more massive BHs being produced by metal-poor stars. Also, the number of BHBs depends on the progenitor's metallicity: metal-poor binaries tend to produce more BHBs than metal-rich ones. The maximum mass of BHs in simulated BHBs is ~ 65 $M_\odot$, but the most massive BHBs do not merge within a Hubble time because their semi-major axes are too large. We find that the maximum mass of BHs in merging BHBs is ~ 45 $M_\odot$ (Figs 4.11 and 4.12). This is consistent with the possible upper mass cut-off inferred from LIGO-Virgo data by Fishbach and Holz (2017) and Wysocki et al. (2018).

On the other hand, our binaries are evolved in isolation. If they were evolved in a dynamically active environment, such as a star cluster, some of the most massive BHs (with mass $45-65$ $M_\odot$) might still merge within a Hubble time, as a consequence of dynamical hardening or dynamical exchanges (e.g. Mapelli, 2016).

We estimate the number of mergers per unit mass of the initial stellar population (Fig. 4.14). If core-collapse SN kicks are high (low), a DNS merger occurs every $\sim 10^5-10^7$ $M_\odot$ ($\sim 10^4-10^6$ $M_\odot$) of stellar population. Thus, low SN kicks boost the number of DNS mergers by at least a factor of 10. The number of DNS mergers per unit mass is weakly sensitive to progenitor's metallicity.

In contrast, the number of both BHNS and BHB mergers per unit mass of stellar population depends on the progenitor's metallicity dramatically. A BHNS merger occurs every $\sim 10^4-10^5$ $M_\odot$ of stellar population if $Z \leq 0.01$ and every $\gtrsim 10^7$ $M_\odot$ of stellar population if $Z > 0.01$. The number of BHNS mergers per unit mass depends mildly on both the assumed CE parameters and natal kicks. In particular, low kicks tend to produce more BHNS mergers at low metallicity and less at high metallicity. Similarly, a BHB merger occurs every $\sim 10^4$ $M_\odot$ of stellar population if $Z \leq 0.002$ and every $\sim 10^7-10^8$ $M_\odot$ of stellar population if $Z \geq 0.02$. The number of BHB mergers per unit mass depends only mildly on the CE parameters. There is no dependence

of BHBs on the assumed natal kicks, but only because we assume that the kick is inversely proportional to the amount of fallback (Fryer et al., 2012). Thus, massive BHs receive always low kicks.

Finally, we estimate the local merger rate density by convolving the number of mergers per unit stellar mass with the cosmic star formation rate density (equation 4.10). Given the large uncertainties on the metallicity evolution of the Universe, we include the metallicity of the progenitor in our calculations to estimate the maximum uncertainty of our predicted merger rates. In all our simulations, the local merger rate density of BHNSs and BHBs is consistent with the values inferred from O1 LIGO-Virgo data, for reasonable assumptions about metallicity evolution. There is no significant dependence of the local merger rate of BHNSs and BHBs on CE parameters and on core-collapse SN kicks (Fig. 4.15).

In contrast, the local merger rate density of DNSs strongly depends on both CE parameters and SN kicks (Fig. 4.15). Only simulations with low SN kicks and high values of α (CC15α3 and CC15α5) match the local merger rate density inferred from GW170817 ($\mathcal{R}_{\rm loc,DNS} = 1540^{+3200}_{-1220}$ Gpc^{-3} yr^{-1}, Abbott et al., 2016a). This result adds another piece to the intricate puzzle of natal kicks and DNS formation.

CHAPTER 5

REVISING NATAL KICK PRESCRIPTIONS IN POPULATION SYNTHESIS SIMULATIONS

Natal kicks are matter of debate and significantly affect the merger rate density of compact objects. Here, we present a new simple formalism for natal kicks of neutron stars (NSs) and black holes (BHs). We describe the magnitude of the kick as $v_{\rm kick} \propto f_{\rm H05}\ m_{\rm ej}\ m_{\rm rem}^{-1}$*, where* $f_{\rm H05}$ *is a normalization factor, drawn from a Maxwellian distribution with one-dimensional root-mean-square velocity* $\sigma = 265\ km\ s^{-1}$*,* $m_{\rm ej}$ *is the mass of the supernova (SN) ejecta and* $m_{\rm rem}$ *is the mass of the compact object. This formalism matches the proper motions of young Galactic pulsars and can naturally account for the differences between core-collapse SNe of single stars, electron-capture SNe and ultra-stripped SNe occurring in interacting binaries. Finally, we use our new kick formalism to estimate the local merger rate density of binary NSs (*$R_{\rm BNS}$*), BH–NS binaries (*$R_{\rm BHNS}$*) and binary BHs (*$R_{\rm BBH}$*), based on the cosmic star formation rate density and metallicity evolution. In our fiducial model, we find* $R_{\rm BNS} \sim 600\ Gpc^{-3}\ yr^{-1}$*,* $R_{\rm BHNS} \sim 10\ Gpc^{-3}\ yr^{-1}$ *and* $R_{\rm BBH} \sim 50\ Gpc^{-3}\ yr^{-1}$*, fairly consistent with the numbers inferred from the LIGO-Virgo collaboration.*

Based on:
Giacobbo N., Mapelli M., to be submitted to Apj

5.1 Introduction

State-of-the-art population-synthesis simulations build on the results of observational constraints and of hydrodynamical models of SN explosion. Most population-synthesis codes (e.g. BSE, Hurley et al., 2000; Hurley et al., 2002; SEBA, Portegies Zwart and Verbunt, 1996b; STARTRACK, Belczynski et al., 2008; MOBSE, Mapelli et al., 2017; Giacobbo et al., 2018; SEVN Spera et al., 2019) implement neutron star (NS) kicks through the Maxwellian distribution derived by Hobbs et al. (2005). The same distribution is used even to model BH kicks, after correcting for linear momentum conservation (e.g. Mapelli et al., 2013; Ziosi et al., 2014) or after including the effect of fallback and failed SN explosions (Fryer et al., 2012). Finally, if massive BHs are allowed to form by direct collapse, no kick is usually assumed apart from the Blaauw mechanism (Fryer et al., 2012).

Several recent studies suggest that this approach is not sufficient to capture the complexity of natal kicks. In particular, Bray and Eldridge (2016) and Bray and Eldridge (2018) propose a new linear relation between the mass of the ejecta (to account for the effect of asymmetries), divided by the mass of the compact object (to conserve linear momentum), and the natal kick. Moreover, natal kicks from electron-capture SNe (ECSNe), which are less energetic than CCSNe, are expected to be significantly low (Dessart et al., 2006; Schwab et al., 2015b; Gessner and Janka, 2018; Giacobbo and Mapelli, 2019b). Furthermore, stars in close binary systems might undergo ultra-stripped SNe, i.e. SN explosions of naked helium stars that were stripped by their compact companion (Tauris et al., 2013; Tauris et al., 2015). In this case, the natal kick is thought to be low, because of the low mass of the ejecta (Tauris et al., 2017; Kruckow et al., 2018). Finally, recent population-synthesis studies (Mapelli and Giacobbo, 2018; Giacobbo and Mapelli, 2018; Chruslinska et al., 2018) suggest that very low kicks (≤ 50 km s^{-1}) are crucial to match the high local merger rate density of BNSs inferred from LIGO-Virgo data (110–3840 Gpc^{-3} yr^{-1}, Abbott et al., 2018).

Here, we propose a new simple prescription for natal kicks which is able to account for both large velocities in young isolated pulsars and small kicks in ultra-stripped SNe, ECSNe and failed SNe. Building upon Bray and Eldridge (2016), we start from the idea that the effect of asymmetries scales with the mass of the ejecta ($m_{\rm ej}$). From linear momentum conservation, we include the dependence of the kick on compact object mass ($m_{\rm rem}$). As a normalization, we take the Maxwellian distribution by Hobbs et al. (2005).

Hence, our new prescription can be written in the form $v_{\rm kick} \propto f_{\rm H05}\, m_{\rm ej}\, m_{\rm rem}^{-1}$,

where $f_{\rm H05}$ is the kick extracted from a Maxwellian with one-dimensional rms $\sigma = 265$ km s^{-1}. For NSs formed from single stars, our formula is basically indistinguishable from Hobbs et al. (2005). For NSs that form in close binaries (going through ECSNe or ultra-stripped SNe), this formalism automatically produces very low kicks, consistent with Beniamini and Piran (2016) and Mapelli and Giacobbo (2018). Finally, low-mass BHs (which form through fallback) tend to have significantly larger kicks than massive BHs, formed via direct collapse.
This paper is organized as follows. In Section 5.2, we describe our new prescriptions for natal kicks, as implemented in MOBSE. Then, we show the effect of our new prescriptions on the distribution of natal kicks (Section 5.3) and we discuss their impact on the merger rate (Section 5.4). Finally, we summarize our results in Section 5.5.

5.2 Numerical method

We implement the new prescriptions for natal kicks in our population synthesis code MOBSE, which is an updated and customized version of BSE (Hurley et al., 2000; Hurley et al., 2002) . Here we briefly summarize the main differences between MOBSE and BSE and we refer to previous papers for more details Giacobbo et al. (2018) and Giacobbo and Mapelli (2018).

5.2.1 MOBSE

Mass loss by stellar winds of massive hot stars is described in MOBSE as $\dot{M} \propto Z^{\beta}$, where $\beta = 0.85, 2.45 - 2.4\Gamma_e$, and 0.05 for electron-scattering Eddington ratio $\Gamma_e \leq 2/3$, $2/3 < \Gamma_e \leq 1$, and $\Gamma_e > 1$, respectively (see Giacobbo et al., 2018 and references therein).
Electron-capture SNe (ECSNe) are modeled as described in Giacobbo and Mapelli (2019b). Core-collapse SNe (CCSNe) are described as in Fryer et al. (2012), including both the rapid and the delayed model: the mass of the compact object formed via a CCSN is determined by the final mass of the carbon-oxygen core and by the amount of fallback.
In this work, we introduce a small but crucial difference with respect to the previous versions of MOBSE: the mass of the proto-NS in the rapid model is $m_{\rm proto} = 1.1$ M$_\odot$, while in Fryer et al., 2012 and in the previous versions of MOBSE we adopted $m_{\rm proto} = 1.0$ M$_\odot$. This change is fundamental to match the mass of observed NSs (Tauris et al., 2017), because with $m_{\rm proto} = 1.0$ M$_\odot$ we drastically overestimated the

fraction of NSs with mass < 1.2 $M_\odot$ (see e.g. Giacobbo and Mapelli, 2018). Finally, MOBSE includes a treatment for pair instability and pulsational pair instability taken from Spera and Mapelli (2017).
Other changes with respect to BSE include the modeling of core radii (according to Hall and Tout, 2014), the treatment of common envelope (CE, we assume that all Hertzsprung-gap donors merge during CE) and the maximum stellar mass (we extend the mass range up to 150 $M_\odot$, Mapelli, 2016). Apart from the changes summarized in this section, single and binary evolution in MOBSE is the same as described in Hurley et al. (2000) and Hurley et al. (2002).

5.2.2 Natal kick prescriptions

To develop the new kick prescriptions, we start from assuming that the Maxwellian distribution derived by Hobbs et al. (2005) is a good description of NS kicks from single star evolution. If new results about proper motions of young single pulsars become available and suggest a significantly different fitting function, we can easily update our prescriptions to include the new fitting function.
Furthermore, we include in our prescriptions the mass of the ejecta $m_{\rm ej}$, because it is reasonable to assume that the magnitude of the kick depends on the total mass ejected during the SN explosion. Finally, to satisfy linear momentum conservation, we also include a term depending on the mass of the compact object $m_{\rm rem}$.
Hence, the new prescription we adopt for SN kicks can be expressed as

$$v_{\rm kick} = f_{\rm H05}\,\frac{m_{\rm ej}}{\langle m_{\rm ej}\rangle}\,\frac{\langle m_{\rm NS}\rangle}{m_{\rm rem}}, \tag{5.1}$$

where $f_{\rm H05}$ is a random number extracted from a Maxwellian distribution with one-dimensional rms $\sigma = 265$ km s^{-1} (Hobbs et al., 2005), $\langle m_{\rm NS}\rangle$ is the average NS mass (in our calculations $\langle m_{\rm NS}\rangle = 1.2$ $M_\odot$) and $\langle m_{\rm ej}\rangle$ is the average mass of the ejecta associated with the formation of a NS of mass $\langle m_{\rm NS}\rangle$ from single stellar evolution.
To check the impact of compact-object mass on the final kicks, we also run some tests with a second prescription, independent of $m_{\rm rem}$:

$$v_{\rm kick} = f_{\rm H05}\,\frac{m_{\rm ej}}{\langle m_{\rm ej}\rangle}. \tag{5.2}$$

These prescriptions have several advantages. Firstly, they are simple to implement in population-synthesis codes. Secondly, they are quite universal: they can be used for both NSs and BHs, for both single and binary star evolution, for both ECSNe and CCSNe (or other flavors of SN, including ultra-stripped SNe).

Table 5.1: Models.

ID	Natal kicks
Ej1	$\sigma = 265$ km s^{-1}, eq. 5.1
Ej2	$\sigma = 265$ km s^{-1}, eq. 5.2
H05	$\sigma = 265$ km s^{-1}, eq 5.3
σ15	$\sigma = 15$ km s^{-1}, eq 5.3

Column 1: name of the simulation; column 2: Natal-kick prescription.

5.2.3 Simulation setup

We used MOBSE to simulate a large set of both single stars and binary systems. For single stars, and for the primary star in binary systems, we randomly draw the initial mass (m_1) from a Kroupa initial mass function (Kroupa, 2001) $\mathfrak{F}(m_1) \propto m_1^{-2.3}$ with $m_1 \in [5-150]\,M_\odot$. The mass of the stellar companion in binaries is derived from the mass ratio as $\mathfrak{F}(q) \propto q^{-0.1}$ with $q = m_2/m_1 \in [0.1-1]$ (following Sana et al., 2012). Finally, the eccentricity e and the orbital period P are also drawn from the distributions proposed by Sana et al. (2012): $\mathfrak{F}(e) \propto e^{-0.42}$ (with $0 \leq e < 1$) and $\mathfrak{F}(P) \propto (P)^{-0.55}$ (with $P = \log_{10}(P/\mathrm{day}) \in [0.15-5.5]$).
We assume the rapid model for CCSNe (Fryer et al., 2012). We assume CE efficiency $\alpha = 5$ (unless otherwise stated) and we derive λ from the formulas in Claeys et al. (2014). In appendix 7, we discuss the impact of different choices of α on our main results.

We have run the following four sets of simulations (see Table 5.1).

Ej1: natal kicks are implemented as in equation 5.1;

Ej2: natal kicks are drawn from equation 5.2;

H05: natal kicks are generated from a Maxwellian with $\sigma = 265$ km s^{-1} for both CCSNe and ECSNe (see model EC265α5 in Giacobbo and Mapelli, 2019b), plus a correction for the amount of fallback following Fryer et al. (2012) (see below equation 5.3);

σ15: natal kicks are drawn from a single Maxwellian with rms= 15 km s^{-1} for both ECSNe and CCSNe (see model CC15α5 in Giacobbo and Mapelli, 2018), plus a correction for the amount of fallback as in Fryer et al. (2012).

Table 5.2: Median values of natal kicks.

Model	NS/BH	Progenitor star	$\tilde{v}_{kick}$ (km s^{-1})
Ej1	NS	single	322
Ej1	NS	binary	188
Ej2	NS	single	351
Ej2	NS	binary	218
H05	NS	single	392
H05	NS	binary	375
σ15	NS	single	22
σ15	NS	binary	21
Ej1	BH	single	30
Ej1	BH	binary	30
Ej2	BH	single	164
Ej2	BH	binary	165
H05	BH	single	127
H05	BH	binary	129
σ15	BH	single	7
σ15	BH	binary	7

Column 1: model; column 2: compact-object type (NS or BH); column 3: whether the progenitor star was born as a single or a binary star; column 4: median value of natal kicks.

The correction for the amount of fallback in models H05 and σ15 is implemented as follows. We draw the natal kick as

$$v_{kick} = (1 - f_{fb})\, f_{H05}, \tag{5.3}$$

where f_{H05} is a random number drawn from the Maxwellian distribution, while f_{fb} is the fallback fraction, defined as $f_{fb} = m_{fb}/(m_{fin} - m_{proto})$, where m_{fin} is the mass of the star at the onset of core collapse and m_{fb} is the mass that falls back and is accreted by the proto-NS (Fryer et al., 2012). The main difference between our new prescriptions and equation 5.3 is that the latter does not depend significantly on the mass of the ejecta (in equation 5.3 $v_{kick} \propto m_{ej}/m_{fin}$, i.e. m_{fin} compensates the impact of m_{ej}).

For each set of simulations we consider 12 different metallicities: Z = 0.0002, 0.0004, 0.0008, 0.0012, 0.0016, 0.002, 0.004, 0.006, 0.008, 0.012, 0.016 and 0.02. For each metallicity, we simulated 10^7 binary systems and 5×10^5 single stars. Thus, for each model we simulate 1.2×10^8 massive binaries and 6×10^6 single stars.

5.3 Results

5.3.1 Natal kicks in single stars

The top panels of Figure 5.1 show the natal kick distribution of NSs born from single stars with solar metallicity ($Z = 0.02$). NS kicks from simulations Ej1 and Ej2 are extremely similar to each other. They both show two different peaks, one centered at $\sim 400-450$ km s^{-1} and produced by CCSNe, the other centered at $\sim 6-8$ km s^{-1} and produced by ECSNe. This happens because $m_{\rm ej}$ of ECSNe is significantly smaller than that of CCSNe, leading to smaller kicks. Thus, our new prescriptions are able to distinguish between CCSN kicks and ECSN kicks, without the need for a separate treatment.
The distribution of NS kicks from CCSNe in simulation H05 (drawn from a single Maxwellian with $\sigma = 265$ km s^{-1}) is remarkably similar to the peak produced by CCSNe in simulations Ej1 and Ej2. This confirms that simulations Ej1 and Ej2 are a good match to the fit by Hobbs et al. (2005) for large NS kicks. On the other hand, runs Ej1 and Ej2 can also naturally reproduce the low kicks of ECSNe. Finally, simulation $\sigma 15$ produces single NS kicks that are significantly lower than the other runs, unable to explain a large fraction of the sample by Hobbs et al. (2005).
The top panels of Figure 5.2 show the natal kick distribution of BHs born from single stars with solar metallicity ($Z = 0.02$). All the four models predict that ~ 60 % of BHs receive approximately no kick, because their progenitors collapse to a BH directly, without SN explosions. The remaining BHs receive a kick. Models H05 and Ej2 predict the largest maximum kicks, up to ~ 450 and ~ 550 km s^{-1}, respectively. In fact, the kick prescriptions in H05 and Ej2 do not depend on compact-object mass. Model $\sigma 15$ predicts the lowest BH kicks (up to ~ 30 km s^{-1}), while model Ej1 ($v_{\rm kick} \leq 100$ km s^{-1}) is intermediate between the considered models, thanks to the dependence on $m_{\rm rem}$.

5.3.2 Natal kicks in binary stars

The bottom panels of Figure 5.1 (Figure 5.2) show the natal kicks of NSs (BHs) formed from the evolution of binary stars with $Z = 0.02$. Binary evolution significantly affects the distribution of NS natal kicks in all models and especially in run Ej1 and Ej2. The Kolmogorov-Smirnov (KS) test confirms that the probability that natal kicks of NSs formed from single stars and from binary evolution are drawn from the same distribution is nearly zero ($< 10^{-20}$). Table 5.2 shows that the median value of NS kicks is significantly lower for binary stars than for single stars in

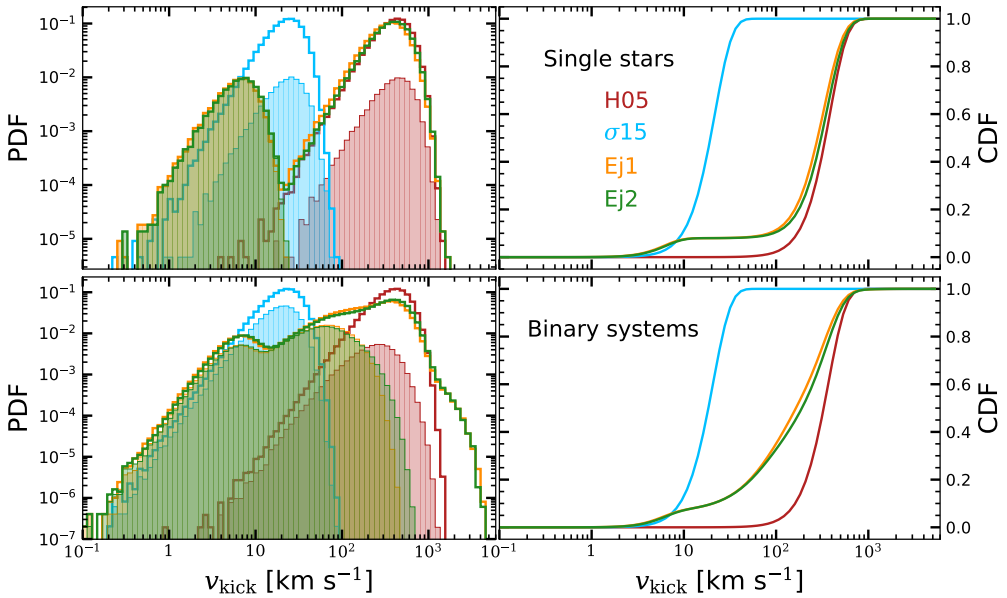

Figure 5.1: Left-hand panels: probability distribution function (PDF) of natal kicks for all NSs formed from single stars (top) and for those formed from binary systems (bottom) at $Z = 0.02$. Orange line: model Ej1; green: Ej2; red: H05; blue: σ15. The filled histograms represent the subset of NSs formed via ECSNe (top) and the subset of NSs that are still gravitationally bound to their companion after the SN (bottom). Right-hand panels: cumulative distribution function (CDF) of natal kicks for all NSs.

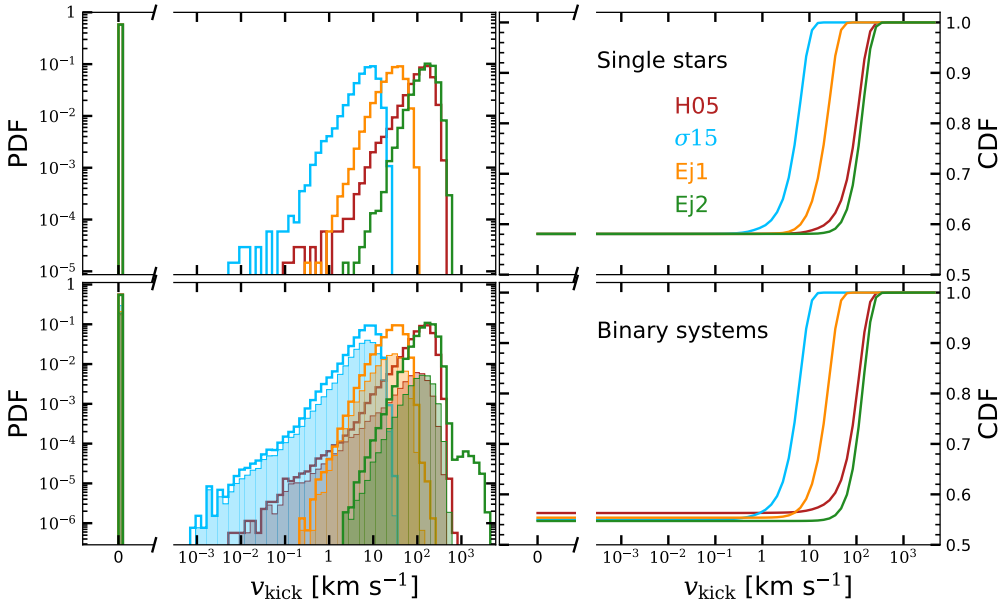

Figure 5.2: Same as Figure 5.1, but for BHs formed from single star evolution (top) and from binary star evolution (bottom) at $Z = 0.02$. The break on the x-axis allows to show BHs with zero natal kick (formed from direct collapse).

models Ej1 and Ej2. In general, binary evolution tends to increase the number of NSs with small kicks, because dissipative mass transfer tends to reduce $m_{\rm ej}$. On the other hand, binary evolution also triggers the formation of few NSs with even larger kicks than in the case of single star evolution. Binary evolution has a smaller impact on NS kicks in models H05 and σ15 by construction (see Table 5.2), because they do not depend significantly on $m_{\rm ej}$. The only effect of binary evolution on models H05 and σ15 is that mass transfer can change $m_{\rm rem}$ and the amount of fallback, hence affecting natal kicks. This affects mostly BHs, while it has negligible impact on NSs. The distribution of NS kicks in simulations Ej1 and Ej2 are very similar to each other, even when we account for binary evolution. As expected, NSs that remain members of a binary system after the kick (filled histograms) have significantly smaller kicks than single NSs in runs Ej1, Ej2 and H05. In model Ej1 (Ej2), the maximum kick undergone by NSs that remain in binaries is $v_{\rm kick} \sim 400$ km s^{-1}(~ 600 km s^{-1}), while the maximum possible NS kick is $v_{\rm kick} \sim 4500$ km s^{-1}(~ 4500 km s^{-1}).
Finally, binary evolution has a different effect on BH kicks. In the case of BHs, dissipative mass transfer affects $m_{\rm rem}$, producing smaller BHs. This explains why the percentage of BHs that undergo no kick decreases (of about 5 per cent) in all models. Table 5.2 shows that the median value of BH kicks is not affected by the binarity of progenitors.

5.3.3 Merger efficiency

For each set of binary simulations we compute the merger efficiency, that is the number of compact-object mergers occurring in a given stellar population, integrated over the Hubble time, divided by the total initial stellar mass. As already described in Mapelli et al. (2017), the merger efficiency η is given by

$$\eta = f_{\rm bin}\, f_{\rm IMF}\, \frac{N_{\rm merg}}{M_{\rm tot,sim}}, \tag{5.4}$$

where $N_{\rm merg}$ is the number of mergers of binary BHs (BBHs), or BH – NS binaries (BHNSs), or binary NSs (BNSs), and $M_{\rm tot,sim}$ is the initial total mass of the simulated binary population. Since we simulated only massive binaries, we introduce two corrections factors: $f_{\rm bin} = 0.5$ (to correct for the fact that ~ 50 per cent of stars are single, Sana et al., 2013) and $f_{\rm IMF} = 0.285$ (to account for the total mass of stars below the minimum mass we simulate).
Figure 5.3 shows η as a function of metallicity for all runs (see Table 5.1). The merger efficiency of both BBHs and BHNSs strongly depends on metallicity: BH mergers are at least two orders of magnitude more common in a metal-poor population

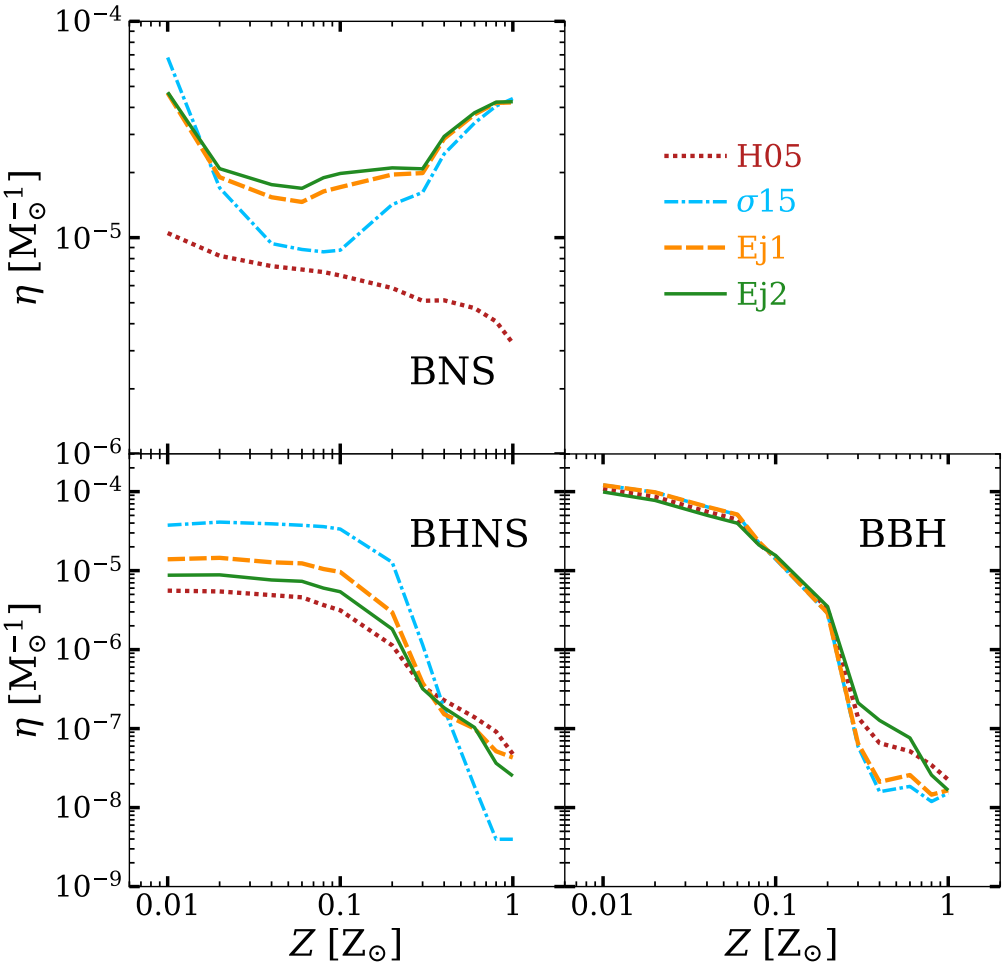

Figure 5.3: Merger efficiency (η from eq. 5.4) as a function of the progenitor's metallicity for all sets of simulations (see Table 5.1). *Top-left:* BNSs; *bottom-left:* BHNSs; *bottom-right:* BBHs.

than in a metal-rich one. This result is well known and is consistent with previous works (Dominik et al., 2013b; Klencki et al., 2018; Giacobbo et al., 2018; Giacobbo and Mapelli, 2018). The merger efficiency of BNSs depends only mildly on metallicity. The decrease of η at intermediate metallicity ($0.0004 \lesssim Z \lesssim 0.04$) in the models with relatively low kicks (Ej1, Ej2 and σ15) is caused by premature mergers of the progenitor stars, because stellar radii during the Hertzsprung gap and the red giant phase are larger at intermediate metallicity (see Giacobbo and Mapelli, 2018; Spera et al., 2019). In model H05, η decreases with increasing metallicity, because the ability of CE to shrink the binary becomes decisive when SN kicks are high: at high metallicity stars lose their envelope quite effectively, reducing the impact of CE.
More importantly, Figure 5.3 shows that our new kick prescriptions (models Ej1, Ej2) produce approximately the same BNS merger efficiency as model σ15, which assumes unrealistically small kicks. For BHNSs, the new kick prescriptions give a

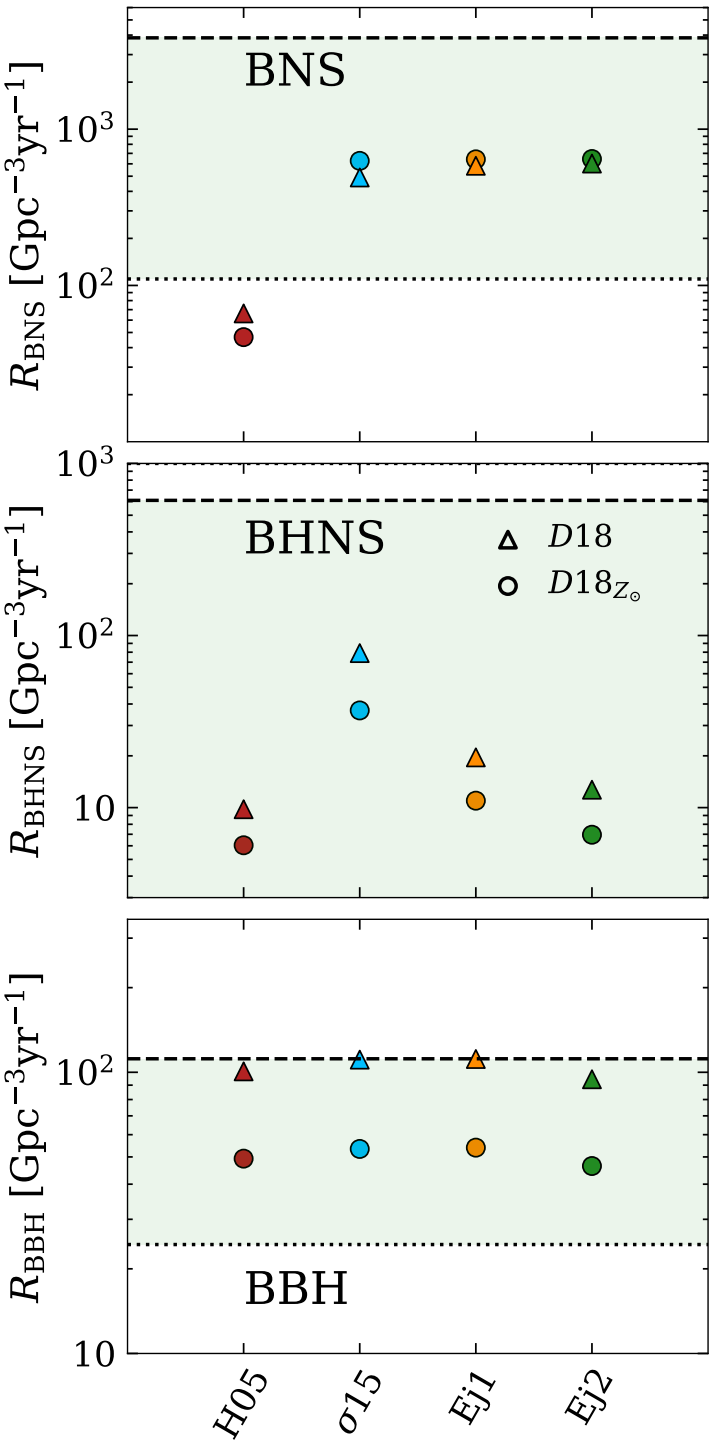

Figure 5.4: Local merger rate density R from eq. 5.5. Top, middle and bottom panel: local merger rate density of BNSs ($R_{\rm BNS}$), BHNSs ($R_{\rm BHNS}$) and BBHs ($R_{\rm BBH}$), respectively. Triangles (circles) assume model $D18$ ($D18_{Z_\odot}$) for the cosmic evolution of metallicity. The green shaded regions represent the 90 per cent confident interval of the merger rate density inferred by Abbott et al. (2019) for BBHs and Abbott et al. (2018) for BNSs and BHNSs.

merger rate efficiency more similar to H05 than to σ15. Finally, the merger efficiency of BBHs is not significantly affected by the new kick prescriptions, because most merging BBHs receive no kick (or very small kick) in all considered models.

5.3.4 Local merger rate

Following Giacobbo and Mapelli (2018) and Spera et al. (2019), we compute the local merger rate density R as

$$R = \frac{1}{H_0\, t_{\rm lb}(z=0.1)} \int_{z_{\rm max}}^{z_{\rm min}} \frac{f_{\rm loc}(z,\, Z)\ {\rm SFR}(z)}{(1+z)\,\mathscr{E}(z)} dz, \tag{5.5}$$

where SFR(z) is the star formation rate density (for which we adopt the fitting formula proposed by Madau and Fragos, 2017), $\mathscr{E}(z) = \left[\Omega_{\rm M}\,(1+z)^3 + \Omega_\Lambda\right]^{1/2}$, $t_{\rm lb}(z = 0.1)$ is the look-back time at redshiftVink2001 $z = 0.1$, and $f_{\rm loc}(z, Z)$ is the fraction of merging systems that formed at a given redshift z and merge in the local Universe ($z \leq 0.1$) per unit solar mass. We assume $z_{\rm max} = 15$ and $z_{\rm min} = 0$. Finally, H_0, $\Omega_{\rm M}$ and Ω_Λ are the cosmological parameters for which we take the values from Planck Collaboration et al. (2016).

The term $f_{\rm loc}(z, Z)$ clearly depends not only on redshift but also on metallicity (which is important especially for BBHs and BHNSs, see Fig. 5.3). We derive $f_{\rm loc}(z, Z)$ directly from the merger efficiency η (equation 5.4), by assuming that all stars formed at a given redshift have the same metallicity. We describe the evolution of metallicity across cosmic time with two different models. In model *D18*, the metallicity evolves with redshift as $\log Z(z)/Z_\odot = -0.24\,z - 0.18$. This formula is the fit to the metallicity evolution of a large sample of damped Lyman-α absorbers (with redshift between 0 and 5) presented in De Cia et al. (2018) (see their figure 4 and Table 1). With respect to previous work (e.g. Rafelski et al., 2012, whose results we used in Giacobbo and Mapelli, 2018), De Cia et al. (2018) consider a larger sample of damped Lyman-α absorbers and make a new correction for dust. This allows them to recover a present-day average metallicity $Z(z = 0) \sim 0.66\ {\rm Z}_\odot$ (where we assume $Z_\odot = 0.02$), much closer to the solar metallicity than previous work.

In the second model we adopt (*D18*$_{Z_\odot}$), the metallicity evolves with redshift as $\log Z(z)/Z_\odot = -0.24\,z$. This model is obtained by re-scaling model *D18* to obtain $Z(z = 0) = Z_\odot$. The reason for this re-scaling is that metallicity measurements from galaxies in the Sloan Digital Sky Survey indicate that the average local metallicity is $Z(z = 0) \sim Z_\odot$ (Gallazzi et al., 2008).

Figure 5.4 shows the local merger rate $R_{\rm BNS}$, $R_{\rm BHNS}$ and $R_{\rm BBH}$ for BNSs, BHNSs and BBHs, respectively, considering both models of metallicity evolution, namely *D18* and $D18_{Z_\odot}$.

The new kick prescriptions Ej1 and Ej2 produce a BNS merger rate $R_{\rm BNS} \sim 600$ Gpc^{-3} yr^{-1}, consistent with the local merger rate inferred from GW170817 ($R_{\rm GW170817} = 110-3840$ Gpc^{-3} yr^{-1}, Abbott et al., 2017e; Abbott et al., 2018). The rate from Ej1 and Ej2 is very similar to the rate we obtain with the low-kick model σ15 and about one order of magnitude higher than the rate we obtain with model H05.

All our models are consistent with the upper limit on BHNSs by Abbott et al. (2018). Models Ej1 and Ej2 produce rates that are significantly smaller than σ15 and slightly higher than H05. Finally, the merger rate density of BBHs is extremely sensitive to metallicity. Model *D18* results in a factor of ~ 2 higher BBH merger rate than model $D18_{Z_\odot}$, but still within the 90 per cent credible interval inferred by the LIGO-Virgo collaboration (LVC, $R_{\rm BBH} \sim 24-112$ Gpc^{-3} yr^{-1}, Abbott et al., 2019). The four kick prescriptions produce approximately the same BBH merger rate density, because all of them suppress natal kicks in massive BHs by approximately the same amount.

5.4 Discussion

Recent studies (Giacobbo and Mapelli, 2018; Giacobbo and Mapelli, 2019b; Mapelli and Giacobbo, 2018; Chruslinska et al., 2018; Belczynski et al., 2018; Kruckow et al., 2018; Chruslinska et al., 2019) have shown that it is quite difficult to match the BNS merger rate inferred from GW170817 ($R_{\rm GW170817}$) with state-of-the-art population-synthesis models. Models describing natal kicks as in Hobbs et al. (2005) produce a merger rate density lower than the range inferred from GW170817. In order to match $R_{\rm GW170817}$, Giacobbo and Mapelli (2018) had to introduce model σ15 with very low natal kicks. On the other hand, model σ15 does not match the observed proper motions of young single pulsars (Hobbs et al., 2005; Verbunt et al., 2017).

Our new kick prescriptions (models Ej1 and Ej2) solve this tension with data, because they match $R_{\rm GW170817}$ and at the same time they reproduce the natal kicks of young pulsars. Moreover, Ej1 and Ej2 naturally account for the difference between kicks produced by CCSNe of single stars, ECSNe and ultra-stripped SNe in binary stars (Tauris et al., 2017).

The only parameter we need to set to a rather unusual value in order to match $R_{\rm GW170817}$ is the α parameter of CE. Our models Ej1 and Ej2 require $\alpha \geq 3$ to match $R_{\rm GW170817}$ (see Appendix D) and we assume $\alpha = 5$ as a fiducial value. According to

the α formalism (Webbink, 1984; Webbink, 1985; de Kool, 1990b), values of $\alpha > 1$ require that additional sources of energy assist the orbital energy of the system in ejecting the envelope (see Ivanova et al., 2013 for a review). Recently, Fragos et al. (2019) have presented one-dimensional hydrodynamic simulations of a neutron-star binary evolving through CE. Their results support very large values of $\alpha \approx 5$, consistent with our work. Once more, this highlights the need for a better physical model of the CE process. Another possibility is that GW170817 was a very lucky event, leading to an overestimate of the local merger rate. A more accurate estimate of the observed merger rate will be available in the next few months, because the third observing run of LVC is currently ongoing.

The key ingredient in our prescriptions is the dependence of $v_{\rm kick}$ on the mass of the ejecta ($v_{\rm kick} \propto m_{\rm ej}$). Models adopting the fallback formalism (Fryer et al., 2012) predict significantly larger kicks for NSs even if they come from ultra-stripped SNe, because in this formalism $v_{\rm kick} \propto m_{\rm ej}/m_{\rm fin}$ (i.e. the contribution of $m_{\rm ej}$ to the kick is compensated by the stellar mass $m_{\rm fin}$ at the onset of the SN). The only models that predict a similar behavior to our prescriptions are those presented in Bray and Eldridge (2016) and Bray and Eldridge (2018). Bray and Eldridge (2018) derive a BNS merger rate density $R_{\rm BNS} \sim 3860$ Gpc^{-3} yr^{-1}. The difference with respect to our results might arise from the calculation of the local merger rate (Bray and Eldridge, 2018 consider only the local SFR, without taking into account the evolution of metallicity across cosmic time) and from different population-synthesis codes.

5.5 Summary

We have proposed a new simple formalism to implement NS and BH kicks in population-synthesis simulations. We describe kick velocities as $v_{\rm kick} \propto f_{\rm H05}\, m_{\rm ej}\, m_{\rm rem}^{-1}$, where $f_{\rm H05}$ is a random number drawn from a Maxwellian distribution with one-dimensional rms $\sigma = 265$ km s^{-1} (Hobbs et al., 2005), $m_{\rm ej}$ is the mass of the ejecta and $m_{\rm rem}$ the mass of the compact object. We have included this formalism in our population-synthesis code MOBSE.

This formalism can naturally account for the differences between core-collapse SNe (CCSNe) of single stars and electron-capture SNe (ECSNe) or ultra-stripped SNe occurring in binary systems. In fact, CCSNe of single stars have larger values of $m_{\rm ej}$ than ECSNe, ultra-stripped SNe and other SNe occurring in interacting binaries. Hence, the kicks of NSs in interacting binary systems are significantly lower than the kicks of single NSs (Fig. 5.1 and Table 5.2).

The kicks of BHs are generally lower than the kicks of NSs (Fig. 5.2 and Table 5.2), because $m_{\rm rem}$ is significantly larger and $m_{\rm ej}$ is generally lower than for NSs (in the case of direct collapse $m_{\rm ej} = 0$, thus the kick is zero).

We estimate the local merger rate density of BNSs ($R_{\rm BNS}$), BHNSs ($R_{\rm BHNS}$) and BBHs ($R_{\rm BBH}$) with the new kick formalism. The merger rate density of BBHs and BHNSs is extremely sensitive to metallicity evolution. With the new kick prescriptions, we find $R_{\rm BBH} \sim 40-50\,{\rm Gpc^{-3}\,yr^{-1}}$ and $R_{\rm BHNS} \sim 5-10\,{\rm Gpc^{-3}\,yr^{-1}}$, when adopting model $D18_{Z_\odot}$ for the cosmic evolution of metallicity. These results are consistent with estimates from the LVC (Abbott et al., 2018; Abbott et al., 2019).

The BNS merger rate density depends very mildly on metallicity evolution. With the new kick formalism, we estimate $R_{\rm BNS} \sim 600-700\,{\rm Gpc^{-3}\,yr^{-1}}$, consistent with the rate inferred from GW170817 (Abbott et al., 2018). Interestingly, the BNS merger rate density we find with the new kick prescriptions is extremely close to the one we derived with our previous model $\sigma 15$ (Giacobbo and Mapelli, 2018), that assumes extremely low NS kicks (drawn from a Maxwellian with one-dimensional rms $\sigma = 15$ km s^{-1}). Model $\sigma 15$ matches $R_{\rm GW170817}$ but is in tension with the proper motions of several young Galactic pulsars, while the new kick formalism overcomes this issue.

In conclusion, our new kick formalism is consistent with both observations of proper motions from young Galactic pulsars (Hobbs et al., 2005) and with the merger rate density of BBHs, BHNSs and BNSs inferred from the LVC (Abbott et al., 2018; Abbott et al., 2019). These results, together with its intrinsic simplicity, make our new kick formalism an interesting prescription for population synthesis simulations.

CHAPTER 6

CONCLUSIONS

In this thesis, I have adopted numerical techniques to investigate the formation and evolution of compact-object binaries (COBs). Specifically, I have explored the effects of natal kicks and common envelope (CE) on the evolution of massive stellar binaries, as well as the impact of the progenitor's metallicity on the properties of compact objects.

To study the formation and evolution of COBs, I used population-synthesis simulations. In particular, I have developed MOBSE, an upgraded and customized version of BSE (one of the most widely used binary population-synthesis codes Hurley et al., 2002). With respect to standard BSE, I have included in MOBSE an up-to-date formalism for the evolution of massive stars, including i) a description of mass loss by stellar winds depending on both metallicity and the electron-scattering Eddington factor; ii) several recent prescriptions for core-collapse, electron-capture, pulsational pair-instability and pair-instability supernovae (SNe), and iii) a new treatment for natal kicks.
First of all, my study confirms that the mass of BHs in BHBs strongly depends on the progenitor's metallicity: metal-poor stars produce heavier BHs (Giacobbo et al., 2018; Giacobbo and Mapelli, 2018). Moreover, even the number of BHBs depends on the progenitor's metallicity. I found that metal-poor binaries tend to produce more BHBs than metal-rich ones. In my simulations, the most massive BHBs have a total mass of about $130\,M_{\odot}$ but they do not merge within a Hubble time because their semi-major axes are too large (Giacobbo et al., 2018; Giacobbo and Mapelli, 2018). In addition, the maximum mass of BHs in merging BHBs is $\sim 45\,M_{\odot}$, in agreement with the possible upper mass cut-off proposed by Fishbach and Holz (2017) and Wysocki et al. (2018) and consistent with O1 and O2 LIGO-Virgo data (Abbott et al., 2019. On the other hand, this upper limit holds only for isolated binary evolution. In the case of dynamical evolution, some of the most massive BHs (with mass $45-65\,M_{\odot}$) might have the chance to merge within a Hubble time as a consequence of dynamical interactions (e.g. Mapelli, 2016; Di Carlo et al., 2019).
With respect to BHBs, DNSs are less sensitive to metallicity, while SN mechanisms have a stronger impact on their evolution. In particular, I studied the effect of the electron-capture SNe (ECSNe) on the formation of (merging) DNSs (Giacobbo and Mapelli, 2019b). ECSNe are expected to be less energetic and to produce slow NSs. I find that slow (but not zero) natal kicks favour the formation of merging DNSs,

especially if the slow NS is the first one to be produced (see Chruslinska et al., 2017; Kruckow et al., 2018 and Tauris et al., 2017 for different arguments). Indeed, when the first SN happens, it is likely that no other processes (e.g. a CE phase) able to shrink the binary have occurred yet. Thus, the system can be easily unbound. In contrast, when the second SN occurs, the system has already passed through a CE, that reduced its semi-larger axis. Thus, a large kick by the second SN facilitates the formation of highly eccentric orbits (if it does not unbind the binary), which are more likely to merge via GW emission.

My simulations also show that the CE phase is crucial for the formation of merging COBs (Giacobbo and Mapelli, 2018). CE can help shrinking the semi-major axis of a binary system enough to allow it to merge in less than a Hubble time.

In order to quantify how many mergers we could expect in a coeval stellar population within a Hubble time, I have defined the merger efficiency (η) as the total number of mergers integrated over a Hubble time divided by the total mass of that population. I found that natal kicks, CE efficiency (α) and metallicity (Z) strongly affect η, but in different way according with the COB type (i.e. BHBs, DNSs, BHNSs). In particular, η for BHBs is significantly higher at low Z (up to four orders of magnitude) than at high Z. I found a similar dependence for BHNSs. In contrast, η for DNSs depends mildly on the metallicity. On the other hand, I found that merging DNSs form more efficiently if we assume low natal kicks. Moreover, I have shown that the easier CE ejection is (high α), the higher η for DNSs. For example, η is boosted by an order of magnitude assuming $\alpha = 5$ instead of $\alpha = 1$. For both BHBs and BHNSs the dependence on α is complicated by the fact that the evolution of the radii of BH progenitors is more sensitive to metallicity.

Finally, I have estimated the local merger rate density (R) (see Giacobbo and Mapelli, 2018; Spera et al., 2019). To do that, I have coupled η from my simulations with some prescriptions for the cosmological metallicity evolution and the star formation rate (SFR) density evolution. My estimates of the BHNS local merger-rate density ($R_{\rm BHNS}$) are always in agreement with that inferred by the LIGO-Virgo collaboration (LVC,$R_{\rm BHNS} < 610$ Gpc^{-3} yr^{-1}, Abbott et al. 2018). On the other hand, my predictions for the local merger rate density of BHBs ($R_{\rm BHB}$) match that of the LVC ($\sim 24-112$ Gpc^{-3} yr^{-1} Abbott et al., 2019) only for specific combinations of SFR, cosmological metallicity evolution and α. In particular, metallicity evolution models where the average metallicity of the Universe reaches higher values ($\gtrsim 0.02$) at redshift ~ 0 produce the best agreement with the BHB merger rate density inferred by the LVC. The estimated merger rate density of DNSs ($R_{\rm DNS}$) is consistent with the value inferred from GW data only if I consider $\alpha \gtrsim 2$ and relatively low natal kicks.

In the last chapter of my Thesis, I have proposed a new prescription for the treatment of natal kicks in population-synthesis simulations, based on the idea that the mass of the ejecta modulates the strength of the natal kicks (see Bray and Eldridge, 2016; Tauris et al., 2017). Adopting this new approach, I have both reproduced the natal kick distribution of observed young Galactic pulsars and I have obtained a $\mathcal{R}_{\rm DNS}$ in agreement with the local merger rate inferred by the LVC.

During my PhD I mainly compared my simulations with the LIGO-Virgo observations but the merger between two compact objects represents only the final stage of the evolution of a massive binary. Indeed, during its life a binary system passes through many different phases. In follow-up studies, I will apply my population-synthesis code MOBSE to study also other observed binaries along the formation path of massive binaries. In particular, I will compare my simulations with the properties of high-mass X-ray binaries and Galactic DNS systems. This will help me to improve and calibrate my models and to better understand the formation channel of COBs.

CHAPTER 7

RIASSUNTO

La prima rilevazione diretta delle onde gravitazionali (GW), GW150914, ha aperto l'era dell'astronomia GW. Oltre a GW150914, durante le prime due sessioni osservative (O1 e O2) sono state segnalate altre dieci detezioni. Nove di esse sono interpretate come la fusione di due buchi neri (BH), mentre la rimanente, GW170817, è associata alla fusione di due stelle di neutroni (NS). Inoltre, l'evento GW170817 è stato accompagnato dall'emissione di radiazioni elettromagnetiche osservate su una vasta gamma di lunghezze d'onda. Ora che sia le binarie di BH (BHBs) che le doppie stelle di neutroni (DNS) sono stati rilevati dalla LIGO-Virgo Collaboration (LVC), la coalescenza di un NS con un BH è l'unico evento di fusione mancante che ci aspettiamo di osservare nella gamma di frequenza dei rivelatori GW a terra. Tuttavia, l'analisi preliminare dell'attuale ciclo di osservazione (O3) sembra suggerire che alcuni segnali potrebbero essere originati dalla fusione di sistemi BHNS.
Pertanto, il rilevamento GW ha confermato che i BHB possono fondersi entro un tempo di Hubble. Inoltre, le osservazioni di GW hanno dimostrato l'esistenza di BH massicci, con massa superiore a $\gtrsim 30\,M_\odot$, e la relazione tra la fusione di due NS e i lampi gamma brevi (sGRB).
Nonostante l'importanza degli oggetti compatti di origine stellare per una gran varietà di processi astrofisici (es. binarie a raggi X, emissione di GW, GRB, ecc), il loro spettro di massa è ancora oggetto di dibattito. I due processi più importanti che influenzano la formazione di residui stellari compatti sono i venti stellari e le esplosioni di supernova (SN). Stelle massicce dove i venti stellari sono efficaci possono perdere la maggior parte della loro massa durante la loro vita e l'esplosione di SN alla fine della loro vita può rimuovere la maggior parte della massa rimanente. Questo dovrebbe produrre BH leggeri ($\lesssim 20\,M_\odot$). D'altra parte, i venti stellari dipendono dalla metallicità stellare. Ci aspettiamo, infatti, che i venti stellari siano più efficienti nelle stelle ricche di metallo che in quelle povere di metallo. In particolare, i venti stellari nelle stelle povere di metallo ($\lesssim 0.5Z_\odot$) possono essere così inefficaci che le stelle trattengono abbastanza materiale da collassare direttamente nei BH evitando l'esplosione di SN. In questo scenario, i BH risultanti sono sostanzialmente più pesanti. Secondo queste previsioni, i BH massicci ($\gtrsim 30\,M_\odot$) potrebbero essere spiegati come residui di progenitori poveri di metallo ($\lesssim 0.5ZZ_\odot$).
Anche la formazione di binarie di oggetti compatti (COB) è oggetto di un intenso dibattito. Una COB può fondersi in un tempo di Hubble solo se la sua separazione

orbitale iniziale è dell'ordine di decine di raggi solari. Quali sono i canali evolutivi che possono portare alla formazione di COB così stretti?
Sono stati proposti diversi scenari per la formazione di COBs e uno dei più importanti è rappresentato dall'evoluzione di sistemi binari massicci e isolati. Infatti, la stragrande maggioranza delle stelle, e soprattutto le stelle massicce, nascono in sistemi binari. Le stelle in binarie strette subiscono diversi processi complessi, che possono influenzare fortemente la massa degli oggetti compatti finali e la loro separazione orbitale (es. trasferimento di massa e inviluppo comune), comunque alcuni di questi processi sono ancora poco compresi.
Lo scopo della mia tesi è quello di studiare la formazione di COB attraverso l'evoluzione di binarie isolate di stelle massicce. Il mio obiettivo è quello di contribuire a capire l'origine degli eventi GW osservati dall'LVC e di fare previsioni per future rilevazioni. Per studiare le COB, ho utilizzato simulazioni di sintesi di popolazione. Quando ho iniziato questo progetto, la maggior parte dei codici di sintesi di popolazione disponibili non includeva i più recenti modelli di venti stellare e le prescrizioni delle SN. Durante il mio dottorato, ho sviluppato MOBSE (che sta per 'Massive Objects in Binary Stellar Evolution'), una versione personalizzata e aggiornata del popolare codice BSE (Hurley et al., 2002). Per quanto riguarda la versione pubblica di BSE, MOBSE contiene equazioni aggiornate per i venti stellari dipendenti dalla metallicità, compresa la dipendenza dei venti stellari dal fattore di Eddington. Inoltre, ho implementato in MOBSE diverse recenti prescrizioni per SNe, un trattamento per le SNe per instabilità di coppia e nuove ricette per calcolare i kick iniziali. Questi ingredienti sono essenziali per catturare l'evoluzione delle stelle massicce. In particolare, con MOBSE è possibile formare BH con massa fino a $\sim 65\,M_\odot$ a seconda della metallicità, mentre con le vecchie prescrizioni non siamo stati in grado di produrre i BH più massicci osservati dall'LVC.
Ho usato MOBSE per simulare l'evoluzione di grandi griglie di stelle binarie massicce ($\gtrsim 10^8$ sistemi per griglia). Poi, ho analizzato tali simulazioni per studiare come la metallicità dei progenitori (Z), l'inviluppo comune (CE) e i kick iniziali influenzano le proprietà delle popolazioni di COB. Ho trovato che i BHB più massicci ($\gtrsim 100\,M_\odot$) possono formarsi solo a bassa metallicità ($Z \lesssim 0.1 Z_\odot$). Tali sistemi con massa totale $\gtrsim 100\,M_\odot$ non si fondono in un Hubble a causa dei loro grandi semi-assi maggiori. Poiché il tempo scala di fusione per emissione di GW dipende fortemente dalla massa degli oggetti compatti, la metallicità incide anche sul tasso di fusione sia dei BHB che dei BHNS. Ho definito l'efficienza di fusione (η) come il numero totale di fusioni integrate in un periodo di Hubble in una popolazione coeva diviso per la massa totale di quella popolazione ($\eta \propto \frac{N_{\rm mergers}}{M_{\rm tot}}$). Ho trovato che

η è di circa quattro ordini di grandezza superiore a basse metallicità ($\eta \sim 10^{-4}\,M_{\odot}^{-1}$ a $Z \simeq 0.01 Z_{\odot}$) che ad alte metallicità (η è $\sim 10^{-8}\,M_{\odot}^{-1}$ a $Z \simeq Z_{\odot}$).
Dalle mie simulazioni, è anche evidente che l'efficienza del CE (misurata dal parametro α) gioca un ruolo importante nella formazione di COB stretti. Per i DNS, ho trovato che più l'inviluppo è facile da espellere (alto α), più alto è η. In particolare, η viene incrementato di circa un ordine di grandezza se assumo $\alpha = 5$ invece di $\alpha \leq 1$. Sia per i BHB che per i BHNS la dipendenza da α è più complicata. Ciò deriva dal fatto che l'evoluzione dei raggi dei progenitori dei BH è più sensibile alla metallicità e i raggi stellari sono cruciali per determinare il risultato della fase CE.
Una delle quantità importanti che l'LVC può dedurre dai rilevamenti di GW è la densità locale del tasso di fusione ($R_{\rm loc}$). Ho adottato un approccio basato sui dati per stimare $R_{\rm loc}$ a partire dalle mie simulazioni. In pratica, ho combinato η (dalle mie simulazioni) con alcune prescrizioni per l'evoluzione della metallicità cosmologica e l'evoluzione della densità di formazione stellare (SFR). Con questo formalismo, ho stimato un $R_{\rm loc}$ per le BHNS fino a poche decine di fusioni $\mathrm{Gpc}^{-3}\,\mathrm{yr}^{-1}$ per tutte le diverse combinazioni di α, kick iniziali, evoluzione cosmologica della metallicità e SFR che ho considerato, coerente con il limite superiore dedotto dall'LVC ($R_{\rm loc,BHNS} \lesssim 610\ \mathrm{Gpc}^{-}3\mathrm{yr}^{-1}$).
D'altra parte, la mia previsione per $R_{\rm loc}$ dei BHB corrisponde a quella dedotta dalla LVC ($R_{\rm loc,BHB} \simeq 24-112\ \mathrm{Gpc}^{-3}\mathrm{yr}^{-1}$) solo per specifiche combinazioni di SFR, evoluzione cosmologica della metallicità e α. In particolare, la densità del tasso di fusione dei BHB è molto sensibile all'evoluzione della metallicità. Infine, sono stato in grado di eguagliare $R_{\rm loc}$ della LVC per i DNS ($R_{\rm loc,DNS} \simeq 110-3840\ \mathrm{Gpc}^{-3}\mathrm{yr}^{-1}$) solo considerando alti α e relativamente bassi kick iniziali.
In particolare, ho proposto una nuova prescrizione per il trattamento dei kick iniziali. L'idea di base è che la forza del kick iniziali è proporzionale alla massa espulsa durante l'esplosione di SN come suggerito da recenti studi idrodinamici. Rispetto alle altre prescrizioni attualmente adottate dai codici di sintesi di popolazioni, questo nuovo approccio permette di ottenere sia la distribuzione dei kick iniziali delle pulsar galattiche giovani sia $R_{\rm loc}$ desumibile dalla LVC. Tuttavia, per eguagliare $R_{\rm loc}$ della LVC ho dovuto adottare un'alta efficienza CE ($\alpha \gtrsim 2$).

Acronyms

BH : black hole

BHB : black hole binary

BHNS : black hole-neutron star

CCSN : core-collapse supernova

CE : common envelope

CMB : cosmic microwave background

COB : compact-object binary

DNS : double neutron star

ECSN : electron-capture supernova

GR : general relativity

GRB : gamma-ray burst

GW : gravitational wave

IMF : initial mass function

LBV : luminous blue variable

MS : main sequance

NS : neutron star

PISN : pair-instability supernova

PPISN : pulsational pair-instability supernova

PTA : pulsar timing array

SFR : star formation rate

SMBH : supermassive black hole

SN : supernova

WR : Wolf-Rayet

ZAMS : zero age main sequence

List of Tables

List of Figures

BIBLIOGRAPHY

Aasi et al. et al. (2015). "Advanced LIGO". In: *Classical and Quantum Gravity* 32.7, 074001, p. 074001.

Abbott, B. P. et al. (2016a). "Astrophysical Implications of the Binary Black-hole Merger GW150914". In: ApJ 818, L22, p. L22.

— (2016b). "Binary Black Hole Mergers in the First Advanced LIGO Observing Run". In: *Physical Review X* 6.4, 041015, p. 041015.

— (2016c). "GW151226: Observation of Gravitational Waves from a 22-Solar-Mass Binary Black Hole Coalescence". In: Phys. Rev. Lett. 116.24, 241103, p. 241103.

— (2016d). "Observation of Gravitational Waves from a Binary Black Hole Merger". In: *Physical Review Letters* 116.6, 061102, p. 061102.

— (2016e). "Upper Limits on the Rates of Binary Neutron Star and Neutron Star-Black Hole Mergers from Advanced LIGOś First Observing Run". In: ApJ 832, L21, p. L21.

Abbott, B. P. et al. (2017a). "Gravitational Waves and Gamma-Rays from a Binary Neutron Star Merger: GW170817 and GRB 170817A". In: ApJ 848, L13, p. L13.

— (2017b). "GW170104: Observation of a 50-Solar-Mass Binary Black Hole Coalescence at Redshift 0.2". In: *Physical Review Letters* 118.22, 221101, p. 221101.

— (2017c). "GW170608: Observation of a 19 Solar-mass Binary Black Hole Coalescence". In: ApJ 851, L35, p. L35.

— (2017d). "GW170814: A Three-Detector Observation of Gravitational Waves from a Binary Black Hole Coalescence". In: *Physical Review Letters* 119.14, 141101, p. 141101.

— (2017e). "GW170817: Observation of Gravitational Waves from a Binary Neutron Star Inspiral". In: Phys. Rev. Lett. 119.16, 161101, p. 161101.

— (2017f). "Multi-messenger Observations of a Binary Neutron Star Merger". In: ApJ 848, L12, p. L12.

Abbott, B. P. et al. (2018). "GWTC-1: A Gravitational-Wave Transient Catalog of Compact Binary Mergers Observed by LIGO and Virgo during the First and Second Observing Runs". In: *arXiv e-prints*.

Abbott, B. P. et al. (2019). "Binary Black Hole Population Properties Inferred from the First and Second Observing Runs of Advanced LIGO and Advanced Virgo". In: ApJ 882.2, L24, p. L24.

Abbott, D. C. and L. B. Lucy (1985). "Multiline transfer and the dynamics of stellar winds." In: ApJ 288, pp. 679–693.

Acernese, F. et al. (2015). “Advanced Virgo: a second-generation interferometric gravitational wave detector”. In: *Classical and Quantum Gravity* 32.2, 024001, p. 024001.

Alexander, K. D. et al. (2017). “The Electromagnetic Counterpart of the Binary Neutron Star Merger LIGO/Virgo GW170817. VI. Radio Constraints on a Relativistic Jet and Predictions for Late-time Emission from the Kilonova Ejecta”. In: ApJ 848.2, p. L21.

Amaro-Seoane, Pau et al. (2017). “Laser Interferometer Space Antenna”. In: *arXiv e-prints*, arXiv:1702.00786, arXiv:1702.00786.

Andrews, J. J. et al. (2015). “Evolutionary Channels for the Formation of Double Neutron Stars”. In: ApJ 801, 32, p. 32.

Antelis, Javier M. and Claudia Moreno (2017). “Obtaining gravitational waves from inspiral binary systems using LIGO data”. In: *Eur. Phys. J. Plus* 132.1. [Erratum: Eur. Phys. J. Plus132,no.2,103(2017)], p. 10.

Antonini, F. et al. (2017). “Binary Black Hole Mergers from Field Triples: Properties, Rates, and the Impact of Stellar Evolution”. In: ApJ 841, 77, p. 77.

Arca Sedda, M. and M. Benacquista (2019). “Using final black hole spins and masses to infer the formation history of the observed population of gravitational wave sources”. In: MNRAS 482.3, pp. 2991–3010.

Arzoumanian, Z. et al. (2002). “The Velocity Distribution of Isolated Radio Pulsars”. In: ApJ 568, pp. 289–301.

Askar, A. et al. (2016). “MOCCA code for star cluster simulation: comparison with optical observations using COCOA”. In: *Star Clusters and Black Holes in Galaxies across Cosmic Time*. Ed. by Y. Meiron et al. Vol. 312. IAU Symposium, pp. 262–263.

Askar, Abbas et al. (2017). “MOCCA-SURVEY Database - I. Coalescing binary black holes originating from globular clusters”. In: MNRAS 464.1, pp. L36–L40.

Atri, P. et al. (2019). “Potential Kick Velocity distribution of black hole X-ray binaries and implications for natal kicks”. In: *arXiv e-prints*.

Banerjee, Sambaran (2018). “Stellar-mass black holes in young massive and open stellar clusters and their role in gravitational-wave generation - II”. In: MNRAS 473.1, pp. 909–926.

Barkat, Z. et al. (1967). “Dynamics of Supernova Explosion Resulting from Pair Formation”. In: *Physical Review Letters* 18, pp. 379–381.

Barrett, Jim W. et al. (2017). “Exploring the Parameter Space of Compact Binary Population Synthesis”. In: *Astroinformatics*. Ed. by Massimo Brescia et al. Vol. 325. IAU Symposium, pp. 46–50.

Belczynski, K. et al. (2002). “A Comprehensive Study of Binary Compact Objects as Gravitational Wave Sources: Evolutionary Channels, Rates, and Physical Properties”. In: ApJ 572, pp. 407–431.

Belczynski, K. et al. (2004). “A Comprehensive Study of Young Black Hole Populations”. In: ApJ 611, pp. 1068–1079.

Belczynski, K. et al. (2007). “On the Rarity of Double Black Hole Binaries: Consequences for Gravitational Wave Detection”. In: ApJ 662, pp. 504–511.

Belczynski, K. et al. (2010). “On the Maximum Mass of Stellar Black Holes”. In: ApJ 714.2, p. 1217.

Belczynski, K. et al. (2016a). “The effect of pair-instability mass loss on black-hole mergers”. In: A&A 594, A97, A97.

Belczynski, K. et al. (2016b). “The first gravitational-wave source from the isolated evolution of two stars in the 40-100 solar mass range”. In: Nature 534, pp. 512–515.

Belczynski, K. et al. (2017). “The evolutionary roads leading to low effective spins, high black hole masses, and O1/O2 rates of LIGO/Virgo binary black holes”. In: *arXiv e-prints*, arXiv:1706.07053, arXiv:1706.07053.

Belczynski, K. et al. (2018). “The origin of the first neutron star - neutron star merger”. In: A&A 615, A91, A91.

Belczynski, Krzysztof et al. (2008). “Compact Object Modeling with the StarTrack Population Synthesis Code”. In: ApJS 174.1, pp. 223–260.

Beniamini, P. and T. Piran (2016). “Formation of double neutron star systems as implied by observations”. In: MNRAS 456, pp. 4089–4099.

Bestenlehner, J. M. et al. (2014). “The VLT-FLAMES Tarantula Survey. XVII. Physical and wind properties of massive stars at the top of the main sequence”. In: A&A 570, A38, A38.

Bethe, H. A. (1990). “Supernova mechanisms”. In: *Reviews of Modern Physics* 62, pp. 801–866.

Bethe, H. A. and G. E. Brown (1998). “Evolution of Binary Compact Objects That Merge”. In: ApJ 506, pp. 780–789.

Bishop, Nigel T. and Luciano Rezzolla (2016). “Extraction of gravitational waves in numerical relativity”. In: *Living Reviews in Relativity* 19.1, 2, p. 2.

Bisnovatyi-Kogan, G. S. (1993). “Asymmetric neutrino emission and formation of rapidly moving pulsars”. In: *Astronomical and Astrophysical Transactions* 3, pp. 287–294.

Blaauw, A. (1961). “On the origin of the O- and B-type stars with high velocities (the “run-away” stars), and some related problems”. In: Bull. Astron. Inst. Netherlands 15, p. 265.

Blondin, J. M. and A. Mezzacappa (2006). “Generating Pulsar Spin in Supernovae”. In: *American Astronomical Society Meeting Abstracts*. Vol. 38. Bulletin of the American Astronomical Society, p. 1099.

Bogomazov, A. I. et al. (2007). “Evolution of close binaries and gamma-ray bursts”. In: *Astronomy Reports* 51, pp. 308–317.

Bond, J. R. et al. (1984). “The evolution and fate of Very Massive Objects”. In: ApJ 280, pp. 825–847.

Bortolas, Elisa and Michela Mapelli (2019). “Can supernova kicks trigger EMRIs in the Galactic Centre?” In: MNRAS 485.2, pp. 2125–2138.

Brandt, W. N. et al. (1995). “On the high space velocity of X-ray Nova SCO 1994: implications for the formation of its black hole”. In: MNRAS 277, pp. L35–L40.

Bray, J. C. and J. J. Eldridge (2016). “Neutron star kicks and their relationship to supernovae ejecta mass”. In: MNRAS 461, pp. 3747–3759.

— (2018). “Neutron star kicks - II. Revision and further testing of the conservation of momentum ‘kick’ model”. In: MNRAS 480, pp. 5657–5672.

Bresolin, F. and R. P. Kudritzki (2004). “Stellar Winds of Hot Massive Stars Nearby and Beyond the Local Group”. In: *Origin and Evolution of the Elements*, p. 283.

Bressan, A. et al. (2012). “PARSEC: stellar tracks and isochrones with the PAdova and TRieste Stellar Evolution Code”. In: MNRAS 427, pp. 127–145.

Brisken, W. F. et al. (2002). “Very Long Baseline Array Measurement of Nine Pulsar Parallaxes”. In: ApJ 571, pp. 906–917.

Brisken, W. F. et al. (2003). “Proper-Motion Measurements with the VLA. II. Observations of 28 Pulsars”. In: AJ 126, pp. 3090–3098.

Bruenn, S. W. et al. (2009). “2D and 3D core-collapse supernovae simulation results obtained with the CHIMERA code”. In: *Journal of Physics Conference Series*. Vol. 180. Journal of Physics Conference Series, p. 012018.

Burgay, M. et al. (2003). “An increased estimate of the merger rate of double neutron stars from observations of a highly relativistic system”. In: *Nature* 426.6966, pp. 531–533.

Burrows, A. (2013). “Colloquium: Perspectives on core-collapse supernova theory”. In: *Reviews of Modern Physics* 85, pp. 245–261.

Burrows, A. and J. Hayes (1996). “Pulsar Recoil and Gravitational Radiation Due to Asymmetrical Stellar Collapse and Explosion”. In: *Physical Review Letters* 76, pp. 352–355.

Burrows, A. et al. (2006). “A New Mechanism for Core-Collapse Supernova Explosions”. In: ApJ 640.2, pp. 878–890.

Carr, B. J. and S. W. Hawking (1974). “Black Holes in the Early Universe”. In: *Gravitational Radiation and Gravitational Collapse*. Ed. by C. Dewitt-Morette. Vol. 64. IAU Symposium, p. 184.

Carr, Bernard et al. (2016). “Primordial black holes as dark matter”. In: Phys. Rev. D 94.8, 083504, p. 083504.

Chen, K.-J. et al. (2014). “Two-dimensional Simulations of Pulsational Pair-instability Supernovae”. In: ApJ 792, 28, p. 28.

Chen, Y. et al. (2015). “PARSEC evolutionary tracks of massive stars up to 350 $M_{\odot}$ at metallicities $0.0001 \leq Z \leq 0.04$”. In: MNRAS 452, pp. 1068–1080.

Chornock, R. et al. (2017). “The Electromagnetic Counterpart of the Binary Neutron Star Merger LIGO/Virgo GW170817. IV. Detection of Near-infrared Signatures of r -process Nucleosynthesis with Gemini-South”. In: ApJ 848.2, p. L19.

Chruslinska, M. et al. (2017). “Constraints on the Formation of Double Neutron Stars from the Observed Eccentricities and Current Limits on Merger Rates”. In: Acta Astron. 67, pp. 37–50.

Chruslinska, M. et al. (2018). “Double neutron stars: merger rates revisited”. In: MNRAS 474, pp. 2937–2958.

Chruslinska, Martyna et al. (2019). “The influence of the distribution of cosmic star formation at different metallicities on the properties of merging double compact objects”. In: MNRAS 482.4, pp. 5012–5017.

Ciufolini, I. and F. Fidecaro, eds. (1996). *Gravitational Waves: Sources and Detectors*.

Claeys, J. S. W. et al. (2014). “Theoretical uncertainties of the Type Ia supernova rate”. In: A&A 563, A83, A83.

Clausen, D. et al. (2013). “Black hole-neutron star mergers in globular clusters”. In: MNRAS 428, pp. 3618–3629.

Colpi, M. et al. (2003). “Probing the Presence of a Single or Binary Black Hole in the Globular Cluster NGC 6752 with Pulsar Dynamics”. In: ApJ 599, pp. 1260–1271.

Cordes, J. M. and D. F. Chernoff (1998). “Neutron Star Population Dynamics. II. Three-dimensional Space Velocities of Young Pulsars”. In: ApJ 505, pp. 315–338.

Coulter, D. A. et al. (2017). “Swope Supernova Survey 2017a (SSS17a), the optical counterpart to a gravitational wave source”. In: *Science* 358, pp. 1556–1558.

Coward, D. M. et al. (2012). “The Swift short gamma-ray burst rate density: implications for binary neutron star merger rates”. In: MNRAS 425, pp. 2668–2673.

Cowperthwaite, P. S. et al. (2017). “The Electromagnetic Counterpart of the Binary Neutron Star Merger LIGO/Virgo GW170817. II. UV, Optical, and Near-infrared Light Curves and Comparison to Kilonova Models”. In: ApJ 848.2, p. L17.

De Cia, A. et al. (2018). “The cosmic evolution of dust-corrected metallicity in the neutral gas”. In: A&A 611, A76, A76.

De Donder, E. and D. Vanbeveren (2004). “The influence of neutron star mergers on the galactic chemical enrichment of r-process elements”. In: New A 9.1, pp. 1–16.

de Kool, M. (1990a). “Common Envelope Evolution and Double Cores of Planetary Nebulae”. In: ApJ 358, p. 189.

— (1990b). “Common Envelope Evolution and Double Cores of Planetary Nebulae”. In: ApJ 358, p. 189.

de Mink, S. E. and K. Belczynski (2015). “Merger Rates of Double Neutron Stars and Stellar Origin Black Holes: The Impact of Initial Conditions on Binary Evolution Predictions”. In: ApJ 814, 58, p. 58.

de Mink, S. E. and I. Mandel (2016). “The chemically homogeneous evolutionary channel for binary black hole mergers: rates and properties of gravitational-wave events detectable by advanced LIGO”. In: MNRAS 460, pp. 3545–3553.

Dessart, L. et al. (2006). “Multidimensional Simulations of the Accretion-induced Collapse of White Dwarfs to Neutron Stars”. In: ApJ 644, pp. 1063–1084.

Dewi, J. D. M. and O. R. Pols (2003). “The late stages of evolution of helium star-neutron star binaries and the formation of double neutron star systems”. In: MNRAS 344, pp. 629–643.

Dewi, J. D. M. and T. M. Tauris (2000). “On the energy equation and efficiency parameter of the common envelope evolution”. In: A&A 360, pp. 1043–1051.

Dewi, J. D. M. et al. (2005). “The spin period-eccentricity relation of double neutron stars: evidence for weak supernova kicks?” In: MNRAS 363, pp. L71–L75.

Di Carlo, Ugo N. et al. (2019). “Merging black holes in young star clusters”. In: MNRAS 487.2, pp. 2947–2960.

Doherty, C. L. et al. (2015). “Super- and massive AGB stars - IV. Final fates - initial-to-final mass relation”. In: MNRAS 446, pp. 2599–2612.

Dominik, M. et al. (2012). “Double Compact Objects. I. The Significance of the Common Envelope on Merger Rates”. In: ApJ 759, 52, p. 52.

— (2013a). “Double Compact Objects. II. Cosmological Merger Rates”. In: ApJ 779, 72, p. 72.

— (2013b). “Double Compact Objects. II. Cosmological Merger Rates”. In: ApJ 779, 72, p. 72.

Dominik, M. et al. (2015). “Double Compact Objects III: Gravitational-wave Detection Rates”. In: ApJ 806, 263, p. 263.

Dunstall, P. R. et al. (2015). “The VLT-FLAMES Tarantula Survey. XXII. Multiplicity properties of the B-type stars”. In: A&A 580, A93, A93.

East, W. E. and F. Pretorius (2012). “Dynamical Capture Binary Neutron Star Mergers”. In: ApJ 760, L4, p. L4.

Einstein, A. (1915). “Zur allgemeinen Relativitätstheorie”. In: *Sitzungsberichte der Königlich Preußischen Akademie der Wissenschaften (Berlin), Seite 778-786.*

— (1916a). “Die Grundlage der allgemeinen Relativitätstheorie”. In: *Annalen der Physik* 354, pp. 769–822.

— (1916b). “Näherungsweise Integration der Feldgleichungen der Gravitation”. In: *Sitzungsberichte der Königlich Preußischen Akademie der Wissenschaften (Berlin), Seite 688-696.*

— (1918). “Über Gravitationswellen”. In: *Sitzungsberichte der Königlich Preußischen Akademie der Wissenschaften (Berlin), Seite 154-167.*

Eldridge, J. J. and E. R. Stanway (2016). “BPASS predictions for binary black hole mergers”. In: MNRAS 462.3, pp. 3302–3313.

Ertl, T. et al. (2016). “A Two-parameter Criterion for Classifying the Explodability of Massive Stars by the Neutrino-driven Mechanism”. In: ApJ 818, 124, p. 124.

Farr, W. M. et al. (2011). “The Mass Distribution of Stellar-mass Black Holes”. In: ApJ 741, 103, p. 103.

Farrow, Nicholas et al. (2019). “The Mass Distribution of Galactic Double Neutron Stars”. In: ApJ 876.1, 18, p. 18.

Faucher-Giguère, C.-A. and V. M. Kaspi (2006). “Birth and Evolution of Isolated Radio Pulsars”. In: ApJ 643, pp. 332–355.

Fishbach, Maya and Daniel E. Holz (2017). “Where Are LIGO’s Big Black Holes?” In: ApJ 851.2, L25, p. L25.

Fisher, R. et al. (2010). “The Role of Variations of Central Density of White Dwarf Progenitors upon Type IA Supernovae”. In: *Gravitation and Astrophysics*. Ed. by J. Luo et al., pp. 335–344.

Flannery, B. P. and E. P. J. van den Heuvel (1975). “On the origin of the binary pulsar PSR 1913 + 16”. In: A&A 39, pp. 61–67.

Foglizzo, T. et al. (2007). “Instability of a Stalled Accretion Shock: Evidence for the Advective-Acoustic Cycle”. In: ApJ 654, pp. 1006–1021.

Foglizzo, T. et al. (2015a). “The Explosion Mechanism of Core-Collapse Supernovae: Progress in Supernova Theory and Experiments”. In: PASA 32, e009, e009.

Foglizzo, Thierry et al. (2015b). “The Explosion Mechanism of Core-Collapse Supernovae: Progress in Supernova Theory and Experiments”. In: PASA 32, e009, e009.

Fong, W. et al. (2015). “A Decade of Short-duration Gamma-Ray Burst Broadband Afterglows: Energetics, Circumburst Densities, and Jet Opening Angles”. In: ApJ 815, 102, p. 102.

Fragos, T. et al. (2009). “Understanding Compact Object Formation and Natal Kicks. II. The Case of XTE J1118 + 480”. In: ApJ 697, pp. 1057–1070.

Fragos, Tassos et al. (2019). “The Complete Evolution of a Neutron-Star Binary through a Common Envelope Phase Using 1D Hydrodynamic Simulations”. In: *arXiv e-prints*, arXiv:1907.12573, arXiv:1907.12573.

Fryer, C. (2014). “Remnant Masses and Compact Binary Mergers”. In: *Proceedings of Frontier Research in Astrophysics (FRAPWS2014) held 26-31 May*, p. 4.

Fryer, C. et al. (1998). “Population Syntheses for Neutron Star Systems with Intrinsic Kicks”. In: ApJ 496, pp. 333–351.

Fryer, C. L. (1999). “Mass Limits For Black Hole Formation”. In: ApJ 522, pp. 413–418.

— (2006). “Fallback in stellar collapse”. In: New A Rev. 50, pp. 492–495.

Fryer, C. L. et al. (2001). “Pair-Instability Supernovae, Gravity Waves, and Gamma-Ray Transients”. In: ApJ 550, pp. 372–382.

Fryer, C. L. et al. (2012). “Compact Remnant Mass Function: Dependence on the Explosion Mechanism and Metallicity”. In: ApJ 749, 91, p. 91.

Fryer, Christopher L. and Alexander Kusenko (2006). “Effects of Neutrino-driven Kicks on the Supernova Explosion Mechanism”. In: ApJS 163.2, pp. 335–343.

Gallazzi, A. et al. (2008). “A census of metals and baryons in stars in the local Universe”. In: MNRAS 383, pp. 1439–1458.

Gessner, A. and H.-T. Janka (2018). “Hydrodynamical Neutron-star Kicks in Electron-capture Supernovae and Implications for the CRAB Supernova”. In: ApJ 865, 61, p. 61.

Giacobbo, N. and M. Mapelli (2018). “The progenitors of compact-object binaries: impact of metallicity, common envelope and natal kicks”. In: MNRAS 480, pp. 2011–2030.

Giacobbo, N. et al. (2018). “Merging black hole binaries: the effects of progenitor’s metallicity, mass-loss rate and Eddington factor”. In: MNRAS 474, pp. 2959–2974.

Giacobbo, Nicola and Michela Mapelli (2019a). "Revising natal kick prescriptions in population synthesis simulations". In: *arXiv e-prints*, arXiv:1909.06385, arXiv:1909.06385.

— (2019b). "The impact of electron-capture supernovae on merging double neutron stars". In: MNRAS 482.2, pp. 2234–2243.

Goldstein, A. et al. (2017). "An Ordinary Short Gamma-Ray Burst with Extraordinary Implications: Fermi-GBM Detection of GRB 170817A". In: ApJ 848, L14, p. L14.

Gräfener, G. and W.-R. Hamann (2008). "Mass loss from late-type WN stars and its Z-dependence. Very massive stars approaching the Eddington limit". In: A&A 482, pp. 945–960.

Gräfener, G. et al. (2011). "The Eddington factor as the key to understand the winds of the most massive stars. Evidence for a Γ-dependence of Wolf-Rayet type mass loss". In: A&A 535, A56, A56.

Gräfener, G. et al. (2012). "Stellar envelope inflation near the Eddington limit. Implications for the radii of Wolf-Rayet stars and luminous blue variables". In: A&A 538, A40, A40.

Grindlay, J. et al. (2006). "Short gamma-ray bursts from binary neutron star mergers in globular clusters". In: *Nature Physics* 2, pp. 116–119.

Gualandris, A. et al. (2005). "Has the Black Hole in XTE J1118+480 Experienced an Asymmetric Natal Kick?" In: ApJ 618, pp. 845–851.

Hall, P. D. and C. A. Tout (2014). "Core radii and common-envelope evolution". In: MNRAS 444, pp. 3209–3219.

Hansen, B. M. S. and E. S. Phinney (1997). "The pulsar kick velocity distribution". In: MNRAS 291, p. 569.

Heger, A. and S. E. Woosley (2002). "The Nucleosynthetic Signature of Population III". In: ApJ 567, pp. 532–543.

Heger, A. et al. (2003). "How Massive Single Stars End Their Life". In: ApJ 591, pp. 288–300.

Herant, Marc et al. (1994). "Inside the Supernova: A Powerful Convective Engine". In: ApJ 435, p. 339.

Hobbs, G. et al. (2005). "A statistical study of 233 pulsar proper motions". In: MNRAS 360, pp. 974–992.

Hulse, R. A. and J. H. Taylor (1974). "A High-Sensitivity Pulsar Survey". In: ApJ 191, p. L59.

— (1975). "Discovery of a pulsar in a binary system." In: *The Astrophysical Journal* 195, pp. L51–L53.

Hurley, J. R. et al. (2000). “Comprehensive analytic formulae for stellar evolution as a function of mass and metallicity”. In: MNRAS 315, pp. 543–569.

Hurley, J. R. et al. (2002). “Evolution of binary stars and the effect of tides on binary populations”. In: MNRAS 329, pp. 8 97–928.

Iben Icko, Jr. and Mario Livio (1993). “Common Envelopes in Binary Star Evolution”. In: PASP 105, p. 1373.

Inomata, Keisuke et al. (2017). “Inflationary primordial black holes for the LIGO gravitational wave events and pulsar timing array experiments”. In: Phys. Rev. D 95.12, 123510, p. 123510.

Ivanova, N. and S. Chaichenets (2011). “Common Envelope: Enthalpy Consideration”. In: ApJ 731.2, L36, p. L36.

Ivanova, N. and R. E. Taam (2004). “Thermal Timescale Mass Transfer and the Evolution of White Dwarf Binaries”. In: ApJ 601, pp. 1058–1066.

Ivanova, N. et al. (2008). “Formation and evolution of compact binaries in globular clusters - II. Binaries with neutron stars”. In: MNRAS 386, pp. 553–576.

Ivanova, N. et al. (2013). “Common envelope evolution: where we stand and how we can move forward”. In: A&A Rev. 21, 59, p. 59.

Ivanova, N. et al. (2015). “On the role of recombination in common-envelope ejections”. In: MNRAS 447.3, pp. 2181–2197.

Izzard, Robert G. et al. (2004). “A new synthetic model for asymptotic giant branch stars”. In: MNRAS 350.2, pp. 407–426.

Janka, H.-T. (2012). “Explosion Mechanisms of Core-Collapse Supernovae”. In: *Annual Review of Nuclear and Particle Science* 62, pp. 407–451.

— (2013). “Natal kicks of stellar mass black holes by asymmetric mass ejection in fallback supernovae”. In: MNRAS 434, pp. 1355–1361.

— (2017). “Neutron Star Kicks by the Gravitational Tug-boat Mechanism in Asymmetric Supernova Explosions: Progenitor and Explosion Dependence”. In: ApJ 837, 84, p. 84.

Janka, H.-T. and E. Mueller (1994). “Neutron star recoils from anisotropic supernovae.” In: A&A 290, pp. 496–502.

Janka, H.-T. et al. (2007). “Theory of core-collapse supernovae”. In: Phys. Rep. 442, pp. 38–74.

Jin, Z.-P. et al. (2015). “The Light Curve of the Macronova Associated with the Long-Short Burst GRB 060614”. In: ApJ 811, L22, p. L22.

Jones, S. et al. (2013). “Advanced Burning Stages and Fate of 8-10 $M_\odot$ Stars”. In: ApJ 772, 150, p. 150.

Jones, S. et al. (2016). “Do electron-capture supernovae make neutron stars?. First multidimensional hydrodynamic simulations of the oxygen deflagration”. In: A&A 593, A72, A72.

Jones, Samuel et al. (2019). “A New Model for Electron-capture Supernovae in Galactic Chemical Evolution”. In: ApJ 882.2, 170, p. 170.

Kitaura, F. S. et al. (2006). “Explosions of O-Ne-Mg cores, the Crab supernova, and subluminous type II-P supernovae”. In: A&A 450, pp. 345–350.

Klencki, J. et al. (2018). “Impact of inter-correlated initial binary parameters on double black hole and neutron star mergers”. In: A&A 619, A77, A77.

Knigge, C. et al. (2011). “Two populations of X-ray pulsars produced by two types of supernova”. In: Nature 479, pp. 372–375.

Kroupa, P. (2001). “On the variation of the initial mass function”. In: MNRAS 322, pp. 231–246.

Kruckow, Matthias U. et al. (2018). “Progenitors of gravitational wave mergers: binary evolution with the stellar grid-based code COMBINE”. In: MNRAS 481.2, pp. 1908–1949.

Kudritzki, R. P. (2002). “Line-driven Winds, Ionizing Fluxes, and Ultraviolet Spectra of Hot Stars at Extremely Low Metallicity. I. Very Massive O Stars”. In: ApJ 577, pp. 389–408.

Kudritzki, R. P. et al. (1987). “Radiation driven winds of hot luminous stars. II - Wind models for O-stars in the Magellanic Clouds”. In: A&A 173, pp. 293–298.

Kudritzki, Rolf-Peter and Joachim Puls (2000). “Winds from Hot Stars”. In: ARA&A 38, pp. 613–666.

Kulkarni, S. R. et al. (1993). “Stellar black holes in globular clusters”. In: Nature 364, pp. 421–423.

Kusenko, A. et al. (2008). “Delayed pulsar kicks from the emission of sterile neutrinos”. In: Phys. Rev. D 77.12, 123009, p. 123009.

Lamberts, A. et al. (2016). “When and where did GW150914 form?” In: MNRAS 463, pp. L31–L35.

Langer, N. (2012). “Presupernova Evolution of Massive Single and Binary Stars”. In: ARA&A 50, pp. 107–164.

Laycock, Silas G. T. et al. (2015). “Revisiting the dynamical case for a massive black hole in IC10 X-1”. In: MNRAS 452.1, pp. L31–L35.

Lee, W. H. et al. (2010). “Short Gamma-ray Bursts from Dynamically Assembled Compact Binaries in Globular Clusters: Pathways, Rates, Hydrodynamics, and Cosmological Setting”. In: ApJ 720, pp. 953–975.

Leitherer, Claus et al. (1992). “Deposition of Mass, Momentum, and Energy by Massive Stars into the Interstellar Medium”. In: ApJ 401, p. 596.

Limongi, Marco (2017). “Supernovae from Massive Stars”. In: *Handbook of Supernovae, ISBN 978-3-319-21845-8. Springer International Publishing AG, 2017, p. 513*, p. 513.

Limongi, Marco and Alessandro Chieffi (2018). “Presupernova Evolution and Explosive Nucleosynthesis of Rotating Massive Stars in the Metallicity Range -3 ≤ [Fe/H] ≤ 0”. In: ApJS 237.1, 13, p. 13.

Livio, Mario and Noam Soker (1988). “The Common Envelope Phase in the Evolution of Binary Stars”. In: ApJ 329, p. 764.

Loveridge, A. J. et al. (2011). “Analytical Expressions for the Envelope Binding Energy of Giants as a Function of Basic Stellar Parameters”. In: ApJ 743, 49, p. 49.

Lyne, A. G. and D. R. Lorimer (1994). “High birth velocities of radio pulsars”. In: Nature 369, pp. 127–129.

Lyne, A. G. et al. (2004). “A Double-Pulsar System: A Rare Laboratory for Relativistic Gravity and Plasma Physics”. In: *Science* 303, pp. 1153–1157.

Madau, P. and M. Dickinson (2014). “Cosmic Star-Formation History”. In: ARA&A 52, pp. 415–486.

Madau, Piero and Tassos Fragos (2017). “Radiation Backgrounds at Cosmic Dawn: X-Rays from Compact Binaries”. In: ApJ 840.1, 39, p. 39.

Maggiore, M. (2008). “BOOK REVIEW: Gravitational Waves, Volume 1: Theory and Experiments”. In: *Classical and Quantum Gravity* 25.20, 209002, p. 209002.

Maiolino, R. et al. In:

Mandel, I. and S. E. de Mink (2016). “Merging binary black holes formed through chemically homogeneous evolution in short-period stellar binaries”. In: MNRAS 458, pp. 2634–2647.

Mannucci, F. et al. (2009). “LSD: Lyman-break galaxies Stellar populations and Dynamics - I. Mass, metallicity and gas at z ˜ 3.1”. In: MNRAS 398, pp. 1915–1931.

Mapelli, M. (2016). “Massive black hole binaries from runaway collisions: the impact of metallicity”. In: MNRAS 459, pp. 3432–3446.

Mapelli, M. and N. Giacobbo (2018). “The cosmic merger rate of neutron stars and black holes”. In: MNRAS 479, pp. 4391–4398.

Mapelli, M. and L. Zampieri (2014). “Roche-lobe Overflow Systems Powered by Black Holes in Young Star Clusters: The Importance of Dynamical Exchanges”. In: ApJ 794, 7, p. 7.

Mapelli, M. et al. (2005). “The fingerprint of binary intermediate-mass black holes in globular clusters: suprathermal stars and angular momentum alignment”. In: MNRAS 364, pp. 1315–1326.

Mapelli, M. et al. (2009). “Low metallicity and ultra-luminous X-ray sources in the Cartwheel galaxy”. In: MNRAS 395, pp. L71–L75.

Mapelli, M. et al. (2010). “Ultra-luminous X-ray sources and remnants of massive metal-poor stars”. In: MNRAS 408, pp. 234–253.

Mapelli, M. et al. (2013). “Dynamics of stellar black holes in young star clusters with different metallicities - I. Implications for X-ray binaries”. In: MNRAS 429, pp. 2298–2314.

Mapelli, M. et al. (2017). “The cosmic merger rate of stellar black hole binaries from the Illustris simulation”. In: MNRAS 472, pp. 2422–2435.

Mapelli, Michela et al. (2018). “The host galaxies of double compact objects merging in the local Universe”. In: MNRAS 481.4, pp. 5324–5330.

Marchant, P. et al. (2016). “A new route towards merging massive black holes”. In: A&A 588, A50, A50.

Margutti, R. et al. (2017). “The Electromagnetic Counterpart of the Binary Neutron Star Merger LIGO/Virgo GW170817. V. Rising X-Ray Emission from an Off-axis Jet”. In: ApJ 848.2, p. L20.

Mennekens, N. and D. Vanbeveren (2014). “Massive double compact object mergers: gravitational wave sources and r-process element production sites”. In: A&A 564, A134, A134.

Meynet, G. and A. Maeder (2005). “Stellar evolution with rotation. XI. Wolf-Rayet star populations at different metallicities”. In: A&A 429, pp. 581–598.

Mirabel, I. F. and I. Rodrigues (2003). “Formation of a Black Hole in the Dark”. In: *Science* 300, pp. 1119–1121.

Mirabel, I. F. et al. (2001). “A high-velocity black hole on a Galactic-halo orbit in the solar neighbourhood”. In: Nature 413, pp. 139–141.

Mirabel, I. F. et al. (2002). “The runaway black hole GRO J1655-40”. In: A&A 395, pp. 595–599.

Miyaji, S. et al. (1980). “Supernova Triggered by Electron Captures”. In: PASJ 32, p. 303.

Muijres, L. E. et al. (2012). “Predictions for mass-loss rates and terminal wind velocities of massive O-type stars”. In: A&A 537, A37, A37.

Müller, B. (2016). “The Status of Multi-Dimensional Core-Collapse Supernova Models”. In: PASA 33, e048, e048.

Nagakura, Hiroki et al. (2019). “Possible Early Linear Acceleration of Proto-neutron Stars via Asymmetric Neutrino Emission in Core-collapse Supernovae”. In: ApJ 880.2, L28, p. L28.

Nelemans, G. et al. (1999). “Constraints on mass ejection in black hole formation derived from black hole X-ray binaries”. In: A&A 352, pp. L87–L90.

Nicholl, M. et al. (2017). “The Electromagnetic Counterpart of the Binary Neutron Star Merger LIGO/Virgo GW170817. III. Optical and UV Spectra of a Blue Kilonova from Fast Polar Ejecta”. In: ApJ 848.2, p. L18.

Nieuwenhuijzen, H. and C. de Jager (1990). “Parametrization of stellar rates of mass loss as functions of the fundamental stellar parameters M, L, and R.” In: A&A 231, pp. 134–136.

Nomoto, K. (1984). “Evolution of 8-10 solar mass stars toward electron capture supernovae. I - Formation of electron-degenerate O + Ne + Mg cores”. In: ApJ 277, pp. 791–805.

— (1987). “Evolution of 8-10 solar mass stars toward electron capture supernovae. II - Collapse of an O + Ne + Mg core”. In: ApJ 322, pp. 206–214.

Nomoto, K. and Y. Kondo (1991). “Conditions for accretion-induced collapse of white dwarfs”. In: ApJ 367, pp. L19–L22.

Ober, W. W. et al. (1983). “Evolution of Massive Pregalactic Stars - Part Two - Nucleosynthesis in Pair Creation Supernovae and Pregalactic Enrichment”. In: A&A 119, p. 61.

O’Connor, E. and C. D. Ott (2011). “Black Hole Formation in Failing Core-Collapse Supernovae”. In: ApJ 730, 70, p. 70.

Oppenheimer, J. R. and G. M. Volkoff (1939). “On Massive Neutron Cores”. In: *Physical Review* 55, pp. 374–381.

Özel, F. et al. (2010). “The Black Hole Mass Distribution in the Galaxy”. In: ApJ 725, pp. 1918–1927.

Paczynski, B. (1976). “Common Envelope Binaries”. In: *Structure and Evolution of Close Binary Systems*. Ed. by Peter Eggleton et al. Vol. 73. IAU Symposium, p. 75.

Paxton, Bill et al. (2011). “Modules for Experiments in Stellar Astrophysics (MESA)”. In: ApJS 192.1, 3, p. 3.

Pejcha, O. and J. L. Prieto (2015). “On the Intrinsic Diversity of Type II-Plateau Supernovae”. In: ApJ 806, 225, p. 225.

Peters, P. C. (1964). “Gravitational Radiation and the Motion of Two Point Masses”. In: *Phys. Rev.* 136 (4B), B1224–B1232.

Petrillo, C. E. et al. (2013). “Compact Object Coalescence Rate Estimation from Short Gamma-Ray Burst Observations”. In: ApJ 767, 140, p. 140.

Petrov, B. et al. (2016). "Two bi-stability jumps in theoretical wind models for massive stars and the implications for luminous blue variable supernovae". In: MNRAS 458, pp. 1999–2011.

Petrovich, C. and F. Antonini (2017). "Greatly Enhanced Merger Rates of Compact-object Binaries in Non-spherical Nuclear Star Clusters". In: ApJ 846, 146, p. 146.

Pfahl, E. et al. (2002). "A New Class of High-Mass X-Ray Binaries: Implications for Core Collapse and Neutron Star Recoil". In: ApJ 574, pp. 364–376.

Phinney, F. S. (1996). "Binaries and Pulsars in Globular Clusters". In: *The Origins, Evolution, and Destinies of Binary Stars in Clusters*. Ed. by E. F. Milone and J.-C. Mermilliod. Vol. 90. Astronomical Society of the Pacific Conference Series, p. 163.

Pian, E. et al. (2017). "Spectroscopic identification of r-process nucleosynthesis in a double neutron-star merger". In: Nature 551, pp. 67–70.

Planck Collaboration et al. (2016). "Planck 2015 results. XIII. Cosmological parameters". In: A&A 594, A13, A13.

Podsiadlowski, P. et al. (2004). "The Effects of Binary Evolution on the Dynamics of Core Collapse and Neutron Star Kicks". In: ApJ 612, pp. 1044–1051.

Podsiadlowski, P. et al. (2005). "The double pulsar J0737-3039: testing the neutron star equation of state". In: MNRAS 361, pp. 1243–1249.

Podsiadlowski, Philipp (2001). "Common-Envelope Evolution and Stellar Mergers". In: *Evolution of Binary and Multiple Star Systems*. Ed. by Ph. Podsiadlowski et al. Vol. 229. Astronomical Society of the Pacific Conference Series, p. 239.

Poelarends, A. J. T. (2007). "Stellar evolution on the borderline of white dwarf and neutron star formation". PhD thesis. Utrecht University.

Poelarends, A. J. T. et al. (2017). "Electron Capture Supernovae from Close Binary Systems". In: ApJ 850, 197, p. 197.

Portegies Zwart, S. F. and S. L. W. McMillan (2000). "Black Hole Mergers in the Universe". In: ApJ 528, pp. L17–L20.

Portegies Zwart, S. F. and F. Verbunt (1996a). "Population synthesis of high-mass binaries." In: A&A 309, pp. 179–196.

— (1996b). "Population synthesis of high-mass binaries." In: A&A 309, pp. 179–196.

Portegies Zwart, S. F. and L. R. Yungelson (1998). "Formation and evolution of binary neutron stars". In: A&A 332, pp. 173–188.

Postnov, K. A. and A. G. Kuranov (2019). "Black hole spins in coalescing binary black holes". In: MNRAS 483.3, pp. 3288–3306.

Prestwich, A. H. et al. (2007). "The Orbital Period of the Wolf-Rayet Binary IC 10 X-1: Dynamic Evidence that the Compact Object Is a Black Hole". In: ApJ 669.1, pp. L21–L24.

Rafelski, M. et al. (2012). "Metallicity Evolution of Damped Lyα Systems Out to z ~ 5". In: ApJ 755, 89, p. 89.

Rastello, S. et al. (2019). "Stellar black hole binary mergers in open clusters". In: MNRAS 483.1, pp. 1233–1246.

Repetto, S. et al. (2012). "Investigating stellar-mass black hole kicks". In: MNRAS 425, pp. 2799–2809.

Repetto, S. et al. (2017). "The Galactic distribution of X-ray binaries and its implications for compact object formation and natal kicks". In: MNRAS 467, pp. 298–310.

Rodriguez, C. L. et al. (2015). "Binary Black Hole Mergers from Globular Clusters: Implications for Advanced LIGO". In: *Physical Review Letters* 115.5, 051101, p. 051101.

Rodriguez, C. L. et al. (2016). "Illuminating Black Hole Binary Formation Channels with Spins in Advanced LIGO". In: ApJ 832, L2, p. L2.

Sagert, I. and J. Schaffner-Bielich (2008). "Pulsar kicks by anisotropic neutrino emission from quark matter in strong magnetic fields". In: A&A 489, pp. 281–289.

Sana, H. et al. (2012). "Binary Interaction Dominates the Evolution of Massive Stars". In: *Science* 337, p. 444.

Sana, H. et al. (2013). "The VLT-FLAMES Tarantula Survey. VIII. Multiplicity properties of the O-type star population". In: A&A 550, A107, A107.

Sathyaprakash, B. S. and B. F. Schutz (2009). "Physics, Astrophysics and Cosmology with Gravitational Waves". In: *Living Reviews in Relativity* 12, 2, p. 2.

Savchenko, V. et al. (2017). "INTEGRAL Detection of the First Prompt Gamma-Ray Signal Coincident with the Gravitational-wave Event GW170817". In: ApJ 848.2, p. L15.

Scheck, L. et al. (2006). "Multidimensional supernova simulations with approximative neutrino transport. I. Neutron star kicks and the anisotropy of neutrino-driven explosions in two spatial dimensions". In: A&A 457, pp. 963–986.

Scheck, L. et al. (2008). "Multidimensional supernova simulations with approximative neutrino transport. II. Convection and the advective-acoustic cycle in the supernova core". In: A&A 477.3, pp. 931–952.

Schutz, B. F. (1989). "Sources of gravitational waves". In: *NASA Conference Publication*. Ed. by R. W. Hellings. Vol. 3046. NASA Conference Publication.

Schwab, J. et al. (2010). "Further Evidence for the Bimodal Distribution of Neutron-star Masses". In: ApJ 719, pp. 722–727.

Schwab, J. et al. (2015a). "Thermal runaway during the evolution of ONeMg cores towards accretion-induced collapse". In: MNRAS 453, pp. 1910–1927.

— (2015b). "Thermal runaway during the evolution of ONeMg cores towards accretion-induced collapse". In: MNRAS 453, pp. 1910–1927.

Sesana, Alberto (2016). "Prospects for Multiband Gravitational-Wave Astronomy after GW150914". In: Phys. Rev. Lett. 116.23, 231102, p. 231102.

Shao, Yong and Xiang-Dong Li (2018). "Black hole/pulsar binaries in the Galaxy". In: MNRAS 477.1, pp. L128–L132.

Siellez, K. et al. (2014). "Simultaneous event detection rates by electromagnetic and gravitational wave detectors in the advanced era of LIGO and Virgo". In: MNRAS 437, pp. 649–655.

Sigurdsson, S. and L. Hernquist (1993). "Primordial black holes in globular clusters". In: Nature 364, pp. 423–425.

Sigurdsson, S. and E. S. Phinney (1993). "Binary–Single Star Interactions in Globular Clusters". In: ApJ 415, p. 631.

— (1995). "Dynamics and Interactions of Binaries and Neutron Stars in Globular Clusters". In: ApJS 99, p. 609.

Silverman, Jeffrey M. and Alexei V. Filippenko (2008). "On IC 10 X-1, the Most Massive Known Stellar-Mass Black Hole". In: ApJ 678.1, p. L17.

Smartt, S. J. (2009). "Progenitors of Core-Collapse Supernovae". In: *Annual Review of Astronomy & Astrophysics* 47, pp. 63–106.

Soares-Santos, M. et al. (2017). "The Electromagnetic Counterpart of the Binary Neutron Star Merger LIGO/Virgo GW170817. I. Discovery of the Optical Counterpart Using the Dark Energy Camera". In: ApJ 848.2, p. L16.

Spera, M. and M. Mapelli (2017). "Very massive stars, pair-instability supernovae and intermediate-mass black holes with the sevn code". In: MNRAS 470, pp. 4739–4749.

Spera, M. et al. (2015). "The mass spectrum of compact remnants from the PARSEC stellar evolution tracks". In: MNRAS 451, pp. 4086–4103.

Spera, M. et al. (2016). "Shedding light on the black hole mass spectrum." In: Mem. Soc. Astron. Italiana 87, p. 575.

Spera, M. et al. (2019). "Merging black hole binaries with the SEVN code". In: MNRAS 485, pp. 889–907.

Stevenson, Simon et al. (2017). “Formation of the first three gravitational-wave observations through isolated binary evolution”. In: *Nature Communications* 8, 14906, p. 14906.

Sukhbold, T. et al. (2016). “Core-collapse Supernovae from 9 to 120 Solar Masses Based on Neutrino-powered Explosions”. In: ApJ 821, 38, p. 38.

Sukhbold, Tuguldur and S. E. Woosley (2014). “The Compactness of Presupernova Stellar Cores”. In: ApJ 783.1, 10, p. 10.

Suwa, Y. et al. (2015). “Neutrino-driven explosions of ultra-stripped Type Ic supernovae generating binary neutron stars”. In: MNRAS 454, pp. 3073–3081.

Taam, Ronald E. and Eric L. Sandquist (2000). “Common Envelope Evolution of Massive Binary Stars”. In: ARA&A 38, pp. 113–141.

Takahashi, K. et al. (2013). “Evolution of Progenitors for Electron Capture Supernovae”. In: ApJ 771, 28, p. 28.

Tang, J. et al. (2014). “New PARSEC evolutionary tracks of massive stars at low metallicity: testing canonical stellar evolution in nearby star-forming dwarf galaxies”. In: MNRAS 445, pp. 4287–4305.

Tauris, T. M. and M. Bailes (1996). “The origin of millisecond pulsar velocities.” In: A&A 315, pp. 432–444.

Tauris, T. M. and J. D. M. Dewi (2001). “Research Note On the binding energy parameter of common envelope evolution. Dependency on the definition of the stellar core boundary during spiral-in”. In: A&A 369, pp. 170–173.

Tauris, T. M. and E. P. J. van den Heuvel (2006). “Formation and evolution of compact stellar X-ray sources”. In: *Compact stellar X-ray sources*. Ed. by W. H. G. Lewin and M. van der Klis, pp. 623–665.

Tauris, T. M. et al. (2013). “Ultra-stripped Type Ic Supernovae from Close Binary Evolution”. In: ApJ 778, L23, p. L23.

Tauris, T. M. et al. (2015). “Ultra-stripped supernovae: progenitors and fate”. In: MNRAS 451, pp. 2123–2144.

Tauris, T. M. et al. (2017). “Formation of Double Neutron Star Systems”. In: ApJ 846, 170, p. 170.

Taylor, J. H. et al. (1979). “Measurements of general relativistic effects in the binary pulsar PSR1913 + 16”. In: Nature 277.5696, pp. 437–440.

Thorne, K. S. (1987). “Book-Review - Black Holes”. In: *Science* 236, p. 1007.

Timmes, F. X. et al. (1996). “The Neutron Star and Black Hole Initial Mass Function”. In: ApJ 457, p. 834.

Toonen, S. et al. (2012). “Supernova Type Ia progenitors from merging double white dwarfs. Using a new population synthesis model”. In: A&A 546, A70, A70.

Tutukov, A. et al. (1973). “Evolution of primaries of massive close binary systems”. In: *Nauchnye Informatsii* 27, p. 3.

Ugliano, M. et al. (2012). “Progenitor-explosion Connection and Remnant Birth Masses for Neutrino-driven Supernovae of Iron-core Progenitors”. In: ApJ 757, 69, p. 69.

van den Heuvel, E. P. J. (1976). “Late Stages of Close Binary Systems”. In: *Structure and Evolution of Close Binary Systems*. Ed. by Peter Eggleton et al. Vol. 73. IAU Symposium, p. 35.

— (2007). “Double Neutron Stars: Evidence For Two Different Neutron-Star Formation Mechanisms”. In: *The Multicolored Landscape of Compact Objects and Their Explosive Origins*. Ed. by T. di Salvo et al. Vol. 924. American Institute of Physics Conference Series, pp. 598–606.

van Loon, J. Th. et al. (2005). “An empirical formula for the mass-loss rates of dust-enshrouded red supergiants and oxygen-rich Asymptotic Giant Branch stars”. In: A&A 438.1, pp. 273–289.

Verbunt, F. et al. (2017). “The observed velocity distribution of young pulsars”. In: A&A 608, A57, A57.

Vigna-Gómez, Alejandro et al. (2018). “On the formation history of Galactic double neutron stars”. In: MNRAS 481.3, pp. 4009–4029.

Vink, J. S. and A. de Koter (2005a). “On the metallicity dependence of Wolf-Rayet winds”. In: A&A 442, pp. 587–596.

Vink, J. S. and G. Gräfener (2012). “The Transition Mass-loss Rate: Calibrating the Role of Line-driven Winds in Massive Star Evolution”. In: ApJ 751, L34, p. L34.

Vink, J. S. et al. (1999). “On the nature of the bi-stability jump in the winds of early-type supergiants”. In: A&A 350, pp. 181–196.

— (2001). “Mass-loss predictions for O and B stars as a function of metallicity”. In: A&A 369, pp. 574–588.

Vink, J. S. et al. (2011). “Wind modelling of very massive stars up to 300 solar masses”. In: A&A 531, A132, A132.

Vink, Jorick S. (2011). “The theory of stellar winds”. In: Ap&SS 336.1, pp. 163–167.

— (2017a). “Mass loss and stellar superwinds”. In: *Philosophical Transactions of the Royal Society of London Series A* 375.2105, 20160269, p. 20160269.

— (2017b). “Winds from stripped low-mass helium stars and Wolf-Rayet stars”. In: A&A 607, L8, p. L8.

— (2018). “Fast and slow winds from supergiants and luminous blue variables”. In: A&A 619, A54, A54.

Vink, Jorick S. and A. de Koter (2005b). “On the metallicity dependence of Wolf-Rayet winds”. In: A&A 442.2, pp. 587–596.

Vink, Jorick S. et al. (2010). “The nature of B supergiants: clues from a steep drop in rotation rates at 22 000 K. The possibility of Bi-stability braking”. In: A&A 512, L7, p. L7.

Voss, R. and T. M. Tauris (2003). “Galactic distribution of merging neutron stars and black holes - prospects for short gamma-ray burst progenitors and LIGO/VIRGO”. In: MNRAS 342, pp. 1169–1184.

Wang, Chen et al. (2016). “The binding energy parameter for common envelope evolution”. In: *Research in Astronomy and Astrophysics* 16.8, 126, p. 126.

Webbink, R. F. (1984). “Double white dwarfs as progenitors of R Coronae Borealis stars and Type I supernovae”. In: ApJ 277, pp. 355–360.

— (1985). “Stellar evolution and binaries”. In: *Interacting Binary Stars*. Ed. by J. E. Pringle and R. A. Wade, p. 39.

Wong, Kaze W. K. et al. (2018). “Expanding the LISA Horizon from the Ground”. In: Phys. Rev. Lett. 121.25, 251102, p. 251102.

Wong, T.-W. et al. (2014). “Understanding Compact Object Formation and Natal Kicks. IV. The Case of IC 10 X-1”. In: ApJ 790, 119, p. 119.

Wongwathanarat, A. et al. (2013). “Three-dimensional neutrino-driven supernovae: Neutron star kicks, spins, and asymmetric ejection of nucleosynthesis products”. In: A&A 552, A126, A126.

Woosley, S. E. (1987). “The birth of neutron stars”. In: *The Origin and Evolution of Neutron Stars*. Ed. by D. J. Helfand and J.-H. Huang. Vol. 125. IAU Symposium, pp. 255–270.

— (2017). “Pulsational Pair-instability Supernovae”. In: ApJ 836.2, 244, p. 244.

Woosley, S. E. et al. (2007). “Pulsational pair instability as an explanation for the most luminous supernovae”. In: Nature 450, pp. 390–392.

Wysocki, Daniel et al. (2018). “Reconstructing phenomenological distributions of compact binaries via gravitational wave observations”. In: *arXiv e-prints*, arXiv:1805.06442, arXiv:1805.06442.

Xu, X.-J. and X.-D. Li (2010). “On the Binding Energy Parameter λ of Common Envelope Evolution”. In: ApJ 716, pp. 114–121.

Yoon, S. C. et al. (2010). “Type Ib/c Supernovae in Binary Systems. I. Evolution and Properties of the Progenitor Stars”. In: ApJ 725.1, pp. 940–954.

Yoshida, T. et al. (2016). “Presupernova neutrino events relating to the final evolution of massive stars”. In: Phys. Rev. D 93.12, 123012, p. 123012.

Zhang, Jianwei et al. (2019). “The mass distribution of Galactic double neutron stars: constraints on the gravitational-wave sources like GW170817”. In: MNRAS 488.4, pp. 5020–5028.

Ziosi, B. M. et al. (2014). “Dynamics of stellar black holes in young star clusters with different metallicities - II. Black hole-black hole binaries”. In: MNRAS 441, pp. 3703–3717.

APPENDIX A: CORE-COLLAPSE SNE

In the following we summarize the main features of the rapid and delayed core-collapse SN mechanisms proposed by Fryer et al. (2012).
In both cases, compact objects form from a proto-compact object $M_{\rm pro}$ that accretes mass from the fallback material $M_{\rm fb}$ which can follow the SN explosion,

$$M_{\rm fb} = f_{\rm fb}(M_{\rm fin} - M_{\rm pro}) \,, \tag{7.1}$$

where $M_{\rm fin}$ is the final mass of the star and $f_{\rm fb}$ is the fallback factor. Starting from the baryonic mass of the compact object, $M_{\rm rem,bar} = M_{\rm pro} + M_{\rm fb}$, and considering the mass loss due to neutrinos it possible to compute the gravitational mass $M_{\rm rem,grav}$. We use the formula suggested by Timmes et al. (1996) for the NSs

$$M_{\rm rem,grav} = \frac{\sqrt{1+0.3M_{\rm rem,bar}}-1}{0.15} \,, \tag{7.2}$$

and the same approach described in Fryer et al. (2012) for BHs,

$$M_{\rm rem,grav} = 0.9 M_{\rm rem,bar} \,. \tag{7.3}$$

Rapid

For the rapid mechanisms, it is assumed a fixed mass of the proto-object, $M_{\rm pro} = 1.0$ $\rm M_\odot$. The value of the fallback factor depends on the mass of the CO core $M_{\rm CO}$ and is given by

$$f_{\rm fb} = \begin{cases} \frac{0.2}{M_{\rm fin}-M_{\rm pro}} & \text{if } \rm M_{CO}/M_\odot < 2.5 \\ \frac{0.286 M_{\rm CO} - 0.514\,\rm M_\odot}{M_{\rm fin}-M_{\rm pro}} & \text{if } 2.5 \le \rm M_{CO}/M_\odot < 6.0 \\ 1.0 & \text{if } 6.0 \le \rm M_{CO}/M_\odot < 7.0 \\ \alpha_{\rm R} M_{\rm CO} + \beta_{\rm R} & \text{if } 7.0 \le \rm M_{CO}/M_\odot < 11.0 \\ 1.0 & \text{if } 11.0 \le \rm M_{CO}/M_\odot, \end{cases} \tag{7.4}$$

where

$$\alpha_{\rm R} \equiv 0.25 - \frac{1.275}{M_{\rm fin}-M_{\rm pro}} \beta_{\rm R} \equiv 1 - 11\alpha_{\rm R} \,. \tag{7.5}$$

The direct collapse of a star into a BH occurs when $f_{\rm fb} = 1.0$ and for the rapid model it is verified in two intervals of core masses, $6.0\,\rm M_\odot \le M_{CO} < 7.0\,M_\odot$ and $11.0\,\rm M_\odot \le M_{CO}$

Delayed

For the delayed model, even the mass of the proto-compact object depends on $M_{\rm CO}$ and it is given by,

$$M_{\rm pro} = \begin{cases} 1.2\,{\rm M}_\odot & \text{if } {\rm M_{core}}/\,{\rm M}_\odot < 2.5 \\ 1.3\,{\rm M}_\odot & \text{if } 3.5 \leq {\rm M_{CO}}/\,{\rm M}_\odot < 6.0 \\ 1.4\,{\rm M}_\odot & \text{if } 6.0 \leq {\rm M_{CO}}/\,{\rm M}_\odot < 11.0 \\ 1.6\,{\rm M}_\odot & \text{if } 11.0 \leq {\rm M_{CO}}/\,{\rm M}_\odot. \end{cases} \tag{7.6}$$

The fallback factor is computed by using the following expressions

$$f_{\rm fb} = \begin{cases} \frac{0.2}{M_{\rm fin}-M_{\rm pro}} & \text{if } {\rm M_{CO}}/\,{\rm M}_\odot < 2.5 \\ \frac{0.5M_{\rm CO}-1.05\,{\rm M}_\odot}{M_{\rm fin}-M_{\rm pro}} & \text{if } 2.5 \leq {\rm M_{CO}}/\,{\rm M}_\odot < 3.5 \\ \alpha_{\rm D} M_{\rm CO} + \beta_{\rm D} & \text{if } 3.5 \leq {\rm M_{CO}}/\,{\rm M}_\odot < 11.0 \\ 1.0 & \text{if } 11.0 \leq {\rm M_{CO}}/\,{\rm M}_\odot, \end{cases} \tag{7.7}$$

where

$$\alpha_{\rm D} \equiv 0.133 - \frac{0.093}{M_{\rm fin} - M_{\rm pro}} \beta_{\rm D} \equiv 1 - 11\alpha_{\rm D}\,. \tag{7.8}$$

Thus, for the delayed model the direct collapse of a star into a BH occurs only if $11.0\,{\rm M}_\odot \leq M_{\rm CO}$.

APPENDIX B: PPISN & PISN

In the following we detail the formulas implemented in MOBSE to describe PPISNe and PISNe, following the the prescriptions described in Spera et al. (2016) and Spera and Mapelli (2017).
To compute the mass of the compact remnant we adopted the formula

$$M_{\rm rem} = f_{\rm p} M_{\rm rem,nop}, \tag{7.1}$$

where $M_{\rm rem,nop}$ is the mass of the compact remnant we would obtain without PPISNe and PISNe and $f_{\rm p}$ is a factor depending on the final Helium core mass of the star. In particular, $f_{\rm p} = 1$ means that remnants will form via direct collapse and $f_{\rm p} = 0$ means that remnants will completely destroy due to PISNe. In Fig. **??** we show the mass spectrum with/without PPISNe and PISNe for both MOBSE1 and MOBSE2 at $Z = 0.0002$.
We use the following expressions to compute $f_{\rm p}$ distinguishing between H-rich stars and WR stars.

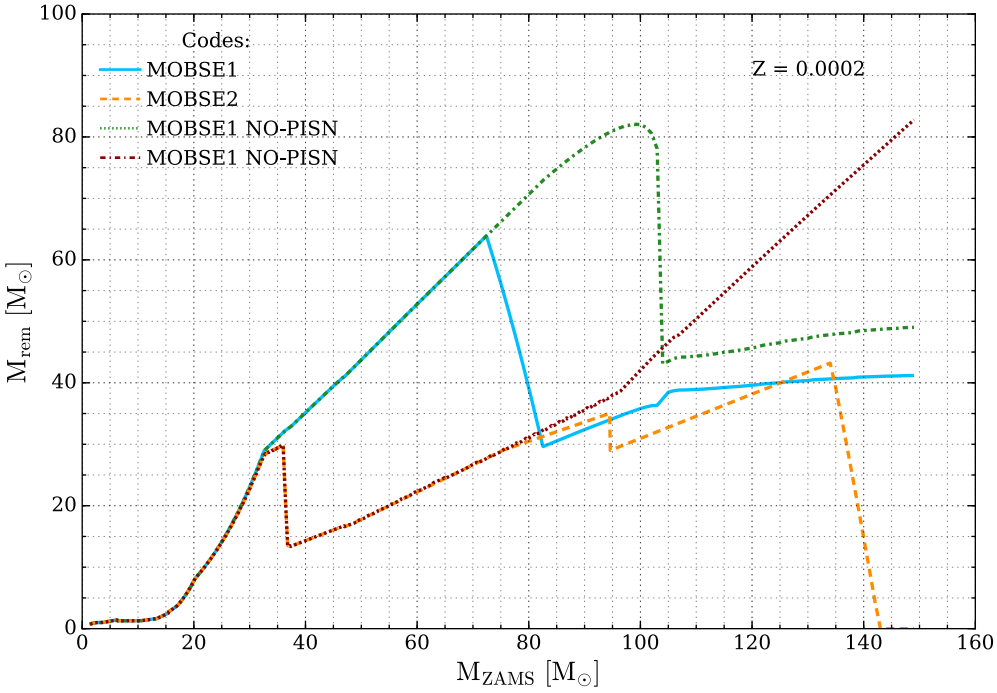

Figure B1: Effect of the PISNe and PPISNe on the mass spectrum of the remnants as a function of the $M_{\rm ZAMS}$ at $Z = 0.0002$. Solid-blue line: MOBSE1 with PISNe and PPISNe; dash-dot-green line: MOBSE1 without PISNe and PPISNe; dashed-yellow line: MOBSE2 with PISNe and PPISNe; dotted-red line: MOBSE2 without PISNe and PPISNe.

Normal stars

$$f_{\rm p} = \begin{cases} 1.0 & \text{if } \mathrm{M_{He}/M_\odot} \leq 32 \\ \frac{(\alpha_{\rm n}-1.0)}{5.0} M_{\rm He} + \frac{(37.0-32.0\alpha_{\rm n})}{5.0} & \text{if } 32 < \mathrm{M_{He}/M_\odot} \leq 37 \\ \alpha_{\rm n} & \text{if } 37 < \mathrm{M_{He}/M_\odot} \leq 60 \\ -\frac{\alpha_{\rm n}}{4.0} M_{\rm He} + 16.0\alpha_{\rm n} & \text{if } 60 < \mathrm{M_{He}/M_\odot} < 64 \\ 0.0 & \text{if } 64 \leq \mathrm{M_{He}/M_\odot} < 135 \\ 1.0 & \text{if } 135 \leq \mathrm{M_{He}/M_\odot}, \end{cases} \tag{7.2}$$

where $\alpha_{\rm n}$ is given by

$$\alpha_{\rm n} = 0.67 \frac{M_{\rm He}}{M_{\rm tot}} + 0.1. \tag{7.3}$$

WR stars

$$f_{\rm p} = \begin{cases} 1.0 \\ \quad \text{if } \mathrm{M_{He}/M_\odot} \leq 32 \\ (M_{\rm He} - 32.0)(0.5226 \frac{M_{\rm He}}{M_{\rm tot}} - 0.52974) + 1.0 \\ \quad \text{if } 32 < \mathrm{M_{He}/M_\odot} \leq 37 \\ \beta \\ \quad \text{if } 37 < \mathrm{M_{He}/M_\odot} \leq 56 \text{ and } \beta < 0.82916 \\ (-0.1381 \frac{M_{\rm He}}{M_{\rm tot}} + 0.1309)(M_{\rm He} - 56) + 0.82916 \\ \quad \text{if } 37 < \mathrm{M_{He}/M_\odot} \leq 56 \text{ and } \beta \geq 0.82916 \\ -0.103645 M_{\rm He} + 6.63328 \\ \quad \text{if } 56 < \mathrm{M_{He}/M_\odot} < 64 \\ 0.0 \\ \quad \text{if } 64 \leq \mathrm{M_{He}/M_\odot} < 135 \\ 1.0 \\ \quad \text{if } 135 \leq \mathrm{M_{He}/M_\odot}. \end{cases} \tag{7.4}$$

where β is given by

$$\beta = (0.5226 * M_{\rm He}/\mathrm{M_\odot} - 0.52974) * 5 + 1. \tag{7.5}$$

APPENDIX C: ECSN IN BINARY EVOLUTION

We describe the impact of binary evolution on the mass range of stars which undergo an ECSN. We consider only the case with $\sigma_{\rm ECSN} = 15$ km s^{-1} and $\sigma_{\rm CCSN} = 265$ km s^{-1}, because different assumptions on natal kicks do not affect the mass range. Thus, we analyze a sub-sample of runs EC15α1 and EC15α5 with metallicity $Z = 0.02, 0.002, 0.0002$ (we randomly select 10^5 binaries for each metallicity).

In Fig. C1, we compare the zero-age main sequence (ZAMS) mass range of single stars which undergo an ECSN (gray regions) with the ZAMS mass distribution of stars which undergo an ECSN as a consequence of binary evolution (green histograms). In agreement with previous studies (e.g. Podsiadlowski et al., 2004; Sana et al., 2012; Dunstall et al., 2015; Poelarends et al., 2017), we find that binary evolution broadens the mass range of stars undergoing an ECSN.

This happens because non-conservative mass transfer changes the mass of close binary members significantly. For instance, it can happen that a primary star with $M_{\rm ZAMS}$ up to ~ 25 M$_\odot$ loses most of its mass and enters the ECSN regime. On the other hand, if a secondary star with $M_{\rm ZAMS} \gtrsim 2.5$ M$_\odot$ accretes enough matter from the companion it can even undergo an ECSN.

The ZAMS mass range of stars undergoing ECSNe seems to be almost insensitive on the efficiency of CE, especially at high metallicity. Furthermore, the mass range mildly depends on metallicity: the lower the metallicity is, the lower the maximum mass for a star to undergo an ECSN as a consequence of mass transfer (this is likely an effect of stellar winds).

Finally, we estimate that ~ 16 per cent of NSs undergo an ECSN if $\alpha = 1$ and $Z = 0.02$, when we account for binary evolution. This percentage increases with decreasing metallicity. In particular, we find that ~ 13 per cent of SNe are ECSNe if $\alpha = 1$ and $Z = 0.002$, and ~ 8 per cent if $\alpha = 1$ and $Z = 0.0002$). If $\alpha = 5$, we find a slightly lower number of ECSNe: $\sim 13, 10, 7$ per cent at $Z = 0.02, 0.002, 0.0002$, respectively.

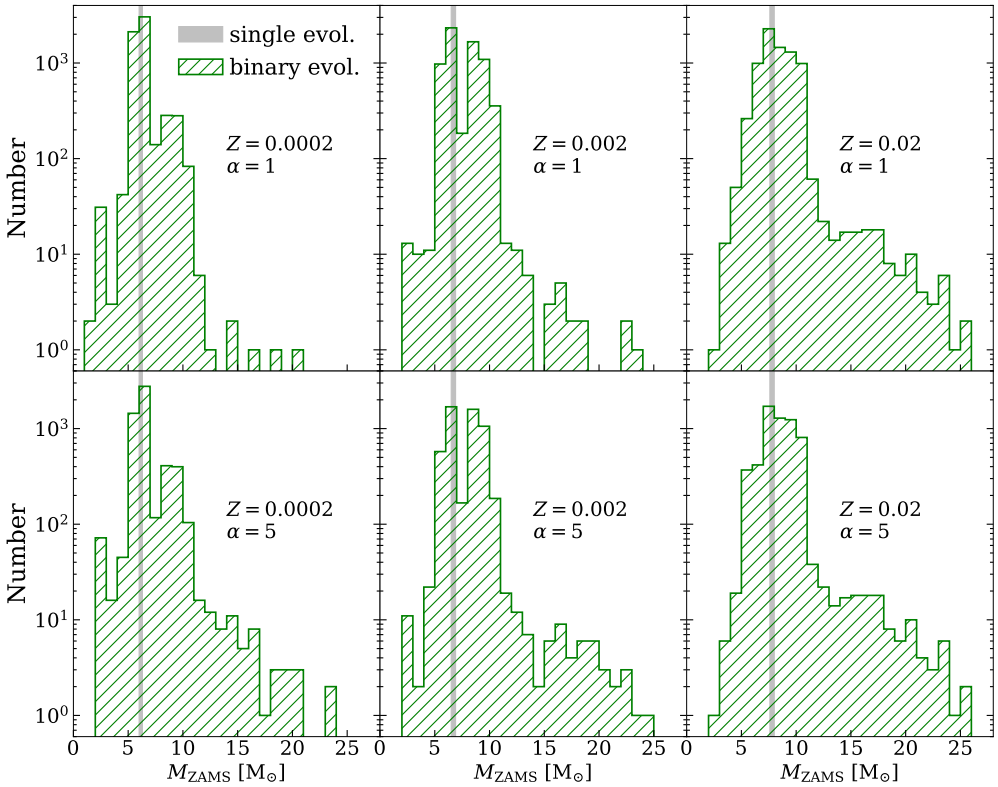

Figure C1: Green hatched histograms: distribution of the zero-age main sequence mass ($M_{\rm ZAMS}$) of binary stars undergoing an ECSN. From left to right: $Z = 0.0002, 0.002$, and 0.02, respectively. For each metallicity, we consider 10^5 binary systems randomly selected from runs EC15α1 (top) and EC15α5 (bottom). Grey shadowed regions (with arbitrary normalization): mass range of single stars undergoing an ECSN.

APPENDIX D: EFFECTS OF CE EFFICIENCY ON THE LOCAL MERGER RATE DENSITY

In the main text we have assumed a fixed value for the efficiency of CE ($\alpha = 5$). In this section, we discuss the impact of α on the merger rate density. To this purpose, we have run eight additional models varying the CE efficiency: Ej1α1, Ej1α2, Ej1α3 and Ej1α4 are the same as Ej1, but for $\alpha = 1, 2, 3$ and 4, respectively. Similarly, Ej2α1, Ej2α2, Ej2α3 and Ej2α4 are the same as Ej2, but for $\alpha = 1$, 2, 3 and 4, respectively. For each model, we have run the same set of simulations as for the ones reported in Table 5.1. We find that the merger rate density of BNSs strongly correlates with the value of α. Only values of α significantly larger than 2 are consistent with the BNS merger rate density inferred from the LVC. The merger rate density of BHNSs shows basically the opposite trend, with the larger value of $R_{\rm BHNS}$ being achieved for the smaller values of α. Finally, the merger rate density of BBHs seems to indicate a bell-shaped dependence on α, with the larger values of $R_{\rm BBH}$ obtained for $\alpha \sim 2-3$. In a follow-up paper, we will discuss the physical motivations of this behavior.

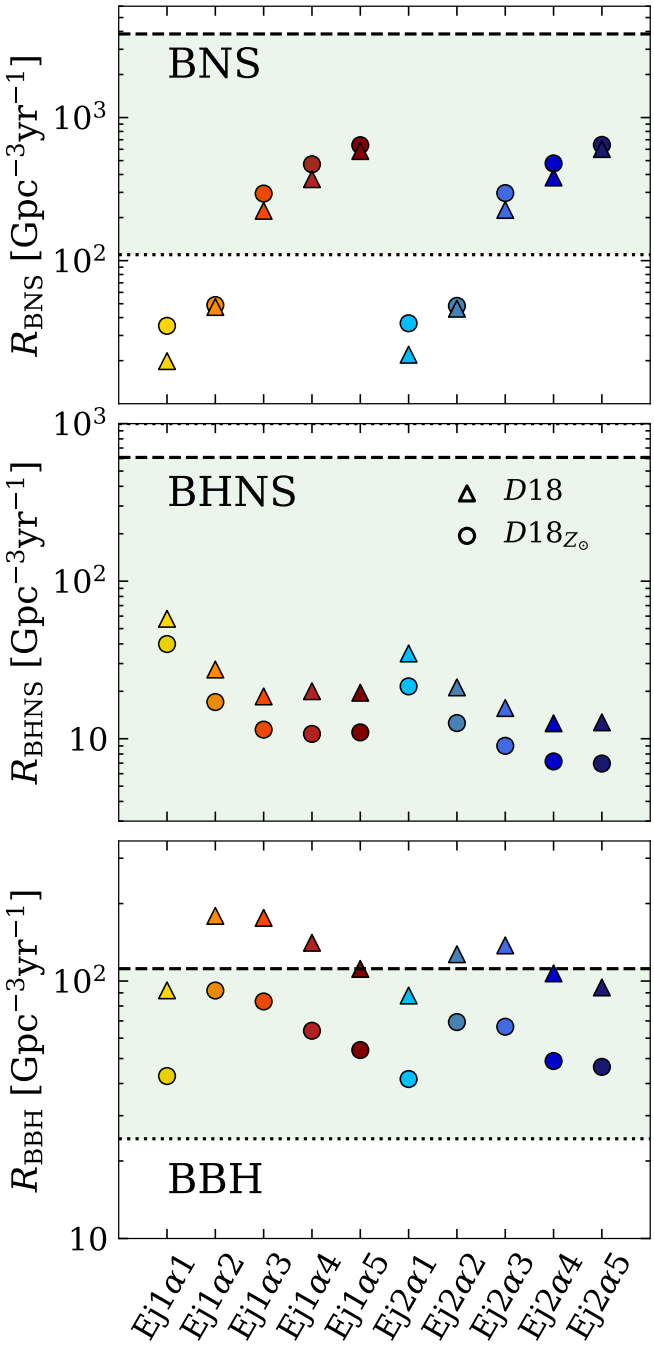

Figure D1: Local merger rate density R from eq. 5.5. Same as Figure 5.4, but here we consider only models Ej1 and Ej2 and we investigate the effect of different values of CE efficiency α =1, 2, 3, 4 and 5 (corresponding to models Ej1α1/Ej2α1, Ej1α2/Ej2α2, Ej1α3/Ej2α3, Ej1α4/Ej2α4 and Ej1α5/Ej2α5). Models labeled as Ej1α5 and Ej2α5 are the same as our models Ej1 and Ej2 in the rest of the paper (hence $\alpha = 5$).